THE UNIVERSITY OF
WARWICK

University of Warwick institutional repository: http://go.warwick.ac.uk/wrap

A Thesis Submitted for the Degree of PhD at the University of Warwick

http://go.warwick.ac.uk/wrap/58600

This thesis is made available online and is protected by original copyright.

Please scroll down to view the document itself.

Please refer to the repository record for this item for information to help you to cite it. Our policy information is available from the repository home page.

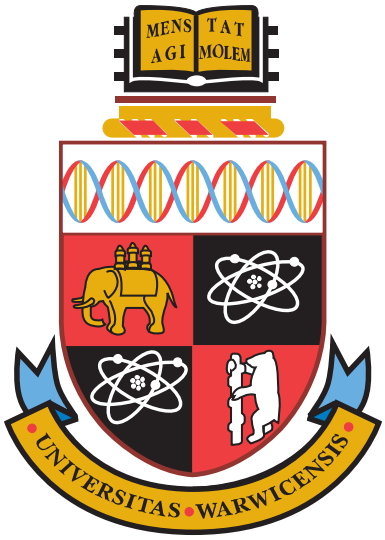

Optical and magnetic resonance studies of point defects in single crystal diamond

by

Ben L. Green

Thesis

Submitted to the University of Warwick

for the degree of

Doctor of Philosophy

Department of Physics

June 2013

THE UNIVERSITY OF WARWICK

Contents

List of Tables

List of Figures

Acknowledgments

This thesis is the product of extraordinary support by a great many people over the past four years. First and foremost I am indebted to Prof. Mark Newton and Dr. Chris Welbourn for expert supervision and guidance, and for steering me into producing enough coherent work for this thesis despite my propensity for being easily distracted. On a personal note, I would like to thank both Mark and Chris for being generous with their time and advice going well beyond the remit of academic supervision, and for having made the past four years truly enjoyable.

I am very grateful to the research team at the Gemological Institute of America (GIA) for both funding and support, and the Diamond Trading Company (DTC) Research Centre group for helpful comments. I am particularly thankful to Dr. Wuyi Wang for his insightful suggestions and for a fantastic industrial placement in New York; and to Dr. David Fisher for early, illuminating discussions. Prof. Michael Baker and Dr. Jon Goss are acknowledged for their many astute comments. Additionally, the mechanical workshop team at Warwick (especially Andy), who made many of the experiments in this thesis possible, are thanked profusely.

I want to thank the whole Warwick Diamond group, every one of whom has taught me something new: Bianca, Andy and Stephanie for putting up with my early idiosyncrasies and for sharing their wisdom; Ulrika for showing me the value of an approach I couldn't understand; Chris for emotional support and a willing ear; Matt for his talent of exposing my ignorance; Mika for endless coffee and for reminding me that there's a bright side to every situation; and Ben and Anton for educating me in spin relaxation and high-frequency microwaves, respectively.

I am grateful to the "PhysicsBoys" Andy, Ash, Ben, Matt and Steve for making my time at Warwick as exciting and enjoyable (and, at times, bearable) as it possibly could be.

I give special thanks to Holly for her constant love and support, for knowing when to push and when to console, and for sharing with me the highs and lows that are a feature of PhD projects.

Finally, I thank my brother, Mum and Dad for their unwavering love and belief in me: it is to them that I dedicate this thesis.

Declaration and published work

I declare that the work presented in this thesis is my own except where stated otherwise, and was carried out entirely at the University of Warwick, during the period of October 2009 to March 2013, under the supervision of Prof. Mark Newton and Dr. Chris Welbourn. The research reported here has not been submitted, either wholly or in part, in this or any other academic institution for admission to a higher degree.

Some parts of the work reported and other work not reported in this thesis have been published, as listed below. It is anticipated that further parts of this work will be submitted for publication in due course.

Published papers

1. P. Kowalska, J. R. Cheeseman, K. Razmkhah, B. Green, L. A. Nafie and A. Rodger, Anal. Chem. **84**(3), 1394 (2012)

2. U. F. S. D'Haenens-Johansson, A. M. Edmonds, B. L. Green, M. E. Newton, G. Davies, P. M. Martineau, R. U. A. Khan, and D. J. Twitchen, Phys. Rev. B **84**(24), 245208 (2011)

Conference presentations and seminar

1. B. L. Green, M. E. Newton and C. M. Welbourn, *Irradiation damage in boron-doped diamond*, Gordon Research Conference — Defects in Semiconductors, University of New England, United States of America, poster presentation (2012)

2. B. L. Green, M. E. Newton, C. M. Welbourn, *Is the 648 nm system the boron interstitial?*, 63rd De Beers Diamond Conference, University of Warwick, Coventry, United Kingdom, oral presentation (2012)

3. B. L. Green, M. E. Newton and C. M. Welbourn, *Uniaxial stress study of the 648 nm system in diamond*, 62nd De Beers Diamond Conference, University of Warwick, Coventry, United Kingdom, poster presentation (2011)

4. B. L. Green, M. E. Newton and C. M. Welbourn, *Uniaxial stress study of the 648 nm system in diamond*, 26th International Conference on Defects in Semiconductors, Nelson, New Zealand, poster presentation (2011)

5. U. F. S. D'Haenens-Johansson, A. M. Edmonds, B. L. Green, M. E. Newton, G. Davies, P. M. Martineau, R. U. A. Khan, and D. J. Twitchen, *Optical properties of the neutral silicon split-vacancy centre in diamond*, Heraeus Seminar: Diamond — spintronics, photonics and bio-applications, Physikzentrum, Bad Honnef, Germany, poster presentation (2011)

6. S. Liggins, B. L. Green, M. E. Newton and C. M. Welbourn, *Optical studies of neutron irradiation damage in natural & synthetic diamond*, 61st De Beers Diamond Conference, University of Warwick, Coventry, United Kingdom, poster presentation (2010)

Abstract

This thesis reports research on point defects in single crystal diamond studied by a number of techniques including electron paramagnetic resonance (EPR), ultraviolet-visible absorption (UV-Vis), photoluminescence (PL) and infrared absorption (IR). Natural diamond samples have been investigated, in addition to high pressure high temperature (HPHT) and chemical vapour deposition (CVD) grown synthetic diamond samples.

The effects of low temperature electron irradiation on boron-doped synthetic diamond have been studied. For samples irradiated with $5 \times 10^{17}\,\mathrm{e^-\,cm^{-2}}$ at 100 K, the post-irradiation neutral boron and neutral vacancy concentrations are found to depend approximately linearly on the starting boron concentration in each sample. A CVD-grown sample is annealed and characterised at each annealing stage by PL, IR and UV-Vis. The results are explained in a model whereby some interstitials are mobile during irradiation and complex with the boron: there is no evidence for the interaction of boron and vacancies.

The 1.913 eV (648.2 nm) photoluminescence transition is studied in type IIb diamond samples under applied uniaxial stress. The transition is found to occur between states of A′ & A″ symmetry. An associated local mode with energy 178.2 meV ($1437\,\mathrm{cm^{-1}}$) is determined to have A′ symmetry. The emission is tentatively ascribed to a boron-containing interstitial complex. Complications of performing uniaxial stress on natural samples are discussed with reference to the 2.526 eV (490.8 nm) emission observed in plastically deformed type IIa diamond.

Using ^{15}N-doped HPHT-grown diamond, a new EPR spectrum is observed and identified as belonging to $(\mathrm{NVN})^-$. Hyperfine analysis shows that the unpaired electron probability density is localised approximately 100 % on the two nearest-neighbour carbon atoms. Using estimates of the ^{14}N quadrupolar interaction strength, $(\mathrm{NVN})^-$ is identified in a ^{14}N-doped synthetic diamond.

The P2 spectrum is created in a ^{15}N-doped synthetic sample following irradiation and HPHT annealing. The published spin Hamiltonian parameters are significantly improved upon and for the first time the P2 spectrum is unambiguously assigned to $(\mathrm{N_3V})^0$. Both $(^{15}\mathrm{N_3V})^0$ and $(^{15}\mathrm{N_s})^0$ are shown to spin polarise upon illumination with light of energy > 2.4 eV, with $(^{15}\mathrm{N_s})^0$ spin polarisation argued to arise due to long-range interaction with $(^{15}\mathrm{N_3V})^0$.

Abbreviations

[X]	Concentration of X
AC	Alternating current
c	Speed of light
CBM	Conduction band minimum
CVD	Chemical vapour deposition
CW	Continuous wave
CWEPR	Continuous wave electron paramagnetic resonance
DFT	Density functional theory
E_A	Activation energy
E_C	Conduction band minimum energy
E_V	Valence band maximum energy
EM	Electromagnetic
ENDOR	Electron nuclear double resonance
EPR	Electron paramagnetic resonance
FTIR	Fourier transform infrared
FTEPR	Fourier transform electron paramagnetic resonance
FWHM	Full width at half maximum
$\hbar\Omega$	Energy of a phonon
$\hbar\omega$	Energy of a photon
HPHT	High pressure high temperature
IR	Infrared absorption
λ	Wavelength of light

LVM	Local vibrational mode
m_e	Mass of an electron
m_p	Mass of a proton
MPCVD	Microwave plasma chemical vapour deposition
NMR	Nuclear magnetic resonance
PC	Personal computer
PL	Photoluminescence
ppm	Parts per million atomic density
T_d	Threshold displacement energy
UV-Vis	Ultraviolet-visible absorption
VBM	Valence band maximum
ZPL	Zero-phonon line

Chapter 1

Introduction

The exploitation of diamond-related technologies has been steadily accelerating over the last half-century. Whilst diamond has been prized since antiquity for its visual properties, it is only within the last 100 years that its material properties have begun to be exploited outside the gem industry.

In addition to its more traditional roles in industrial machining and abrasives, diamond is now being employed as an electrochemical sensor [1–4], as a window and heat transport material for microwave sources and high-power infrared lasers [5–8], in high resolution magnetometers [9, 10], and even in active electronics [11]. Furthermore, there is currently a strong focus on certain defects in diamond for potential quantum computing and cryptography applications [12–17].

All of these applications rely on diamond's extraordinary material properties: diamond possesses extreme hardness [18]; the highest room-temperature thermal conductivity of any material [18]; can be doped from electrical insulator to superconductor [19]; is chemically inert and biologically compatible [20]. However, for many technological uses it is the combination of these properties in one material that makes diamond particularly attractive. For example, in electronic heatsinking applications, its thermal conductivity and electrical insulating properties are utilised to create a material which can transport heat very quickly and which may be bonded directly to an active device. An extensive review of the mechanical properties of diamond (including recent advances) is given in [21], while table 1-1

	Si	SiC	GaN	Diamond
Bandgap (eV)	1.1	3.2	3.44	5.47
Breakdown field ($\mathrm{MV\,m^{-1}}$)	30	300	500	2000
Electron mobility ($\mathrm{cm^2\,V^{-1}\,s^{-1}}$)	1450	900	440	4500
Hole mobility ($\mathrm{cm^2\,V^{-1}\,s^{-1}}$)	480	120	200	3800
Thermal conductivity ($\mathrm{W\,m^{-1}\,K^{-1}}$)	150	500	130	2400

Table 1-1 A comparison of some of the electronic properties of various semiconductors, taken from [22, 23].

gives a brief comparison of the electrical properties of diamond relative to competitive materials.

Diamond's extreme macroscopic properties are due to its microscopic structure. Carbon atoms in diamond adopt a face-centred cubic lattice on a two-atom basis, with coordinates $(0, 0, 0)$ and $(\frac{1}{4}, \frac{1}{4}, \frac{1}{4})$ relative to the conventional unit cell (see figure 1-1). Diamond is therefore a homonuclear material composed of carbon atoms tetrahedrally connected by covalent sp^3 bonds [20]. The 1.54 Å sp^3 bonds are short (c.f. 5.67 and 5.43 Å for silicon and germanium, respectively [24]) and as a result, diamond exhibits the highest atomic density of any solid at $1.76 \times 10^{23}\,\mathrm{cm^{-3}}$ [25]. A combination of the atomic density and high C-C bond energy ($83\,\mathrm{kcal\,mol^{-1}}$) lends diamond its strength, hardness and thermal conductivity [25].

1.1 Defects and impurities

The properties of diamond, as a wide band gap semiconductor, are sensitive to impurity and defect concentrations on the order of parts per million (ppm) and lower. Early spectroscopic investigations on diamond noted that samples fell broadly into one of two populations, with discrimination performed by infrared (IR) absorption measurements [26]. It was later showed that the features used for classification were related to nitrogen [27–29] and boron [30, 31] (see table 1-2).

The classification system, although coarse, is still very useful even today: knowledge of the type, growth method and processing history (irradiation, annealing etc.) allows the prediction of gross optical properties for the majority of samples.

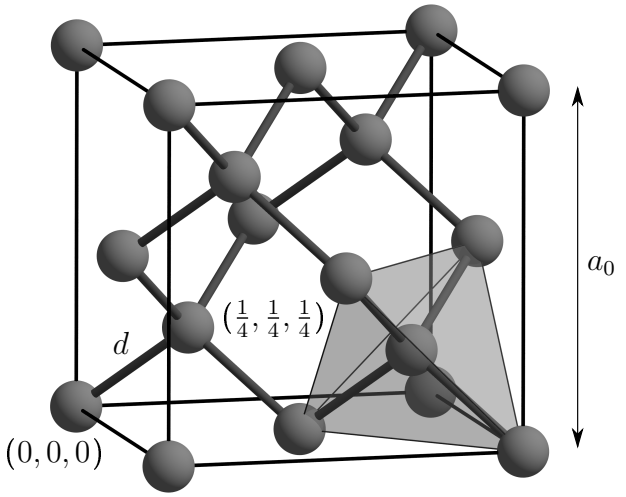

Figure 1-1 A conventional diamond unit cell, with room-temperature cell length a_0 = 3.57 Å and nearest-neighbour C-C bond length d = 1.54 Å [20]. The tetrahedral symmetry of the diamond lattice is highlighted on the right.

As diamond synthesis has improved over the last 40 years to the point where diamonds with particular properties may be grown, the understanding of trace defects, sample history importance and growth mechanisms has increased dramatically. Synthetic diamond trade now dwarfs the natural diamond market in terms of volume, with over 95 % of the mass of all diamonds sold in 2010 being artificially produced [32] (primarily for abrasive applications).

Defects in a crystalline material may be extended e.g. dislocations, inclusions, grain boundaries, or point defects e.g. interstitials, vacancies and substitutional impurities. This thesis is concerned with the study of point defects in diamond, and their effect on the optical and electronic properties of diamond.

1.2 Motivation for study

Diamond's status as a gemstone relies primarily on its superlative optical properties. There have been attempts to "improve" the optical properties of inferior diamond samples for decades, but the identification of traditional treatments (laser drilling, fracture filling and coating etc.) is now routine. Detection of synthetic samples is performed by several methods, but primarily by studying the growth

Type	Subtype	Description
I		Nitrogen concentration detectable by infrared absorption measurements ($\gtrsim 1$ ppm, approx 98 % of natural diamonds [33])
	Ia	Nitrogen impurities are aggregated
	IaA	Nitrogen is primarily in the form of two nitrogen atoms nearest neighbour, known as the A-centre [27]
	IaB	Nitrogen is primarily in the form of four nitrogen atoms surrounding a vacancy, known as the B-centre [29, 34]
	Ib	Nitrogen is incorporated as isolated substitutional atoms
II		Nitrogen concentration undetectable by infrared absorption measurements
	IIa	No nitrogen or boron detectable by infrared absorption
	IIb	Infrared absorption due to substitutional boron

Table 1-2 Diamond classification is based on spectral features observed in infrared absorption measurements: this table gives the classifications used to refer to diamonds with certain properties.

morphology of a sample under above-band-gap illumination [35, 36].

Approximately a decade ago, it was shown that high temperature high pressure treatment can improve the brown colour [37] present in a significant proportion of natural diamonds [38], significantly increasing their market value: these diamonds cannot be identified by their growth morphology alone, and more complex techniques are required for positive identification of treatment. Treatments have become steadily more sophisticated and may now involve multiple heat and / or irradiation sessions to both improve the market value of a sample, and attempt to evade detection of treatment (which lowers the monetary value of the sample). Fancy colours may be introduced: a brown nitrogen-containing diamond may be turned fancy pink by HPHT treatment, irradiation, and moderate-temperature annealing. In order to maintain confidence in the diamond gemstone market, it is vital that stones of different growth origin and treatment history are distinguishable.

This thesis employs advances in diamond synthesis and sample processing to address some of the fundamental gaps that still remain in the understanding of defects in diamond, even after decades of rigorous scientific investigation. Photoluminescence spectroscopy, a very sensitive technique routinely employed in gem

identification, is used to probe several different luminescence centres. The results are applicable both to understanding of general defects in diamond, and to the physics and possible applications of the specific defects studied.

1.3 Structure of this thesis

The remainder of this thesis proceeds as follows:

- Chapter 2 gives a background on point defects in diamond, different methods of diamond synthesis, and the effects of irradiation of intrinsic diamond.
- The theory of point groups and uniaxial stress is reviewed in chapter 3, and examples of its application to diamond are given. New calculations for interpreting uniaxial stress data in backscatter-geometry photoluminescence are tabulated.
- Chapter 4 presents background theory on experimental techniques, as well as details on some of the specific equipment used to acquire data for this thesis.
- Chapter 5 contains an irradiation and annealing study on synthetic type IIb diamond. The differences between irradiation in type I, type IIa, and type IIb diamond are discussed.
- In chapter 6, uniaxial stress photoluminescence measurements on one of the transitions identified in chapter 5 are reported in both natural and synthetic samples.
- Chapters 7 and 8 present electron paramagnetic resonance investigations of nitrogen aggregates in ^{15}N-doped synthetic diamond.
- A summary of the presented work, the conclusions, and suggested extensions are given in chapter 9.

References

1. Y. V. Pleskov, *Russian Journal of Electrochemistry* **38**, 1275 (2002).
2. N. R. Wilson *et al.*, *The Journal of Physical Chemistry B* **110**, 5639 (2006).
3. L. Hutton *et al.*, *Analytical Chemistry* **81**, 1023 (2009).
4. A. Moore *et al.*, *Chemical Communications* **47**, 7656 (2011).
5. K. Takahashi *et al.*, *Review of Scientific Instruments* **71**, 4139 (2000).
6. M. Thumm, *Diamond and Related Materials* **10**, 1692 (2001).
7. R. S. Balmer *et al.*, *Journal of Physics: Condensed Matter* **21**, 364221 (2009).
8. P. Maquet *et al.*, *Fusion Engineering and Design*, In press, Title: Development of ITER diagnostic window assemblies (2013).
9. J. M. Taylor *et al.*, *Nature Physics* **4**, 810 (2008).
10. L.-S. Bouchard *et al.*, *New Journal of Physics* **13**, 025017 (2011).
11. Y. Gurbuz *et al.*, *Solid-State Electronics* **49**, 1055 (2005).
12. A. Gruber *et al.*, *Science* **276**, 2012 (1997).
13. F. Jelezko, J. Wrachtrup, *Physica Status Solidi (A)* **203**, 3207 (2006).
14. A. M. Stoneham, A. H. Harker, G. W. Morley, *Journal of Physics: Condensed Matter* **21**, 364222 (2009).
15. P. C. Maurer *et al.*, *Science* **336**, 1283 (2012).
16. N. Mizuochi *et al.*, *Nature Photonics* **6**, 299 (2012).
17. H. Bernien *et al.*, *Nature* **497**, 86 (2013).
18. P. W. May, *Endeavour Magazine* **19**, 101 (1995).
19. E. A. Ekimov *et al.*, *Nature* **428**, 542 (2004).
20. J. E. Field, in *The Properties of Natural and Synthetic Diamond*, ed. by J. E. Field (Academic Press, London, 1992), p. 667.
21. J. E. Field, *Reports on Progress in Physics* **75**, 126505 (2012).
22. S. Hadlington, *IEE Review* **51**, 30 (2005).
23. C. D. Clark, P. J. Dean, P. V. Harris, *Proceedings of the Royal Society of London A* **277**, 312 (1964).
24. S. Kasap *et al.*, in *Springer Handbook of Electronic and Photonic Materials*, ed. by S. Kasap, P. Capper (Springer US, 2007), p. 47.
25. R. J. Narayan, R. D. Boehm, A. V. Sumant, *Materials Today* **14**, 154 (2011).

26. R. Robertson, J. J. Fox, A. E. Martin, *Philosophical Transactions A* **232**, 463 (1934).
27. G. Davies, *Journal of Physics C: Solid State Physics* **9**, L537 (1976).
28. R. M. Chrenko, R. E. Tuft, H. M. Strong, *Nature* **270**, 141 (1977).
29. J. H. N. Loubser, J. A. van Wyk, *32nd Diamond Conference* (1981).
30. A. T. Collins, A. W. S. Williams, *Journal of Physics C: Solid State Physics* **4**, 1789 (1971).
31. R. Chrenko, *Physical Review B* **7**, 4560 (1973).
32. *The Global Diamond Industry* (Bain & Company, Inc., 2011).
33. R. Berman, in *The Properties of Natural and Synthetic Diamond*, ed. by J. E. Field (Academic Press, London, 1992), p. 291.
34. R. Jones, P. R. Briddon, S. Öberg, *Philosophical Magazine Letters* **66**, 67 (1992).
35. C. Welbourn, M. Cooper, P. Spear, *Gems and Gemology* **32**, 156 (1996).
36. P. Martineau *et al.*, *Gems and Gemology* **40**, 2 (2004).
37. D. Fisher, R. A. Spits, *Gems and Gemology*, 42 (2000).
38. D. Fisher, *Lithos* **112**, 619 (2009).

Chapter 2

Point defects in diamond

This chapter presents a brief summary of those aspects of current understanding relating to diamond which are of relevance to the material in this thesis. Synthesis methods are reviewed, as are the effects of irradiation on intrinsic material. Finally, the different forms in which nitrogen is incorporated in diamond are reviewed.

2.1 Synthesis of diamond

Since the first reproducible reports of synthesis of diamond in 1955 [1], two successful and scalable methods of diamond growth have emerged: high temperature high pressure (HPHT) growth; and chemical vapour deposition (CVD) growth.

2.1.1 HPHT synthesis

HPHT synthesis replicates the thermodynamic conditions under which diamond is the stable phase of carbon (see figure 2-1). High pressures are used to stabilise diamond as the stable form during growth, and high temperatures are needed overcome the chemical kinetic cost associated with the breaking of sp^2 and formation of sp^3 bonds [2].

During HPHT synthesis, the growth materials are packed into a small growth capsule which is then loaded into the high pressure apparatus. Temperature changes

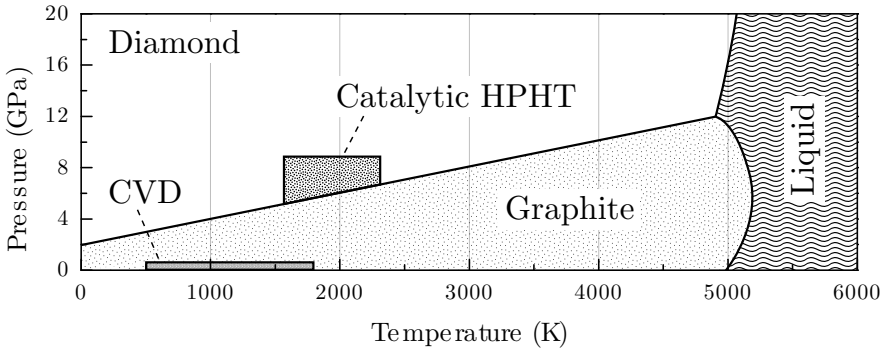

Figure 2-1 Relevant area of the carbon phase-space, adapted from [3]. The pressure range over which CVD growth is performed has been taken from [4] and is exaggerated for clarity.

are achieved by resistive heating either of internal capsule components [1, 5] or of the entire capsule externally. The carbon source, typically diamond or graphite, is transported to a seed crystal by either a solubility or temperature gradient. Direct conversion of graphite to diamond requires exceptionally high temperatures and pressures (see NCD, below); therefore the majority of HPHT diamond growth employs a metallic solvent/catalyst (usually alloys such as FeNi or FeCo [2]) to substantially lower the required temperature and pressure relative to direct conversion. Typical catalytic growth conditions are approximately 1200–1500 °C at 5–6 GPa [6–8].

HPHT diamond is grown as several different forms including single crystal, polycrystalline (PCD), and nano-polycrystalline (NCD). PCD and NCD differ not only in grain size, as the names suggest, but also in fundamental structure. PCD is sintered from diamond powder using a high-cobalt solvent/catalyst to promote inter-grain binding [9–12], and typically employs a grain size of 1–25 µm [13]; NCD is produced by direct conversion (without a catalyst) of graphite powder to diamond nanocrystals (typically 10–20 nm in size [14]) at temperatures and pressures of 2300–2500 °C and 12–25 GPa [14–17].

Details of a growth capsule and synthesis materials suitable for use in a temperature gradient system are given in §7.1, and further information on the process of HPHT synthesis is available in several reviews [2, 18].

2.1.1.1 Characteristics of HPHT-grown diamond

Where no attempt is made to prevent the inclusion of nitrogen, it is the dominant impurity incorporated into HPHT-grown diamond. Nitrogen sources include atmospheric nitrogen, solvent/catalyst impurities, and adsorbates on capsule components [7]. The addition of a nitrogen-getter such as Ti or Al can reduce the nitrogen concentration in the final material, with the drawback being the potential incorporation of the getter [19, 20].

The morphology of HPHT-grown material is a function of growth temperature and pressure [21], in addition to the growth materials used (solvent/catalyst, nitrogen getters etc.). The morphology during growth is important due to differential uptake of defects in different growth sectors [22]. For instance, nitrogen is most soluble in {1 1 1} sectors, with decreasing solubility in {1 0 0}, {1 1 3} and {1 1 0} sectors, respectively [23]. The solubility of nitrogen in diamond is very high: it has been incorporated up to 3000 ppm in single crystal diamond [24].

As with nitrogen, boron is readily included into the growing crystal if the growth capsule contains any boron source [23, 25]. Its inclusion is found to promote {1 1 5} growth, with the relative uptake of boron in different sectors dependent on the doping level [26, 27]. Boron acts an acceptor in diamond [28], with nitrogen a deep donor [29]: the overall majority carrier therefore depends on the relative concentrations of the two. Additionally, as both nitrogen and boron are incorporated with sector-dependent efficiencies and moderately-doped diamond is essentially an insulator [30], different sectors of the same diamond may conduct by different mechanisms.

Impurity uptake can have a significant effect on growth rate, in addition to growth morphology. Growth-zoning experiments, where growth conditions are modified during growth in order to leave markers for post-growth analysis, record growth rates from 12 to 180 $\mu m\,h^{-1}$ in the same sector at different points during growth [31]. There is a strong link between the growth rate, uptake of nitrogen, and uptake of metallic solvent/catalyst, with higher growth rates indicative of higher solvent/catalyst uptake [31–33].

Despite the solubility of impurities like nitrogen and boron into diamond during growth, very high purity, high crystalline quality HPHT diamond has become available in recent years [34, 35].

2.1.2 CVD synthesis

Unlike HPHT growth, which emulates natural growth conditions, CVD growth of diamond occurs outside the diamond-stable region of the carbon phase-space (figure 2-1), and relies on chemical kinetics rather than thermodynamics during growth [36].

During modern CVD growth, carbon is deposited epitaxially onto a substrate directly from the gas phase. Atomic hydrogen at the surface promotes sp^3 diamond growth by etching sp^2 carbon and hence preventing growth of graphitic carbon [36]. Activation of the reactants (primarily by dissociation of molecular hydrogen to atomic hydrogen [37]) may be achieved by several methods including direct hot-filament heating [38] and microwave plasma heating [39]. Hot-filament approaches are prone to contamination from the filament material itself (e.g. tungsten), and so the highest-purity diamond is grown by microwave plasma CVD (MPCVD) [37].

MPCVD growth operates within a very large parameter space: source gasses, temperatures, plasma shape and power density, dopant gasses, substrate material etc. are all potential variables. Typically, input gasses are H_2-CH_4 ($[H_2] \gg [CH_4]$) and growth is operated at several different temperature and plasma power density regimes, usually at a microwave frequency of 2.45 GHz [40, 41]. MPCVD growth rates may range over 1–150 $\mu m\, h^{-1}$ [42], with higher growth rates tending to produce lower film quality [43–46]. Modern reviews of MPCVD growth are available in [37, 47].

As with HPHT-grown diamond, CVD diamond can be grown in both polycrystalline and single crystalline forms. Where non-diamond substrates are used, the final material is usually polycrystalline due to a combination of lattice constant mismatch and simultaneous nucleation at multiple sites on the surface. Competition from the initially high number of differently-oriented grains (with nucleation

densities of up to $10^{12}\,\mathrm{cm}^{-2}$ [48]) acts to reduce the total number of grains as the film grows, leading to macroscopic differences between the early- and late-growth material [49].

Single crystal CVD-grown diamond can be grown on diamond substrates (homoepitaxial growth), or carefully prepared multilayer non-diamond structures (heteroepitaxial growth) [50]: using the latter method, single crystal wafers with diameters up to 100 mm have been produced [51].

In addition to the surface / bulk structure, polycrystalline and single crystal material possess different optical, electrical and mechanical properties, and hence are utilised in different application areas; [4] gives a modern overview of the applications of CVD diamond. Only single crystal diamond is investigated in this thesis.

2.1.2.1 Characteristics of CVD-grown diamond

The material and orientation used for the substrate has significant effects on the final CVD-grown material. Any crystallographic defects present at the substrate surface pre-growth will propagate through the CVD sample as it grows, leading to high dislocation densities [52–54]. Chemical etching of the substrate to remove e.g. polishing damage has been successful in reducing dislocation densities [55]. {1 0 0} substrate orientations currently allow the highest-quality single crystal growth, with low-strain HPHT substrates employed in optical applications to minimise birefringence [56, 57].

Nitrogen is often incorporated as a dominant impurity in CVD-grown material, as with HPHT-grown and natural diamond. Whilst the incorporation efficiency (probability of being incorporated onto the surface relative to that of a carbon) is low, at approximately 10^{-5}–10^{-4} [58, 59], it is difficult to exclude all sources of nitrogen from the growth atmosphere. Small quantities of nitrogen in the chamber (up to 100 ppm) are found to modify the growth morphology of the sample [58, 60–62], in addition to significant increases in growth rate by a factor of 2.5 [59]. High concentrations (up to 2 % number density in the gas phase) have a detrimental

effect on film quality [63]. Nitrogen concentrations as low as 0.2 ppb have been observed in CVD-grown material [59].

Boron-doped CVD diamond may exhibit semiconducting, metallic, or even superconducting behaviour [64, 65]. Its incorporation efficiency is much higher than nitrogen, with efficiencies as high as 10^{-2}–10^{-1} [66]. As with nitrogen, the incorporation of boron modifies the morphology of the sample during growth [43, 61, 67, 68].

Etching of silicon containing materials inside the reactor — windows, components, potentially the substrate itself — can lead to incorporation of silicon into the growing diamond [69]. In turn, silicon-related defects such as (SiV) may then be frozen-in during growth [70, 71], presumably primarily as substitutional silicon (which has yet to be identified).

Hydrogen, the dominant element in the gas phase by number density, is also incorporated into the sample during growth at levels of up to 1 atomic percent in polycrystalline material [72]. A number of hydrogen-related defects have been identified by electron paramagnetic resonance (EPR) and infrared (IR) absorption studies.

2.2 Irradiation damage in diamond

Irradiation and subsequent characterisation has long been employed in the investigation of semiconductors. Fundamental study of the irradiation-introduced damage, both intrinsic and extrinsic, can provide great insight into the physical and chemical processes occurring inside the crystal.

Scientific interest in the irradiation of diamond was first reported in 1904, with radium salts as the radiation source [73]. Increasing radiation doses were observed to impart a strong green colour to the samples. The seminal work of Clark et al. in the mid-1950s was the first systematic spectroscopic investigation into irradiation damage (and subsequent annealing) in diamond [74, 75].

When a radiation-hard material such as diamond is irradiated with high energy

particles, a constituent atom may be knocked off its lattice site if the incident particle transfers kinetic energy to the atom of greater than the threshold energy T_d (see §4.5). The exact details of the remaining damage post-irradiation depends upon the conditions under which the irradiation is performed (a discussion of irradiation conditions is given in §5.1.1), but generally irradiation will introduce both interstitials and vacancies into the lattice [76].

Irradiation damage defects can introduce new mid-gap levels as well as increase disorder in the crystal: it therefore has a profound effect on the optical and electronic properties of a given sample [74, 75, 77–81].

2.2.1 Vacancies

The vacancy in diamond has been studied extensively, both experimentally and theoretically [82]: the first spectroscopic and theoretical investigations were carried out in 1956 and 1957, respectively [74, 83].

The neutral vacancy, $(\mathrm{V})^0$, is associated with optical absorption at 1.6–3.1 eV — see figure 2-2. The most striking optical feature is the doublet at 1.673 eV (741.1 nm) and 1.665 eV (744.6 nm), which, together with its associated vibronic band, is labelled GR1. A mixture of uniaxial stress measurements [84–86] and theoretical analysis [83, 87–94] have assigned the doublet to a transition between a $^1\mathrm{E}$ ground state and $^1\mathrm{T}_2$ excited state at a centre with $\mathscr{T}_\mathrm{d}$ symmetry. Both ground and excited states undergo a dynamic Jahn-Teller distortion, with the lower-energy transition at 1.665 eV arising from **E** phonon interactions at the $^1\mathrm{E}$ state [87, 89, 91]. The transitions GR2—8 are also associated with electronic transitions at the neutral vacancy [91, 95, 96].

The ground state of $(\mathrm{V})^0$ has zero net spin [97], as in silicon [94]. However, EPR has been observed from a $^5\mathrm{A}_2$ excited state when certain samples are illuminated with light of energy quantum greater than 3.1(1) eV [98]: it is currently unclear what sample attributes are required for the observation of this state.

An optical absorption transition known as ND1, at an energy of 3.150(1) eV, was shown by uniaxial stress to arise between A_2 and T_1 states at a $\mathscr{T}_\mathrm{d}$ defect [99].

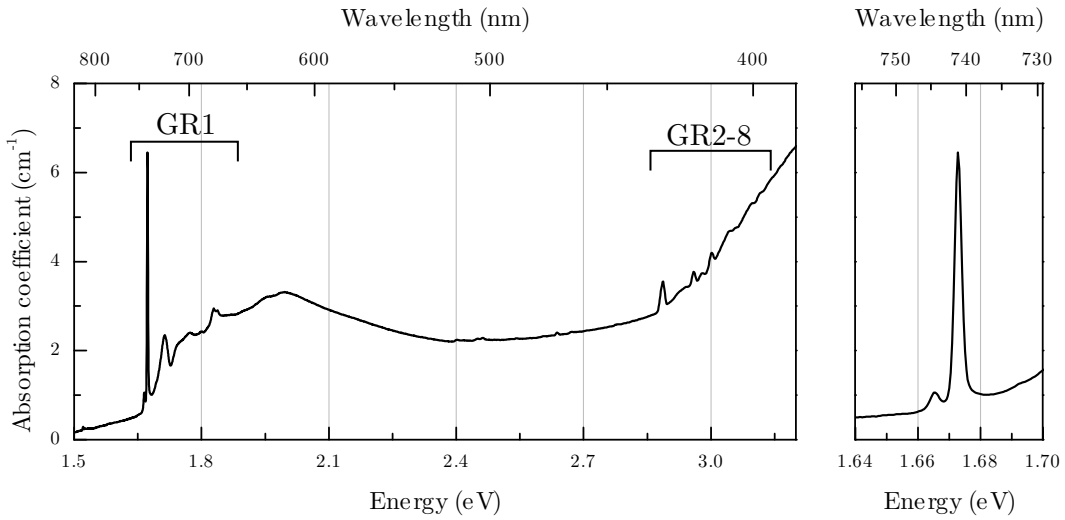

Figure 2-2 The optical absorption spectrum associated with $(V)^0$. A close-cropped view of the GR1 doublet is given to the right. Spectrum collected with the sample held at 80 K.

The transition was later assigned to $(V)^-$ by considering its relationship to GR1 in nitrogen-rich diamond [100]. The ground state is a spin-quartet $^4A_2$ state, and has been identified in EPR [101, 102]. The vacancy is observed in its negative charge state in material with a local excess of donors (see §2.3.1).

The migration of $(V)^0$ and $(V)^-$ occurs at an energy of 2.3(3) eV [79, 103]. An intermediate annealing stage is observed with an activation energy of 1.7(2) eV [104], after which the intensity of GR1 may drop by up to 15 %, and the ZPL may narrow by up to a factor of two [105]: this is associated with recombination of vacancies with nearby interstitials [103, 104].

Once $(V)^0$ becomes mobile, it may complex with other impurities to form e.g. (NV), (BV), (SiV) etc. [106]. In high-purity low-dislocation material, vacancies aggregate to form divacancies, which are identified as R4/W6 in EPR [107] and are known to correlate with the optical absorption band TH5 [108]. Higher-order vacancy aggregates are believed to give rise to a brown colouration in plastically-deformed diamond [109, 110].

2.2.2 Interstitials

There are several distinct sites for an interstitial in a tetrahedrally-coordinated homonuclear material: tetrahedral site, hexagonal, bond-centred and $\langle 0\,0\,1\rangle$- or $\langle 1\,1\,0\rangle$-split interstitials [111]. Many different theoretical investigations, using a number of different approaches, favour the $\langle 0\,0\,1\rangle$-split interstitial ($\mathrm{I}_{\langle 0\,0\,1\rangle}$) as the lowest-energy configuration [111–114].

$\mathrm{I}^0_{\langle 0\,0\,1\rangle}$ has $\mathscr{D}_{2\mathrm{d}}$ symmetry, and is known to migrate with an activation energy of 1.6 eV [103, 104]. $\mathrm{I}^0_{\langle 0\,0\,1\rangle}$ is associated with both the $S = 1$ EPR-active defect R2 [115], and optical absorption features at 1.685 and 1.859 eV [115–118]. No other charge states of $\mathrm{I}_{\langle 0\,0\,1\rangle}$ have been identified.

During irradiation, aggregation of interstitials may occur, to form the di-$\langle 0\,0\,1\rangle$-split interstitial complex R1 [119]. R1 is formed even during low-temperature ($T < 100$ K) electron irradiation [120]: this is important as it reveals that some interstitials are mobile during irradiation despite the 1.6 eV measured barrier [104]. This effect was explained by the introduction of I^*, a hypothetical highly-mobile interstitial assumed to be present during irradiation due to the ionising effects of high-energy incident electrons [103]. I^* was measured to have an effective migration energy of approximately 0.3 eV, and interstitial aggregation during low-temperature irradiation is assumed to proceed by migration of I^* [103].

2.3 Impurities in diamond

Nitrogen is the most abundant impurity in the majority of natural diamond [121], and is easily incorporated into HPHT- and CVD-grown diamond if preventative measures are not taken [2]. Dispersed substitutional nitrogen is a donor, with a deep ionisation energy of 1.7 eV [29], and the optical properties of most nitrogen-containing diamond are dominated by nitrogen-related defects.

Substitutional nitrogen, $(\mathrm{N_s})^0$, was one of the first EPR-active defects studied in diamond: its hyperfine structure and symmetry were described in 1959 [122]. In its neutral charge state the defect suffers a distortion along one of its $\langle 1\,1\,1\rangle$ bonds,

lowering its symmetry to $\mathscr{C}_{3v}$: this is due to the extra electron (of the nitrogen, effective valency +1 in diamond) occupying an anti-bonding orbital localised along one of the N-C bonds [123].

Dispersed substitutional nitrogen also gives rise to one-phonon infrared absorption; both $(N_s)^0$ [124–126] and $(N_s)^+$ [127] have been assigned characteristic one-phonon absorption spectra.

2.3.1 Nitrogen-containing aggregates

Many defects in diamond which contain one or more nitrogen atoms have been identified, several of which exist in different charge states. Substitutional nitrogen has been observed as $(N_s)^+$ [127], $(N_s)^0$ [125] and $(N_s)^-$ [128]. Nearest-neighbour nitrogen pairs are known as A centres and give rise to infrared and UV absorption in the neutral charge state [129], and EPR in the ionised state [130].

Higher aggregates tend to involve vacancies: $(NV)^0$ [131–133], $(NV)^-$ [134–137], $(NVN)^0$ [138, 139] and $(N_3V)^0$ [140–143] have all been identified in optical and EPR measurements, while the H2 optical line at 1.256 eV is thought to be $(NVN)^-$ [144–146]. The aggregation mechanisms and characteristics of nitrogen-related defects are the subject of chapters 7 and 8.

2.3.2 Hydrogen in diamond

Due to the very high concentrations of hydrogen in a CVD growth chamber, it is unsurprising that hydrogen-containing defects are frequently observed. In CVD-grown diamond, hydrogen-containing analogues of several nitrogen-vacancy aggregates have been identified: $(NVH)^-$ and $(NVH)^0$ have been identified by EPR [147, 148] and IR [149, 150], respectively. Additionally, there is growing experimental and theoretical evidence that a mid-infrared absorption transition at 3107 cm^{-1} arises at a defect with the constituents $(N_3VH)^0$ [151].

Other confirmed hydrogen-containing defects include the vacancy-hydrogen defect $(VH)^-$, identified by EPR [152], and a boron-hydrogen complex $(BH)^0$ has been

inferred from boron passivation experiments [153, 154]. A defect containing the constituents $(SiV_2H)^0$ was assigned to an EPR spectrum by a mixture of experimental analysis and first-principles calculations [70].

2.3.3 Charge transfer

The equilibrium between the neutral and negative charge states of defects in nitrogen-containing diamond depends on the acceptor levels of the defects themselves, and the local concentration of nitrogen. As noted above, $(N_s)^0$ is a donor with an ionisation energy of 1.7 eV: if a defect X^0 with an acceptor level shallower than $E_C - 1.7\,\text{eV}$ is in close proximity to $(N_s)^0$, charge transfer may occur by

$$(N_s)^0 + X^0 \rightarrow (N_s)^+ + X^- \ .$$

The proximity between the two defects required for this process to occur has been estimated as ten lattice spacings [30].

Charge transfer effects may also occur via the conduction or valence band, by excitation of a charge carrier into a band and then trapping by a distant defect. The transfer might be long-lived, as in deep traps often observed in CVD-grown material [155], or transient, as is often the case for short-range transfer effects [128, 156]. Usually, the charge carrier is ionised by application of high-energy light, and the reverse process is achieved by heating in the dark [71].

References

1. F. P. Bundy *et al.*, *Nature* **176**, 51 (1955).
2. R. Burns, G. Davies, in *The Properties of Natural and Synthetic Diamond*, ed. by J. E. Field (Academic Press, London, 1992), p. 395.
3. F. P. Bundy *et al.*, *Carbon* **34**, 141 (1996).
4. R. S. Balmer *et al.*, *Journal of Physics: Condensed Matter* **21**, 364221 (2009).
5. G. Davies, T. Evans, *Proceedings of the Royal Society of London A* **328**, 413 (1972).
6. H. Kanda, T. Sekine, in *Properties, Growth and Applications of Diamond*, ed. by M. Nazaré, A. J. Neves (IEE - Inspec, London, 2001), B1.1.
7. C. Strömann *et al.*, WO 2006/061672 (2006).
8. R. A. Spits, C. Dodge, WO 2010/082029 (2010).
9. H. Katzman, W. F. Libby, *Science*, New Series **172**, 1132 (1971).
10. S.-M. Hong *et al.*, *Journal of Materials Science Letters* **10**, 164 (1991).
11. B. Yao *et al.*, *Journal of Materials Science Letters* **14**, 931 (1995).
12. Y. Zhang *et al.*, *High Pressure Research* **29**, 325 (2009).
13. B. M. De Leeuw-Morrison, C. R. Jonker, R. W. N. Nilen, WO 2008/053430 (2008).
14. T. Irifune *et al.*, *Nature* **421**, 599 (2003).
15. H. Sumiya, T. Irifune, *Sumitomo Electric Technical Review*, 52 (2005).
16. H. Sumiya, T. Irifune, English, *Journal of Materials Research* **22**, 2345 (2007).
17. C. Xu *et al.*, *International Journal of Refractory Metals and Hard Materials* **36**, 232 (2013).
18. H. Kanda, T. Sekine, in *Properties and Growth of Diamond*, ed. by G. Davies (IEE - Inspec, London, 1994), p. 401.
19. H. M. Strong, R. M. Chrenko, *The Journal of Physical Chemistry* **75**, 1838 (1971).
20. R. H. Wentorf, *The Journal of Physical Chemistry* **75**, 1833 (1971).
21. A. T. Collins, S. C. Lawson, *Philosophical Magazine Letters* **60**, 117 (1989).
22. F. Frank *et al.*, *Journal of Crystal Growth* **100**, 354 (1990).

23. R. C. Burns *et al.*, *Journal of Crystal Growth* **104**, 257 (1990).
24. Y. Borzdov *et al.*, *Diamond and Related Materials* **11**, 1863 (2002).
25. R. H. Wentorf, H. P. Bovenkerk, *The Journal of Chemical Physics* **36**, 1987 (1962).
26. M.-L. T. Rooney, *Journal of Crystal Growth* **116**, 15 (1992).
27. A. T. Collins, *Philosophical Transactions A* **342**, 233 (1993).
28. R. Chrenko, *Physical Review B* **7**, 4560 (1973).
29. R. G. Farrer, *Solid State Communications* **7**, 685 (1969).
30. A. T. Collins, *Journal of Physics: Condensed Matter* **14**, 3743 (2002).
31. Y. Babich, B. Feigelson, A. Yelisseyev, *Diamond and Related Materials* **13**, 1802 (2004).
32. Y. V. Babich, B. N. Feigelson, *Geochemistry International* **47**, 94 (2009).
33. Y. V. Babich, B. N. Feigelson, *Inorganic Materials* **45**, 616 (2009).
34. R. Burns *et al.*, *Diamond and Related Materials* **8**, 1433 (1999).
35. R. C. Burns *et al.*, *Journal of Physics: Condensed Matter* **21**, 364224 (2009).
36. J. C. Angus, *Journal of Applied Physics* **39**, 2915 (1968).
37. J. E. Butler *et al.*, *Journal of Physics: Condensed Matter* **21**, 364201 (2009).
38. A. Argoitia, C. S. Kovach, J. C. Angus, in *Handbook of Industrial Diamonds and Diamond Films*, ed. by M. A. Prelas, G. Popovici, L. K. Bigelow (Marcel Dekker, New York, 1997), p. 797.
39. M. Kamo *et al.*, *Journal of Crystal Growth* **62**, 642 (1983).
40. A. J. S. Fernandes *et al.*, in *Properties, Growth and Applications of Diamond*, ed. by M. Nazaré, A. Neves (IEE - Inspec, London, 2001), B1.6.
41. J. Achard *et al.*, *Journal of Physics D: Applied Physics* **40**, 6175 (2007).
42. C.-s. Yan *et al.*, *Proceedings of the National Academy of Sciences* **99**, 12523 (2002).
43. H. Okushi, *Diamond and Related Materials* **10**, 281 (2001).
44. M. Kasu, N. Kobayashi, *Diamond and Related Materials* **12**, 413 (2003).
45. A. Chayahara *et al.*, *Diamond and Related Materials* **13**, 1954 (2004).
46. A. Tallaire *et al.*, *Physica Status Solidi (A)* **202**, 2059 (2005).

47. P. K. Bachmann, in *Handbook of Industrial Diamonds and Diamond Films*, ed. by M. A. Prelas, G. Popovici, L. K. Bigelow (Marcel Dekker, New York, 1997), p. 821.
48. J. W. Baldwin *et al.*, *Diamond and Related Materials* **15**, 2061 (2006).
49. C. Wild, N. Herres, P. Koidl, *Journal of Applied Physics* **68**, 973 (1990).
50. M. Schreck *et al.*, *Applied Physics Letters* **78**, 192 (2001).
51. M. Fischer *et al.*, *Diamond and Related Materials* **17**, 1035 (2008).
52. P. Martineau *et al.*, *Gems and Gemology* **40**, 2 (2004).
53. P. Martineau *et al.*, *Physica Status Solidi (C)* **6**, 1953 (2009).
54. P. M. Martineau *et al.*, *Journal of Physics: Condensed Matter* **21**, 364205 (2009).
55. A. Tallaire *et al.*, *Physica Status Solidi (A)* **201**, 2419 (2004).
56. T. Bauer *et al.*, *Diamond and Related Materials* **14**, 266 (2005).
57. G. Bogdan *et al.*, *Physica Status Solidi (A)* **202**, 2066 (2005).
58. R. Samlenski *et al.*, *Applied Physics Letters* **67**, 2798 (1995).
59. A. Tallaire *et al.*, *Diamond and Related Materials* **15**, 1700 (2006).
60. S. Jin, T. D. Moustakas, *Applied Physics Letters* **65**, 403 (1994).
61. W. Ahmed *et al.*, *Vacuum* **56**, 153 (2000).
62. J. Achard *et al.*, *Diamond and Related Materials* **16**, 685 (2007).
63. L. Bergman *et al.*, *Journal of Applied Physics* **76**, 3020 (1994).
64. E. A. Ekimov *et al.*, *Nature* **428**, 542 (2004).
65. T. Yokoya *et al.*, *Nature* **438**, 647 (2005).
66. R. Samlenski *et al.*, *Diamond and Related Materials* **5**, 947 (1996).
67. T. Borst, P. Münzinger, O. Weis, *Diamond and Related Materials* **3**, 515 (1994).
68. P. Kania, G. Francz, P. Oelhafen, *Diamond and Related Materials* **3**, 696 (1994).
69. J. Barjon *et al.*, *Physica Status Solidi (A)* **202**, 2177 (2005).
70. U. F. S. D'Haenens-Johansson *et al.*, *Physical Review B* **82**, 155205 (2010).
71. U. F. S. D'Haenens-Johansson *et al.*, *Physical Review B* **84**, 245208 (2011).
72. B. Dischler *et al.*, *Physica B: Condensed Matter* **185**, 217 (1993).
73. W. Crookes, *Proceedings of the Royal Society of London* **74**, 47 (1904).

74. C. D. Clark, R. W. Ditchburn, H. B. Dyer, *Proceedings of the Royal Society of London A* **234**, 363 (1956).

75. C. D. Clark, R. W. Ditchburn, H. B. Dyer, *Proceedings of the Royal Society of London A* **237**, 75 (1956).

76. A. Mainwood, *Diamond and Related Materials* **7**, 504 (1998).

77. H. B. Dyer, *British Journal of Applied Physics* **17**, 419 (1966).

78. E. A. Burgemeister, C. A. J. Ammerlaan, G. Davies, *Journal of Physics C: Solid State Physics* **13**, L691 (1980).

79. G. Davies *et al.*, *Physical Review B* **46**, 13157 (1992).

80. D. W. Palmer, in *Properties and Growth of Diamond* (IEE - Inspec, 1994), p. 5.1.

81. I. Kiflawi *et al.*, *Journal of Physics: Condensed Matter* **19**, 046216 (2007).

82. A. Mainwood, A. M. Stoneham, *Journal of Physics: Condensed Matter* **9**, 2453 (1997).

83. C. Coulson, M. Kearsley, *Proceedings of the Royal Society of London A* **241**, 433 (1957).

84. W. A. Runciman, *Proceedings of the Physical Society* **86**, 629 (1965).

85. C. D. Clark, J. Walker, *Proceedings of the Royal Society of London A* **334**, 241 (1973).

86. G. Davies, C. M. Penchina, *Proceedings of the Royal Society of London A* **338**, 359 (1974).

87. M. Lannoo, A. Stoneham, *Journal of Physics and Chemistry of Solids* **29**, 1987 (1968).

88. C. Coulson, F. Larkins, *Journal of Physics and Chemistry of Solids* **32**, 2245 (1971).

89. A. Stoneham, *Solid State Communications* **21**, 339 (1977).

90. G. Davies, *Solid State Communications* **32**, 745 (1979).

91. G. Davies, C. Foy, *Journal of Physics C: Solid State Physics* **13**, 2203 (1980).

92. G. Davies, *Reports on Progress in Physics* **44**, 787 (1981).

93. J. Lowther, *Journal of Physics and Chemistry of Solids* **45**, 127 (1984).

94. A. Stoneham, *Materials Science and Engineering: B* **11**, 211 (1992).

95. J. Walker, L. A. Vermeulen, C. D. Clark, *Proceedings of the Royal Society of London A* **341**, 253 (1974).
96. A. M. Stoneham, A. Mainwood, presented at the 7th International Conference on Shallow-Level Centers in Semiconductors, ed. by C. A. J. Ammerlaan, B. Pajot, p. 165.
97. I. N. Douglas, W. A. Runciman, *Journal of Physics C: Solid State Physics* **10**, 2253 (1977).
98. J. van Wyk *et al.*, *Physical Review B* **52**, 12657 (1995).
99. G. Davies, E. C. Lightowlers, *Journal of Physics C: Solid State Physics* **3**, 638 (1970).
100. G. Davies, *Nature* **269**, 498 (1977).
101. J. Isoya *et al.*, *Physical Review B* **45**, 1436 (1992).
102. D. Twitchen *et al.*, *Diamond and Related Materials* **8**, 1572 (1999).
103. M. Newton *et al.*, *Diamond and Related Materials* **11**, 618 (2002).
104. L. Allers, A. T. Collins, J. Hiscock, *Diamond and Related Materials* **7**, 228 (1998).
105. A. T. Collins, presented at the Radiation Effects in Semiconductors 1976, ed. by N. B. Urli, J. W. Corbett, p. 346.
106. J. Goss *et al.*, *Physical Review B* **72**, 035214 (2005).
107. D. J. Twitchen *et al.*, *Physical Review B* **59**, 12900 (1999).
108. M. A. Lea-Wilson, J. N. Lomer, J. A. Van Wyk, *Philosophical Magazine Part B* **72**, 81 (1995).
109. L. S. Hounsome *et al.*, *Physical Review B* **73**, 125203 (2006).
110. U. Bangert *et al.*, *Journal of Physics: Condensed Matter* **21**, 364208 (2009).
111. S. Breuer, P. Briddon, *Physical Review B* **51**, 6984 (1995).
112. C. Weigel *et al.*, *Physical Review B* **8**, 2906 (1973).
113. A. Mainwood, F. Larkins, A. Stoneham, *Solid-State Electronics* **21**, 1431 (1978).
114. J. P. Goss *et al.*, *Physical Review B* **63**, 195208 (2001).
115. D. Hunt *et al.*, *Physical Review B* **61**, 3863 (2000).
116. G. Davies, H. Smith, H. Kanda, *Physical Review B* **62**, 1528 (2000).
117. G. Davies *et al.*, *Physica Status Solidi (A)* **186**, 187 (2001).

118. H. E. Smith, PhD thesis, King's College London, 2004.
119. D. Twitchen *et al.*, *Physical Review B* **54**, 6988 (1996).
120. D. Hunt, PhD thesis, St. Peter's College, Oxford, 1999.
121. T. Evans, Z. Qi, *Proceedings of the Royal Society of London A* **381**, 159 (1982).
122. W. Smith *et al.*, *Physical Review* **115**, 1546 (1959).
123. P. Briddon, R. Jones, *Physica B: Condensed Matter* **185**, 179 (1993).
124. A. T. Collins, G. S. Woods, *Philosophical Magazine Part B* **46**, 77 (1982).
125. G. S. Woods, J. A. Van Wyk, A. T. Collins, *Philosophical Magazine Part B* **62**, 589 (1990).
126. S. R. Boyd, I. Kiflawi, G. S. Woods, *Philosophical Magazine Part B* **69**, 1149 (1994).
127. S. C. Lawson *et al.*, *Journal of Physics: Condensed Matter* **10**, 6171 (1998).
128. R. Ulbricht *et al.*, *Physical Review B* **84**, 165202 (2011).
129. G. Davies, *Journal of Physics C: Solid State Physics* **9**, L537 (1976).
130. O. Tucker, M. Newton, J. Baker, *Physical Review B* **50**, 15586 (1994).
131. G. Davies, *Journal of Physics C: Solid State Physics* **12**, 2551 (1979).
132. Y. Mita, *Physical Review B* **53**, 11360 (1996).
133. S. Felton *et al.*, *Physical Review B* **77**, 081201 (2008).
134. G. Davies, M. E. R. Hamer, *Proceedings of the Royal Society of London A* **348**, 285 (1976).
135. J. H. N. Loubser, J. A. van Wyk, *Diamond Research* **11**, 11 (1977).
136. A. Mainwood, *Physical Review B* **49**, 7934 (1994).
137. S. Felton *et al.*, *Journal of Physics: Condensed Matter* **21**, 364212 (2009).
138. G. Davies, M. H. Nazaré, M. F. Hamer, *Proceedings of the Royal Society of London A* **351**, 245 (1976).
139. J. van Wyk, G. S. Woods, *Journal of Physics: Condensed Matter* **7**, 5901 (1995).
140. P. Crowther, P. Dean, *Journal of Physics and Chemistry of Solids* **28**, 1115 (1967).
141. M. Y. Shcherbakova, V. A. Nadolinnyi, E. V. Sobolev, *Journal of Structural Chemistry* **19**, 261 (1978).

142. J. A. van Wyk, *Journal of Physics C: Solid State Physics* **15**, L981 (1982).
143. Y. Mita *et al.*, *Philosophical Magazine Letters* **76**, 93 (1997).
144. Y. Mita *et al.*, *Journal of Physics: Condensed Matter* **2**, 8567 (1990).
145. S. C. Lawson *et al.*, *Journal of Physics: Condensed Matter* **4**, 3439 (1992).
146. Y. Mita *et al.*, *Diamond and Related Materials* **2**, 768 (1993).
147. C. Glover *et al.*, *Physical Review Letters* **90**, 185507 (2003).
148. A. Edmonds, PhD thesis, University of Warwick, 2008.
149. R. J. Cruddace, PhD thesis, University of Warwick, 2007.
150. S. Liggins, PhD thesis, University of Warwick, 2010.
151. J. P. Goss *et al.*, presented at the 63rd Diamond Conference, O26.
152. C. Glover *et al.*, *Physical Review Letters* **92**, 135502 (Mar. 2004).
153. J. Chevallier *et al.*, *Physical Review B* **58**, 7966 (Sept. 1998).
154. J. Goss *et al.*, *Physical Review B* **65**, 115207 (2002).
155. R. U. A. Khan *et al.*, *Journal of Physics: Condensed Matter* **21**, 364214 (2009).
156. J.-M. Mäki *et al.*, *Physical Review Letters* **107**, 217403 (2011).

Chapter 3

Symmetry & groups

3.1 Symmetries in physics

Symmetry has been exploited as a method to simplify or classify problems in physics for many years. In addition to simple geometric symmetries, other symmetries such as time-reversal, particle exchange and charge symmetry have been investigated. The primary utility of symmetry in physics is simplification of a problem without requiring detailed knowledge of the Hamiltonian of the system.

The symmetries most relevant to the current work are described in terms of point groups: the geometric symmetry operations which transform a system into itself about a fixed point. A given point group symmetry operation $\hat{R}$ which leaves the system unchanged (maps it onto itself) must therefore commute with the Hamiltonian of that system i.e.

$$\hat{R}(\hat{\mathcal{H}}\psi_n) = \hat{\mathcal{H}}(\hat{R}\psi_n) = \hat{R}E_n\psi_n = E_n\hat{R}\psi_n$$

where ψ_n is the n^{th} eigenfunction of the system [1].

3.2 Theory of groups

Many mathematically rigorous treatments of group theory in physics exist (see [2, 3]), and only the relevant results are summarised here; nevertheless, it is useful to

define a group formally (adapted from [4]):

Definition A set $\mathscr{G}$ of elements $a, b, \ldots$ form a group under a given binary operation if:

i. The product ab of any two elements is an element of $\mathscr{G}$,

$$ab = c, c \in \mathscr{G} \ .$$

ii. The products of the elements obey the associative law,

$$(ab)c = a(bc) \ .$$

iii. There exists an element e, the identity, which satisfies

$$ea = ae = a \ .$$

iv. For each element a there exists another element a^{-1} such that

$$a^{-1}a = aa^{-1} = e \ .$$

Practically, the binary operation is usually taken to be matrix multiplication. There are several notations for labelling point group symmetry operations: in accordance with most of the published work on diamond point groups, the Schönflies notation will be used. The possible point group symmetry operations are given in table 3-1.

e	The identity
c_n	Rotation about $2\pi/\mathrm{n}$
σ_h	Horizontal mirror plane (perpendicular to the principal axis)†
σ_v	Vertical mirror plane (parallel to the principal axis)
i	Coordinate inversion
s_n	Improper rotation about $2\pi/\mathrm{n}$ (i.e. a rotation followed by a coordinate inversion i)

Table 3-1 The possible point group symmetry operations. Taken from Johnston [5]. †The principal axis is the axis which possesses the highest order rotational symmetry.

An atomic site in a perfect diamond lattice possesses $\mathscr{T}_\mathrm{d}$ (tetrahedral) symmetry, a high symmetry group consisting of 24 elements. Any defect in the lattice must

therefore be a subgroup of $\mathscr{T}_\mathrm{d}$ and hence of equal or lower symmetry. For example, many simple defect in diamond possess $\mathscr{C}_{3\mathrm{v}}$ (trigonal) symmetry, with the elements

$$\mathscr{C}_{3\mathrm{v}} = \{e, c_3, c_3^2, \sigma_\mathrm{v}, \sigma_\mathrm{v}', \sigma_\mathrm{v}''\} ,$$

where c_n^m is a rotation about $2\pi\mathrm{m/n}$. The operations are illustrated in figure 3-1.

One may consider each of the symmetry operations as transforming (mapping) a point x onto a point x': in figure 3-1, the operation c_3 transforms α onto β. Note that it is convention to read multiple operations right to left i.e. $\sigma_\mathrm{v}c_3$ implies that σ_v should be performed on the result of c_3; additionally, for rotations, anticlockwise is taken to be the positive sense.

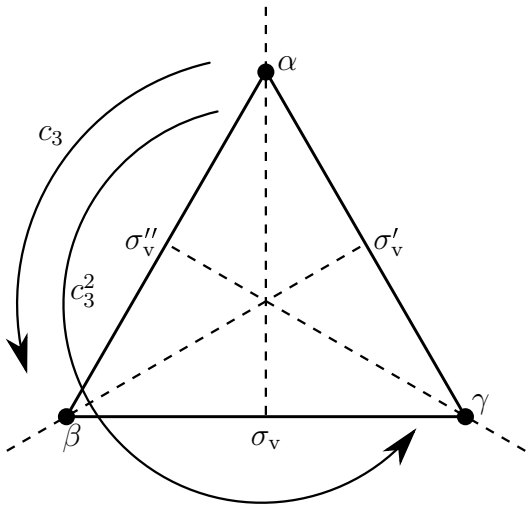

Figure 3-1 Illustration of the operations of the $\mathscr{C}_{3\mathrm{v}}$ group. The operation e leaves the points $\{\alpha, \beta, \gamma\}$ unchanged. See table 3-1 for a description of the notation.

3.3 Matrix representations

The above notation is very useful for describing concisely the relevant symmetry operations in abstract; however, it is convenient when working on practical problems to represent each element of the group by an object, and to define the binary operation under which the group is closed.

Definition A representation $D(\mathscr{G})$ is a homomorphism of $\mathscr{G}$ onto a group of linear

operators[1] $\hat{P}$ that map a space $\mathscr{L}$ onto itself [2].

$$D(\mathscr{G}) : \hat{R} \in \mathscr{G} \to \hat{P}(\hat{R}) \equiv \hat{P}_{\hat{R}} \, .$$

In less opaque language, a representation $D(\mathscr{G})$ of a group $\mathscr{G}$ is a set of linear operators which retain the same algebraic structure as the group itself. Using the operations illustrated in figure 3-1, it can be seen that $e = c_3^2 c_3$: a representation of $\mathscr{C}_{3\mathrm{v}}$ must then preserve $\hat{P}_e = \hat{P}_{c_3^2} \hat{P}_{c_3}$ (and all other relations).

By choosing a set of basis functions $\{f_1, \ldots, f_n\}$ in a space $\mathscr{L}^n$, the operators $\hat{P}_{\hat{R}}$ may be defined in terms of $n \times n$ matrices [1]:

$$\hat{P}_{\hat{R}} f_i = \sum_{j=1}^{n} D_{ji}(\hat{R}) f_j \, , \quad i = 1, \ldots, n.$$

Here, the matrix $\mathbf{D}(\hat{R})$ describes the effect of $\hat{P}_{\hat{R}}$ in the basis $\{f_i\}$. The choice of basis functions is not unique, and in general will depend on the problem at hand.

Having chosen to define the operators $\hat{P}_{\hat{R}}$ in terms of matrices, the binary operation under which the group is closed is taken to be matrix multiplication. Note that matrices obey the associative law, (possibly) have an inverse, and there exists an identity matrix as required by the definition of a group.

3.3.1 Constructing a matrix representation

The chosen basis, of dimension n, may be written as a basis vector $\boldsymbol{f} = (f_1, \ldots, f_n)$. The matrix representation $\mathbf{D}(\hat{R})$ of each group operation $\hat{R}$ then describes how the operation transforms the basis vector $\boldsymbol{f}$. With recourse once more to figure 3-1, it is obvious by inspection that $(\gamma, \alpha, \beta) = \hat{P}_{c_3}(\alpha, \beta, \gamma)$. This transform may be written as

$$(\gamma, \alpha, \beta) = (\alpha, \beta, \gamma) \begin{pmatrix} 0 & 1 & 0 \\ 0 & 0 & 1 \\ 1 & 0 & 0 \end{pmatrix} = (\alpha, \beta, \gamma) \mathbf{D}(c_3^2) \, . \tag{3-1}$$

Thus, the matrix $\mathbf{D}(c_3^2)$ describes correctly the effect of the operation $\hat{P}_{c_3^2}$. The matrices corresponding to each of the other operations of the group may also be

[1] A linear operator $\hat{A}$ satisfies $\hat{A}(f)\hat{A}(g) = \hat{A}(fg)$ and $t\hat{A}(f) = \hat{A}(tf)$ for any pair of functions f, g and scalar t.

written down by inspection (3-2). The form and dimensionality of each matrix will depend on the basis functions chosen initially, and the group of all matrix representations $\mathbf{D}(\hat{R})$ of the operations $\hat{R}$ of a group form the group representation $D(\mathscr{G})$.

$$\begin{array}{lll} \mathbf{D}(e) = \begin{pmatrix} 1 & 0 & 0 \\ 0 & 1 & 0 \\ 0 & 0 & 1 \end{pmatrix} & \mathbf{D}(c_3) = \begin{pmatrix} 0 & 0 & 1 \\ 1 & 0 & 0 \\ 0 & 1 & 0 \end{pmatrix} & \mathbf{D}(c_3^2) = \begin{pmatrix} 0 & 1 & 0 \\ 0 & 0 & 1 \\ 1 & 0 & 0 \end{pmatrix} \\ \chi(e) = 3 & \chi(c_3) = 0 & \chi(c_3^2) = 0 \\ \mathbf{D}(\sigma_\mathrm{v}) = \begin{pmatrix} 1 & 0 & 0 \\ 0 & 0 & 1 \\ 0 & 1 & 0 \end{pmatrix} & \mathbf{D}(\sigma_\mathrm{v}') = \begin{pmatrix} 0 & 0 & 1 \\ 0 & 1 & 0 \\ 1 & 0 & 0 \end{pmatrix} & \mathbf{D}(\sigma_\mathrm{v}'') = \begin{pmatrix} 0 & 1 & 0 \\ 1 & 0 & 0 \\ 0 & 0 & 1 \end{pmatrix} \\ \chi(\sigma_\mathrm{v}) = 1 & \chi(\sigma_\mathrm{v}') = 1 & \chi(\sigma_\mathrm{v}'') = 1 \end{array} \tag{3-2}$$

3.3.2 Reducible representations

Any group may have an infinite number of representations [6]: representation theory is used to reduce any given representation to a set of irreducible representations – the representations which contain all the information about the group under the chosen basis without redundancy. When working with matrix representations, reducing a representation corresponds to finding a set of lower-dimensional matrices whose direct sum is a complete description of the group. Any representation, given a suitable transform, is necessarily expressible as the direct sum of one or more irreducible representations of the group. For instance, using the basis in figure 3-1, $\mathscr{C}_{3\mathrm{v}}$ can be reduced to the direct sum of a two-dimensional and a one-dimensional matrix representation (see §3.3.4).

It is important to note that even though a representation may be irreducible, it is not unique. The form of an irreducible representation is dependent on the basis used to generate the representation. However, it is trivial to show (see [2, §4.4.2]) that the trace of any representation of an operation is invariant under a similarity

transform[2] of the basis. The character χ of a representation is defined as

$$\chi(\hat{R}) = \sum_{i}^{n} D_{ii}(\hat{R}) = \mathrm{Tr}\{\mathbf{D}(\hat{R})\} \quad \forall \hat{R} \in \mathscr{G} \, .$$

Thus, using the representation $D(\mathscr{G})$ given in (3-2), $\chi(c_3^2) = 0$ and $\chi(e) = 3$. A further simplification may be made: two operations $\hat{R}_1$ and $\hat{R}_2$ are conjugate if there exists an operation $\hat{S}$ in the group such that

$$\hat{R}_2 = \hat{S}^{-1}\hat{R}_1\hat{S} \, . \tag{3-3}$$

For example, in $\mathscr{C}_{3\mathrm{v}}$, $c_3^{-1}\sigma_\mathrm{v}c_3 = \sigma_\mathrm{v}'$, hence σ_v and σ_v' are conjugate and belong to the same conjugacy class. As (3-3) is a similarity transform, and the character (trace) of a representation is unchanged by such a transform, all operations $\hat{R}$ of the same class c have the same character (e.g. $\chi(c_3) = \chi(c_3^2)$).

3.3.3 Character tables

Having determined that the character of an irreducible representation of a group is invariant under similarity transforms, the character table may be introduced. A character table gives the character of all possible irreducible representations of a group (under any and all bases). In chemistry and physics, each irreducible representation is often known as a symmetry species.

Extensive tabulations of character and product tables are available from many sources e.g. [1, 8]. The construction of a character table, although simple, is beyond the scope of this thesis: a very accessible account and corresponding example is given in Atkins [1, §5.10]. The character table for $\mathscr{C}_{3\mathrm{v}}$ is given in table 3-2.

$\mathscr{C}_{3\mathrm{v}}$	e	$2c_3$	$3\sigma_\mathrm{v}$
$\mathbf{A_1}$	1	1	1
$\mathbf{A_2}$	1	1	−1
$\mathbf{E}$	2	−1	0

Table 3-2 The $\mathscr{C}_{3\mathrm{v}}$ character table

[2] Two $n \times n$ matrices $\mathbf{A}$ and $\mathbf{B}$ are similar if $\mathbf{B} = \mathbf{R}^{-1}\mathbf{A}\mathbf{R}$ where $\mathbf{R}$ is an $n \times n$ invertible matrix. $\mathbf{A}$ and $\mathbf{B}$ represent the same linear transform under different bases, and $\mathbf{R}$ is the change of basis matrix [7]. A similarity transform preserves angles and changes all distances by the same ratio.

A	One dimensional state which is symmetric about the principal rotation axis
B	One dimensional state which is antisymmetric about the principal rot^{n} axis
E	Two dimensional (doubly degenerate) state
T	Three dimensional (triply degenerate) state
$\mathbf{X_g}$	Symmetric with respect to inversion (gerade = even)
$\mathbf{X_u}$	Antisymmetric with respect to inversion (ungerade = odd)
$\mathbf{X_1}$	Symmetric with respect to a rotation about a secondary axis
$\mathbf{X_2}$	Antisymmetric with respect to a rotation about a secondary axis
$\mathbf{X}'$	State is symmetric with respect to a horizontal mirror plane σ_h
$\mathbf{X}''$	State is antisymmetric with respect to a horizontal mirror plane σ_h

Table 3-3 Mulliken symbols used to describe irreducible representations [9]. **A**, **B**, **E** and **T** give the dimensionality of the representation, all others are used as modifiers e.g. $\mathbf{T_{2u}}$.

The symmetry species $\mathbf{A_x}$ are one dimensional representations which transform symmetrically under a rotation about the principal axis; the species **E** is a two dimensional representation (and distinct from the operation e). The species $\mathbf{A_x}$ are usually referred to as singlets; **E**, a doublet. A brief description of the different possible irreducible representations is given in table 3-3.

3.3.4 Reducing a matrix representation

To determine which symmetry species a given basis spans, it is useful to formalise the construction of a representation from irreducible representations: the representation $D(\mathscr{G})$ of a given group $\mathscr{G}$ can be written as the direct sum of the irreducible representations $\mathbf{D}^{(l)}$ of the symmetry species l i.e.

$$D(\mathscr{G}) = \sum_l \oplus\, a_l \mathbf{D}^{(l)} \,. \tag{3-4}$$

As the characters of both $D(\mathscr{G})$ and $\mathbf{D}^{(l)}$ are invariant under a similarity transform, it is possible to write

$$\chi(\hat{R}) = \sum_l a_l \chi^{(l)}(\hat{R}) \,.$$

The coefficients are determined as

$$a_l = \frac{1}{h} \sum_c g(c) \chi^{(l)*}(c) \chi(c) \,, \tag{3-5}$$

where h is the order (number of elements) of the group, and $g(c)$ is the number of members of the class c [1]. (This result is derived from the orthogonality relations

of the characters of irreducible representations, which is itself derived from the great / grand / group orthogonality theorem [3].) To clarify, $\chi(c)$ is the character of any matrix representation of the class c under the basis in question, and $\chi^{(l)}(c)$ is the character of the class c under the symmetry species l. From table 3-2 and (3-1), it is evident that $\chi(c_3) = 0$, while $\chi^{(\mathrm{E})}(c_3) = -1$. The coefficients a_l under the basis given in figure 3-1 are therefore

$$\begin{aligned} a_{\mathbf{A_1}} &= \frac{1}{6}(1\cdot 1\cdot 3 + 2\cdot 1\cdot 0 + 3\cdot 1\cdot 1) &&= 1 \\ a_{\mathbf{A_2}} &= \frac{1}{6}(1\cdot 1\cdot 3 + 2\cdot 1\cdot 0 + 3\cdot (-1)\cdot 1) &&= 0 \\ a_{\mathbf{E}} &= \frac{1}{6}(1\cdot 2\cdot 3 + 2\cdot (-1)\cdot 0 + 3\cdot 0\cdot 1) &&= 1\,. \end{aligned}$$

Therefore, this representation spans $D(\mathscr{G}) = \mathbf{A}_1 \oplus \mathbf{E}$ (3-4).

3.3.5 Symmetry-adapted basis functions

The basis chosen at the beginning of this section was arbitrary. In practice, it is convenient to find a symmetry-adapted basis: linear combinations of the original basis functions which transform as irreducible representations. In order to determine the symmetry-adapted basis corresponding to any given symmetry species l, the character projection operator $\hat{p}^{(l)}$ is required [1]

$$\hat{p}^{(l)} = \frac{d_l}{h} \sum_{\hat{R}\in\mathscr{G}} \chi^{(l)*}(\hat{R})\hat{P}_{\hat{R}}\,, \tag{3-6}$$

where d_l is the dimensionality of the symmetry species. In this form, the projection operator acts to project a set of basis functions $\{f_j\}$ into a set of linear combinations, each of which transforms as the irreducible representation $\mathbf{D}^{(l)}$:

$$\hat{p}^{(l)} f_j = \frac{d_l}{h} \sum_{\hat{R}\in\mathscr{G}} \chi^{(l)*}(\hat{R})\hat{P}_{\hat{R}} f_j = \sum_i f_i^{(l)}$$

As with previous sections, the group $\mathscr{C}_{3\mathrm{v}}$ will be considered. Initially, the effect of each operation $\hat{P}_{\hat{R}}$ on each member of the basis f_j will be calculated (giving $\hat{P}_{\hat{R}} f_j$). For the basis given in figure 3-1, the transforms are calculated on the left of table 3-4.

	$\hat{P}_{\hat{R}} f_j$			$\chi^{(l)*}(\hat{R})$		
	α	β	γ	$\mathbf{A_1}$	$\mathbf{A_2}$	$\mathbf{E}$
e	α	β	γ	1	1	2
c_3	β	γ	α	1	1	−1
c_3^2	γ	α	β	1	1	−1
σ_v	α	γ	β	1	−1	0
σ_v'	γ	β	α	1	−1	0
σ_v''	β	α	γ	1	−1	0

Table 3-4 The transform table for the basis $\{\alpha, \beta, \gamma\}$ of figure 3-1 (left); the characters of the symmetry species under the symmetry operations of the group $\mathscr{C}_{3v}$ (right).

To obtain $\chi^{(l)*}(\hat{R})\hat{P}_{\hat{R}} f_j$, the results on the left of table 3-4 are multiplied by the character of the respective operation under the species l (right of table 3-4).

Finally, to obtain the sum $\sum_{\hat{R}\in\mathscr{G}} \chi^{(l)*}(\hat{R})\hat{P}_{\hat{R}} f_j$, each of the columns on the left of table 3-4, multiplied by the corresponding character on the right, are summed:

$$\hat{p}^{\mathbf{A_1}}\{\alpha, \beta, \gamma\} = \frac{1}{3}(\alpha + \beta + \gamma) \tag{3-7a}$$

$$\hat{p}^{\mathbf{A_2}}\{\alpha, \beta, \gamma\} = 0 \tag{3-7b}$$

$$\hat{p}^{\mathbf{E}}\alpha = \frac{1}{3}(2\alpha - \beta - \gamma) \tag{3-7c}$$

$$\hat{p}^{\mathbf{E}}\beta = \frac{1}{3}(2\beta - \gamma - \alpha) \tag{3-7d}$$

$$\hat{p}^{\mathbf{E}}\gamma = \frac{1}{3}(2\gamma - \alpha - \beta) \tag{3-7e}$$

That (3-7b) is null for all members of the original basis is another expression of the fact that the basis does not span $\mathbf{A_2}$. The total number of linear combinations (symmetry-adapted basis functions) should equal the sum of the dimensionalities of the irreducible representations spanned by the basis (in this case, $d_{\mathbf{A_1}} + d_{\mathbf{E}} = 3$). As the projection for $\mathbf{A_1}$ contains only one expression (3-7a), we will use it as the first symmetry-adapted basis function

$$f_1 = \alpha + \beta + \gamma \, .$$

It is evident by inspection that the obtained projections for $\mathbf{E}$ (3-7c–3-7e) are not linearly independent. Therefore, one of the combinations is taken (arbitrarily),

and an orthogonal combination is constructed from the other two:

$$f_2 = 2\alpha - \beta - \gamma$$

$$f_3 = \beta - \gamma$$

The original basis vector $\boldsymbol{f} = (\alpha, \beta, \gamma)$ and the symmetry-adapted basis vector $\boldsymbol{f}' = (f_1, f_2, f_3)$ are related by the transform $\boldsymbol{f}' = \boldsymbol{f}\mathbf{c}$, with

$$\mathbf{c} = \begin{pmatrix} 1 & 0 & 2 \\ 1 & -1 & -1 \\ 1 & 1 & -1 \end{pmatrix}.$$

Using this matrix, it is also possible to transform the matrix representations of (3-2) to the new basis by $\mathbf{D}' = \mathbf{c}^{-1}\mathbf{D}\mathbf{c}$. The new representations are given in (3-8).

$$\mathbf{D}'(e) = \begin{pmatrix} 1 & 0 & 0 \\ 0 & 1 & 0 \\ 0 & 0 & 1 \end{pmatrix} \quad \mathbf{D}'(c_3) = \begin{pmatrix} 1 & 0 & 0 \\ 0 & -\frac{1}{2} & -\frac{3}{2} \\ 0 & \frac{1}{2} & -\frac{1}{2} \end{pmatrix} \quad \mathbf{D}'(c_3^2) = \begin{pmatrix} 1 & 0 & 0 \\ 0 & -\frac{1}{2} & \frac{3}{2} \\ 0 & -\frac{1}{2} & -\frac{1}{2} \end{pmatrix}$$

$$\mathbf{D}'(\sigma_v) = \begin{pmatrix} 1 & 0 & 0 \\ 0 & -1 & 0 \\ 0 & 0 & 1 \end{pmatrix} \quad \mathbf{D}'(\sigma_v') = \begin{pmatrix} 1 & 0 & 0 \\ 0 & \frac{1}{2} & \frac{3}{2} \\ 0 & \frac{1}{2} & -\frac{1}{2} \end{pmatrix} \quad \mathbf{D}'(\sigma_v'') = \begin{pmatrix} 1 & 0 & 0 \\ 0 & \frac{1}{2} & -\frac{3}{2} \\ 0 & -\frac{1}{2} & -\frac{1}{2} \end{pmatrix} \tag{3-8}$$

All of the matrices in 3-8 are in block diagonal form and can therefore be represented in each case by the direct sum of a one dimensional and a two dimensional matrix:

$$\mathbf{D}' = \begin{pmatrix} \mathbf{D}^{(1)}(\hat{R}) & 0 \\ 0 & \mathbf{D}^{(2)}(\hat{R}) \end{pmatrix}.$$

These representations are now irreducible: there is no similarity transform which will simultaneously transform all $\mathbf{D}^{(2)}(\hat{R})$ into block diagonal form. Thus, the matrix representation of the group may be written as $\mathbf{D}^{(3)} = \mathbf{D}^{(1)} \oplus \mathbf{D}^{(2)}$ (c.f. (3-4)) and is known as fully reduced. There is now a 1-to-1 correspondence between the matrix representations and the symmetry species: the one dimensional representation is $\mathbf{D}^{(\mathbf{A_1})}(\hat{R})$, and the two dimensional, $\mathbf{D}^{(\mathbf{E})}(\hat{R})$.

$\mathscr{D}_{2d}$	e	$2s_4$	c_{2z}	$2c_2'$	$2\sigma_d$
$\mathbf{A_1}$	1	1	1	1	1
$\mathbf{A_2}$	1	1	1	−1	−1
$\mathbf{B_1}$	1	−1	1	1	−1
$\mathbf{B_2}$	1	−1	1	−1	1
$\mathbf{E}$	2	0	−2	0	0

Table 3-5 The $\mathscr{D}_{2d}$ character table

3.4 An example in diamond

In order to illustrate the use of the previous section and its practical application in semiconductor defect research, the $\langle 0\,0\,1\rangle$-split self-interstitial in diamond, $I_{\langle 0\,0\,1\rangle}$, will be considered. The self-interstitial has $\mathscr{D}_{2d}$ symmetry, the character table of which is given in table 3-5. As a basis, two p-type orbitals are chosen. The operations of the group are illustrated in figure 3-2 and the matrix representations of the operations for this basis are given in (3-9).

$$\begin{aligned}
\mathbf{D}(e) &= \begin{pmatrix} 1 & 0 \\ 0 & 1 \end{pmatrix} & \mathbf{D}(c_{2z}) &= \begin{pmatrix} -1 & 0 \\ 0 & -1 \end{pmatrix} & \mathbf{D}(\sigma_d) &= \begin{pmatrix} 1 & 0 \\ 0 & -1 \end{pmatrix} & \mathbf{D}(\sigma_d') &= \begin{pmatrix} -1 & 0 \\ 0 & 1 \end{pmatrix} \\
\chi(e) &= 2 & \chi(c_{2z}) &= -2 & \chi(\sigma_d) &= 0 & \chi(\sigma_d') &= 0 \\
\mathbf{D}(c_2') &= \begin{pmatrix} 0 & 1 \\ 1 & 0 \end{pmatrix} & \mathbf{D}(c_2'') &= \begin{pmatrix} 0 & -1 \\ -1 & 0 \end{pmatrix} & \mathbf{D}(s_4) &= \begin{pmatrix} 0 & 1 \\ -1 & 0 \end{pmatrix} & \mathbf{D}(s_4^3) &= \begin{pmatrix} 0 & -1 \\ 1 & 0 \end{pmatrix} \\
\chi(c_2') &= 0 & \chi(c_2'') &= 0 & \chi(s_4) &= 0 & \chi(s_4^3) &= 0
\end{aligned} \tag{3-9}$$

To determine the irreducible representations spanned by this basis, (3-5) is computed for each symmetry species with non-zero character $\chi(\hat{R})$:

$$\begin{aligned}
a_{\mathbf{A_1}} &= \tfrac{1}{8}(1\cdot 1\cdot 2 + 1\cdot 1\cdot(-2)) &&= 0 \\
a_{\mathbf{A_2}} &= \tfrac{1}{8}(1\cdot 1\cdot 2 + 1\cdot 1\cdot(-2)) &&= 0 \\
a_{\mathbf{B_1}} &= \tfrac{1}{8}(1\cdot 1\cdot 2 + 1\cdot 1\cdot(-2)) &&= 0 \\
a_{\mathbf{B_2}} &= \tfrac{1}{8}(1\cdot 1\cdot 2 + 1\cdot 1\cdot(-2)) &&= 0 \\
a_{\mathbf{E}} &= \tfrac{1}{8}(1\cdot 2\cdot 2 + 1\cdot(-2)\cdot(-2)) &&= 1\,.
\end{aligned}$$

The chosen basis therefore spans only **E**, and does not require a symmetry adapted

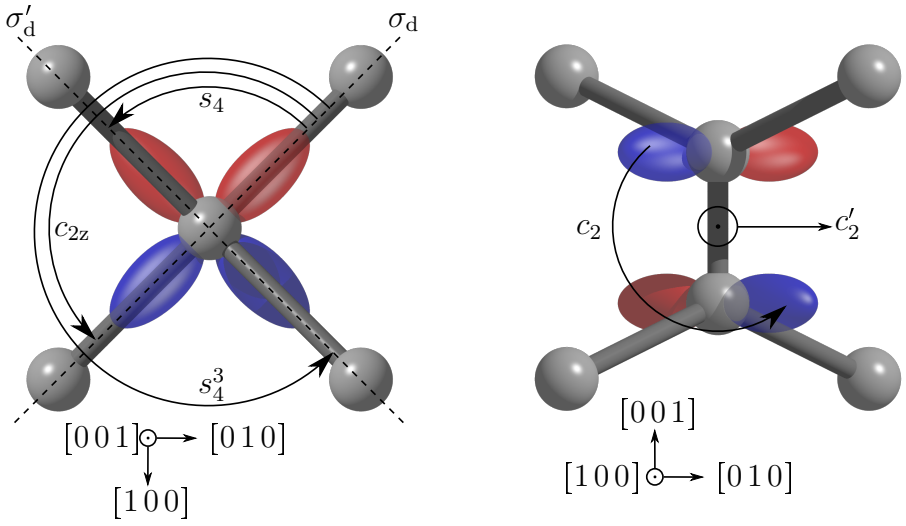

(a) View down $[00\bar{1}]$ **(b)** View down $[\bar{1}00]$

Figure 3-2 The $I_{\langle 001\rangle}$-split self-interstitial in diamond. The lobes represent p_X and p_Y orbitals, with blue (closest) part of the wavefunction being positive, and red being negative.

basis to be calculated. (If the calculation were performed, it would simply give the identity matrix as the transform matrix.)

3.5 Calculation of many-electron states

Once the (symmetry-adapted) electronic states and their dimensionality have been determined, the next step in understanding the electronic structure is to populate those states. A distinction needs to be made here between one-electron states and many-electron states:

One-electron Unpopulated states; determined by the symmetry of the defect and the chosen basis alone. The states calculated in the previous section were one-electron states.

Many-electron Those states which arise when the one-electron states are populated by electrons. The many-electron states for the $I_{\langle 001\rangle}$-split interstitial will be calculated in this section.

Due to Pauli exclusion, each one-electron state may contain only two electrons, multiplied by its dimensionality: an $\mathbf{A_1}$ state is one-dimensional, and may contain

only two electrons; an **E** state may contain four.

In order to determine the nature of the many-electron states, the one-electron states are populated. Here, one-electron states will be represented by lowercase letters x which transform as the irreducible representation **X**; their electronic population is represented as a superscript e.g. x^2. The symmetry of the resulting many-electron states is given by taking the direct product of the state occupied by each electron i.e. for x^2 the many-electron states are given by the result of $\mathbf{X} \otimes \mathbf{X}$. As with character tables, it is trivial (albeit time consuming) to calculate the direct product tables (see [1, §5.14]), and standard direct product tables are usually employed [8].

$\mathscr{D}_{2d}$	$\mathbf{A_1}$	$\mathbf{A_2}$	$\mathbf{B_1}$	$\mathbf{B_2}$	$\mathbf{E}$
$\mathbf{A_1}$	$\mathbf{A_1}$	$\mathbf{A_2}$	$\mathbf{B_1}$	$\mathbf{B_2}$	$\mathbf{E}$
$\mathbf{A_2}$		$\mathbf{A_1}$	$\mathbf{B_2}$	$\mathbf{B_1}$	$\mathbf{E}$
$\mathbf{B_1}$			$\mathbf{A_1}$	$\mathbf{A_2}$	$\mathbf{E}$
$\mathbf{B_2}$				$\mathbf{A_1}$	$\mathbf{E}$
$\mathbf{E}$					$\mathbf{A_1} + [\mathbf{A_2}] + \mathbf{B_1} + \mathbf{B_2}$

Table 3-6 The direct product table for the $\mathscr{D}_{2d}$ group (amongst others not considered here)

The neutral self-interstitial, $I^0_{\langle 0\,0\,1\rangle}$, contains only two unpaired electrons, and only one one-electron state, e (in this basis). Therefore, there is only one possible configuration, e^2, leading to the many electron states

$$e \times e = {}^1A_1 + {}^3A_2 + {}^1B_1 + {}^1B_2 \,,$$

as given by table 3-6. The superscript on the many-electron states denotes the spin multiplicity, given by $2S+1$, where S is the effective spin of the state. When considering the square of an irreducible representation with a dimensionality greater than one (i.e. not **A** or **B**), the antisymmetric part of the square is known analytically, and indicated by square brackets in direct product tables (see table 3-6). As it is the spatial part of the wavefunction being investigated, and the wavefunction for a fermion must be overall antisymmetric, the particles must therefore be spin symmetric, giving the highest spin multiplicity.

At this point, the symmetries and spin multiplicities have been calculated for the many-electron states arising from the one-electron states. These properties can be used to predict (or interpret) many attributes of the system in question, including details on electronic and vibrational transitions. Unfortunately, group theory gives no information on the energetic ordering of the many-electron states: experimental results and electronic theories such as DFT must be used. In some cases, Hund's rules may be used as a guideline, giving in this case the $^3\mathrm{A}_2$ state as the ground state: the specifics of the electronic structure of $\mathrm{I}^0_{\langle 0\,0\,1\rangle}$ have been studied at length [10–12].

3.6 Uniaxial stress

Uniaxial stress is a technique by which stress along a single axis is applied to a sample. Stress applied to a crystal (and therefore a defect) can act to lift two types of degeneracy: electronic and orientational [13, 14]. Orientational degeneracy arises from the number of equivalent directions that a defect may orient itself into: for a tetragonal defect such as $\mathrm{I}_{\langle 0\,0\,1\rangle}$, there are three such equivalent directions. Additionally, uniaxial stress may lift electronic degeneracy inherent in e.g. **E** states.

Applied stress of magnitude σ is described by the stress tensor $\boldsymbol{\sigma}$, with components

$$\boldsymbol{\sigma} = \begin{pmatrix} \sigma_{xx} & \sigma_{xy} & \sigma_{xz} \\ \sigma_{yx} & \sigma_{yy} & \sigma_{yz} \\ \sigma_{zx} & \sigma_{zy} & \sigma_{zz} \end{pmatrix} , \tag{3-10}$$

where $\sigma_{ij} = \sigma \cos(\theta_i) \cos(\theta_j)$ and θ_i is the angle between the axis of stress and the ith crystal axis [15]. Due to diamond's interpenetrating face-centred cubic structure, the corresponding stress tensor is symmetric. The component σ_{ij} represents a compression if $i = j$, with $i \neq j$ components representing shear stress [16].

The perturbation due to stress (to first order) is expressed as

$$\hat{V} = \sum_{ij} \mathrm{a}_{ij} \sigma_{ij} , \tag{3-11}$$

where σ_{ij} are the elements of the stress tensor and a_{ij} are electronic operators (see [13]). Full expressions of $\hat{V}$ together with detailed workings of its effects for various centres are given in [13, 14, 17]. The total Hamiltonian of the system may therefore be written

$$\hat{\mathcal{H}} = \hat{\mathcal{H}}_0 + \hat{V} \ ,$$

with $\hat{\mathcal{H}}_0$ as the unperturbed Hamiltonian.

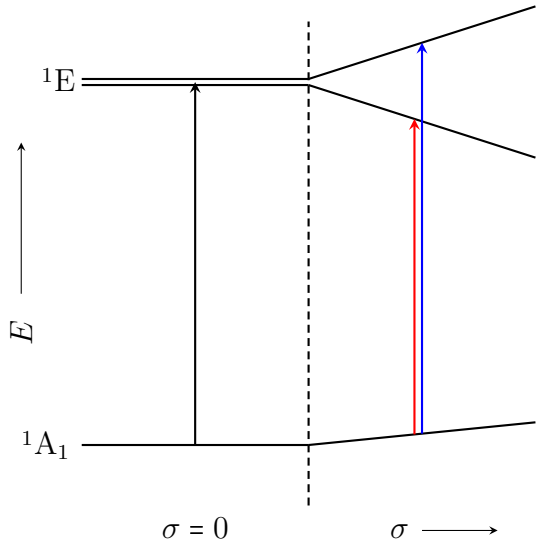

(a) State energy shifts as a function of increasing stress σ. Note: the energy shifts are exaggerated.

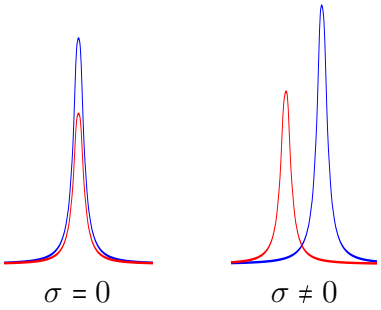

(b) Schematic of potential observations during an optical absorption experiment at zero (left) and non-zero applied stress.

Figure 3-3 Illustration of the effect of applied uniaxial stress on the orbital energy levels (top) and the measured spectrum (bottom) of a point defect. The energy levels and symmetries given are arbitrary.

The symmetry breaking due to the applied perturbation leads to state splitting, as can be seen in figure 3-3. It is evident that any transition between e.g. the ^{1}E and ^{1}A$_1$ states will display a greater change in transition energy as a function of increasing stress. This splitting is what makes uniaxial stress a powerful tool

when trying to determine point defect symmetry in semiconductors: the number of spectral components observed when uniaxial stress is applied along a certain direction, along with their relative intensities, is a fingerprint of the point group symmetry of the defect. Extensive tabulations of splittings and intensities are available for different point group symmetries [8, 18], but care must be taken when the defect involved is preferentially oriented i.e. non-equilibrium populations in all equivalent directions. If a defect is preferentially aligned then the standard tables no longer apply (as they assume isotropy). See §3.8.2 for further discussion.

3.6.1 Zero by symmetry

Group theory can identify whether an integral is necessarily zero by symmetry. An integral may coincidentally be zero for reasons other than symmetry. In the case of uniaxial stress, group theory can greatly simplify the calculations by allowing significant parts of the calculation to be ignored.

For two states ψ_l and $\psi_{l'}$ interacting under a perturbation $\hat{V}$, the matrix element between the states is written

$$\int \psi_l^* \hat{V} \psi_{l'} \, d\tau = \langle \psi_l | \hat{V} \mid \psi_{l'} \rangle \ . \tag{3-12}$$

If the integral does not contain a component which transforms totally symmetrically within the point group of the centre (e.g. as $\mathbf{A_1}$), then the integral over all space is necessarily zero by symmetry. For this not to be the case, the product of the two irreducible representations $\Gamma^{(\hat{V})} \otimes \Gamma^{(l')}$ must contain $\Gamma^{(l)}$: in this manner, transitions which necessarily have zero probability can be easily identified.

3.7 Calculation for a tetragonal defect

Continuing the discussion of the defect $\mathrm{I}_{\langle 0\,0\,1\rangle}$ (see §3.4), consider a centre of tetragonal symmetry: the X, Y, and Z axes of the defect are chosen to be aligned parallel to the crystal axes $x \| [1\,0\,0]$, $y \| [0\,1\,0]$, and $z \| [0\,0\,1]$ respectively.

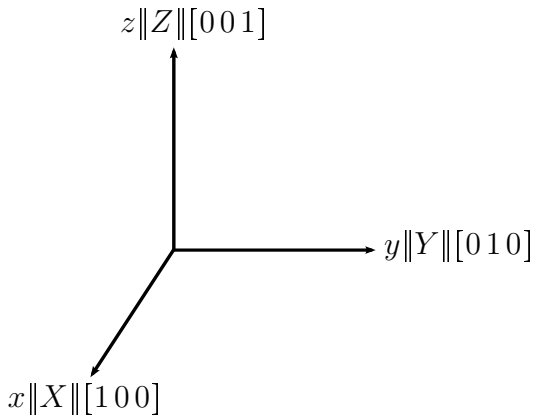

Figure 3-4 Illustration of the stress and defect axes in terms of Miller indices.

The perturbation due to the applied stress can be written as (3-11), with the stress tensor components given by (3-10). The Hamiltonian then takes the form [17]

$$\hat{\mathcal{H}} = \hat{\mathcal{H}}_0 + \hat{V} \tag{3-13}$$

$$\begin{aligned} &= \hat{\mathcal{H}}_0 + \hat{\mathrm{a}}_{\mathrm{A}_1}\sigma_{zz} + \hat{\mathrm{a}}'_{\mathrm{A}_1}\left(\sigma_{xx} + \sigma_{yy}\right) + \hat{\mathrm{a}}_{\mathrm{B}_1}\left(\sigma_{xx} - \sigma_{yy}\right) \\ &\quad + \hat{\mathrm{a}}_{\mathrm{B}_2}\sigma_{xy} + \hat{\mathrm{a}}_{\mathrm{E_x}}\sigma_{zx} + \hat{\mathrm{a}}_{\mathrm{E_y}}\sigma_{yz} \end{aligned} \tag{3-14}$$

Each of the electronic operators $\hat{\mathrm{a}}_\gamma$ transforms as its subscript.

For a $\mathscr{D}_{2\mathrm{d}}$ centre, there are three sites which are related by the rotation matrices ${}^{i}\mathbf{R}_{\mathscr{D}_{2\mathrm{d}}}$. In matrix form, the rotations are

$$\begin{array}{ccc} {}^{1}\mathbf{R}_{\mathscr{D}_{2\mathrm{d}}} & {}^{2}\mathbf{R}_{\mathscr{D}_{2\mathrm{d}}} & {}^{3}\mathbf{R}_{\mathscr{D}_{2\mathrm{d}}} \\ \begin{pmatrix} 1 & 0 & 0 \\ 0 & 1 & 0 \\ 0 & 0 & 1 \end{pmatrix} & \begin{pmatrix} 0 & 0 & 1 \\ 1 & 0 & 0 \\ 0 & 1 & 0 \end{pmatrix} & \begin{pmatrix} 0 & 1 & 0 \\ 0 & 0 & 1 \\ 1 & 0 & 0 \end{pmatrix} \end{array} . \tag{3-15}$$

In order to calculate the effect of the stress on each of the symmetry sites, the stress tensor is calculated in the crystal frame and then transformed into the coordinate system of each site: this process generates three new matrices ${}^{i}\boldsymbol{\sigma} = {}^{i}\mathbf{R}^{-1}_{\mathscr{D}_{2\mathrm{d}}}\,\boldsymbol{\sigma}\,{}^{i}\mathbf{R}_{\mathscr{D}_{2\mathrm{d}}}$.

3.7.1 Transition between an $\mathbf{A_1}$ state and an E state

To determine the possible transitions between two states, it is useful to determine which transitions have necessarily zero probability (i.e. there is no overlap between

the two states). For two states α and β interacting under a perturbation $\hat{V}$, the relevant matrix is given in table 3-7. The off-diagonal elements represent mixing between states, which causes a non-linear dependence of the state energy as a function of applied stress. As the relevant wavefunctions are real and hermitian, $\langle \alpha \mid \hat{V} \mid \beta \rangle = \langle \beta \mid \hat{V} \mid \alpha \rangle$ [19].

	α	β
α	$\langle \alpha \lvert \hat{V} \rvert \alpha \rangle$	$\langle \alpha \lvert \hat{V} \rvert \beta \rangle$
β	$\langle \beta \lvert \hat{V} \rvert \alpha \rangle$	$\langle \beta \lvert \hat{V} \rvert \beta \rangle$

Table 3-7 Matrix elements for states α, β under a perturbation $\hat{V}$

In analysing the optical transitions, it is assumed that the ground and excited states are well separated in energy and hence there is no state mixing between them. For an operator $\hat{O}_{\Gamma_r}$ transforming as the rth basis vector of the irreducible representation Γ, the matrix elements are given by [17]

$$\langle E_\alpha | \hat{O}_{\Gamma_r} | E_\beta \rangle = [E \| \hat{O} \| E] \, \langle \Gamma_r E_\beta | E_\alpha \rangle^* \tag{3-16}$$

where $\langle \Gamma_r E_\beta | E_\alpha \rangle$ are the Clebsch-Gordan coupling coefficients and α and β run over X, Y. A discussion of Clebsch-Gordan coupling coefficients is beyond this thesis: a description and tables for some groups can be found in [20]. The effect of (3-16) is that the element $[E \| \hat{O} \| E]$ is independent of α, β, Γ. Constants for each of the matrix elements may then be defined [14, 17]:

$$\begin{aligned}
A_1 &= [E \| \hat{\mathrm{a}}_{\mathrm{A}_1} \| E] \equiv \langle E_X \| \hat{\mathrm{a}}_{\mathrm{A}_1} \| E_X \rangle = \langle E_Y \| \hat{\mathrm{a}}_{\mathrm{A}_1} \| E_Y \rangle \\
A_2 &= [E \| \hat{\mathrm{a}}'_{\mathrm{A}_1} \| E] \equiv \langle E_X \| \hat{\mathrm{a}}'_{\mathrm{A}_1} \| E_X \rangle = \langle E_Y \| \hat{\mathrm{a}}'_{\mathrm{A}_1} \| E_Y \rangle \\
B &= [E \| \hat{\mathrm{a}}_{\mathrm{B}_1} \| E] \equiv \langle E_X \| \hat{\mathrm{a}}_{\mathrm{B}_1} \| E_X \rangle = - \langle E_Y \| \hat{\mathrm{a}}_{\mathrm{B}_1} \| E_Y \rangle \\
C &= [E \| \hat{\mathrm{a}}_{\mathrm{B}_2} \| E] \equiv \langle E_X \| \hat{\mathrm{a}}_{\mathrm{B}_2} \| E_Y \rangle = \langle E_Y \| \hat{\mathrm{a}}_{\mathrm{B}_2} \| E_X \rangle \ .
\end{aligned}$$

All other matrix elements are zero i.e. there is no overlap between the two states under that operator. A secular matrix between the two orthogonal $\mathbf{E}$ bases may then be constructed:

$$\begin{array}{c} \\ \mathbf{E_X} \\ \mathbf{E_Y} \end{array} \begin{array}{c} \begin{array}{cc} \mathbf{E_X} & \mathbf{E_Y} \end{array} \\ \begin{pmatrix} \alpha + \beta & \gamma \\ \gamma & \alpha - \beta \end{pmatrix} \end{array} \qquad \begin{cases} \alpha &= A_1 \sigma_{zz} + A_2 (\sigma_{xx} + \sigma_{yy}) \\ \beta &= B (\sigma_{xx} - \sigma_{yy}) \\ \gamma &= C \sigma_{xy} \end{cases} . \tag{3-17}$$

Uniaxial stress results may be considered in two ways: taking a single site and considering the inequivalent stress directions; or considering each site in turn and only a single stress direction — the latter approach has been taken here.

3.7.1.1 [0 0 1] stress

For $\sigma \| [0\,0\,1]$ there are two inequivalent sets of sites: site 1 has its Z-axis parallel to the applied stress; sites 2 and 3 have their principal axis perpendicular to the applied stress. The stress tensor for each site is (3-10),

$$\begin{matrix} {}^1\boldsymbol{\sigma} \\ \begin{pmatrix} 0 & 0 & 0 \\ 0 & 0 & 0 \\ 0 & 0 & 1 \end{pmatrix} \end{matrix} \quad \begin{matrix} {}^2\boldsymbol{\sigma} \\ \begin{pmatrix} 0 & 0 & 0 \\ 0 & 1 & 0 \\ 0 & 0 & 0 \end{pmatrix} \end{matrix} \quad \begin{matrix} {}^3\boldsymbol{\sigma} \\ \begin{pmatrix} 1 & 0 & 0 \\ 0 & 0 & 0 \\ 0 & 0 & 0 \end{pmatrix} \end{matrix} \quad .$$

Therefore the Hamiltonian for each site and corresponding eigenvalues and eigenvectors for the secular matrix (3-17) become

Site	Hamiltonian	Eigenvalues	Eigenvectors
1	$\hat{\mathcal{H}}_0 + \hat{\mathrm{a}}_{\mathrm{A}_1}$	A_1, A_1	$\|E_X\rangle, \|E_Y\rangle$
2	$\hat{\mathcal{H}}_0 + \hat{\mathrm{a}}'_{\mathrm{A}_1} - \hat{\mathrm{a}}_{\mathrm{B}/_1}$	$A_2 \pm B$	$\|E_Y\rangle, \|E_X\rangle$
3	$\hat{\mathcal{H}}_0 + \hat{\mathrm{a}}'_{\mathrm{A}_1} + \hat{\mathrm{a}}_{\mathrm{B}/_1}$	$A_2 \pm B$	$\|E_X\rangle, \|E_Y\rangle$

Stress along [0 0 1] will therefore lift electronic degeneracy for two sites (2 & 3), and simply shift their energy in an identical way for the remaining site.

3.7.1.2 [1 1 1] stress

With stress applied along the [1 1 1] direction, all $\langle 1\,0\,0 \rangle$ are equivalent, and the stress tensor is identical for all sites:

$$\begin{matrix} {}^1\boldsymbol{\sigma}, {}^2\boldsymbol{\sigma}, {}^3\boldsymbol{\sigma} \\ \frac{1}{3} \begin{pmatrix} 1 & 1 & 1 \\ 1 & 1 & 1 \\ 1 & 1 & 1 \end{pmatrix} \end{matrix} \quad .$$

Correspondingly, the Hamiltonian and eigensystem is the same for all sites,

Site	Hamiltonian	Eigenvalues	Eigenvectors
$1,2,3$	$\hat{\mathcal{H}}_0 + \frac{1}{3}(\hat{a}_{A_1} + 2\hat{a}'_{A_1} + \hat{a}_{B_2})$	$A_1 + 2A_2 \pm C$	$\frac{\lvert E_X\rangle \pm \lvert E_Y\rangle}{\sqrt{2}}$

3.7.1.3 [1 1 0] stress

Finally, [1 1 0] stress is considered. The stress matrices are

$$\begin{matrix} {}^1\boldsymbol{\sigma} \\ \frac{1}{2}\begin{pmatrix} 1 & 1 & 0 \\ 1 & 1 & 0 \\ 0 & 0 & 0 \end{pmatrix} \end{matrix} \quad \begin{matrix} {}^2\boldsymbol{\sigma} \\ \frac{1}{2}\begin{pmatrix} 1 & 0 & 1 \\ 0 & 0 & 0 \\ 1 & 0 & 1 \end{pmatrix} \end{matrix} \quad \begin{matrix} {}^3\boldsymbol{\sigma} \\ \frac{1}{2}\begin{pmatrix} 0 & 0 & 0 \\ 0 & 1 & 1 \\ 0 & 1 & 1 \end{pmatrix} \end{matrix} \quad .$$

Inserting them into (3-17) gives the following results

Site	Hamiltonian	Eigenvalues	Eigenvectors
1	$\hat{\mathcal{H}}_0 + \hat{a}_{A_1} + \frac{\hat{a}_{B_2}}{2}$	$A_2 \pm \frac{C}{2}$	$\frac{\lvert E_X\rangle \pm \lvert E_Y\rangle}{\sqrt{2}}$
2,3	$\hat{\mathcal{H}}_0 + 12(\hat{a}_{A_1} + \hat{a}'_{A_1} \pm \hat{a}_{B_1})$	$A_1 + A_2 \pm B$	$\lvert E_Y\rangle, \lvert E_X\rangle$

3.8 Relative intensities of optical transitions

The intensity of an electric dipole transition between an initial state ψ_i and a final state ψ_f may be written as

$$\langle \psi_f | \hat{E} | \psi_i \rangle \tag{3-18}$$

where $\hat{E}$ is the electric dipole operator. The dipole operator has a particular symmetry in a given group, and by (3-12) the symmetry of the operator may be used to determine possible transitions between states for a given point group symmetry. For example, in the $\mathscr{D}_{2d}$ group, the dipole operator transforms as $\mathbf{B_2} \oplus \mathbf{E}$: transitions between $\mathbf{A}$ states are therefore forbidden (see table 3-6).

In the intensity calculations, the following assumptions are made [21]:

- the incoming light is absorbed directly at the centre which is producing the emission

- the absorption occurs between the two states which participate in the luminescence
- the excitation is linearly polarised and sub band-gap in energy
- no thermalisation occurs between degenerate states
- equivalent centres are populated equally.

Additionally, the strength of the dipole oscillator in each case is taken to be unity: as transitions are considered only between like centres, the relative intensities will not be affected by this simplification.

The intensity I^i of emission at the ith symmetry-related site of a given centre is [18]

$$I^i \propto \left(l_a^i l_i + m_a^i m_i + n_a^i n_i\right)^2 \left(l_e^i l_d + m_e^i m_d + n_e^i n_d\right)^2 \tag{3-19}$$

where l, m, n are direction cosines relative to the crystal axes. The centre absorbs with an electric dipole vector

$$\boldsymbol{a}^i = \left(l_a^i, m_a^i, n_a^i\right) ,$$

and emits via a dipole oriented as $\boldsymbol{e}^i$. The polarisation of the electric field of the incoming and detected light are given as $\boldsymbol{i}$ and $\boldsymbol{d}$, respectively. I^i may therefore be written

$$I^i \propto \left(\boldsymbol{i} \cdot \boldsymbol{a}^i\right)^2 \left(\boldsymbol{e}^i \cdot \boldsymbol{d}\right)^2 \tag{3-20}$$

Relative intensities are, for common scenarios, well tabulated in both absorption and photoluminescence. However, published photoluminescence tables include only 90° geometry, where the emission collection is perpendicular to the excitation [18]. All photoluminescence measurements in this thesis have been performed in backscatter geometry, and therefore the relative intensities need to be recalculated (§3.9).

3.8.1 Tetragonal example

With reference to the previous section (§3.7), this example will consider a $\mathbf{A_1} \leftrightarrow \mathbf{E}$ transition at a tetragonal ($\mathscr{D}_{2\mathrm{d}}$) centre. The dipoles for absorption and emission

are $\{X, Y\}$ for each site. Consider uniaxial stress applied along $[0\,0\,1]$. The polarisation of the incoming electric field parallel and perpendicular to the applied stress are taken to be $\boldsymbol{i}_\parallel = [0\,0\,1]$ and $\boldsymbol{i}_\perp = [1\,1\,0]$, respectively. In the following calculations, $\boldsymbol{d}_{\perp b}$ and $\boldsymbol{d}_{\perp p}$ will be used to denote the detection polarisation vector perpendicular to the applied stress in backscatter and 90° configurations, respectively: where both dipoles are equivalent, $\boldsymbol{d}_{\perp b,p}$ will be used.

	Absorption				Emission			
	$\boldsymbol{i}_\parallel$		$\boldsymbol{i}_\perp$		$\boldsymbol{d}_\parallel$		$\boldsymbol{d}_{\perp b,p}$	
	$\boldsymbol{E_X}$	$\boldsymbol{E_Y}$	$\boldsymbol{E_X}$	$\boldsymbol{E_Y}$	$\boldsymbol{E_X}$	$\boldsymbol{E_Y}$	$\boldsymbol{E_X}$	$\boldsymbol{E_Y}$
Site 1	0	0	$\frac{1}{2}$	$\frac{1}{2}$	0	0	$\frac{1}{2}$	$\frac{1}{2}$
Site 2	0	1	$\frac{1}{2}$	0	0	1	$\frac{1}{2}$	0
Site 3	1	0	0	$\frac{1}{2}$	1	0	0	$\frac{1}{2}$

(a) Interaction cross-sections for absorption and emission at each site.

	Absorption		Emission			
			$\boldsymbol{i}_\parallel$		$\boldsymbol{i}_\perp$	
	$\boldsymbol{i}_\parallel$	$\boldsymbol{i}_\perp$	$\boldsymbol{d}_\parallel$	$\boldsymbol{d}_{\perp b,p}$	$\boldsymbol{d}_\parallel$	$\boldsymbol{d}_{\perp b,p}$
A_1	0	2	0	0	0	2
$A_2 + B$	4	0	4	0	2	0
$A_2 - B$	0	2	0	2	0	1

(b) Relative intensities of different stress-split components.

Table 3-8 Interaction cross-sections and relative transition intensities for an $\mathbf{A_1} \leftrightarrow \mathbf{E}$ transition at a $\mathscr{D}_{2\mathrm{d}}$ centre with stress applied along $[0\,0\,1]$. See text for details of excitation and detection geometries.

The absorption and emission cross-section for each dipole at each site is given by (3-20) and (3-15) and are calculated in table 3-8a. The interaction cross-sections are then used in conjunction with the eigenstates for each site in order to produce the relative intensities of the stress-split transitions, as given in table 3-8b.

3.8.2 Preferential orientation

Standard tabulations of relative intensities assume equilibrium populations i.e. all equivalent orientations of a given centre are populated equally. There are several important cases where the assumption of isotropy is not valid due to production of defects by anisotropic processes. Examples of such processes include plastic deformation (e.g. slip bands), reorientation of centres due to local strain fields, and certain synthetic growth methods (e.g. CVD).

Unfortunately, recalculating the predicted relative intensities for a given population is not straightforward: in addition to understanding the dipole orientation at a given centre, knowledge of which site contributes to a particular transition is required. This necessitates performing the group theoretical calculation as given in §3.6.

In order to accelerate such calculations in the future, the tables in §3.9 give both the sites involved with a given transition, and the orientation of the electronic dipole for a given dipole transition. When used in conjunction with the site references given in appendix A, it is possible to quickly construct a program to calculate relative intensities for arbitrary populations.

3.9 Intensity tables

Relative intensities are tabulated for point groups and transition symmetries relevant to this thesis. The relative intensities have been normalised only within a given point group symmetry, applied stress direction, and technique i.e. absorption and emission are normalised independently.

For a monoclinic I defect, the low symmetry places few restrictions on dipole orientation. As such, there are two distinct situations:

- For transitions between like states ($\mathbf{A}'(\mathbf{A}'') \leftrightarrow \mathbf{A}'(\mathbf{A}'')$), the dipole is orientated along the Z axis of the defect, perpendicular to the mirror plane.
- For transitions between like states ($\mathbf{A}'(\mathbf{A}'') \leftrightarrow \mathbf{A}''(\mathbf{A}')$), the dipole is orien-

tated anywhere in the XY mirror plane of the defect.

In the latter case, the dipole is taken to be along the Y axis of the defect. It should be noted that these two cases are mislabelled in [18] but are correct in [21]. Intensities for an arbitrary dipole direction may be calculated by using either table 3-9 or 3-10 in conjunction with table 3-11.

		$\boldsymbol{\sigma}\parallel[0\,0\,1]$		$\boldsymbol{\sigma}\parallel[1\,1\,1]$		$\boldsymbol{\sigma}\parallel[1\,1\,0]$	
Sym.[a]	Trans.[b]	Energy	$\boldsymbol{i}_\parallel$:$\boldsymbol{i}_\perp$	Energy	$\boldsymbol{i}_\parallel$:$\boldsymbol{i}_\perp$	Energy	$\boldsymbol{i}_\parallel$:$\boldsymbol{i}_\perp$
Tet.	$\mathbf{A} \leftrightarrow \mathbf{E}$	A_1	0:2	$\frac{1}{3}(A_1 + 2A_2 + C)$	4:1	$\frac{1}{2}(A_1 + A_2 + B)$	1:1
$\mathscr{D}_{2\mathrm{d}}$	$\mathbf{B} \leftrightarrow \mathbf{E}$	$A_2 + B$	4:0	$\frac{1}{3}(A_1 + 2A_2 - C)$	0:3	$\frac{1}{2}(A_1 + A_2 - B)$	0:0
		$A_2 - B$	0:2			$A_2 + \frac{1}{2}C$	1:0
						$A_2 - \frac{1}{2}C$	0:1
Tri.	$\mathbf{A} \leftrightarrow \mathbf{A}$	A_1	1:1	$A_1 + 2A_2$	3:0	$A_1 + A_2$	1:0
$\mathscr{C}_{3\mathrm{v}}$				$\frac{1}{3}(3A_1 - 2A_2)$	1:4	$A_1 - A_2$	0:1
	$\mathbf{A} \leftrightarrow \mathbf{E}$	$A_1 - 2B$	4:1	$A_1 + 2A_2$	0:6	$A_1 + A_2 + C - B$	0:3
		$A_1 + 2B$	0:3	$\frac{1}{3}(3A_1 - 2A_2 - 4C)$	16:1	$A_1 + A_2 - C + B$	1:0
				$\frac{1}{3}(3A_1 - 2A_2 + 4C)$	0:9	$A_1 - A_2 + C + B$	0:1
						$A_1 - A_2 - C - B$	3:0
Rho.I	$\mathbf{A} \leftrightarrow \mathbf{B}$	A_1	0:1	$\frac{1}{3}(A_1 + 2A_2 + 2A_3)$	4:1	$A_2 + A_3$	1:0
$\mathscr{C}_{2\mathrm{v}}$		A_2	2:1	$\frac{1}{3}(A_1 + 2A_2 - 2A_3)$	0:3	$\frac{1}{2}(A_1 + A_2)$	1:2
						$A_2 - A_3$	0:0
	$\mathbf{A} \leftrightarrow \mathbf{A}$	A_1	1:0	$\frac{1}{3}(A_1 + 2A_2 + 2A_3)$	1:1	$A_2 + A_3$	0:1
	$\mathbf{B} \leftrightarrow \mathbf{B}$	A_2	0:1	$\frac{1}{3}(A_1 + 2A_2 - 2A_3)$	1:1	$\frac{1}{2}(A_1 + A_2)$	2:0
						$A_2 - A_3$	0:1
Mon.I	$\mathbf{A}' \leftrightarrow \mathbf{A}''$	A_1	0:1	$\frac{1}{3}(A_1 + 2A_2 + 2A_3)$	0:6	$A_2 + A_3$	0:2
$\mathscr{C}_{1\mathrm{h}}$		A_2	2:1	$\frac{1}{3}(A_1 + 2A_2 - 2A_3 - 4A_4)$	4:1	$\frac{1}{2}(A_1 + A_2 - 2A_4)$	1:1
				$\frac{1}{3}(A_1 + 2A_2 - 2A_3 + 4A_4)$	4:1	$\frac{1}{2}(A_1 + A_2 + 2A_4)$	1:1
						$A_2 - A_3$	2:0
	$\mathbf{A}' \leftrightarrow \mathbf{A}'$	A_1	0:1	$\frac{1}{3}(A_1 + 2A_2 + 2A_3)$	8:2	$A_2 + A_3$	2:0
	$\mathbf{A}'' \leftrightarrow \mathbf{A}''$	A_2	2:1	$\frac{1}{3}(A_1 + 2A_2 - 2A_3 - 4A_4)$	0:3	$\frac{1}{2}(A_1 + A_2 - 2A_4)$	1:1
				$\frac{1}{3}(A_1 + 2A_2 - 2A_3 + 4A_4)$	0:3	$\frac{1}{2}(A_1 + A_2 + 2A_4)$	1:1
						$A_2 - A_3$	0:2

Table 3-9 Predicted relative intensities for electronic dipole transitions at point defects of different symmetries measured by optical absorption spectroscopy.

[a]Point group symmetry
[b]Transition symmetry

		$\boldsymbol{\sigma}\parallel[0\,0\,1]$			$\boldsymbol{\sigma}\parallel[1\,1\,1]$			$\boldsymbol{\sigma}\parallel[1\,1\,0]$		
Sym.[a]	Trans.[b]	Energy	$\boldsymbol{i}_\parallel$ $\boldsymbol{d}_\parallel$:$\boldsymbol{d}_\perp$	$\boldsymbol{i}_\perp$ $\boldsymbol{d}_\parallel$:$\boldsymbol{d}_\perp$	Energy	$\boldsymbol{i}_\parallel$ $\boldsymbol{d}_\parallel$:$\boldsymbol{d}_\perp$	$\boldsymbol{i}_\perp$ $\boldsymbol{d}_\parallel$:$\boldsymbol{d}_\perp$	Energy	$\boldsymbol{i}_\parallel$ $\boldsymbol{d}_\parallel$:$\boldsymbol{d}_\perp$	$\boldsymbol{i}_\perp$ $\boldsymbol{d}_\parallel$:$\boldsymbol{d}_\perp$
Tet.	$\mathbf{A} \leftrightarrow \mathbf{E}$	A_1	0:0	0:2	$\frac{1}{3}(A_1 + 2A_2 + C)$	16:4	16:3	$\frac{1}{2}(A_1 + A_2 + B)$	1:1	1:1
$\mathscr{D}_{2d}$	$\mathbf{B} \leftrightarrow \mathbf{E}$	$A_2 + B$	4:0	2:0	$\frac{1}{3}(A_1 + 2A_2 - C)$	0:12	0:15	$\frac{1}{2}(A_1 + A_2 - B)$	0:0	0:0
		$A_2 - B$	0:2	0:1				$A_2 + \frac{1}{2}C$	2:0	2:0
								$A_2 - \frac{1}{2}C$	0:2	0:2
Tri.	$\mathbf{A} \leftrightarrow \mathbf{A}$	A_1	1:1	1:2	$A_1 + 2A_2$	27:0	0:0	$A_1 + A_2$	1:0	0:0
$\mathscr{C}_{3v}$					$\frac{1}{3}(3A_1 - 2A_2)$	1:4	4:24	$A_1 - A_2$	0:0	0:1
	$\mathbf{A} \leftrightarrow \mathbf{E}$	$A_1 - 2B$	8:2	8:1	$A_1 + 2A_2$	0:0	0:54	$A_1 + A_2 + C - B$	0:3	0:9
		$A_1 + 2B$	0:6	0:9	$\frac{1}{3}(3A_1 - 2A_2 - 4C)$	128:8	80:3	$A_1 + A_2 - C + B$	1:0	3:0
					$\frac{1}{3}(3A_1 - 2A_2 + 4C)$	0:72	0:63	$A_1 - A_2 + C + B$	0:3	0:1
								$A_1 - A_2 - C - B$	9:0	3:0
Rho.I	$\mathbf{A} \leftrightarrow \mathbf{B}$	A_1	0:0	0:4	$\frac{1}{3}(A_1 + 2A_2 + 2A_3)$	32:8	8:3	$A_2 + A_3$	4:0	0:0
$\mathscr{C}_{2v}$		A_2	4:2	2:1	$\frac{1}{3}(A_1 + 2A_2 - 2A_3)$	0:0	0:27	$\frac{1}{2}(A_1 + A_2)$	1:2	2:4
								$A_2 - A_3$	0:0	0:0
	$\mathbf{A} \leftrightarrow \mathbf{A}$	A_1	2:0	0:0	$\frac{1}{3}(A_1 + 2A_2 + 2A_3)$	2:2	2:3	$A_2 + A_3$	0:0	0:1
	$\mathbf{B} \leftrightarrow \mathbf{B}$	A_2	0:0	0:1	$\frac{1}{3}(A_1 + 2A_2 - 2A_3)$	2:2	2:3	$\frac{1}{2}(A_1 + A_2)$	1:0	0:0
								$A_2 - A_3$	0:0	0:1
Mon.I	$\mathbf{A}' \leftrightarrow \mathbf{A}''$	A_1	0:0	0:4	$\frac{1}{3}(A_1 + 2A_2 + 2A_3)$	0:0	0:54	$A_2 + A_3$	0:0	0:8
$\mathscr{C}_{1h}$		A_2	4:2	2:1	$\frac{1}{3}(A_1 + 2A_2 - 2A_3 - 4A_4)$	32:8	8:3	$\frac{1}{2}(A_1 + A_2 - 2A_4)$	1:1	1:1
					$\frac{1}{3}(A_1 + 2A_2 - 2A_3 + 4A_4)$	32:8	8:3	$\frac{1}{2}(A_1 + A_2 + 2A_4)$	1:1	1:1
								$A_2 - A_3$	8:0	0:0
	$\mathbf{A}' \leftrightarrow \mathbf{A}'$	A_1	0:0	0:4	$\frac{1}{3}(A_1 + 2A_2 + 2A_3)$	64:16	16:6	$A_2 + A_3$	8:0	0:0
	$\mathbf{A}'' \leftrightarrow \mathbf{A}''$	A_2	4:2	2:1	$\frac{1}{3}(A_1 + 2A_2 - 2A_3 - 4A_4)$	0:0	0:27	$\frac{1}{2}(A_1 + A_2 - 2A_4)$	1:1	1:1
					$\frac{1}{3}(A_1 + 2A_2 - 2A_3 + 4A_4)$	0:0	0:27	$\frac{1}{2}(A_1 + A_2 + 2A_4)$	1:1	1:1
								$A_2 - A_3$	0:0	0:8

Table 3-10 Predicted relative intensities for electronic dipole transitions at point defects of different symmetries measured by photoluminescence.

[a] Point group symmetry
[b] Transition symmetry

			$\boldsymbol{\sigma}\parallel[001]$		$\boldsymbol{\sigma}\parallel[111]$		$\boldsymbol{\sigma}\parallel[110]$	
Sym.[a]	Trans.[b]	D[c]	Energy	Sites	Energy	Sites	Energy	Sites
Tet.	$\mathbf{A}\leftrightarrow\mathbf{E}$	X,Y	A_1	$1_{X,Y}$	$\frac{1}{3}(A_1+2A_2+C)$	$(1\text{–}3)_X$	$\frac{1}{2}(A_1+A_2+B)$	$2_X,3_Y$
$\mathscr{D}_{2d}$	$\mathbf{B}\leftrightarrow\mathbf{E}$		A_2+B	$2_Y,3_X$	$\frac{1}{3}(A_1+2A_2-C)$	$(1\text{–}3)_X$	$\frac{1}{2}(A_1+A_2-B)$	$2_Y,3_X$
			A_2-B	$2_X,3_Y$			$A_2+\frac{1}{2}C$	1_Y
							$A_2-\frac{1}{2}C$	1_X
Tri.	$\mathbf{A}\leftrightarrow\mathbf{A}$	Z	A_1	1–4	A_1+2A_2	1	A_1+A_2	1, 2
$\mathscr{C}_{3v}$					$\frac{1}{3}(3A_1-2A_2)$	2–4	A_1-A_2	3, 4
	$\mathbf{A}\leftrightarrow\mathbf{E}$	X,Y	A_1-2B	$(1\text{–}4)_Y$	A_1+2A_2	$1_{X,Y}$	A_1+A_2+C-B	$(1,2)_X$
			A_1+2B	$(1\text{–}4)_X$	$\frac{1}{3}(3A_1-2A_2-4C)$	$2_Y,(3,4)_X$	A_1+A_2-C+B	$(1,2)_Y$
					$\frac{1}{3}(3A_1-2A_2+4C)$	$2_X,(3,4)_Y$	A_1-A_2+C+B	$(3,4)_Y$
							A_1-A_2-C-B	$(3,4)_X$
Rho.I	$\mathbf{A}\leftrightarrow\mathbf{B}$	Y	A_1	1, 2	$\frac{1}{3}(A_1+2A_2+2A_3)$	2, 4, 6	A_2+A_3	2
$\mathscr{C}_{2v}$			A_2	3–6	$\frac{1}{3}(A_1+2A_2-2A_3)$	1, 3, 5	$\frac{1}{2}(A_1+A_2)$	3–6
							A_2-A_3	1
	$\mathbf{A}\leftrightarrow\mathbf{A}$	Z	A_1	1, 2	$\frac{1}{3}(A_1+2A_2+2A_3)$	2, 4, 6	A_2+A_3	2
	$\mathbf{B}\leftrightarrow\mathbf{B}$		A_2	3–6	$\frac{1}{3}(A_1+2A_2-2A_3)$	1, 3, 5	$\frac{1}{2}(A_1+A_2)$	3–6
							A_2-A_3	1
Mon.I	$\mathbf{A}'\leftrightarrow\mathbf{A}''$	Y	A_1	1–4	$\frac{1}{3}(A_1+2A_2+2A_3)$	1, 3, 5, 7, 10, 12	A_2+A_3	1, 3
$\mathscr{C}_{1h}$			A_2	5–12	$\frac{1}{3}(A_1+2A_2-2A_3-4A_4)$	2, 6, 9	$\frac{1}{2}(A_1+A_2-2A_4)$	5, 8, 10, 11
					$\frac{1}{3}(A_1+2A_2-2A_3+4A_4)$	4, 8, 11	$\frac{1}{2}(A_1+A_2+2A_4)$	6, 7, 9, 12
							A_2-A_3	2, 4
	$\mathbf{A}'\leftrightarrow\mathbf{A}'$	Z	A_1	1–4	$\frac{1}{3}(A_1+2A_2+2A_3)$	1, 3, 5, 7, 10, 12	A_2+A_3	1, 3
	$\mathbf{A}''\leftrightarrow\mathbf{A}''$		A_2	5–12	$\frac{1}{3}(A_1+2A_2-2A_3-4A_4)$	2, 6, 9	$\frac{1}{2}(A_1+A_2-2A_4)$	5, 8, 10, 11
					$\frac{1}{3}(A_1+2A_2-2A_3+4A_4)$	4, 8, 11	$\frac{1}{2}(A_1+A_2+2A_4)$	6, 7, 9, 12
							A_2-A_3	2, 4

Table 3-11 Site-by-site electronic dipole contributions to each transition. For transitions to or from an orbitally degenerate state, components of the dipole are indicated as subscripts.

[a]Point group symmetry
[b]Transition symmetry
[c]Dipole orientation

References

1. P. W. Atkins, R. S. Friedman, *Molecular Quantum Mechanics* (Oxford University Press, 3rd edition, 1997).
2. W. Ludwig, C. Falter, *Symmetries in Physics*, ed. by P. Fulde (Springer-Verlag, 1988).
3. S. Sternberg, *Group theory and physics* (Cambridge University Press, 1994).
4. P. H. E. Meijer, E. Bauer, *Group Theory: The Application to Quantum Mechanics* (North-Holland Pub. Co., Amsterdam, 1962).
5. K. A. A. Johnston, PhD thesis, King's College London, 2000.
6. R. Mirman, *Group Theory: An Intuitive Approach* (World Scientific Publishing Co. Pte. Ltd., Singapore, 1995), ISBN: 981-02-2183-5.
7. C. J. H. Schutte, *The Theory of Molecular Spectroscopy* (North-Holland Publishing Company, 1976).
8. P. W. Atkins, M. S. Child, C. S. G. Phillips, *Tables for group theory* (Oxford University Press, 1970).
9. F. A. Cotton, *Chemical Applications of Group Theory* (John Wiley & Sons, ed. 3, 1990).
10. J. P. Goss *et al.*, *Physical Review B* **63**, 195208 (2001).
11. D. Hunt *et al.*, *Physical Review B* **61**, 3863 (2000).
12. H. E. Smith *et al.*, *Physical Review B* **69**, 045203 (2004).
13. A. A. Kaplyanskii, *Optics and Spectroscopy* **16**, 329 (1964).
14. A. A. Kaplyanskii, *Optics and Spectroscopy* **16**, 557 (1964).
15. S. Liggins *et al.*, *Physical Review B* **81**, 1 (2010).
16. G. Davies, in *Identification of defects in semiconductors*, ed. by M. Stavola (Academic Press, 1998), vol. 51B, chap. Optical measurements of point defects, p. 1.
17. A. E. Hughes, W. A. Runciman, *Proceedings of the Physical Society* **90**, 827 (1967).
18. K. Mohammed, G. Davies, A. T. Collins, *Journal of Physics C: Solid State Physics* **15**, 2779 (1982).
19. H. E. Smith, PhD thesis, King's College London, 2004.

20. J. S. Griffith, *The Theory of Transition Metal Ions* (Cambridge University Press, Cambridge, 1961).

21. K. Mohammed, PhD thesis, King's College London, 1982.

Chapter 4

Experimental details

4.1 Optical absorption spectroscopy

4.1.1 Theory

As an electromagnetic (EM) wave propagates through a medium, it is attenuated due to several absorption and scattering mechanisms. For energies in the visible to near-UV range, scattering mechanisms in diamond are generally unimportant and attenuation occurs through absorption of the incident light by electronic dipoles in the medium. Classically, an EM wave with angular frequency ω travelling in one dimension through a material has intensity $I(z,\omega)$ at position z given by [1]

$$I(z,\omega) = I_{0,\omega} e^{-\alpha(\omega) z} \ ,$$

where $I_{0,\omega}$ is the intensity at position $z = 0$, and $\alpha(\omega)$ is the absorption coefficient of the material at frequency ω. In an experiment, the final intensity $I_t(\omega)$ is measured after the light has exited the material of total thickness t, and is recorded as absorbance $A(\omega)$, where (neglecting surface reflection)

$$A(\omega) = -\log_{10}\left(\frac{I_t(\omega)}{I_{0,\omega}}\right) \ .$$

The measured absorbance is then linearly related to the absorption coefficient by

$$\alpha(\omega) = \frac{\log_e(10)}{t} A(\omega) \ .$$

For absorption which is not intrinsic to a material i.e. introduced by impurities, structural defects etc., the absorption coefficient is also usually normalised by concentration such that a given number density of absorbing defects will produce a given absorption coefficient. Ultraviolet-visible absorption (UV-Vis) spectroscopy is therefore a quantitative technique: this property is exploited often in the study of materials, where it is not just the nature of the absorbing species that is important, but also the quantity.

4.1.1.1 Electronic dipoles in diamond

Within this thesis, two distinct classes of electronic dipole will be considered: those which excite vibrational modes in the lattice; and those which cause an electronic transition. In the former case, the incoming EM wave interacts with an instantaneous dipole caused by zero-point atomic motion in the lattice; in the latter the absorption occurs at a permanent dipole moment.

A perfect diamond, as with other tetrahedrally-bonded homonuclear materials, cannot absorb light in the one-phonon region due to lattice symmetry [2]; intrinsic diamond two- and three-phonon absorption is appreciable between approximately 190–500 meV (1500–4000 cm^{-1}) [3]. The maximum frequency vibration which may propagate through the diamond lattice corresponds to 165 meV (1332 cm^{-1}), which is achieved at the Brillouin zone-centre: this is therefore also the characteristic Raman frequency for diamond [4]. The addition of impurities or lattice defects destroys the local symmetry, and many common impurities in diamond cause significant absorption in the one-phonon region [5].

In terms of optical energies, diamond has a large (indirect) band gap of E_g = 5.47 eV (227 nm) [6], and apart from multi-phonon absorption, perfect diamond is transparent to light of energy $0 < \hbar\omega < 5.47\,\mathrm{eV}$. As with vibrational frequencies, defects in the crystal lattice (both extrinsic and intrinsic) can introduce additional absorption features, which are often used as a spectral fingerprint of a particular defect.

4.1.1.2 Defect-induced transitions

Transitions between a defect-induced in-gap state and either of the bands (conduction or valence band) will appear as a broad, largely featureless continuum. However, transitions between two localised, in-gap states will manifest as a sharp (narrow in energy, in diamond ~ 1 meV) spectral line known as a zero-phonon line (ZPL).

Electron-phonon coupling leads to additional absorption features which are known as vibronic structure. This effect arises because the movement of the local atoms perturbs the electronic wavefunction, causing changes in the energy of the orbital. Many centres couple primarily to several distinct phonon frequencies, giving them a vibronic structure which is characteristic of the defect and which represents the low-frequency phonon density of states at the defect. An overview of vibronic spectra in diamond and corresponding numerical analysis is given in [7].

As most optical work is performed at low temperature ($\leq 80\,\mathrm{K}$), the transition occurs from the lowest-energy vibrational state, and the ZPL corresponds to the lowest (highest) energy transition of the vibronic structure for absorption (emission): this is illustrated in figure 4-1.

Vibronic systems are often described in terms of a configuration coordinate Q (figure 4-1). Q is an overall measure of the total atomic energy of a defect system and implicitly accounts for relative atomic motion and effective masses at the defect [8]. Configuration coordinate diagrams display electronic transitions as vertical lines, with vibrational changes being associated with a change in Q. This construction is a consequence of the Born-Oppenheimer approximation, which states that due to the heavy nature of the ions in a material, the nuclear and electronic motion may be considered as independent — the ions simply provide a periodic background potential to the electronic states. The electronic wavefunction may therefore be written as the product of electronic ($\psi(r)$) and vibrational ($\chi(Q)$) parts [9]:

$$\Psi = \psi(r)\chi_n(Q) \ ,$$

with n being the vibrational quantum number of the electronic state.

In simple situations in it conventional to consider the vibrational potential as harmonic, with $V \propto Q^2$, as shown in figure 4-1a. In general, the configuration coordinate of the ground and excited states at a given defect will not be identical [10].

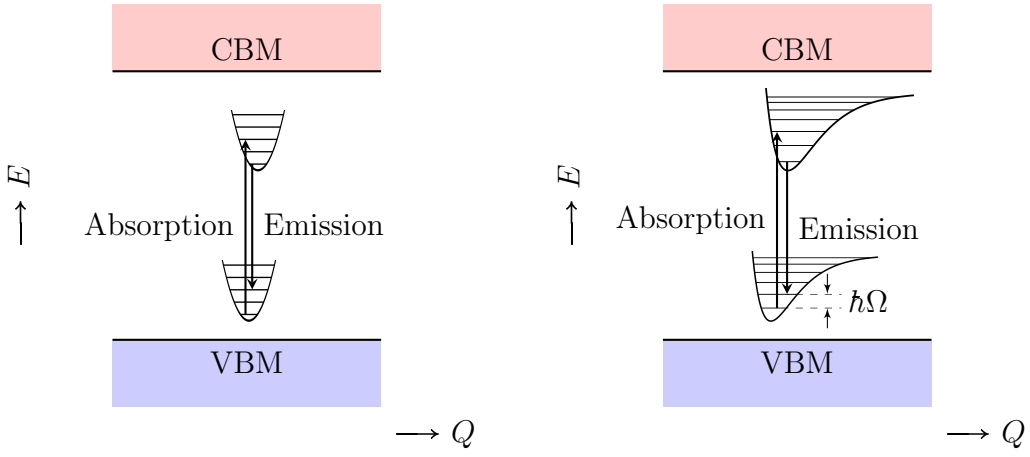

(a) Harmonic potential **(b)** Anharmonic potential

Figure 4-1 Vibronic coupling in a semiconductor at low temperature. Both absorption and emission transitions originate from the lowest vibrational sublevel (thin lines) of the electronic state (thick lines). The transition may involve the creation of a phonon, increasing (decreasing) the energy of the transition for absorption (emission). A zero-phonon line occurs between the same vibrational sublevels of each electronic state. Relative energies are not to scale.

In the special case that the vibronic coupling is to a phonon mode whose frequency is higher than the lattice propagation frequency (165 meV), the corresponding vibration is localised in both frequency and space, and will appear as a sharp spectral line known as a local vibrational mode (LVM). Consistent with their high frequency, LVMs usually occur at either light impurities or highly-strained sites [9]. LVMs are often crucial in the understanding of the origin of a particular electronic transition, in part due to the greater precision and accuracy of theoretical predictions of vibrational frequencies relative to electronic frequencies [11].

4.1.1.3 Isotope effects on zero-phonon lines

When two crystals are grown with identical methods but using different isotopes of a dopant, any ZPL originating at a defect containing the dopant may exhibit

a small shift in energy. Isotope effects have been observed previously in diamond [12–14], most strikingly in the $(SiV)^-$ centre [15, 16]. An extensive discussion of isotopic effects on ZPLs was given by Hughes [17]: the discussion here will follow the summary given by Davies [9]. In particular, the energy changes associated with changing the host isotope are not considered here.

In order to account for a change in ZPL transition energy due to isotope substitution, anharmonicity of the vibrational modes must be considered (figure 4-1b): for purely harmonic potentials ($V \propto Q^2$, figure 4-1a), both the ground and excited states change in the same manner and no change in transition energy is detected [9].

ZPL energy shifts under dopant isotopic substitution are primarily associated with a change in zero-point motion of the nuclei. Treating the nuclear motion as a mass on a spring with effective mode mass m^*, the associated mode frequency shift is

$$\frac{\omega_a}{\omega_b} = \sqrt{\frac{m_b^*}{m_a^*}}$$

for two isotopes a & b [11]. The associated ZPL shift is

$$\hbar\omega_a - \hbar\omega_b = \Delta E_{\mathrm{ZPL}} = \frac{1}{2}\left(1 - \sqrt{\frac{m_a^*}{m_b^*}}\right)\left(\hbar\Omega_{e,a} - \hbar\Omega_{g,a}\right) \tag{4-1}$$

where g, e denote ground and excited electronic states, respectively [9], and $\hbar\Omega$ is the energy of a phonon. In general, $\hbar\Omega_e < \hbar\Omega_g$ (defect is less tightly bound) and so shifts in heavy-isotope material are expected to be positive: this is interpreted as a "softening" of the mode, which in turn lowers the zero-point energy.

4.1.2 Isotope effects on local vibrational modes

The effects of isotopic substitution on LVMs are usually interpreted using the diatomic mass on a spring model. Here, a host atom of mass M is attached by a spring with spring constant k to an impurity atom of mass m. A correction to account for the vibration of the host is applied by multiplying M by an empirical constant χ. Under the substitution of isotope a with isotope b, a mode with frequency Ω_a involving an impurity with mass m_a will change to frequency Ω_b

with the relationship [18]

$$\frac{\Omega_a}{\Omega_b} = \sqrt{\frac{m_b(m_a + \chi M)}{m_a(m_b + \chi M)}} .$$

Often the vibration of the host is neglected, and the ratio $\frac{\Omega_a}{\Omega_b}$ is approximated as $\sqrt{\frac{m_a}{m_b}}$ [12]. A review of the background theory of isotopic substitution on LVMs, along with experimental results in semiconductors, is given in [18].

4.1.3 Experimental detail

4.1.3.1 Fourier transform infrared absorption

Infrared measurements presented in this thesis were performed across the range 0.04–1.30 eV (300–10 500 cm^{-1}) at room temperature using a PerkinElmer Spectrum GX Fourier transform infrared (FTIR) absorption spectrometer. During each measurement, the sample chamber and optical bench were continuously purged with dry nitrogen gas in order to minimise atmospheric absorption.

There are many published works concerned with the operation and mathematical description of FTIR spectrometers (see e.g. [19, 20]) — the particulars have no bearing on the conclusions drawn in this thesis and hence are omitted. Nevertheless, it is worthy of note that Fourier transform spectrometers illuminate the sample with broadband light across the entire spectral range: for samples which are sensitive to charge effects at these energies (e.g. silicon), a dispersive spectrometer may be more appropriate.

4.1.3.2 Ultraviolet-visible absorption

A PerkinElmer Lambda 1050 dispersive spectrometer was used to collect all UV-Vis spectra presented in this thesis. The spectrometer monochromates the light before it is incident on the sample. All measurements were performed with the sample mounted into an Oxford Instruments Optistat continuous flow cryostat and held at 80 K. A spectral range of 0.7–6.2 eV (1800–200 nm) at a step-size of 1 nm was used. The sample was held in place using packed indium, and helium was used as the exchange gas inside the sample chamber of the cryostat.

4.2 Photoluminescence

When a defect absorbs an incident photon and undergoes an electronic dipole transition to an excited state, there are several mechanisms by which the system may lower its overall energy: one of the most efficient is by emission of a photon (figure 4-1), which typically occurs on the order of nanoseconds in diamond [21]. This process is known as photoluminescence (PL, c.f. cathodoluminescence (excitation by electron beam), or thermoluminescence due to the input of heat), and it provides vital information on excited states of defects.

The analysis of photoluminescence transitions is often more complicated than optical absorption transitions as it must deal with non-equilibrium level populations, and the energetic decay is intimately concerned with both radiative and non-radiative processes. A discussion of photoluminescence processes under sub-band-gap illumination is given in §6.4.3.

All photoluminescence measurements in this thesis were performed on one of two dispersive Renishaw inVia Raman spectrometers. The lasers and associated diffraction gratings are given in table 4-1. For all non-stress measurements (see next section for details on stress measurements), the sample was mounted onto the copper cold-finger of an Oxford Instruments MicrostatHe continuous flow cryostat and held at a temperature of 8–100 K. The cryostat was mounted onto a home-built bracket and xyz-stage to provide spatial selectivity and focusing control.

	Laser line		1st-order Raman		Grating
Laser type	$\hbar\omega$ (eV)	λ (nm)	$\hbar\omega$ (eV)	λ (nm)	(1 mm^{-1})
HeCd	3.815	325.0	3.650	339.7	3600
HeCd	2.808	441.6	2.642	469.2	2400
Ar^+	2.410	514.5	2.245	552.4	1800
HeNe	1.959	632.8	1.794	691.0	1800
Solid state	1.579	785.0	1.414	876.7	1200

Table 4-1 The lasers and grating densities used for photoluminescence measurements.

4.3 Uniaxial stress

The splitting of photoluminescence transitions under applied uniaxial stress (see §3.6 for theory) were recorded using the spectrometer described in §4.2. The uniaxial stress cell uses high-pressure nitrogen to apply stress to a ram and hence to the sample via a rod and anvil (figure 4-2). The cell was mounted into a modified Oxford Instruments Optistat continuous flow liquid helium cryostat for low-temperature measurements. A new vacuum casing for the Optistat was designed and built in order to reduce the distance between the sample and the microscope objective of the spectrometer. The stress cell and cryostat were mounted onto an aluminium plate and bolted to two heavy-duty stages (xy: Newport M-401; z: Newport M-MVN120), and the entire assembly was mounted onto a table constructed from mk Profile[1] parts.

During experiments, the gas pressure was regulated by a Bronkhorst El-Press 602CV mass flow controller connected to a computer. The temperature at the sample was monitored and controlled by an Oxford Instruments ITC4 connected to a resistive heater inside the cryostat. Software was written to control and record both the pressure and temperature at the sample.

As detailed in §3.8, the interpretation of photoluminescence uniaxial stress data requires knowledge of the polarisation of different stress-split components. All the lasers used for photoluminescence had an extinction ratio (intensity of the two orthogonal polarisation components) of better than 100:1. Incident laser polarisation was rotated using half-waveplates, and the detection was polarised using a sheet polariser and half-waveplate. The plane of detection polarisation was chosen for maximum spectrometer sensitivity. The results of polarisation tests are given in figure 4-3, and have extinction ratios of between 50 and 100:1.

[1] `www.mk-group.com`

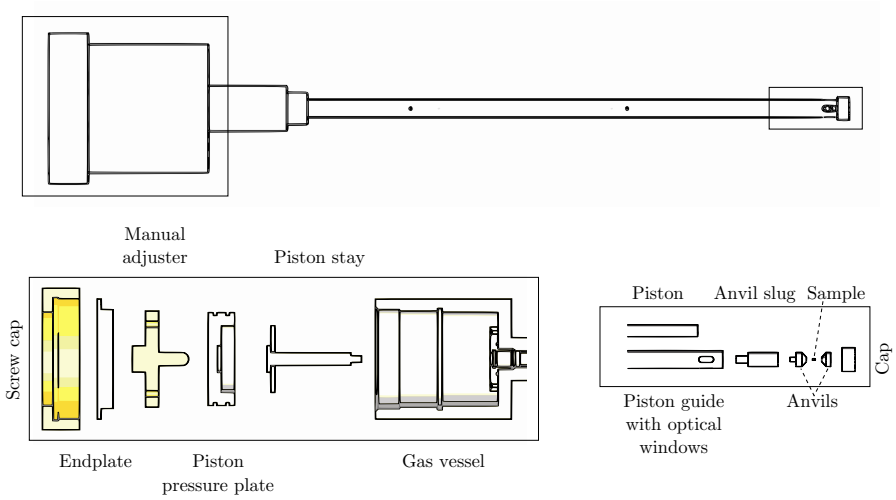

(a) Detail view of the uniaxial stress cell

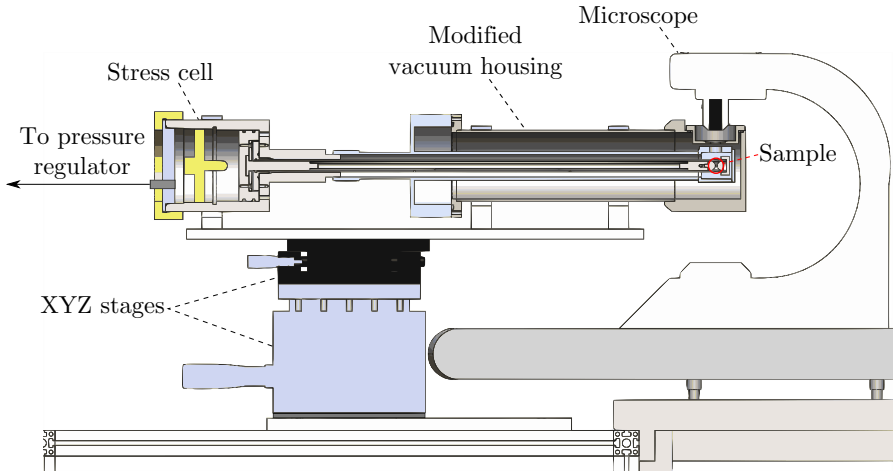

(b) The stress cell mounted into the continuous flow cryostat and inserted in the spectrometer

Figure 4-2 Illustration of the experimental apparatus to apply uniaxial stress at cryogenic sample temperatures inside a photoluminescence microscope spectrometer.

4.4 Electron paramagnetic resonance

Electron paramagnetic resonance (EPR) is a powerful technique which can directly provide information about an electron's wavefunction and local nuclear environment. Its power comes from the ability to both monitor and manipulate the electronic magnetic moment by the application of several types of electromagnetic field. There exist many in-depth treatments of both continuous wave (CW) and pulsed EPR (FTEPR) [22–24] — only the relevant parts of CWEPR will be summarised here .

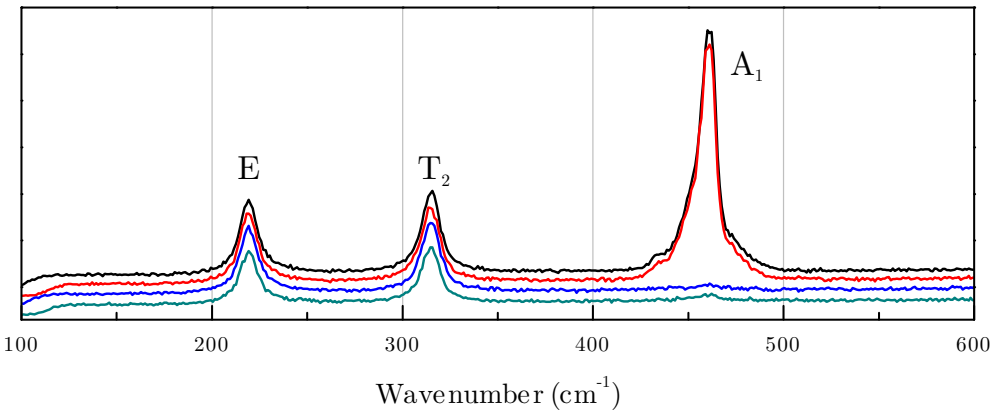

Figure 4-3 Polarisation tests carried out on CCl_4 (carbon tetrachloride). As CCl_4 is a liquid, there is no anisotropy beyond the polarisation of the light itself, and so the polarisation planes will be denoted 1 and 2, with the two planes mutually orthogonal. Incident polarisation is denoted by $\boldsymbol{i}$, and detection by $\boldsymbol{d}$. Top to bottom, the spectra are therefore $(\boldsymbol{i}_1, \boldsymbol{d}_1)$, $(\boldsymbol{i}_2, \boldsymbol{d}_2)$, $(\boldsymbol{i}_1, \boldsymbol{d}_2)$ and $(\boldsymbol{i}_2, \boldsymbol{d}_1)$. The low frequency modes have (from low to high frequency) $\mathbf{E}$ and $\mathbf{T_2}$ symmetry and hence are unaffected by polarisation changes, but the high frequency mode has symmetry $\mathbf{A_1}$ and hence is not observed when incident and detection polarisations are orthogonal. Spectra have been offset for clarity, and no correction has been made for the response function of the instrument.

4.4.1 Performing an experiment

In the very simplest case, a system which contains only a single unpaired electron possesses two magnetic sublevels, which are degenerate in the absence of a magnetic field (see figure 4-4). When a magnetic field B is applied, the energy difference between the two levels is

$$\Delta E = g_e \mu_B B \,, \tag{4-2}$$

where g_e and μ_B are defined in §4.4.2.

To perform a typical EPR experiment, a sample is mounted into a microwave resonator and placed between the pole-pieces of an electromagnet. The microwave resonator is connected via waveguide or coaxial cable to a microwave bridge, which contains both microwave generation and microwave detection electronics. It is conventional to use a fixed-frequency microwave source, and to sweep the magnetic field (see figure 4-4): when the energetic splitting of the levels involved is equal in energy to the microwave quantum i.e. $\hbar\omega = \Delta E$ (4-2), then the microwave

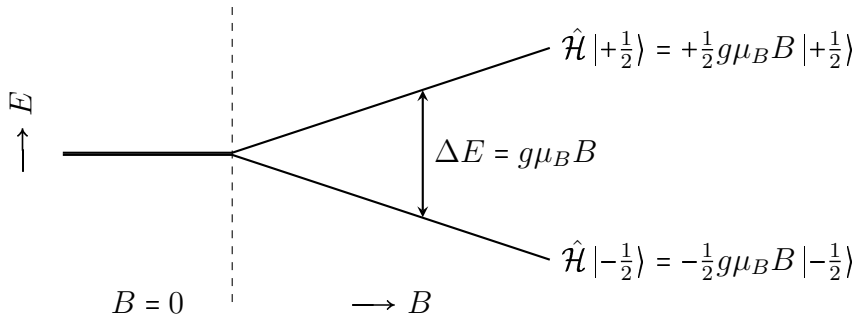

Figure 4-4 Electronic Zeeman effect for a system with effective spin $S = \frac{1}{2}$. As the applied magnetic field is swept, the energy of the spin-up and spin-down (parallel and anti-parallel to the applied field, respectively) change energy, with the energy difference between the levels given by ΔE.

quantum will be absorbed by the spin system, an effect known as resonance. This absorption causes a small change in impedance of the resonator and hence reflection of microwaves at the interface between the waveguide and the resonator, which are in turn detected by the bridge and recorded as a signal. In modern spectrometers, this signal is sent to a computer controlling the spectrometer for storage. Further detail on practical EPR spectrometers is available in [24, 25].

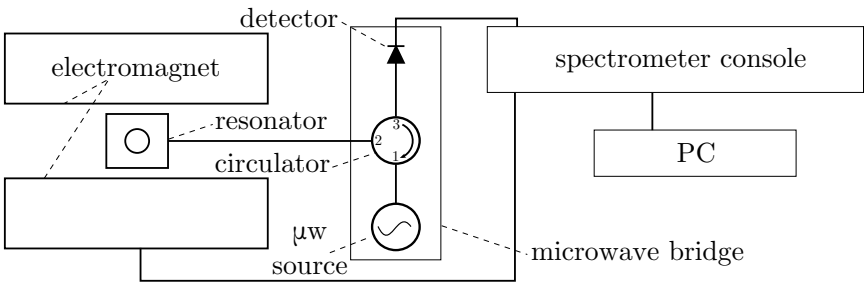

Figure 4-5 Simplified schematic of an EPR spectrometer. Components not relevant to the data presented in this thesis have been omitted.

Historically, the magnetic fields used in EPR have been defined by the frequencies available (most of which correspond to military radar or communication bands). The two frequencies used in this thesis are X-band (8–12 GHz, g_e at approximately 290–430 mT) and Q-band (30–50 GHz, g_e at approximately 1000–1800 mT).

Due to the low energy of microwave-frequency EM radiation (microwave quanta are much lower in energy than thermal fluctuations), a conventional CWEPR spectrometer employs several noise-rejection techniques. One of the primary

noise-rejection techniques involves modulation of the external field B: the signal recorded at the detector is then phase-sensitively demodulated at this frequency, providing a very high degree of noise rejection of other frequencies and phases. As with other AC techniques (atomic force microscopy, low-level optical detection), the signal is recorded as approximately the first-derivative of the response from the sample. Although it is possible to numerically integrate the response, this is associated with problems when dealing with noisy data, and it is usual to present the data without further processing (for example, in figure 4-6).

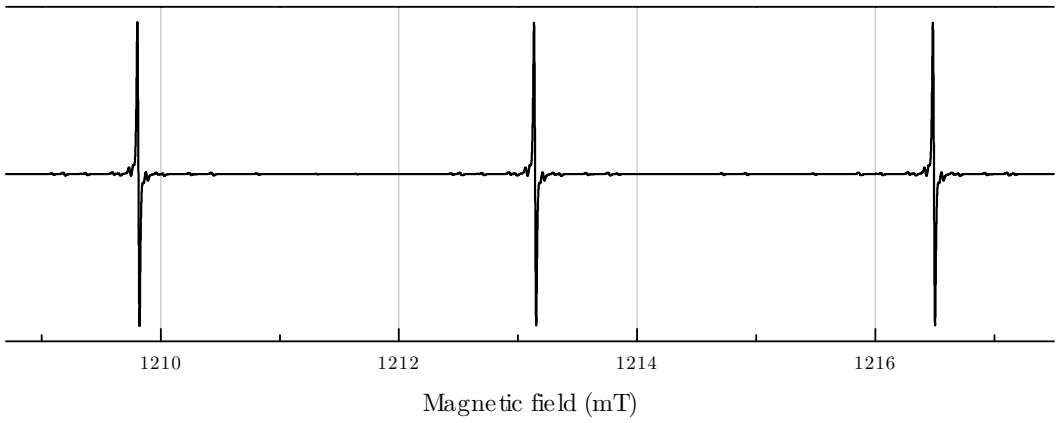

Figure 4-6 A simulated EPR spectrum of substitutional nitrogen in diamond: the approximately first-derivative lineshape caused by phase-sensitive demodulation is evident.

4.4.2 Theory

The typical treatment of an unpaired electron in a CWEPR experiment is by the spin Hamiltonian, a macroscopic Hamiltonian which contains terms corresponding to each of the different interactions that modify the energy of the electron. The Hamiltonian usually takes the form

$$\hat{\mathcal{H}} = \underbrace{\mu_{\mathrm{B}} \boldsymbol{B}^{\mathrm{T}} \cdot \mathbf{g} \cdot \hat{\boldsymbol{S}}}_{\text{electronic Zeeman}} + \underbrace{\hat{\boldsymbol{S}}^{\mathrm{T}} \cdot \mathbf{D} \cdot \hat{\boldsymbol{S}}}_{\text{zero-field}} + \overbrace{\sum_{i}^{n} \{ \underbrace{-\mu_{\mathrm{N}} \boldsymbol{B}^{\mathrm{T}} \cdot g_{\mathrm{N}} \cdot \hat{\boldsymbol{I}}_i}_{\text{nuclear Zeeman}} + \underbrace{\hat{\boldsymbol{S}}^{\mathrm{T}} \cdot \mathbf{A}_i \cdot \hat{\boldsymbol{I}}_i}_{\text{hyperfine}} + \underbrace{\hat{\boldsymbol{I}}_i{}^{\mathrm{T}} \cdot \mathbf{P}_i \cdot \hat{\boldsymbol{I}}_i}_{\text{quadrupole}} \}}^{\text{sum over nuclei}} \; .$$

Each of the interactions will be discussed in turn in the following sections.

4.4.2.1 Electronic Zeeman interaction

A magnetic moment $\hat{\boldsymbol{\mu}}$ placed into a magnetic field $\boldsymbol{B}$ has energy $E = -\hat{\boldsymbol{\mu}} \cdot \boldsymbol{B}$ (the Zeeman effect). The magnetic dipole for an electron contains contributions from its orbital angular momentum $\hat{\boldsymbol{L}}$, and its intrinsic angular momentum (known as spin) $\hat{\boldsymbol{S}}$:

$$\hat{\boldsymbol{\mu}} = -\frac{e\hbar}{2m_e}(\hat{\boldsymbol{L}} + g_e\hat{\boldsymbol{S}}) = -\mu_B(\hat{\boldsymbol{L}} + g_e\hat{\boldsymbol{S}}) \ , \tag{4-3}$$

where g_e is a dimensionless quantity relating the spin and magnetic moment of a free electron. The total energy of a bound electron also includes contributions due to interaction between the electron's spin and its motion (spin-orbit coupling):

$$\hat{\mathcal{H}} = \mu_B \boldsymbol{B} \cdot (\hat{\boldsymbol{L}} + g_e\hat{\boldsymbol{S}}) + (\lambda_{\mathrm{SO}}\hat{\boldsymbol{L}} \cdot \hat{\boldsymbol{S}}) \ ,$$

with the strength of spin-orbit coupling described by λ_{SO}. The $\hat{\boldsymbol{L}}$ and $\lambda_{\mathrm{SO}}\hat{\boldsymbol{L}} \cdot \hat{\boldsymbol{S}}$ terms are often approximated as contributions to the tensor $\mathbf{g}$, and (4-3) may be written as

$$\hat{\mathcal{H}}_{eZ} = \mu_B \boldsymbol{B}^{\mathrm{T}} \cdot \mathbf{g} \cdot \hat{\boldsymbol{S}} \ ,$$

where $\mathbf{g} = g_e\mathbf{1} + 2\lambda_{\mathrm{SO}}\boldsymbol{\Lambda}$, and $\boldsymbol{\Lambda}$ is the spin-orbit coupling matrix. In an experiment, it is convention to take the applied magnetic field as being aligned along the z direction i.e. $\boldsymbol{B} = (0, 0, B)$, and so the effective electronic Zeeman Hamiltonian becomes

$$\hat{\mathcal{H}}_{eZ} = g\mu_B B\hat{S}_z \ . \tag{4-4}$$

In the quantum-mechanical formalism, the spin of an electron is quantised along z with spin quantum number $m_S = \frac{n}{2}$, where n is an integer. The operator $\hat{S}_z$ applied to a state $|m_S\rangle$ retrieves the angular momentum value:

$$\hat{S}_z |m_S\rangle = m_S |m_S\rangle \ , \tag{4-5}$$

and so an unpaired electron will have energy $\hat{\mathcal{H}} |m_S\rangle = E |m_S\rangle = g\mu_B B m_S |m_S\rangle$ — this is illustrated in figure 4-4.

4.4.2.2 Zero-field interaction

The zero-field term exists only for centres with spin $S \geq 1$, and has the effect of lifting the $(2S + 1)$-fold degeneracy even in the absence of an external magnetic field. The tensor $\mathbf{D}$ represents an electronic potential at the centre: contributions to $\mathbf{D}$ include the spin-orbit interaction and dipolar interactions between electrons.

In the principal axes of the interaction, the Hamiltonian $\hat{\mathcal{H}}_{zf} = \hat{\boldsymbol{S}}^{\mathrm{T}} \cdot \mathbf{D} \cdot \hat{\boldsymbol{S}}$ is commonly written

$$\hat{\mathcal{H}}_{zf} = D[\{S_z^2 - \tfrac{1}{3}S(S+1)\} + E(S_x^2 - S_y^2)] \,, \tag{4-6}$$

where $D = \frac{3}{2}D_z$, and $E = \frac{1}{2}(D_x - D_y)$ is a measure of rhombicity.

4.4.2.3 Nuclear Zeeman interaction

The nuclear Zeeman represents the interaction of a non-zero nuclear magnetic moment ($I > 0$) with a magnetic field. The nuclear Zeeman is directly analagous to the electronic Zeeman interaction (4-4), with $g_{\mathrm{N}}, \mu_{\mathrm{N}}$ corresponding to g, μ_B:

$$\hat{\mathcal{H}}_{nZ} = -g_N \mu_{\mathrm{N}} B \hat{I}_z \,,$$

where $\hat{I}_z |m_I\rangle = m_I |m_I\rangle$ (c.f. (4-5)).

The proton magnetic moment is a factor of $m_p/m_e \approx 2000$ smaller than the electronic magnetic moment, so that the energies involved are much smaller (the nuclear Zeeman is often negligible at X-band frequencies). This difference in magnetic moment strengths is the reason that nuclear magnetic resonance (NMR) has historically required larger applied fields than EPR.

4.4.2.4 Hyperfine interaction

The hyperfine interaction arises from coupling of the unpaired electronic spin S and any local, non-zero nuclear spin I. The hyperfine interaction is the source of one of the most powerful aspects of EPR spectroscopy: the ability to chemically determine the local environment of an electron. EPR spectroscopy, and especially

hyperfine and zero-field interactions, have been extensively used to characterise and identify defects in semiconductors (most notably in silicon) [26–28].

The chemical sensitivity of the hyperfine interaction has several sources: relative isotopic abundances and corresponding I, g_N values. For instance, boron has two naturally-occurring isotopes, ^{10}B ($I = 3$, 20 % abundant) and ^{11}B ($I = 3/2$, 80 % abundant): no other element possesses these relative isotopic abundances and nuclear spin values and therefore any hyperfine structure which may be described as such may be unambiguously attributed to boron.

There are two contributions to the measured hyperfine interaction:

- Fermi contact interaction, arising from non-zero unpaired electron probability density at the nucleus (only true for s-shell electrons). The spherically-symmetric nature of s-shell orbits means that this interaction is isotropic.
- Dipolar hyperfine interaction, a change in energy due to the energy of the nuclear magnetic dipole moment in the magnetic field generated by the electrons. This interaction is anisotropic and reveals information about the geometric symmetry of local nuclear magnetic moments (and hence their geometrical configuration).

The hyperfine interaction is further discussed in §7.3.3.1.

4.4.2.5 Quadrupole interaction

When a nucleus with spin $I \geq 1$ is placed in an electric field gradient, there is an interaction between the field gradient and the nuclear quadrupole moment, which arises due to non-spherical charge distribution inside the nucleus. The electric field gradient is generated by the anisotropic distribution of charge at the paramagnetic centre, and is zero for a nucleus in a site with perfect cubic symmetry.

The quadrupole interaction is defined by the tensor $\mathbf{P}$:

$$\hat{\mathcal{H}}_{qp} = \hat{\boldsymbol{I}}_i \cdot \mathbf{P}_i \cdot \hat{\boldsymbol{I}}_i \,. \tag{4-7}$$

It is usual to make $\mathbf{P}$ traceless ($\mathrm{tr}(\mathbf{P}) = 0$) by subtracting a constant which shifts all energy levels equally, and hence has no effect on the resulting spectrum. In the

principal axes of the interaction, (4-7) is commonly written

$$\hat{\mathcal{H}}_{qp} = P_{\parallel}\left[\left\{I_z^2 - \tfrac{1}{3}I(I+1)\right\} + \tfrac{1}{3}\eta\left(I_x^2 - I_y^2\right)\right] ,$$

where $P_{\parallel} = \frac{3}{2}P_z$, and $\eta = (P_x - P_y)/P_z$ is a measure of rhombicity (c.f. (4-6)).

4.4.2.6 Transition probabilities

Consider a spin system containing an effective spin S and a single I nucleus: the Hamiltonian is given by the nuclear and electronic Zeeman terms, and the hyperfine coupling terms. The energy matrix of the system may be constructed by calculating all matrix elements $\langle m_S', m_I'|\hat{\mathcal{H}}_{\mu w}|m_S, m_I\rangle$ where $\hat{\mathcal{H}}_{\mu w} = \mu_B \boldsymbol{B}_{\mu w}^{T} \cdot \mathbf{g} \cdot \hat{\boldsymbol{S}}$ is the Hamiltonian of the microwave field perturbation. The eigenvalues of this matrix are the energy levels of the spin system, and the transition probabilities between each state are proportional to $|\langle m_S', m_I'|\hat{\mathcal{H}}_{\mu w}|m_S, m_I\rangle|^2$.

For EPR measurements performed in the conventional geometry (external field $\boldsymbol{B}$ perpendicular to the linearly-polarised (in the lab frame) microwave field $\boldsymbol{B}_1$), conservation of momentum leads to the following selection rules for an EPR transition:

$$\Delta m_S = \pm 1; \quad \Delta m_I = 0 .$$

In the case that the Zeeman interaction dominates, the off-diagonal terms of the energy matrix will be small, and m_S, m_I will be good quantum numbers i.e. each state is well-described as a pure $|m_S, m_I\rangle$ state. At lower fields where quadrupolar, zero-field or hyperfine interactions become comparable to the Zeeman interaction, off-diagonal terms become significant and m_S, m_I are no longer good quantum numbers: states become admixtures of different m_S, m_I character (state-mixed) and this in turn gives rise to so-called "forbidden transitions" ($\Delta m_I \neq 0$) becoming weakly allowed.

In general, the lineshape functions employed during simulations of EPR spectra are generated in frequency space, and a correction $\frac{\partial B}{\partial \hbar\omega}$ is required to convert to the field-swept space used during experiments [29, 30]. When using simulations to quantify experimental results, this factor can be significant: in the diamond

defect $(\mathrm{NV})^-$ (with effective spin $S = 1$), the ratio between the $|\mathrm{m}_S\rangle = -1 \rightarrow +1$ and $|\mathrm{m}_S\rangle = -1 \rightarrow 0$ transitions is 7 when the correction is neglected, and 12.6 with the correction included. Experimental results collected at Warwick to check the validity of the correction record a ratio of $13(2)$. Therefore, when using the $|\mathrm{m}_S\rangle = -1 \rightarrow +1$ transition to quantify the concentration of $(\mathrm{NV})^-$, as described in [31], the correction must be taken into account in order to avoid a factor of 2 error in the concentration.

4.4.3 Simulation and fitting

As the phenomenological contributions to the energy levels of a simple spin-system are well-understood, simulation of EPR spectra is commonplace and one of the most powerful methods to gain understanding of experimental data. By performing least-squares fitting of simulated energies to experimentally-measured energies, the different parameters in the spin Hamiltonian can be obtained with a high degree of accuracy.

EasySpin 4.0 [32] (in the programming environment MATLAB[2]) was used for the simulation of spectra with known spin Hamiltonian parameters. Extensions were written by the author to support the embedding into a crystal of symmetry $\mathscr{T}_\mathrm{d}$ defects whose symmetry is a subgroup of $\mathscr{T}_\mathrm{d}$ (see [33] for a tabulation of all different subgroups and their effect on EPR spectra). Effectively, these extensions place several crystals inside the simulated experiment, with relative orientations defined by the symmetry of the defect, and then all crystals are simulated simultaneously.

Least-squares fitting to experimental spectra in order to optimise linewidths and relative intensities was performed using a MATLAB tool written by another group member, Matthew Dale, which implements the pseudo-modulation protocol outlined by Hyde [34].

EPR-NMR, a full matrix-diagonalisation code written in FORTRAN [35], was used for optimisation of spin Hamiltonian parameters by least-squares fitting.

[2]MATLAB version 8.0, `www.mathworks.com`

4.5 Electron irradiation

The primary energy-loss mechanism for a high-energy electron scattering through an insulating solid is by ionising the material as it passes through [36, 37]. Direct momentum transfer from the electron to an atom are typically modelled as colliding billiard balls. For a relativistic electron of mass m_e accelerated to energy E and incident on a particle of mass M, the maximum recoil energy of the particle is [38, 39]

$$T_{max} = \frac{2m_eE}{M}\left(\frac{E}{m_ec^2} + 2\right) .$$

In the case of a 2 MeV electron hitting a carbon atom, the maximum recoil energy of the atom is 1 keV — approximately 0.05 % of the incident electron energy. If the energy imparted to the atom is greater than the displacement threshold energy T_d, then the atom will be ejected from its site with kinetic energy $T - T_d$. The most recent experimental results measure T_d as approximately 40 eV [40]. The probability of secondary damage due to the ejected atom is small [36, 37, 41].

4.6 Annealing

Classically, the migration or reconfiguration of atoms (equivalently vacancies) in a lattice involves the breaking and formation of bonds and requires energy. During an annealing experiment, energy is provided to the crystal in the form of heat: as the input energy increases, higher-energy processes begin to occur at appreciable rates. Whilst at temperature, the concentration of a given defect may change as defects migrate to sinks such as vacancies, (internal) surfaces, or other defects.

Aggregate defects often have two characteristic energies associated with them: the energy required to destroy the aggregate initially (one or more of the constituents migrates away); and the energy required for the defect to migrate as a unit. If the dissociation energy is lower than the migration energy, then the defect will be effectively stationary until destroyed.

4.6.1 First-order kinetics

The formation and destruction of a defect is usually modelled by chemical kinetics: in this thesis both first- and second-order processes are considered. A first-order process requires only enough energy for the process to occur — sources and sinks are assumed to be infinite. This is often encountered when defects are lost by migration to e.g. dislocations (infinite sinks) or are formed at the surface (infinite sources).

Consider an isolated defect on a lattice site: it may be visualised as vibrating at a frequency ν_0 around a low-potential point in a periodic background potential defined by the lattice. During each vibration, there is a chance that the defect will overcome the potential barrier on either side of it (which may not be equal), and 'hop' onto the next lattice site. Classically, the probability that the defect will overcome the barrier will follow a Gaussian distribution

$$p_A = \exp\left(\frac{-E_A}{k_B T}\right) ,$$

where E_A is the potential barrier to be overcome, and is known as the activation energy. The process occurs at a characteristic frequency of ν_0 Hz: the rate of change in concentration of the defect is therefore

$$K = \nu_0 \exp\left(\frac{-E_A}{k_B T}\right) .$$

For a first-order process where defect X $\rightarrow$ Y (Y may be another defect, or destruction), the rate of change of concentration is given by the differential equation

$$\frac{d[\mathrm{X}]}{dt} = -K[\mathrm{X}] ,$$

and hence K is known as the rate constant of the process. For an initial concentration $[\mathrm{X}]_0$ at $t = 0$, the solution is given by the Arrhenius equation

$$[\mathrm{X}] = [\mathrm{X}]_0 \exp(-Kt) .$$

4.6.2 Second-order kinetics

If the sources or sinks are finite (e.g. [X]+[X] $\rightarrow$ [Y]), and the concentrations of the source reactants are changed appreciably during annealing, then the reaction rate

depends on the concentration of reactants. For a process involving the migration of two like defects, the rate of change in concentration is given by

$$\frac{d[\mathrm{X}]}{dt} = -K[\mathrm{X}]^2$$

with corresponding solution

$$\frac{1}{[\mathrm{X}]} = \frac{1}{[\mathrm{X}]_0} + Kt\ .$$

4.6.3 Annealing procedure

All anneals at temperatures below 1600 °C were performed using an Elite Thermal Systems horizontal tube furnace. At all times during annealing the alumina tube interior was held under a non-oxidising atmosphere to prevent graphitisation of the sample. At temperatures of above 1000 °C the sample was buried under a sacrificial layer of diamond grit as further protection against graphitisation. Samples were held at temperature for 14 h during each anneal.

Some chapters report experiments on samples which were annealing under HPHT conditions: the processing was performed by Suncrest Diamonds,[3] and the details of each anneal have been recorded at the start of respective chapters.

4.7 Fitting

Several methods exist in the literature for quantifying the strength of various optical absorption bands: in general, a linear, quadratic or cubic baseline is subtracted and the experimental data are integrated [42, 43]; other methods are based on the "height" (absorption coefficient) of the spectrum at a specified point [44, 45]. Both approaches suffer in the cases where the data are noisy or the band has contributions from different sources. In order to counter these problems, the optical data requiring quantification have been fitted with a simulated linefunction, and the simulation has been integrated. Wherever possible, a linear baseline has been

[3] `http://www.suncrestdiamonds.com/`

used as small changes in anchor points for spline-fit baselines can have dramatic effects on the integrated intensity.

The functions used for fitting were of Lorentzian, Gaussian, Voigt[4] or pseudo-Voigt[5] type. In cases of significant asymmetry, split functions were used, allowing different linewidths above and below the centroid of the line. In these cases, a pseudo-Voigt was employed in order to avoid the computationally expensive integration operations required to generate a pure Voigt function for each iteration of the least-squares fitting tool. Even slight asymmetry can dramatically affect the quality of fit (figure 4-7).

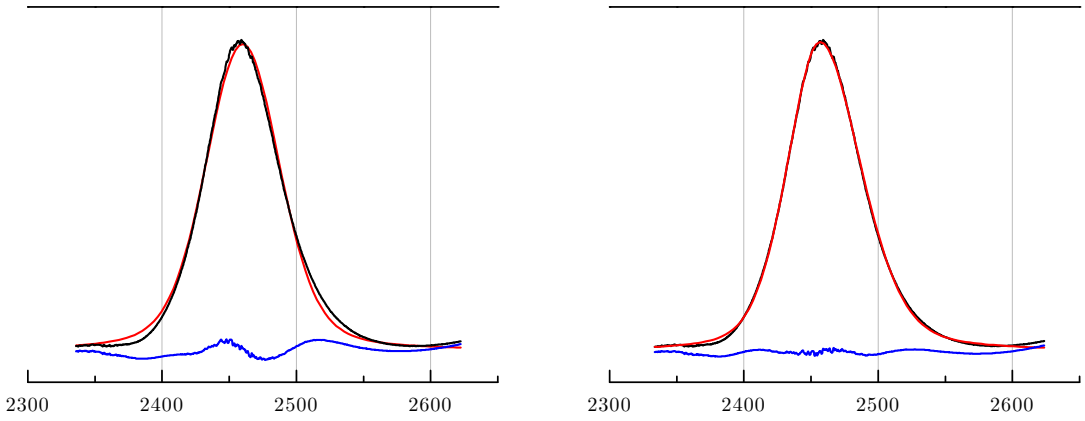

(a) Voigt **(b)** Split pseudo-Voigt

Figure 4-7 Simulated lineshape profiles fitted to the 2460 cm^{-1} of neutral substitutional boron. In each case, the noisy line is the experiment, the smooth curve is the simulated fit, and the lower line is the residual. The difference in integrated intensity between the two fits is approximately 5 %.

In order to test the validity and reproducibility of the different approaches, the 1.673 eV GR1 absorption of the neutral vacancy and the 2460 cm^{-1} of the neutral boron acceptor have been fitted across a range of concentrations using several different approaches, and plotted in figure 4-8. Methods 1–3 respectively were performed using: split pseudo-Voigt, linear baseline; split pseudo-Voigt, spline baseline; integration of experimental data, linear baseline.

[4]Convolution of Gaussian and Lorentzian profiles.

[5]Linear combination of Gaussian and Lorentzian profiles. Maximum deviation from true Voigt profile < 1 % [46].

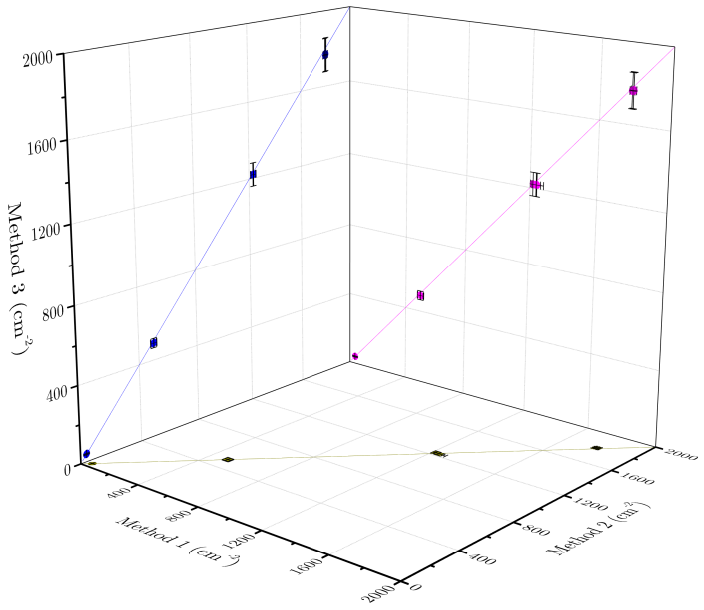

(a) 2460 cm^{-1} of the neutral boron acceptor

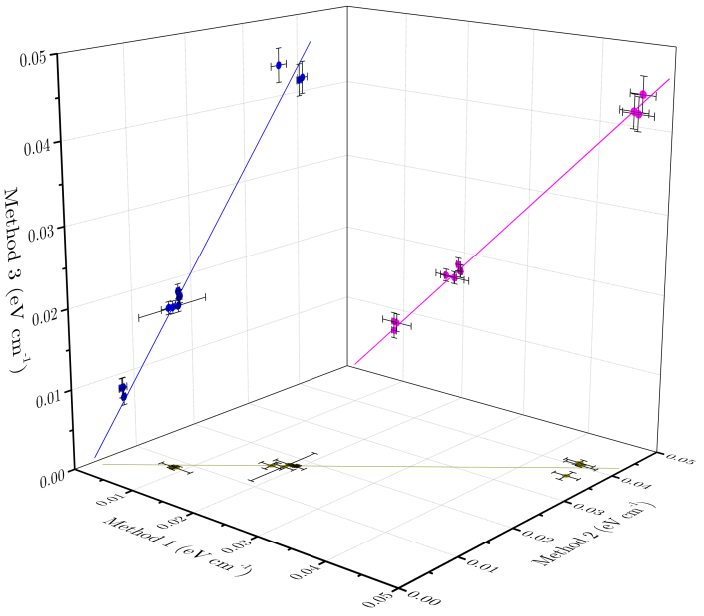

(b) 1.673 eV of the neutral vacancy

Figure 4-8 Correlation between three different fitting methods for absorption lines at mid-infrared and visible energies. In each case statistical fluctuation is small, but systematic effects exist between the different methods. See text for details of each method.

In addition to providing a good fit to the experimental data, it is imperative that the chosen linefunction has a justifiable physical basis for its use — a perfect fit may be constructed from higher-order polynomials or sums of sinusoidal functions, but such a fit gives no information about the system under consideration.

A zero phonon line occurring at an optically-active centre in a perfect crystal is given by a Lorenztian distribution [47]. Strain due to point defects and dislocations lead to Lorentzian and Gaussian broadening, respectively [48, 49]. Additionally, any resonance recorded during an experiment is a convolution of the natural response of the system under study with the response of the instrument, which is itself often complex. As such, the use of a Voigt-type profile to fit observed lineshapes is well-justified.

Finally, if there is a correlation between a strain mechanism and a given optical centre, then the broadening effect is no longer symmetric [48]: self-interstitials within a few lattice sites of the neutral vacancy are thought to contribute to asymmetric broadening of the ZPL [45]. In cases such as these, the constraint on the split pseudo-Voigt that the ratio of Gaussian and Lorentzian components ought to be identical on either side was relaxed, in order to achieve a good fit. These procedures were employed primarily for the optical stress data in chapter 6 and quantifying optical transitions in chapter 5.

References

1. M. Fox, *Optical Properties of Solids* (Oxford University Press, Oxford, 2008).
2. M. Lax, E. Burstein, *Physical Review* **97**, 39 (1955).
3. J. R. Hardy, S. D. Smith, *Philosophical Magazine* **6**, 1163 (1961).
4. D. Krishnamurti, *Proceedings of the Indian Academy of Sciences - Section A* **40**, 211 (1954).
5. R. Robertson, J. J. Fox, A. E. Martin, *Philosophical Transactions A* **232**, 463 (1934).
6. C. D. Clark, P. J. Dean, P. V. Harris, *Proceedings of the Royal Society of London A* **277**, 312 (1964).
7. G. Davies, *Journal of Physics C: Solid State Physics* **3797** (1974).
8. F. Seitz, *Transactions of the Faraday Society* **35**, 74 (1939).
9. G. Davies, in *Identification of defects in semiconductors*, ed. by M. Stavola (Academic Press, 1998), vol. 51B, chap. Optical measurements of point defects, p. 1.
10. G. Davies, *Reports on Progress in Physics* **44**, 787 (1981).
11. J. P. Goss, PhD thesis, University of Exeter, 1997.
12. A. T. Collins *et al.*, *Journal of Physics C: Solid State Physics* **21**, 1363 (1988).
13. G. Davies *et al.*, *Journal of Physics: Condensed Matter* **9**, 3871 (1997).
14. K. Iakoubovskii, G. Davies, *Physical Review B* **70**, 245206 (2004).
15. C. D. Clark *et al.*, *Physical Review B* **51**, 16681 (1995).
16. J. P. Goss *et al.*, *Physical Review Letters* **77**, 3041 (1996).
17. A. E. Hughes, *Proceedings of the Physical Society* **88**, 449 (1966).
18. M. D. McCluskey, *Journal of Applied Physics* **87**, 3593 (2000).
19. P. Griffiths, J. A. De Haseth, *Fourier Transform Infrared Spectroscopy* (John Wiley & Sons, Hoboken, ed. 2, 2007).
20. B. C. Smith, *Fundamentals of Fourier Transform Infrared Spectroscopy* (CRC Press, Boca Raton, 1996).
21. M. F. Thomaz, G. Davies, *Proceedings of the Royal Society of London A* **362**, 405 (1978).

22. A. Abragam, B. Bleaney, *Electron Paramagnetic Resonance of Transition Ions* (Dover Publications, Inc., New York, ed. 2, 1986).
23. A. Schweiger, G. Jeschke, *Principles of pulse electron paramagnetic resonance spectroscopy* (Oxford University Press, Oxford, 2001).
24. J. A. Weil, J. R. Bolton, *Electron Paramagnetic Resonance* (John Wiley & Sons, Hoboken, ed. 2, 2007).
25. C. P. Poole, *Electron Spin Resonance* (Dover Publications, Inc., New York, ed. 2, 1983).
26. G. Watkins, J. Corbett, *Physical Review* **134**, A1359 (1964).
27. G. Watkins, *Physical Review* **155**, 802 (1967).
28. G. Watkins, *Physical Review B* **12**, 5824 (1975).
29. R. Aasa, T. Vänngård, *Journal of Magnetic Resonance (1969)* **19**, 308 (1975).
30. G. van Veen, *Journal of Magnetic Resonance (1969)* **30**, 91 (1978).
31. C. Glover, PhD thesis, 2003.
32. S. Stoll, A. Schweiger, *Journal of Magnetic Resonance* **178**, 42 (2006).
33. A. Edmonds, PhD thesis, University of Warwick, 2008.
34. J. S. Hyde *et al.*, *Applied Magnetic Resonance* **1**, 483 (1990).
35. M. J. Mombourquette, J. A. Weil, D. G. McGavin, *EPR-NMR*, 1997, `www.chem.queensu.ca/eprnmr`.
36. A. Mainwood, *Diamond and Related Materials* **7**, 504 (1998).
37. B. Campbell *et al.*, *Nuclear Instruments and Methods in Physics Research Section A* **476**, 680 (2002).
38. J. Bourgoin, M. Lannoo, *Point Defects in Semiconductors II* (Springer-Verlag, Berlin, 1983).
39. D. W. Palmer, in *Properties and Growth of Diamond* (IEE - Inspec, 1994), p. 5.1.
40. J. Koike, D. M. Parkin, T. E. Mitchell, *Applied Physics Letters* **60**, 1450 (1992).
41. B. Campbell, a. Mainwood, *Physica Status Solidi (A)* **181**, 99 (2000).
42. G. Davies *et al.*, *Physical Review B* **46**, 13157 (1992).
43. M. Newton *et al.*, *Diamond and Related Materials* **11**, 618 (2002).

44. A. T. Collins, presented at the 61st Diamond Conference, P5.

45. I. Kiflawi *et al.*, *Journal of Physics: Condensed Matter* **19**, 046216 (2007).

46. G. K. Wertheim, *Review of Scientific Instruments* **45**, 1369 (1974).

47. A. M. Stoneham, *Proceedings of the Physical Society* **89**, 909 (1966).

48. A. M. Stoneham, *Reviews of Modern Physics* **41**, 82 (1969).

49. G. Davies, *Journal of Physics C: Solid State Physics* **3**, 2474 (1970).

Chapter 5

Irradiation damage in type IIb diamond

5.1 Background

The very first systematic studies on irradiation damage in diamond included data on type IIb material [1], despite them comprising only approximately 0.1 % of the population of natural diamonds. In the following years, however, the vast majority of work on irradiated diamond has been performed on type I and type IIa material, with the subsequent effect that the knowledge of irradiation damage in type IIb material is significantly less advanced relative to the other major diamond classes. Even relatively straightforward annealing experiments on the primary effects of irradiation damage are poorly understood [2]: these data will be reviewed and re-analysed during the course of this chapter.

In recent years, the interest in synthetic boron-doped diamond has dramatically increased. Boron-doped diamond is now employed as an electrochemical sensor [3, 4], in active electronics [5–7] and as a neutron detector [8]. Furthermore, several attempts have been made to dope diamond post-growth using boron ion implantation [9, 10], introducing lattice damage which is poorly characterised. In all cases, a better understanding of fundamental processes in type IIb material is desirable.

5.1.1 Irradiation damage in type IIa diamond

The primary products of irradiation damage in type IIa material are isolated neutral vacancies ($(V)^0$) and $\langle 0\,0\,1\rangle$-split self-interstitials ($I_{\langle 0\,0\,1\rangle}$, R2 in EPR) [11]. Lower concentration defects observable by EPR immediately post-irradiation include the di-$\langle 0\,0\,1\rangle$-split interstitial R1 [12], and even the tri-interstitial complex O3 [13]: the assignment of both of these complexes is supported by local spin-DFT results [14].

Information on the isolated self-interstitial became forthcoming only when high-purity (synthetic) material was irradiated at 100 K and lower. The rate of production of $(V)^0$ at 300 K was shown to be approximately equal to that observed for irradiation at 100 K. Post-irradiation $I^0_{\langle 0\,0\,1\rangle}$ concentrations were equal to $(V)^0$ concentrations following irradiation at 100 K, and approximately a factor of 4 lower after irradiation at 300 K [15, 16]. It was found that the rate of production of R1 as a function of irradiation dose (at an electron energy of 2 MeV) was identical at 100 and 300 K, whereas the production of O3 was zero at 100 K [17].

These data have been interpreted as suggesting that the primary difference between irradiation at 100 K and 300 K is the mobility of self-interstitials during irradiation [16]. A different form of the self-interstitial (I^*), produced either by electronic excitation or charge transfer and with undefined structure and electronic behaviour, was inferred from the production rates of self-interstitials as a function of irradiation temperature. I^* was assumed to diffuse through the lattice by the process $I^0_{\langle 0\,0\,1\rangle} \rightarrow I^* \rightarrow I^0_{\langle 0\,0\,1\rangle} \rightarrow I^*$ etc., with a migration energy for I^* of 0.3 eV: I^* is therefore mobile during irradiation for temperatures above approximately 140 K. The view that the difference in production rate does not occur due to an intermediate annealing stage between 100 and 300 K is supported by the following experiment detailed in [17]: a sample was irradiated at 100 K and transferred to an EPR spectrometer without heating above 110 K. The sample was then annealed in stages up to 300 K, with no change observed in the concentrations of R2, R1 or O3.

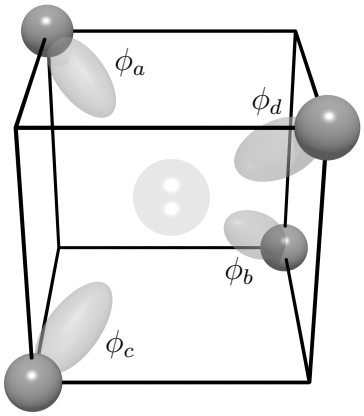

Figure 5-1 A single, isolated vacancy in diamond. The "cage" formed by the four carbons nearest-neighbour to the vacancy has been illustrated. This diagram follows the molecular representation of [18].

5.1.2 Irradiation damage in type IIb diamond

The primary difference that might be expected on irradiation of type IIb diamond relative to type IIa diamond is the charge state in which the intrinsic defects are formed. This would be a mirror of the situation in nitrogen-doped diamond where the majority of defects formed upon irradiation are intrinsic rather than nitrogen-containing, but are generally found in their negative charge state.

A major gap in the physical understanding of point defects in diamond is the unambiguous identification of $(\mathrm{V})^+$, the positively-charged vacancy. The electronic configuration of the different charge states of the vacancy in diamond were one of the first theoretically treated defects in a semiconductor [18]. Coulson and Kearsley argued that the properties of the vacancy were determined entirely by the orbitals pointing into the vacancy (figure 5-1) — in effect, an isolated molecule embedded in a background lattice.

Following Coulson and Kearsley, the one-electron wavefunctions may be formed by linear combinations of atomic orbitals:

$$
\begin{aligned}
\mathrm{a}_1 &\left\{ \quad \phi_a + \phi_b + \phi_c + \phi_d \right. \\
\mathrm{t}_2 &\left\{ \begin{array}{l} \phi_a + \phi_b - \phi_c - \phi_d \\ \phi_a - \phi_b - \phi_c + \phi_d \\ \phi_a - \phi_b + \phi_c - \phi_d \, . \end{array} \right.
\end{aligned}
$$

Assuming that the vacancy retains its tetrahedral symmetry, the positive vacancy (three electrons) can exist in the following configurations:

$$\begin{aligned} a_1^2 t_2^1 &\rightarrow {}^2T_2 \\ a_1^1 t_2^2 &\rightarrow {}^2A_1 + {}^2E + {}^4T_1 + {}^2T_1 + {}^2T_2 \\ a_1^0 t_2^3 &\rightarrow {}^4A_2 + {}^2E + {}^2T_1 + {}^2T_2 \ , \end{aligned}$$

where multiple states of the same spin-multiplicity and symmetry have been omitted.

The ground state of $(V)^+$ is predicted to be the $^2T_2$ many-electron state with the one-electron configuration $a_1^2 t_2^1$ [19]. The defect may suffer a Jahn-Teller distortion in the ground state: both tetragonal [20] and trigonal [21] configurations have been predicted. In any case, the ground state should be EPR-active.

A tetragonal $S = \frac{1}{2}$ EPR signal has been reported in HPHT-grown type IIb diamond after room temperature electron or proton irradiation [22]. Weak ^{13}C hyperfine signals were also observed, with the interaction aligned approximately along $\langle 1\,1\,1 \rangle$. The signal was assigned to the positive vacancy based on sample history and spectral symmetries. The assignment is not certain: the strength of the ^{13}C hyperfine interaction suggests a total localisation of the unpaired electron probability density on the four nearest neighbour carbon atoms of only 20 % (see §7.3.3.2 for calculation details), significantly lower than the $\approx 90\,\%$ predicted by DFT calculations [23].

Several different optical transitions have been proposed as belonging to $(V)^+$: mid- [24] and near-infrared [25] absorptions discussed further in §5.4.1.1 and §5.4.2.4 respectively; and a pair of photoluminescence emissions belonging to the same centre [26–28]. The photoluminescence transitions were observed in boron-doped material ([B] = 1–60 ppm) following electron irradiation. However, a lack of correlation between changes in GR1 and the transitions under UV illumination casts doubt on the assignment to $(V)^+$ [28].

Other defects potentially produced by irradiation and annealing of boron-doped diamond might be expected include interstitial- and vacancy-related centres. The boron-vacancy complex (BV), in contrast to (NV), is predicted to have a migration

energy far higher than its dissociation energy of 1.8 eV [29]. Both $(V)^-$ and $(V)^0$ have been measured to migrate with an energy of 2.3 eV [16, 30]: if $(V)^+$ is mobile at similar energies then any (BV) formed by annealing must involve the migration of a boron-containing defect. In contrast, B_nV with $n > 1$ are expected to be stable to high temperature, if a mechanism for their formation exists [31, 32].

Boron-interstitial complexes have been the subject of several theory papers [29, 31–35]. There is disagreement in the literature about the lowest energy configuration, with a $\langle 1\,0\,0\rangle$-split interstitial (B_i) favoured by some calculations [33, 34], and a substitutional boron nearest-neighbour to a $\langle 1\,0\,0\rangle$-split carbon interstitial preferred by others [31]. Boron-related interstitials are discussed extensively in §5.5.

5.2 Experimental details

A suite of seven samples was irradiated at low temperature and then studied. One of the samples was then annealed between 100–1400 °C in 100 °C steps. The samples were characterised before and after irradiation, and at each annealing stage.

5.2.1 Samples & irradiation

Results for seven samples are reported in this chapter: six samples of type IIb, with boron concentrations varying from ≈0.8–2.7 ppm; and a seventh sample of type IIa used as a control owing to the better understanding of radiation damage in IIa material.

All samples were irradiated to a total dose of $5 \times 10^{17}\,e^-\,cm^{-2}$ over a period of 5 h (flux approximately $2.8 \times 10^{13}\,e^-\,cm^{-2}\,s^{-1}$). During irradiation, the samples were mounted onto the cold finger of a continuous flow liquid nitrogen cryostat and held at a temperature of 100 K. Post-irradiation, the samples were allowed to warm to room temperature before any measurements were performed.

5.2.2 Photoluminescence spectroscopy

Photoluminescence is a very powerful technique often employed in the study of semiconductor materials. Photoluminescence measurements regularly achieve sensitivities down to the single emitter level in specialised circumstances [36, 37], and parts per trillion levels in low-temperature bulk measurements [38]. Unfortunately, unlike absorption spectroscopies, photoluminescence is not a strictly quantitative technique: many competing (generally unmeasured) processes modify the intensity of the emission such that it may not be proportional to the input laser power. Such effects include self-absorption, non-radiative decay (to a different excited state or even a neighbouring defect) and excitation via emission from other defects, amongst others [39–41].

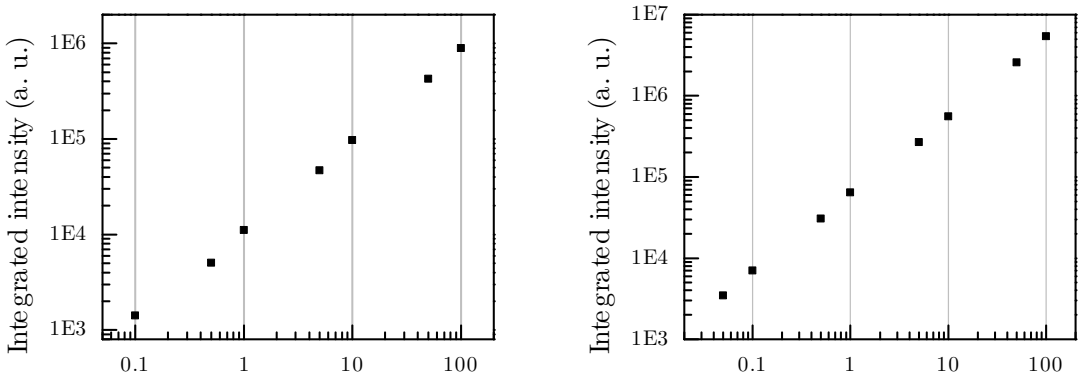

(a) 1st-order Raman **(b)** GR1

Figure 5-2 Integrated intensity of the 1st-order Raman line (left) and GR1 (1.673 eV) as a function of input laser power across 3 orders of magnitude. In both cases, the integrated intensity is directly proportional to the input laser power. Both sets of data taken with excitation at 1.939 eV (632.8 nm).

A quantitative measurement requires the photoluminescence intensity to be proportional to both the input laser power and the sample volume being probed. The intensity of the 1st-order Raman line is linear in terms of both of these variables [42] (see figure 5-2a), but for photoluminescence this corresponds to the ideal case: excitation directly into the vibronic band of a defect and emission directly between two symmetry-allowed states. In general, any given PL spectrum will contain both transitions which are linear and transitions which are non-linear in terms of the

input laser power. Therefore all PL spectra are normalised to the integrated intensity of the 1st-order Raman line. The linear PL case is shown for the GR1 ZPL (1.673 eV) excited by a laser at 1.939 eV (632.8 nm) in sample e (figure 5-2b).

With all of this in mind, the data reported here have been measured, wherever possible, with the laser excitation energy closest in energy to the emission line. The excitations used during the study were 3.815 eV (325.0 nm), 2.808 eV (441.6 nm), 2.410 eV (514.5 nm), 1.959 eV (632.8 nm) and 1.579 eV (785.0 nm).

5.3 Irradiation

In the following sections, the irradiation and annealing results will be presented with minimal interpretation, and the results as a whole are discussed in §5.5.

5.3.1 Results

Post-irradiation, all type IIb samples showed a reduction in absorption by the uncompensated boron acceptor. All samples displayed some GR1 absorption, but it was very weak for many samples. The pre- and post-irradiation concentrations of (neutral) boron, vacancies and interstitials are given in table 5-1. Throughout this chapter, the following constants will be used to convert integrated absorption (A) or absorption coefficient (H) to concentration:

$$A_{1673} = 1.2(3) \times 10^{-16}\ [(\mathrm{V})^0]\ \mathrm{meV\,cm^{-1}}, \tag{5-1}$$

$$A_{1859} = 1.0(2) \times 10^{-17}\ [\mathrm{I}^0_{\langle 0\,0\,1\rangle}]\ \mathrm{meV\,cm^{-1}}, \tag{5-2}$$

$$\text{and } H_{2460} = 5.4(7) \times 10^{-17}\ [(\mathrm{B_s})^0]\ \mathrm{cm^{-2}} \tag{5-3}$$

for neutral vacancies [43], neutral interstitials [11] and the neutral boron acceptor [44], respectively. All errors throughout this chapter are given with the systematic uncertainties in calibration constants omitted.

Sample	Growth	Mass (mg)	Type	Initial $[(B_s)^0]_i$	Post-irradiation $[(B_s)^0]_f$	$[(V)^0]_f$	$[I^0_{\langle 001\rangle}]_f$
a	HPHT	9.2	IIb	1.8	0.2	< 0.1	0.0
b	HPHT	11.1		1.4	0.0	0.4	0.0
c	HPHT	4.9		2.0	0.5	< 0.1	0.0
d	HPHT	4.7		0.5	0.0	0.8	0.7
e	HPHT	9.3		2.7	0.9	0.1	0.2
f	CVD	20.9		0.8	0.0	0.9	0.0
g	HPHT	21.3	IIa	0.0	0.0	2.0	1.8

Table 5-1 Details of the samples employed in this study. All concentrations are in ppm with statistical errors of approximately ±0.1 ppm in each case. Pre-irradiation concentration of vacancies and interstitials were measured as zero for all samples. All samples were irradiated with 2 MeV electrons to a total dose of 5×10^{17} $e^- cm^{-2}$.

5.3.1.1 Type IIa vs. type IIb

Post-irradiation UV-Vis spectra for samples g and f are given in figure 5-3: it is immediately apparent that the concentrations of introduced neutral vacancies and interstitials are different between the two samples. The neutral vacancy (GR1 in absorption / emission) concentration is significantly lower in the type IIb sample, and no interstitials whatsoever are visible, putting an upper limit on $[I^0_{\langle 001\rangle}]_f$ of approximately 0.1 ppm. Sample g also shows absorption known as ND1, which is attributed the negatively-charged vacancy $(V)^-$ [43]: although the absorption appears significant, the oscillator strength associated with $(V)^-$ is between 4 [30] and 8 [45] times stronger than that of $(V)^0$, giving $[(V)^-]_f < 0.1$ ppm. It is assumed that the $(V)^-$ concentration in sample g is present in small sectors with [N] > [B].

R11 has been strongly correlated with known absorption due to $I^0_{\langle 001\rangle}$ [11, 46], and is suggested to arise from electronic absorption to higher-energy states at $I^0_{\langle 001\rangle}$— this observation is supported by the data recorded during this study.

5.3.1.2 Electron irradiation of type IIb diamond

In Collins' work on electron irradiation of type IIb material [2], two samples were irradiated at different temperatures (100 and 300 K) with 2 MeV electrons at suc-

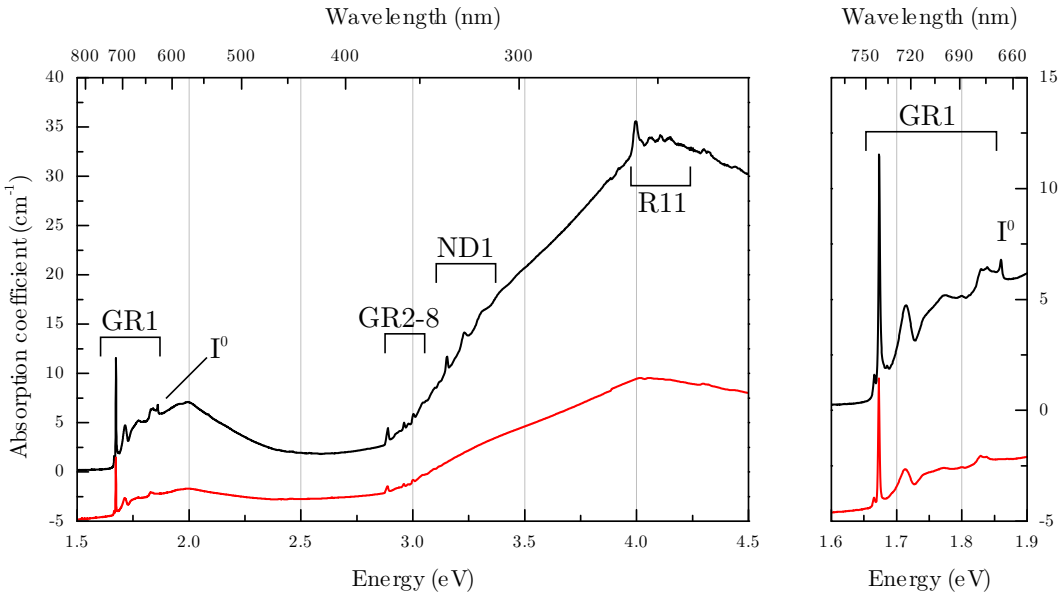

Figure 5-3 Comparison of post-irradiation UV-Vis spectra for samples g (top, type IIa HPHT-grown) and f (type IIb, CVD-grown). Both samples were irradiated at 100 K with 2 MeV electrons to a dose of 5×10^{17} e$^-$ cm^{-2}. The spectra have been offset by 5 cm^{-1} for clarity. Concentration of $(V)^0$ approximately 2.0(1) ppm and 0.9(1) ppm for samples g and f, respectively. Sample g contains 1.8(1) ppm $I^0_{\langle 001\rangle}$. A close-cropped view of the GR1 region is given to the right. See text for descriptions of the labels.

cessive doses, and the remaining boron concentration was measured at each irradiation stage. The results of these irradiations are plotted in figure 5-4. The estimated neutral vacancy concentration (top axis) has been calculated using the production rate 1.5(1) cm^{-1} derived from successive irradiations of type IIa material [11].

Collins notes that the removal of the boron appears to be non-linear: the data presented may also be interpreted as several different linear regions, as would be observed if there were regions of different boron concentration in the samples. Under this interpretation, neutral boron loss rates may be calculated for the different linear regions (for the 100 K data), with the displayed fits corresponding to rates of 5.6×10^{16} e$^-$ cm^{-2} ppm^{-1} and 1.5×10^{17} e$^-$ cm^{-2} ppm^{-1}; at the dose used in this study, the maximum boron loss would be 8.9 ppm and 3.3 ppm, respectively.

In this work, neutral vacancy and boron concentrations were measured for all samples post-irradiation (table 5-1), and the results are given in graphical form in figure 5-5. For those samples which contained a significant amount of neutral

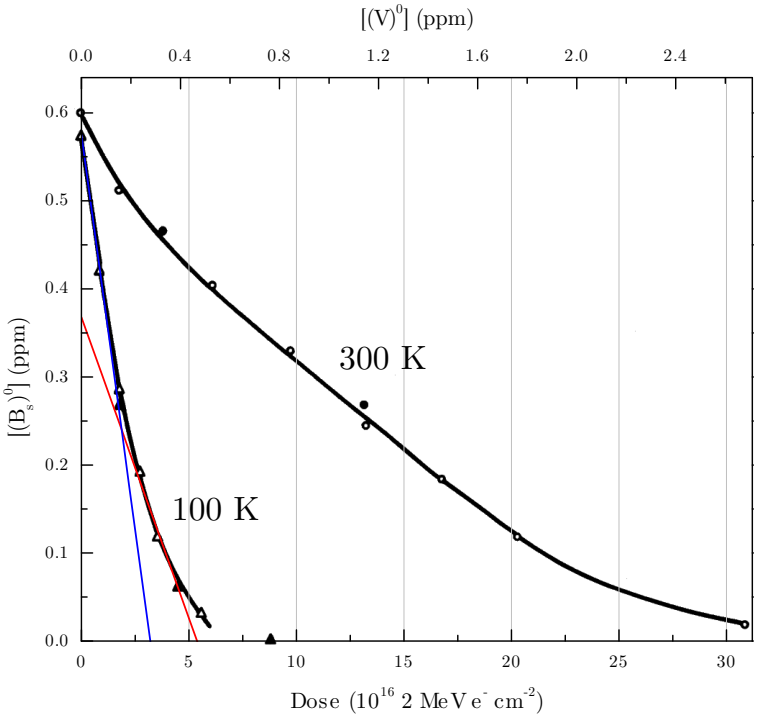

Figure 5-4 Remaining neutral boron concentration as function of total electron dose at 100 and 300 K. The estimated vacancy concentration has been calculated using an introduction rate of $1.5(1)\,\mathrm{cm}^{-1}$ [11]. Data taken from Collins [2]. The blue (left) and red linear fits give neutral boron loss rates of $5.6 \times 10^{16}\,\mathrm{e}^{-}\,\mathrm{cm}^{-2}\,\mathrm{ppm}^{-1}$ and $1.5 \times 10^{17}\,\mathrm{e}^{-}\,\mathrm{cm}^{-2}\,\mathrm{ppm}^{-1}$, respectively.

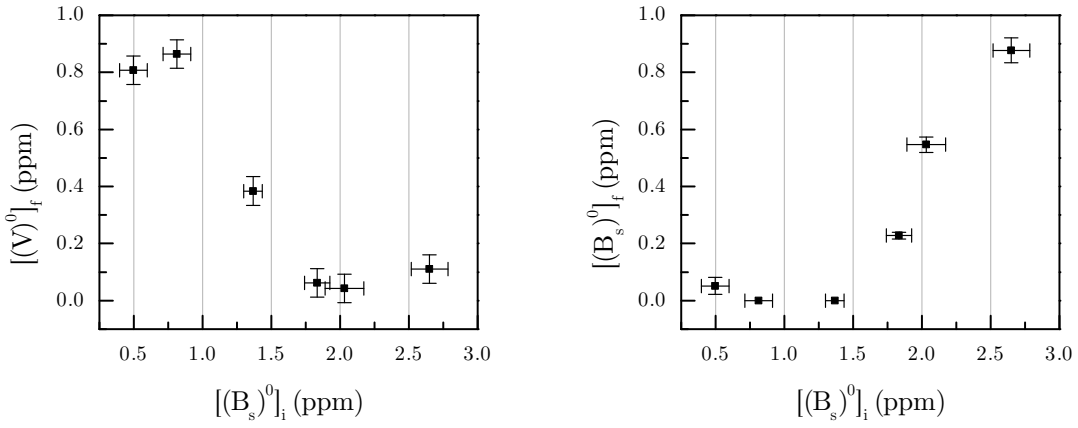

(a) Neutral vacancy **(b)** Neutral boron

Figure 5-5 Post-irradiation vacancy and neutral boron concentration as a function of initial neutral boron concentration for samples a–f. All irradiations performed to a total dose of $5 \times 10^{17}\,\mathrm{e}^{-}\,\mathrm{cm}^{-2}$ at a temperature of 100 K.

boron post-irradiation (> 0.05 ppm), the loss of boron at this dose and irradiation temperature is measured as $1.5(2)$ ppm — approximately half the lower rate extrapolated from figure 5-4. It should be noted that the total vacancy concentration measured in the type IIa sample (which was irradiated simultaneously) was $2.0(1)$ ppm, also approximately half the $4.3(2)$ ppm predicted by the introduction rate $1.5(1)\,\mathrm{cm}^{-1}$ [11]. The discrepancies may be due to different beam characteristics, electron fluxes (the flux is not given in the paper [11] or corresponding thesis [17]), or systematic errors in the measuring apparatus used by the two different facilities during irradiation.

5.4 Annealing

The type IIb CVD-grown sample (sample f) was annealed from 100–1400 °C in 100 °C stages, with each anneal lasting 14 h and performed under a non-oxidising atmosphere. At each stage, the sample was measured using UV-Vis and IR absorption spectroscopies, in addition to photoluminescence measurements performed with all five available excitation energies. A summary of all features discussed in both absorption and luminescence is given in table 5-2 at the end of this section (page 106).

5.4.1 Absorption spectroscopy

At each annealing stage the neutral boron concentration was measured using room-temperature IR spectroscopy, and the neutral vacancy concentration was measured using UV-Vis spectroscopy. Within experimental error, the vacancy concentration (upper pane of figure 5-6) is unchanged up to 600 °C, where it begins to anneal out. As noted previously, immediately post-irradiation the neutral boron concentration in this sample was undetectable and only begins to recover at temperatures of 900 °C and higher.

Infrared absorption measurements post-irradiation (figure 5-7) contain only intrinsic diamond absorption and a relatively strong band at approximately 553 meV

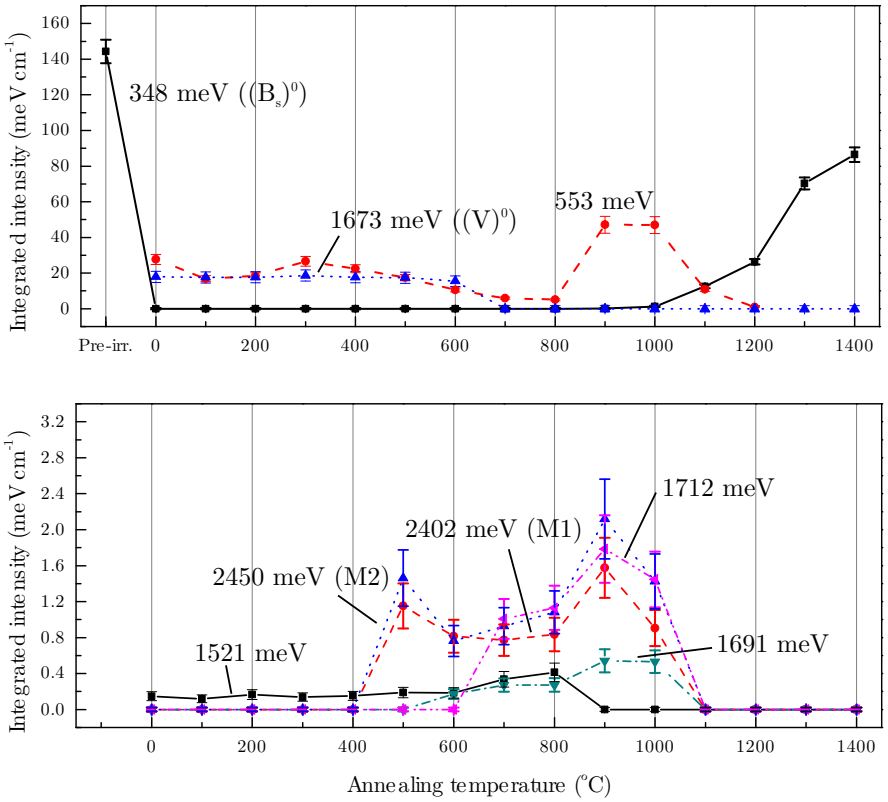

Figure 5-6 Integrated intensity of all features measured by IR or UV-Vis absorption spectroscopy during the annealing study. Data have been spread across two plots for clarity: the vertical scale of the upper pane is a factor of 50 larger than the vertical scale of the bottom pane. Energy labels are given, as well as names or atomic assignments where either exists. Lines are guides to the eye only. Axis mark "Pre-irr.": pre-irradiation.

(4460 cm^{-1}). This absorption has been reported previously in electron-irradiated boron-doped synthetic diamond, and attributed to both the positive vacancy [24] and a boron-interstitial complex [47].

Annealing curves for all measurable absorption lines are given in figure 5-6. By far the most intense absorptions observed belong to (B$_s$)^0, (V)^0 and 553 meV. No evidence for the confirmed divacancy complex TH5 (R4/W6 in EPR [48, 49]) was recorded at any annealing temperature. The M1 and M2 transitions have been attributed to a divacancy complex due to their annealing behaviour [50], but the available literature on them is sparse: as the lines are weak in the sample studied, and no corresponding PL was recorded, they will not be discussed further.

The lines at 1691 and 1712 meV have been reported previously in silicon-doped HPHT synthetic diamond [51], and will be discussed further in §5.4.2.3. Finally,

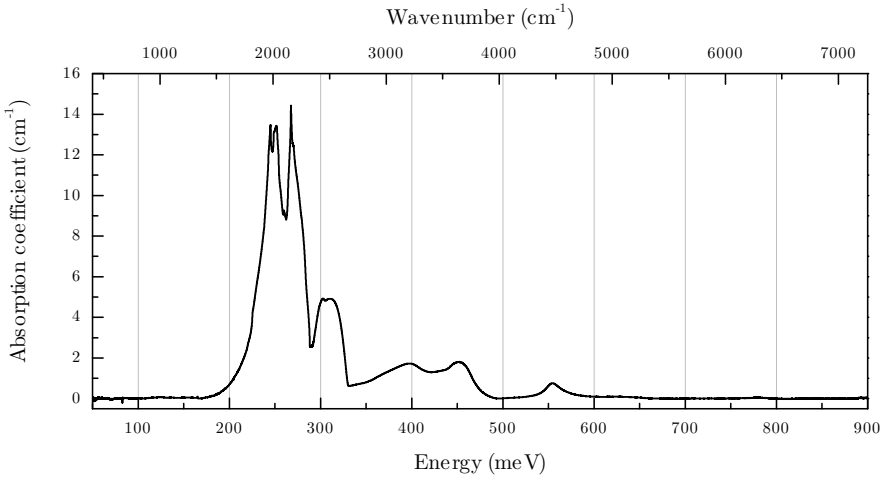

Figure 5-7 Post-irradiation IR spectrum of sample f. All absorption below 500 meV is intrinsic; the only defect-related feature being the intense, asymmetric absorption visible at 553 meV.

the 1521 meV transition is discussed in §5.4.2.4.

5.4.1.1 553 meV in infrared absorption

Immediately post-irradiation, the only non-intrinsic features visible in UV-Vis and IR absorption spectroscopy were $(V)^0$ (GR1) and an absorption at 553 meV (figure 5-7). The latter was strong, with a maximum integrated intensity approximately a factor of 3 larger than GR1 (figure 5-6). The line was first reported in 2007 [24] after irradiation of a type IIb synthetic diamond (growth method unreported) with 7.4×10^{18} e$^-$ cm^{-2} at an electron energy of 2.2 MeV.

Further investigations by the same author detailed experiments on HPHT-grown synthetic samples with highly heterogeneous (sector-dependent) boron concentrations [47]. Successive irradiations with 2.2 MeV electrons found that the integrated intensity of the 553 meV transition was independent of electron dose in the low-boron regions, and approximately linearly dose-dependent in the high boron regions. When taken together with the fact that the transition is only reported in type IIb material, these results strongly suggest that its observation depends on the presence of boron: it may directly or indirectly involve a charge effect, and / or contain boron as an atomic constituent.

In the same paper, isochronal annealing measurements of the 553 meV transition

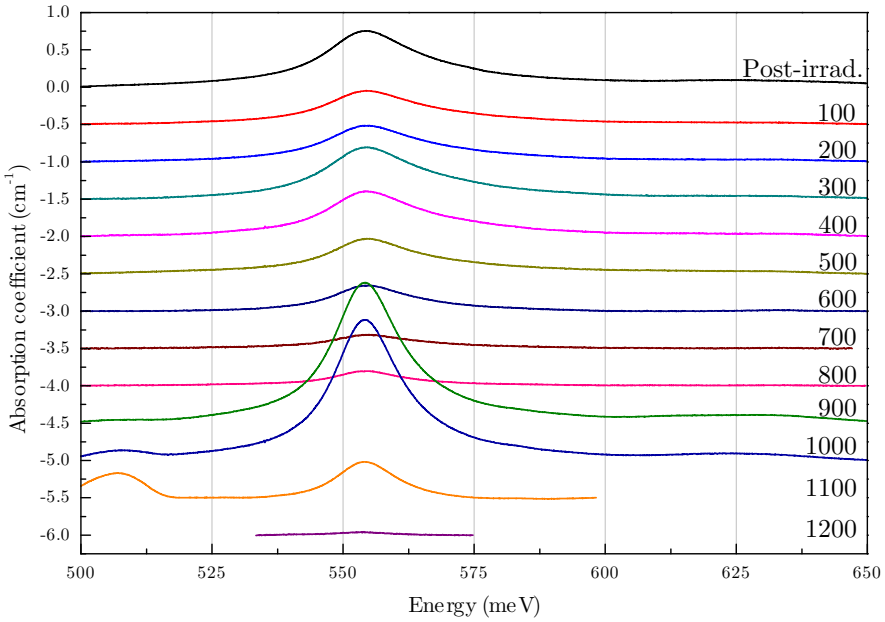

Figure 5-8 The 553 meV line in sample f is observed immediately after irradiation, and its integrated intensity slowly decreases before significantly narrowing and dramatically increasing in intensity. The line anneals out approximately as the neutral boron begins to recover. After annealing at 1100 and 1200 °C the integrated intensity of the neutral boron features is significantly larger than the 553 meV feature and so the corresponding spectra have been truncated for clarity. Each spectrum has been offset by 0.5 cm^{-1}.

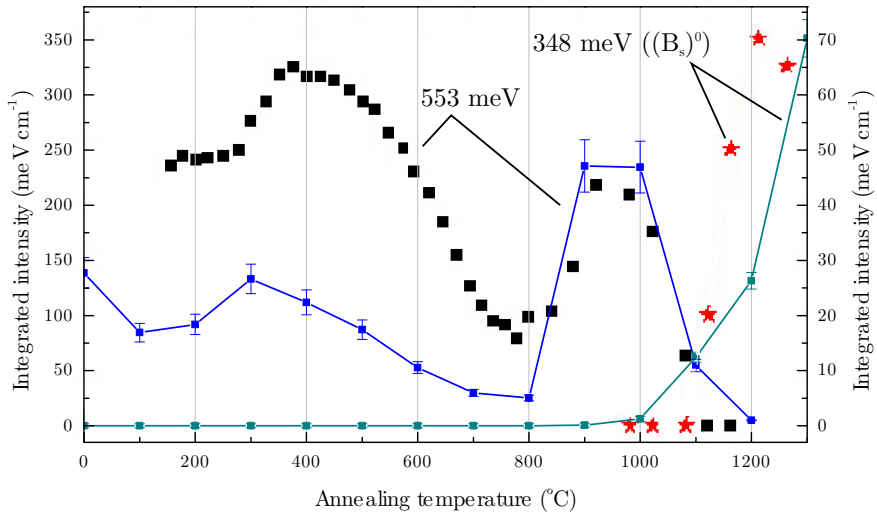

Figure 5-9 Isochronal annealing data for the 553 meV transition in sample f. Data taken during this study displayed with connecting lines and uses the vertical scale to the right; unconnected results adapted from [47] and displayed using the scale to the left. Annealing times for the two datasets were 14 and 0.5 h, respectively.

in the boron-rich sector showed a qualitatively similar behaviour to that recorded during this study — the two datasets are combined in figure 5-9. Similar changes in linewidth were also recorded, with the FWHM at 900 °C being approximately 70 % of the FWHM at 200 °C in both cases.

5.4.2 Photoluminescence

Due to the problems inherent in the quantification of results obtained by photoluminescence, all results in the following section have been normalised to the 1st-order Raman emission line as described in §5.2.2. At each annealing stage, measurements were taken from at least three points on the sample (sample f) with each laser excitation in turn, and each spot was measured using several different laser powers covering at least an order of magnitude of input power. The errors attributed to each data point are representative of both the errors in the fitting process and the spread of obtained results. No photoluminescence was observed under 3.815 eV excitation across the entire annealing temperature range — the only visible features being the 1st- and 2nd-order Raman lines — and hence no data taken with this excitation will be presented.

Post-irradiation, all lasers other than 3.815 eV revealed a multitude of emission lines with integrated intensities covering four orders of magnitude. By 1400 °C, only one weak photoemission was visible (at high incident laser power) across all excitation energies. The annealing results for the most intense (maximum intensity within a factor of 100 less than peak GR1 intensity) emission lines are given in figure 5-10. The annealing data have been presented together in order to facilitate ease of comparison, but for the purposes of analysis the results from each laser excitation will be treated separately, from high to low energy.

5.4.2.1 2.808 eV photoexcitation

The observation of $(NV)^0$ (2.156 eV, 575.1 nm) confirms the presence of nitrogen in this sample. It is difficult to accurately quantify the nitrogen concentration as the close proximity of nitrogen and boron will lead to charge transfer effects

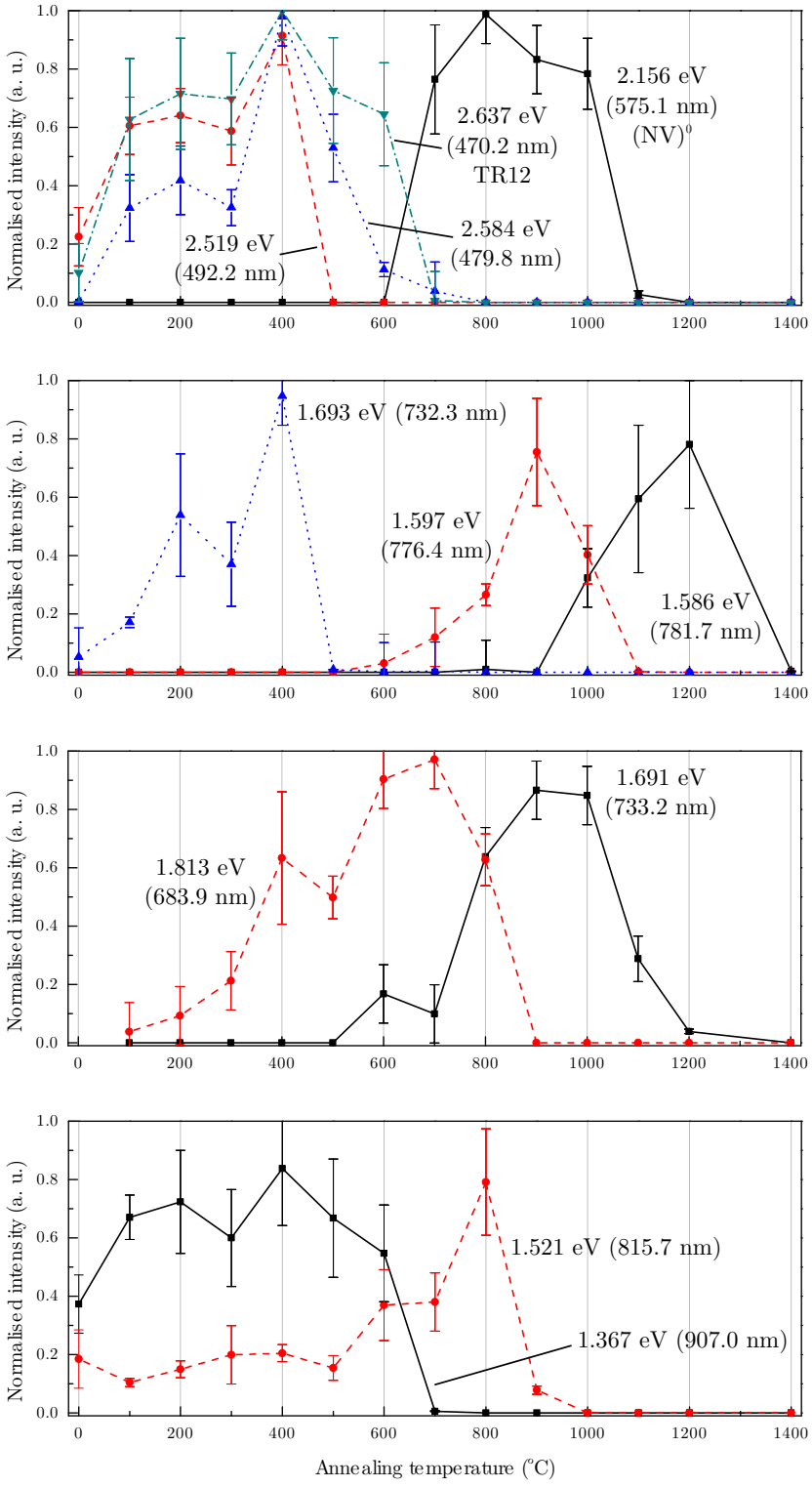

Figure 5-10 Annealing behaviour of the most intense luminescence lines encountered during the study of sample f. Excitation energy from top to bottom: 2.808 eV (441.6 nm), 2.410 eV (514.5 nm), 1.959 eV (632.8 nm) and 1.579 eV (785.0 nm). The maximum emission intensity of all lines displayed was within a factor of 100 of the peak intensity of GR1.

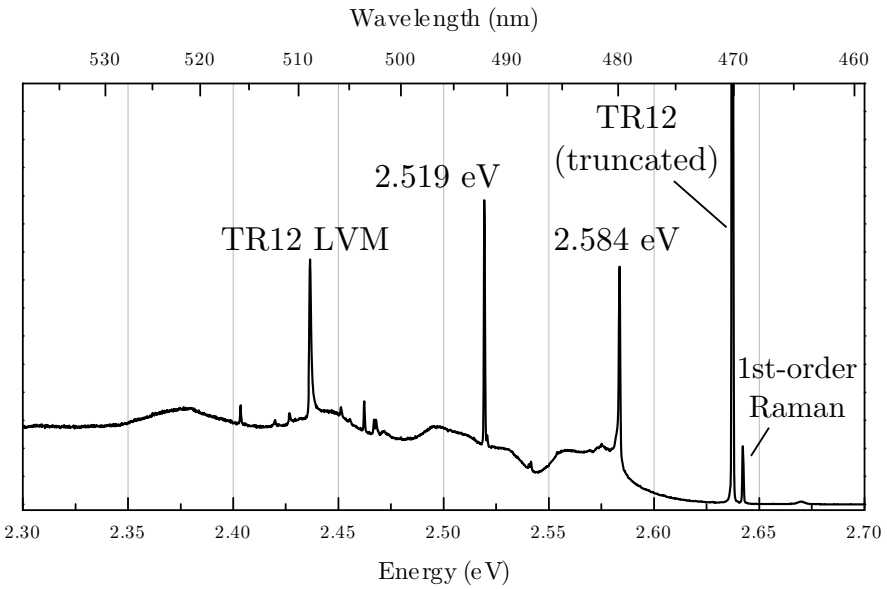

Figure 5-11 Representative spectrum of the most intense features in sample f as observed under excitation at 2.808 eV (441.6 nm). The spectrum was taken post-400 °C anneal using an approximate laser input power of 0.04(2) mW.

i.e. $(N_s)^0 + (B_s)^0 \rightarrow (N_s)^+ + (B_s)^-$. The pre-irradiation concentration of $(N_s)^+$ was certainly below the detection threshold for IR spectroscopy (approximately 0.5 ppm), and it is EPR-silent. No known spectral features are attributed to $(B_s)^-$. Post-irradiation low-temperature EPR measurements put an upper limit on $(N_s)^0$ at sub-ppb levels — at least three orders of magnitude lower than the initial boron concentration. As would be expected in this material, no $(NV)^-$ (1.945 eV, 637.5 nm) was observed at any stage.

TR12 (2.637 eV, 470.2 nm) is a defect produced by irradiation of all diamond types, and tentatively attributed to an intrinsic interstitial-containing complex by its production and annealing behaviour [52, 53]. For successive irradiations at a given electron irradiation energy TR12 intensity is proportional to the intensity of GR1, and its introduction rate is strongly dependent both on the energy [52] and the flux rate [25] of the incident electrons. In luminescence, TR12 is associated with an intense local mode with the approximate frequency 199 meV [54]: during this study, the local mode was recorded at a frequency of 200 meV and with an intensity directly proportional to the intensity of TR12 at all annealing temperatures.

A line observed by cathodoluminescence at 2.520 eV (c.f. 2.519 eV (492.2 nm) in

photoluminescence here) has been reported in the literature as commonly observed in both natural and synthetic type IIb samples [55]. As no associated vibronic structure is visible either in this study or previous work, it is difficult to say with any certainty whether or not they belong to identical defects. Its annealing behaviour is similar to 1.693 eV and consistent with a defect which either contains an interstitial, or is destroyed by the migration of interstitials.

5.4.2.2 2.410 eV photoexcitation

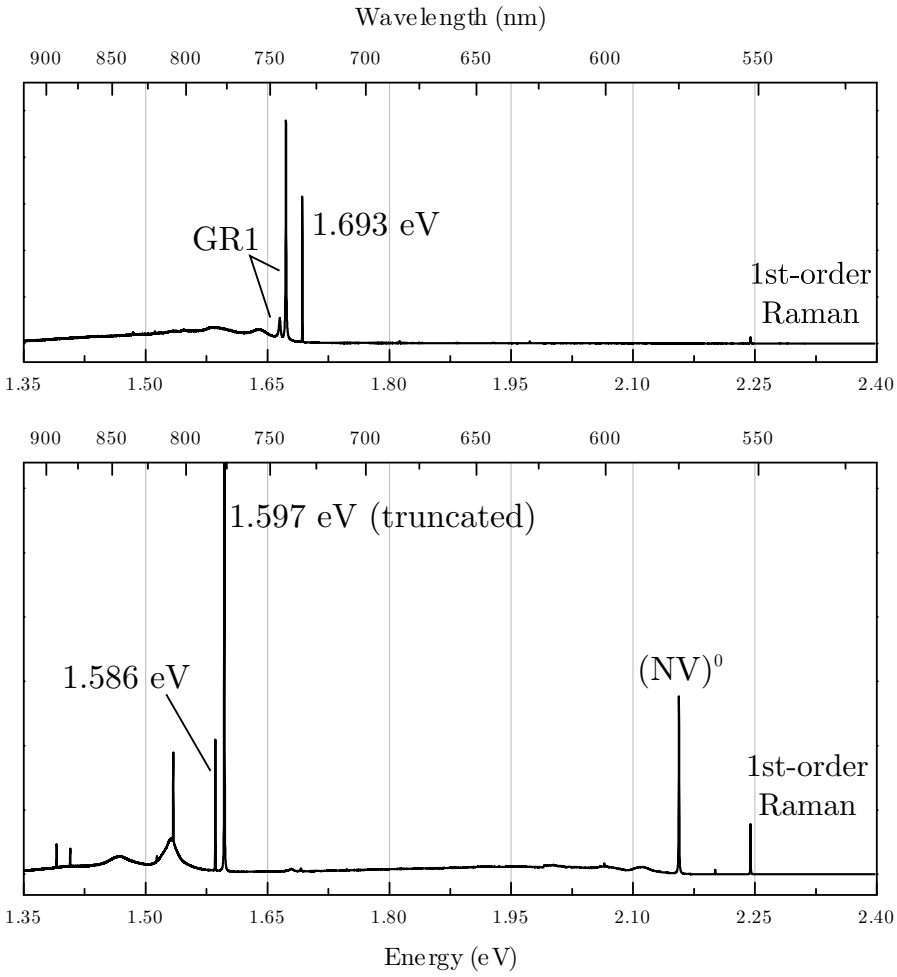

Figure 5-12 Representative spectra of the most intense features in sample f as observed under excitation at 2.410 eV (514.5 nm). Top: post 400 °C anneal, input laser power approximately 0.05(3) mW; bottom: post 1000 °C anneal, input laser power approximately 0.5(3) mW.

The emission observed at 1.693 eV (732.3 nm, see figure 5-12) may or may not be the same as emission lines at 732 nm previously reported after low-energy, high-flux, high-dose electron-irradiation of type IIb material [26–28]. The lineshape

is slightly asymmetric to the high-energy side (the 732 nm line is described as having "an irregular shape" [27]) and very narrow, with a FWHM of approximately 0.4 meV at 80 K. The temperature at which it anneals is coincident with the expected migration temperature of $I^0_{(0\,0\,1)}$.

When considering measurements collected with laser excitation at either 2.410 or 1.959 eV it is important to realise that for spectra taken at annealing temperatures below 700 °C, the results are dominated by GR1 emission (figure 5-12, top). The intensity of the emission necessitates low input laser power in order to avoid saturating the photodetector: weaker lines at energies below 1.67 eV are thus masked by GR1 luminescence. The annealing behaviour of the luminescence at 1.597 eV (776.4 nm) is therefore unknown for annealing temperatures below approximately 600 °C (figure 5-10).

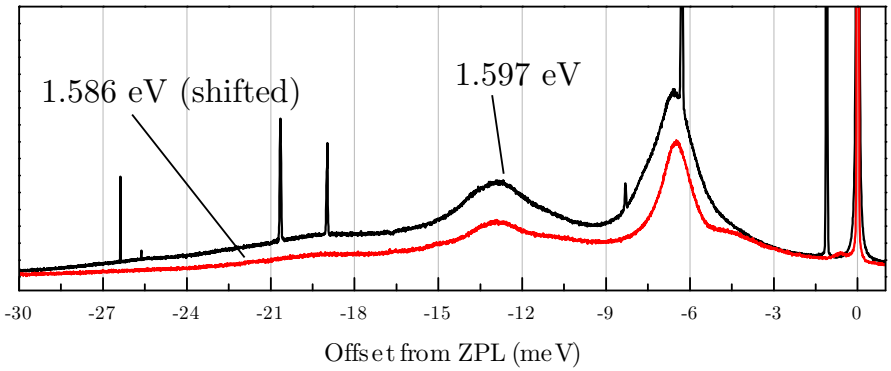

Figure 5-13 Comparison of the vibronic bands belonging to the luminescence lines 1.597 and 1.586 eV, recorded after anneals at 1000 and 1200 °C, respectively. The 1.586 eV spectrum has been shifted and scaled such that the ZPL energies and intensities are identical.

A cathodoluminescence line has been reported at 1.594 eV (777.8 nm) in diamond following implantation with B^+ ions and annealing at 1000 °C [56, 57] (the original references are unavailable to the author): this may or may not be the same emission observed here at 1.597 eV. The author is unaware of any mention of emission at 1.586 eV (781.8 nm) in the literature. Qualitatively, the annealing behaviour of the 1.597 eV emission at high temperature resembles that of the 553 meV absorption line visible in IR measurements (figure 5-6), with the intensity growing before annealing out just as $[(B_s)^0]$ begins to increase.

It is noteworthy that the vibronic structures of the 1.597 and 1.586 eV lines are

very similar (figure 5-13). Quasi-local vibrations in diamond have been understood as a single impurity with an effective mass that reflects either an impurity atom or large, tightly-bound cluster [58]. Using the same approach (originally described in [59]) for a phonon frequency of 6.6(1) meV suggests an effective mass of the order of thousands of atomic mass units: clearly, this approach is not valid in the case of these two transitions.

5.4.2.3 1.959 eV photoexcitation

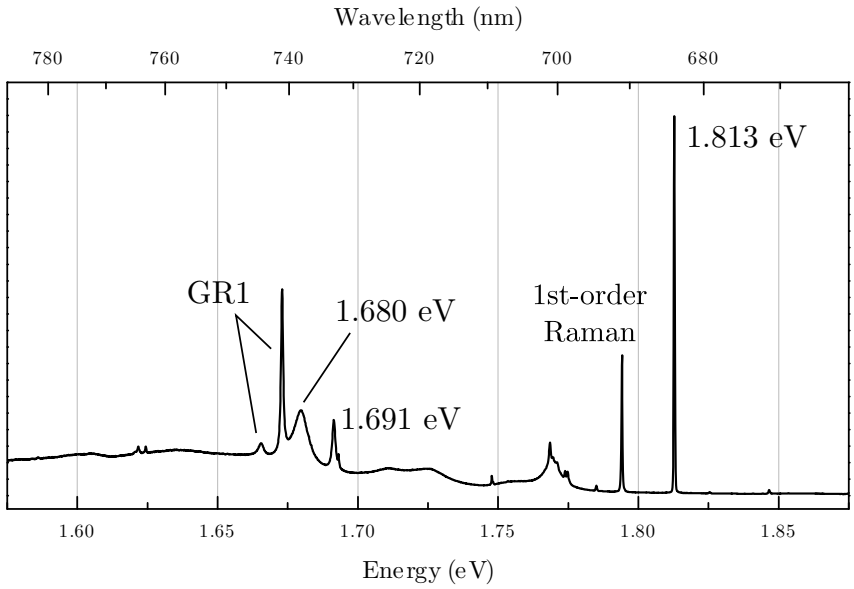

Figure 5-14 Representative spectrum of the most intense features in sample f as observed under excitation at 1.959 eV (632.8 nm). The spectrum was taken post-800 °C anneal using an approximate laser input power of 4(2) mW.

As with the previous section, any low-energy emissions excited at 1.959 eV will have been obscured by GR1 emission at temperatures lower than 700 °C, and hence only relatively high-energy emissions have generally been observed.

The author is unaware of any reports of luminescence at 1.813 eV (683.9 nm) in the literature. This emission line is interesting in that it is formed either during irradiation or by annealing at 100 °C (figure 5-10), and it survives the destruction of $(V)^0$. The vibronic structure indicates coupling to a phonon of frequency 44(1) meV (figure 5-14, visible at approximately 1.77 eV — the sharp features are unrelated ZPLs). At maximum intensity (700 °C), the integrated

intensity was approximately half the maximum integrated intensity of GR1.

The intensity of the emission lines at 1.691 and 1.680 eV (733.2 and 738.0 nm, respectively) are proportional to each other across the entire annealing range and are therefore assumed to belong to the same centre. It is unclear whether the lower energy line is purely electronic or a phonon-assisted transition, but the linewidth (6.5 meV, identical at all annealing temperatures) would suggest the latter.

A ZPL at 1.691 eV was also visible in absorption measurements, with qualitatively similar annealing behaviour as the luminescence centre (figures 5-6 (absorption) and 5-10): the features are therefore ascribed to electronic transitions at the same centre. As with the luminescence line, the absorption spectrum displays a broad absorption close in energy to the ZPL and which is proportional to the ZPL at all annealing temperatures — PL and UV-Vis spectra are given in figure 5-15. It is tempting to assign the weaker features observed in both spectra to an anti-Stokes shift (phonon annihilation) [60], but more data are required to definitively assign all three features to the same defect.

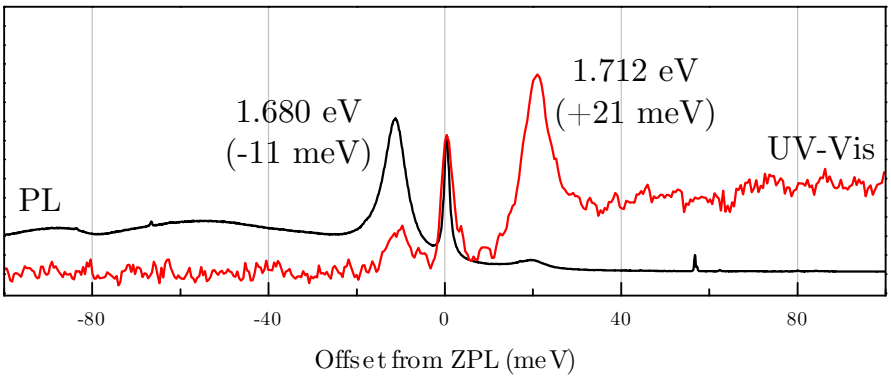

Figure 5-15 Comparison of PL and UV-Vis spectra of sample f post-900 °C anneal. The spectra have been arbitrarily scaled such that the ZPL intensities match. The assumed vibronic features have been given both in absolute energy and offset from the ZPL at 1.691 eV. Both spectra collected with the sample at 80 K.

Features at 1.679, 1.691 and 1.711 eV have been reported in optical absorption studies of intentionally silicon-doped HPHT-grown diamond [51]. Although initially ascribed to silicon-containing centres, the authors noted that there was no apparent correlation between the production of the features and the presence of silicon in the growth capsule [51]. The three lines were found to have similar an-

nealing behaviour to one another, and here are noted to have qualitatively similar behaviour to the corresponding lines observed in this study. Furthermore, the relative intensities of the features in absorption (figure 2, [51]) matches the relative ratios observed here.

Later work observed some of the centres in type Ia natural diamond and heavily-strained polycrystalline CVD material; the analysis of these features was complicated by the presence of strong 1.682 eV (737.1 nm) absorption due to $(SiV)^-$ [61, 62]. Evidently, further work on a wider range of samples is required in order to understand the relationship between and origin of these features.

5.4.2.4 1.579 eV photoexcitation

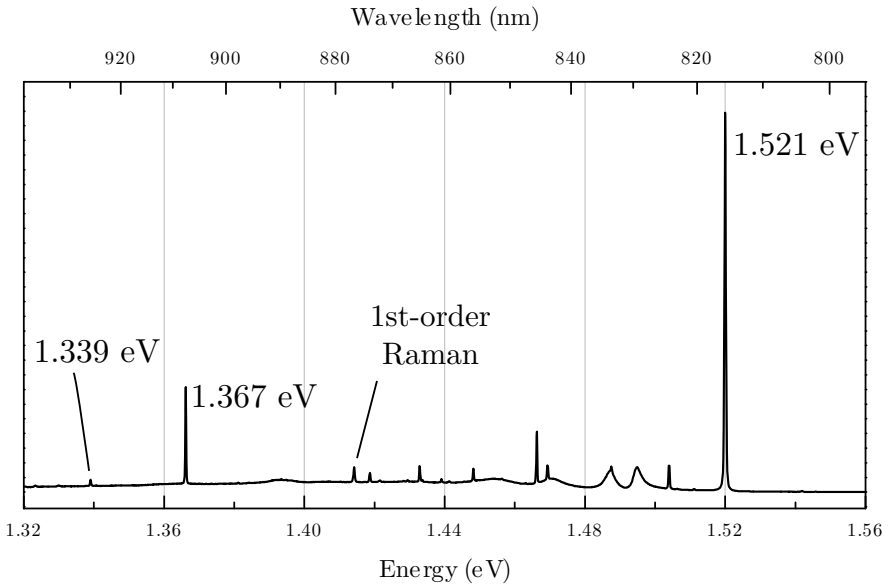

Figure 5-16 Representative spectrum of the most intense features in sample f as observed under excitation at 1.579 eV (785.0 nm). The spectrum was taken post-600 °C anneal using an approximate laser input power of 0.5(3) mW.

The 1.521 eV (815.2 nm) transition was first reported in absorption during studies upon electron-irradiation of type IIa and IIb material [54]. Shortly after, it was reported in cathodoluminescence studies of electron-irradiated type IIb diamond [63]. The transition was shown to be strongly photochromic in absorption [64], with photons of energy $\hbar\omega > 2$ eV enhancing the absorption at 1.521 eV, and $1.5 < \hbar\omega < 2$ eV bleaching out the feature.

Campbell studied electron-irradiated type IIa (nominally — highest concentration impurity: neutral boron at < 0.5 ppm) material and found that both the 1.521 eV and 1.367 eV (907.0 nm) transitions were flux-dependent — changing the beam flux by two orders of magnitude from 12 to 0.3 $\mu A\,cm^{-2}$ dropped absorption intensity of the two features from 6 and 2 cm^{-1} respectively to zero [25]. It is worthy of note that the beam fluxes in the two absorption studies above ([54] and [64]) were also high at $> 20\,\mu A\,cm^{-2}$ (c.f. $\approx 4.5\,\mu A\,cm^{-2}$ here).

The annealing results obtained for 1.521 eV during this study are qualitatively similar across both emission and absorption (figures 5-6 (absorption) and 5-10), and broadly similar to the results obtained by Campbell [25]. No attempts were made to take photochromic effects into account in either this or Campbell's study — the similarity of the annealing behaviour suggests that photochromic effects were not as strong in these synthetic samples as in the original natural sample studied by O'Donnell [64]. Campbell made the observation that the annealing behaviour was broadly similar in profile to that of R4/W6, a divacancy complex [48] — the results obtained here are not inconsistent with that suggestion. Possibly, it may be a different charge state of a divacancy complex (TH5, R4/W6 or other) — that it has only been observed in type IIb and IIa material to this point implies that it is either in a neutral or positive charge state.

The 1.521 eV feature was observed during this study in both absorption and emission, although the absorption strength was too weak to discern any spectral characteristics beyond the ZPL itself. Previous descriptions of the vibronic structure in absorption mention only a broad, weak vibronic band with phonon energy $\hbar\Omega \approx 60$ meV [25, 64]. In contrast, the photoluminescence spectrum reveals relatively strong, narrow vibronic features with mode energies $\hbar\Omega = 25.1(5), 32.8(5)$ meV (figure 5-17). A photoluminescence excitation experiment would be useful to determine exactly the absorption profile of the centre.

The complete breakdown of spectral mirror symmetry about the ZPL suggests a Jahn-Teller-type effect [65, 66], implying a nominally high-symmetry centre with relatively simple atomic structure: further work is required to gain a better understanding of this centre.

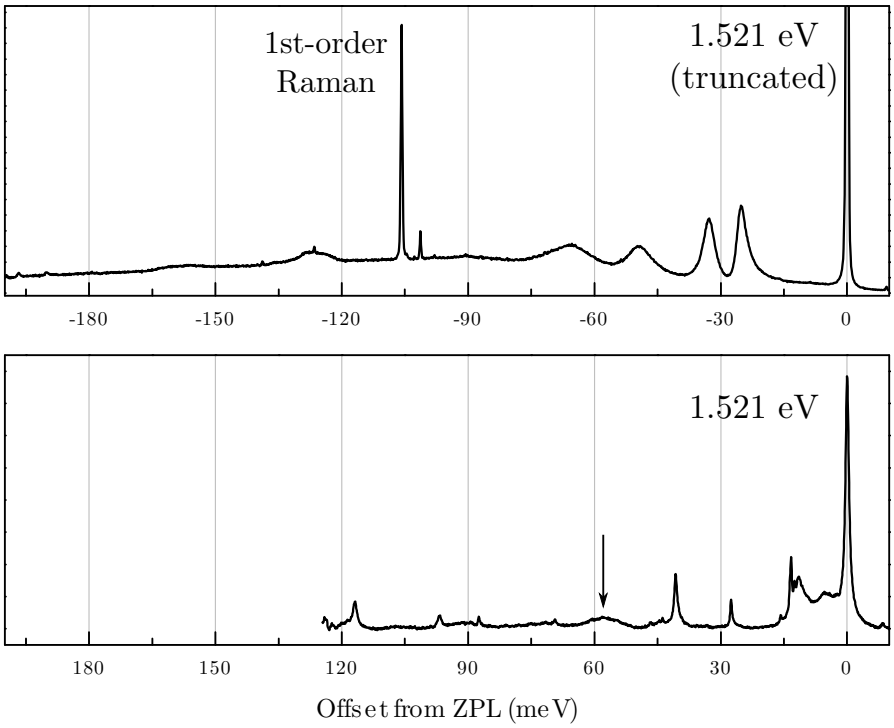

Figure 5-17 Vibronic structure of the 1.521 eV ZPL in emission (top) and absorption. Top: all broad features are proportional to the integrated intensity of the ZPL at all annealing temperatures and laser input powers, and hence are assumed to be vibronic features of 1.521 eV. Bottom: All features are unrelated to the ZPL (as determined by different annealing behaviour) except the weak vibronic mode indicated. Absorption spectrum from [25].

The 1.367 eV feature (907.0 nm) anneals in the same way as the neutral vacancy, both in absorption [25] and emission (figure 5-10 — author not aware of reports of luminescence at this energy). Carbon isotopic substitution studies using 1:1 ^{12}C:^{13}C revealed a 1:4:6:4:1 intensity fine structure in the absorption ZPL, suggesting four equivalent carbons. The local mode split with the ratios 1:3:3:1, giving a minimum of three equivalent carbons. These data were interpreted as a defect on a substitutional site with four nearest neighbour carbons, each of which is back-bonded to three additional carbons [25]. Unfortunately, no information was available on the entity at the substitutional site — vacancy, impurity etc. The production of the transition in type IIb material was used to suggest it as a candidate for a transition at $(V)^+$. Inconclusive uniaxial stress results with indeterminate symmetry assignment confused the simple understanding of the transition to that point: uniaxial stress measurements performed using photoluminescence would allow the excited state to be probed, and possibly help to disentangle the existing

results.

In luminescence, the 1.367 eV transition correlates in intensity at all annealing temperatures with a feature at 1.339 eV (925.9 nm). This is too close (28 meV) to the ZPL to be a local mode, but may be a transition at the same centre. Uniaxial stress studies assigned an absorption at 1.317 eV to a partially forbidden excited state transition at the same centre as 1.367 eV [25] — this transition was not observed in luminescence (as might be expected given the assumed origin of the absorption). Finally, the silicon CCD used for spectral collection was not sensitive enough at long wavelengths to pick up the reported local mode which, if at the same frequency as the mode in absorption, would manifest at approximately 1.186 eV (1045 nm).

All of the sparse reports of both the 1.367 and 1.521 eV transitions were based on studies of type IIb (or boron-containing) material; it seems then that their production depends in some way on the presence of boron. It may simply be the case that both transitions are very sensitive to the local charge environment and are efficient acceptors, precluding their existence (in this charge state) in nitrogen-containing material and even type IIa material. Theoretical results suggest that $(\mathrm{V})^+$ is the stable charge state of the vacancy only with a Fermi level (local environment [67]) of less than $E_V + 1\,\mathrm{eV}$ [19] — other defects will be equally sensitive. Alternatively, the initial production of the centres may depend on the Fermi level during irradiation, or either one may contain boron as an atomic constituent.

E (eV)	λ (nm)	Laser[a]	Temp. (°C) In	Out	Notes
2.637	470.2	1	–	700	TR12, §5.4.2.1
2.584	479.8	1	–	700	§5.4.2.1
2.519	492.2	1	–	400	§5.4.2.1
2.450	506.1	Abs.	400	1000	M2, §5.4.1
2.417	513.0	1	700	1100	
2.402	516.2	Abs.	400	1000	M1, §5.4.1
2.395	517.7	1	700	1100	
2.156	575.1	1,2	700	1100	$(NV)^0$, §5.4.2.1
2.126	583.2	1	700	800	
1.974	628.1	2	100	600	
1.913	648.1	1–3	–	700	Chapter 6
1.813	683.9	2,3	100	800	§5.4.2.3
1.693	732.3	2,3	–	400	§5.4.2.2
1.691	733.2	3, abs.	600	1200	§5.4.2.3
1.673	741.1	1–3, abs.	–	700	$(V)^0$
1.597	776.4	2	600	1000	§5.4.2.2
1.586	781.7	2,3	800	1200	§5.4.2.2
1.565	792.2	3	800	–	
1.534	808.2	2,3	800	1000	
1.521	815.1	3,4, abs.	–	900	§5.4.2.4
1.367	907.0	4	–	700	§5.4.2.4
0.553	2242	Abs.	–	1100	§5.4.1
0.348	3563	Abs.	1000	–	$(B_s)^0$, §5.4.1

[a] 1–4: Laser excitation at 2.808, 2.410, 1.959 and 1.579 eV, respectively. Abs: absorption.

Table 5-2 Summary of the more intense lines encountered in photoluminescence and absorption during the annealing study. Names are given where known, in addition to links to relevant sections where further information is available. Temperature gives the range over which the feature was visible (inclusive — feature still visible at higher temperature); where upper temperature has been omitted, feature was not seen to anneal out.

5.5 Discussion

5.5.1 Effect of electron irradiation in type IIb diamond

Post low-temperature electron irradiation of boron-doped diamond, the immediate observations are:

- The neutral vacancy concentration depends on the initial uncompensated boron concentration.
- The loss of uncompensated boron during irradiation depends both on dose and irradiation temperature.

It is well-reported that in type IIb diamond the production rate of GR1 is significantly lower than in type IIa material, and many studies report a threshold dose required before GR1 is observed [47, 68]. The general assumption made in past studies has been that the vacancy production rate is similar in the two types, but that in type IIb material the vacancies are being created as $(\mathrm{V})^{+}$ rather than $(\mathrm{V})^{0}$. Thus, the threshold dose required for the observation of GR1 (assuming a homogeneous crystal) is simply the dose required to compensate the initial neutral boron concentration. The idea of a threshold dose is broadly supported by the results of this study: if a linear fit to the non-zero neutral vacancy and residual boron concentration is performed, only a small overlap is observed where both the vacancy and neutral boron are observed in the same crystal (figure 5-18). This overlap can easily be attributed to heterogeneous boron concentrations in the HPHT samples; a similar irradiation study on a suite of homogeneous single-sector samples would confirm this.

The compensated vacancies picture is self-consistent until the neutral interstitials are also taken into account: not only is the vacancy concentration low relative to type IIa material, but the concentration of $\mathrm{I}^{0}_{\langle 0\,0\,1\rangle}$ is also reduced. From table 5-1, it is noted that the reference type IIa sample (sample g) contained $[(\mathrm{V})^{0}]_f = 2.0(1)\,\mathrm{ppm}$ and $[\mathrm{I}^{0}_{\langle 0\,0\,1\rangle}]_f = 1.8(1)\,\mathrm{ppm}$ post-irradiation. In the case of the CVD sample (sample f): $[(\mathrm{B_s})^{0}]_i = 0.8(1)\,\mathrm{ppm}$; $[(\mathrm{V})^{0}]_f = 0.9(1)\,\mathrm{ppm}$ and $[\mathrm{I}^{0}_{\langle 0\,0\,1\rangle}]_f < 0.1\,\mathrm{ppm}$. As mentioned in §5.3.1.2, the vacancy production in the IIa

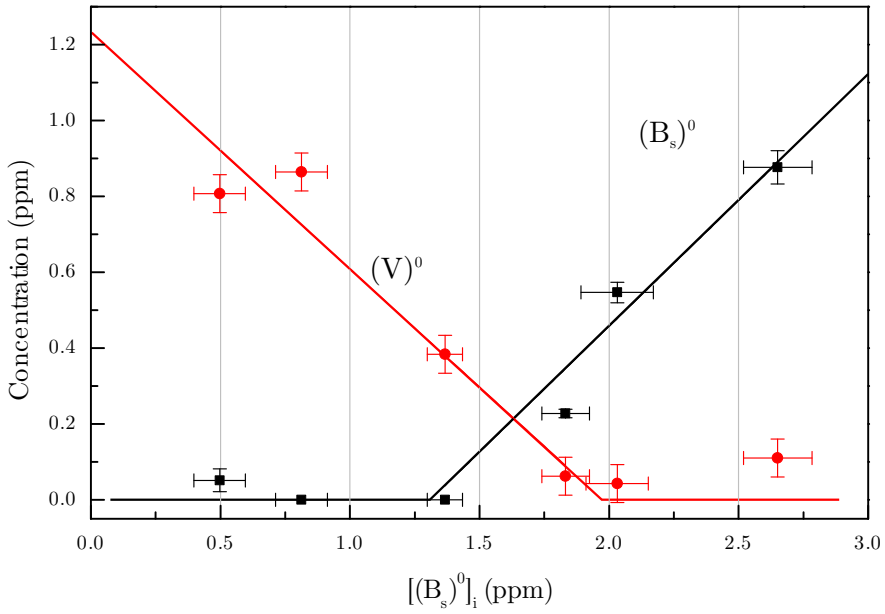

Figure 5-18 Post-irradiation neutral vacancy and neutral boron concentration as a function of initial neutral boron concentration for samples a–f. All irradiations performed to a total dose of $5 \times 10^{17}\,\mathrm{e^-\,cm^{-2}}$ at a temperature of 100 K. Lines are linear fits to non-zero values, each with gradient $|m| = 0.6(1)$, and are pinned at zero from the x-intercept onward.

sample is approximately half that predicted by the published production rate of $1.5(1)\,\mathrm{cm^{-1}}$ [11]. Equally, the loss of boron post-irradiation is approximately 1.5(2) ppm (figure 5-18) — approximately half the lower rate extrapolated from the data of Collins (figure 5-4) [2]. Together, these data are taken to imply that the actual electron dose delivered to the samples during irradiation was approximately half the measured value of $5 \times 10^{17}\,\mathrm{e^-\,cm^{-2}}$ (doses are typically calculated from beam flux calibrations rather than in-situ measurements): the total vacancy concentration and boron loss are then consistent with the respective published data [2, 11].

If the vacancy creation rate is assumed to be similar in the type IIa and IIb material, then a total of ≈ 3 ppm drop in neutral interstitials and vacancies combined must be accounted for by an initial uncompensated boron concentration of ≈ 1 ppm in sample f. Even if the calibration constants for these defects are taken at the most favourable end of their uncertainties, these effects still cannot be explained purely on a charge basis.

A clue may lie in the variable-temperature irradiation work by Collins [2], which showed a change in the rate of boron removal at different sample temperatures during irradiation. Variable-temperature damage studies of type IIa material demonstrated that the ratio $[I^0_{\langle 0\,0\,1\rangle}]$:$[(V)^0]$ is sensitive to sample temperature during irradiation. At 100 K, $[I^0_{\langle 0\,0\,1\rangle}] = [(V)^0]$ (within calibration constant error); for irradiation at approximately 140 K, $[I^0_{\langle 0\,0\,1\rangle}] \lessapprox 70\,\% \, [(V)^0]$ with no material change in the absolute vacancy concentration [15]. The primary difference between irradiation of type IIa material at 100 K and 300 K is therefore interstitial-related — any vacancy-related effects are below detection uncertainties. In Collins' work, the rate of boron removal was approximately five times more rapid when a sample was irradiated at 100 K rather than 300 K (figure 5-4), similar to the ratio of interstitial introduction at these temperatures in type IIa material of ≈ 4 [15]. Furthermore, the fact that no fluctuations were observed in the boron concentration during the annealing study suggests that boron has undergone a structural change e.g. complexing with an intrinsic irradiation damage defect, rather than simply changing charge state. All of these data are consistent with the loss of boron during irradiation being attributable, at least in part, to interaction with self-interstitials: this idea will form the cornerstone of the general model presented here.

5.5.2 Interstitial migration during irradiation

Following the approach outlined by Newton et al. [16], a high-mobility self-interstitial I^{**} is assumed to be present during irradiation. I^{**} differs from the I^* of the original paper in that it is mobile even during irradiation at 100 K. Given the nature of the samples under investigation, it seems likely that this lowered migration energy c.f. interstitials in other diamond types is due to charge state of I^{**}. In contrast to nitrogen-doped diamond, where donor effects are highly localised [67], in boron-doped diamond the uncompensated boron wavefunction is diffuse [69] and the idea of a "Fermi level" has meaning (at least on a microscopic scale). As with I^*, the motion of I^{**} through the lattice is mediated by electronic excitation and / or charge transfer, and will diffuse either as I^{**} or by

the process $I^{**} \rightarrow I \rightarrow I^{**} \rightarrow I$ etc [70]. The data available are insufficient to determine any properties of I^{**}, and without any details on its particulars the following macroscopic results are attributed to its presence:

- Vacancy-interstitial annihilation is increased during irradiation relative to other types of diamond, such that the absolute concentrations of $(V)^0$ and $I^0_{\langle 0\,0\,1\rangle}$ are lower than those measured in type IIa material irradiated under similar conditions.
- Enhanced diffusion of I^{**} during irradiation leads to the creation of boron-interstitial complexes which survive irradiation.

The latter point suggests a mechanism such as

$$B_s + I^{**} \rightarrow (B_sI) \quad \text{or} \quad B_s + I^{**} \rightarrow I_B \ ,$$

where (B_sI) and I_B are a boron nearest-neighbour to a carbon interstitial, and a carbon-boron interstitial, respectively.

Boron-interstitial complexes are predicted to take one of several configurations of similar total energy, each of which is stable at low annealing temperatures: furthermore, all boron-interstitial configurations act as donors [31]. The implication is that for every boron atom lost to a boron-interstitial complex another becomes electronically inactive, making the removal process as a whole incredibly efficient.

Although it may seem redundant to suggest another highly mobile interstitial in addition to I^*, the lack of strained vacancies [46], neutral interstitials, and a GR1 annealing stage at interstitial mobility temperatures suggests that the situation here is demonstrably different to that encountered in type IIa material.

5.5.3 Annealing of electron-irradiated type IIb diamond

The annealing behaviour of $(V)^0$ and $(B_s)^0$ provide further evidence for the interstitial-centric picture of irradiation damage in boron-containing diamond. The corresponding annealing curves obtained during this and Collins' investigations [2] are given in figure 5-19. Although the sample origins and electron doses were different between the two studies (see figure description), the most

obvious difference is that Collins' sample still contained uncompensated boron post-irradiation. The "reverse annealing" of GR1 at approximately 200 °C is not seen in annealing studies of type IIa material, where the GR1 absorption linewidth is expected to narrow and its intensity to decrease due to self-annihilation with trapped interstitials in close proximity [16].

No reverse annealing phenomenon was observed in sample f, where no uncompensated boron was present post-irradiation, but it was observed in sample e, the only other sample of the suite to have been annealed (and also the sample with the highest initial $[(\mathrm{B_s})^0]_i$). Sample e was annealed to 600 °C as part of the 1.913 eV luminescence study in chapter 6. Unfortunately, absorption measurements were not performed at each annealing stage, but the post-600 °C UV-Vis and IR measurements show an increase in $[(\mathrm{V})^0]$ of $0.2(1)$ ppm (figure 5-20) and a decrease in $[(\mathrm{B_s})^0]$ of $0.4(1)$ relative to the post-irradiation pre-anneal measurements. Additionally, the initial concentration of $\mathrm{I}^0_{\langle 0\,0\,1\rangle}$ ($0.2(1)$ ppm) had dropped to zero.

It is not obvious why the changes in $[(\mathrm{V})^0]$ and $[(\mathrm{B_s})^0]$ shown in figure 5-19b are not simultaneous. The loss of $(\mathrm{B_s})^0$ at ≈ 300 °C is well-fitted by first-, second- or mixed-order kinetic processes with an activation energy of $E_A = 1.6$ eV — the same obtained for the mobility of $\mathrm{I}^0_{\langle 0\,0\,1\rangle}$ [16]. (The data are insufficient to determine the order of the process, and all forms suggest reasonable attempt frequencies.) Within the working model, the loss of boron is attributed to structural complexing with interstitials, and as previously mentioned any boron-interstitial may compensate a further substitutional boron atom. Quantitatively, this model fits with the observed changes in sample g post-600 °C anneal: $\Delta\mathrm{I}^0_{\langle 0\,0\,1\rangle} = -0.2(1)$ ppm; $\Delta(\mathrm{B_s})^0 = -0.4$ ppm. Additionally, Collins noted that the loss of $(\mathrm{B_s})^0$ was concomitant with the loss of the optical feature at 1.859 eV (due to $\mathrm{I}^0_{\langle 0\,0\,1\rangle}$), suggesting interstitial-boron interaction. Nevertheless, caution must be exercised — there will surely be other interstitial traps and charge-sensitive defects within the crystal, and the agreement may be purely coincidental.

This interpretation of the process behind the loss of uncompensated boron then leaves the cause of the change in vacancy concentration as an entirely separate process, as suggested by the disparity in annealing temperatures. The simplest

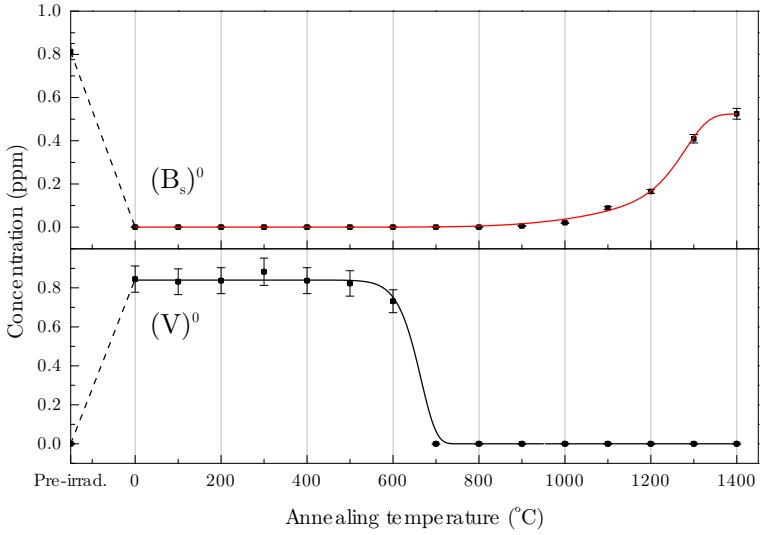

(a) Sample f, dose 5×10^{17} e$^-$ cm^{-2}. Top: the red line is a mixed first- (f = 2×10^8 Hz, E_A = 3 eV) and second- (f = 5×10^{11} Hz ppm^{-1}, E_A = 3.7 eV) order simulation. Bottom: for the neutral vacancy, a first-order simulation is shown with E_A = 2.3 eV [30]. Each annealing stage was 14 h.

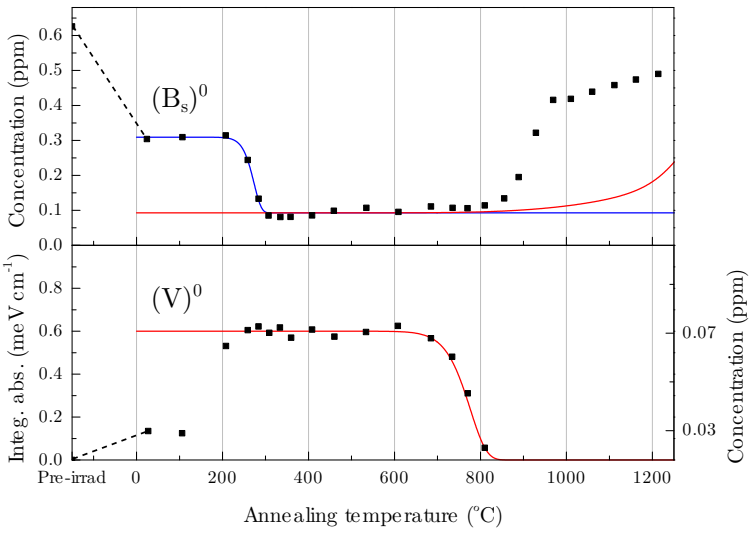

(b) Data taken by Collins on a natural type IIb sample irradiated at 100 K to a total dose of 1.7×10^{16} e$^-$ cm^{-2} [2]. Top: blue line is mixed first- and second-order simulation using E_A = 1.6 eV (for migration of $I^0_{\langle 0\,0\,1\rangle}$ [16]); red line is the same mixed-order simulation shown in top pane of above figure. Bottom: second-order (E_A = 2.3 eV) vacancy migration simulation. [(V)^0] estimated from given peak absorption and linewidths assuming a purely Lorentzian profile, and should be treated with caution. Each annealing stage was 12 h.

Figure 5-19 Concentrations of neutral substitutional boron (top in each image) and the neutral vacancy as a function of annealing temperature. In both cases, electron energy was 2 MeV.

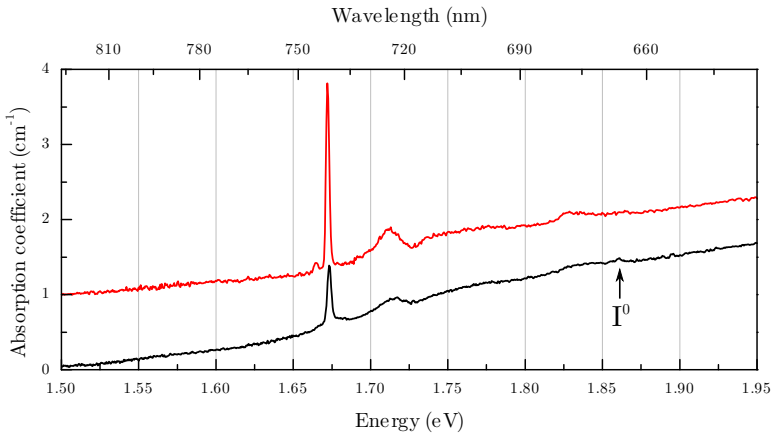

Figure 5-20 UV-Vis spectra of sample e pre- (bottom) and post-anneal at 600 °C, with $(V)^0$ concentrations of 0.1 and 0.3 ppm, respectively. Pre-anneal $I^0_{\langle 0\,0\,1\rangle}$ (indicated at 1.859 eV) concentration was 0.2(1) ppm. Spectra offset for clarity.

explanation is a charge effect, for example $(V)^+ + X^- \rightarrow (V)^0 + X^0$. The change in $[(V)^0]$ was not observed in the CVD sample, where the initial boron concentration was significantly lower than the estimated introduced vacancy concentration. One problem with this model is that the initial assumption made at the start of this chapter was that $(V)^0$ was created in low-boron (IIa-like) regions of the high-boron concentration samples. However, no reverse annealing is observed in pure type IIa material, and if the change is driven by charge transfer then it may suggest long-range transport of charge carriers. Further studies are required in order to determine whether reverse annealing occurs in very homogeneous highly-boron-doped samples (or whether GR1 is observed at all). It is noted that if boron is efficiently removed by interstitial complexes during irradiation as supposed, little to no $(V)^+$ will be created in samples with no residual uncompensated boron, and any potential studies of $(V)^+$ must utilise samples with high starting boron concentrations relative to the input irradiation dose.

It is interesting to note that (B_sI) (a substitutional boron nearest neighbour to an $I_{\langle 0\,0\,1\rangle}$-split interstitial) is predicted to be mobile at energies of 1.4 eV (2.1 eV) in the positive (neutral) charge state [31]. The binding energy of the neutral and positive charge states are calculated as 4.8 and 5.8 eV, respectively [31]. The positive charge state (assumedly the stable charge configuration in the presence of substitutional boron) will therefore migrate at energies similar to the carbon

interstitial $I^0_{\langle 0\,0\,1\rangle}$ by the repeating process

$$(B_sI) \rightarrow (B_i) \rightarrow (B_i) \rightarrow (IB_s)$$

where the middle step corresponds to a through-bond migration (c.f. nitrogen interstitial [71]).

No further changes are observed in either this or Collins' study until the vacancy begins to migrate (figure 5-19). Using the published value of 2.3 eV for migration of the vacancy [16, 30], it is found that the data from this study are best fitted using first-order kinetics whereas the data from Collins are best fitted as a second-order process. This may reflect the differing origins of the two samples employed: CVD-grown in this investigation, natural in Collins' case. CVD-grown samples are well-known to contain high dislocation densities which are grown-in from the substrate-sample interface [72]: in context, they represent infinite sinks for migrating vacancies, and are the assumed cause of the first-order kinetics observed. In the natural sample, the assumed dislocation density is lower and the destruction of neutral vacancies is supposed to proceed by the formation of divacancies, as in type IIa material [48].

The last stage in the annealing behaviour in both studies is the recovery of $(B_s)^0$. This recovery has also been reported elsewhere [47] (replicated here in figure 5-9). Although the start of the recovery is relatively constant across all studies at approximately 900–1000 °C, the form of the recovery is very different in all cases. Here, isothermal anneals on several samples would be instrumental in extracting the different rates and energies of the migration / dissociation processes involved. In all cases it seems that at least 60 % of the initial boron concentration may be recovered by annealing to approximately 1200–1400 °C. Unfortunately, no higher temperature data are available to confirm whether or not it will reach pre-irradiation levels. Nevertheless, this result is in stark contrast to the irradiation and annealing processes observed in nitrogen-containing defects in diamond, where higher-temperature anneals lead to ever higher-order aggregates and their vacancy-containing analogues (see §7.2), at least until temperatures of ≈ 2000 °C are reached [73].

This discussion has neglected the effect of hydrogen in the CVD material. No

known hydrogen-related defects were observed by any of the spectroscopic techniques employed, and the general results were in qualitative agreement with a previous irradiation study of natural type IIb diamond [2]. Additionally, hydrogen is usually incorporated only at the trace level in high quality single crystal CVD-grown type IIb diamond [74–76]. Future studies may indicate the need to take hydrogen into account.

5.5.4 Spectral features in electron-irradiated type IIb diamond

Some of the spectral features reported here are also reported in type IIa diamond (e.g., TR12, GR1 etc) and are attributed to intrinsic radiation damage defects: their production is expected. Several of the luminescence lines show unique spectral characteristics with at least one (1.521 eV) showing features suggestive of high symmetry. As noted by Campbell [25] the annealing behaviour of 1.521 eV is qualitatively the same as the divacancy, suggesting it may be a differently-charged divacancy. EPR measurements have identified a defect consistent with a negatively charged divacancy [77], although first-principles calculations conclude that only the neutral state is stable in diamond [78].

The absorption at 553 meV (§5.4.1.1) has been directly linked to the presence of boron [47], and its strength in absorption suggests that it is produced in significant quantities. Boron isotopic studies might not be particularly fruitful here due to the linewidth of the transition, but uniaxial stress to determine the symmetry (after annealing at approximately 900 °C to narrow the linewidth) would be useful in excluding certain atomic structures. Of all the spectral features reported in this study, the 553 meV is the strongest feature which is strongly linked to the presence of boron: its identification might provide a starting point for a more concrete understanding of electron irradiation damage in type IIb material as a whole.

5.5.5 The $^5A_2$ excited state of $(V)^0$

It is noteworthy that the $^5A_2$ excited state of the neutral vacancy was observed by photoexcited EPR in all measured samples post-irradiation (samples b, d and f, spectrum in figure 5-21). The excited state has been reported in only one sample previously [79]. The conventional model for the production of the state relies on ionisation of $(V)^-$, rather than an internal transition of $(V)^0$ [79]. With reference to the electronic vacancy model (§5.1.2), the excited state is populated by the process

$$E^-(^4A_2) + \hbar\omega(> 3.150\,\text{eV}) \rightarrow E^-(^4T_1) \rightarrow E^0(^5A_2) + e^- \ ,$$

where E^- and E^0 denote energy levels of $(V)^-$ and $(V)^0$, respectively [19]. The electron is understood to transfer to a nearby acceptor (nitrogen aggregates or $(N_s)^+$ in the original samples) [19]. However, there are problems with this explanation: the original paper noted that the excited state was not observed in many samples containing nitrogen, $(V)^-$ and $(V)^0$ [79]; and the subsequent theoretical explanation of the population of the state predicted that the state would not be observed in low-nitrogen material [19]. The observation of the excited state in these samples is at odds with the second point, and the first suggests that other defects are important in the population / suppression of the excited state.

The author is unaware of reports of the $^5A_2$ excited state in type IIa material and this would tend to rule out a purely internal transition of $(V)^0$. The photoexcitation dependence in the type IIb samples studied here was found to be similar to the published energies, with 2.95 eV light not populating the state, and the population efficiency being approximately equal at 3.05(5) and 3.3 eV: this narrows down the excitation threshold from a window of 250 meV ([79]) to 100 meV. It appears that the excitation occurs at energies below the ZPL transition of $(V)^-$ at 3.150 eV [80], ruling out $(V)^-$ as the population mechanism in these samples. No sharp feature was visible around 3.0(5) eV in either luminescence or optical absorption measurements, but a band-to-defect continuum would be masked by GR1 in these samples (see figure 5-3).

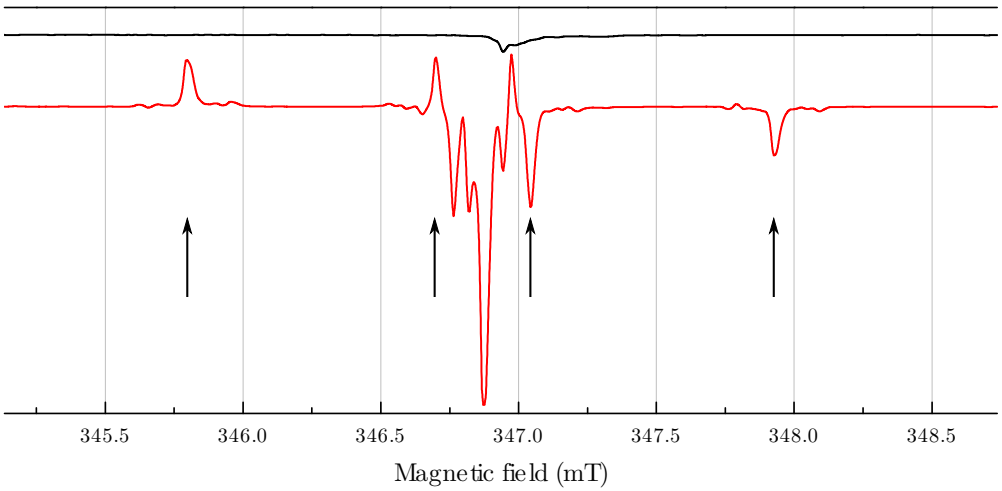

Figure 5-21 EPR spectra of sample f post-irradiation but pre-anneal. Top: no illumination; bottom: excitation by a solid state laser emitting at 3.07 eV (404 nm) with an approximate power of 100 mW. Lines belonging to the $^5A_2$ excited state of $(V)^0$ have been indicated; the different phase of high- and low-field lines indicates spin polarisation (see §8.2.1 and the original paper [79]). Both spectra recorded at a microwave frequency of 9.7403 GHz and a sample temperature of 50 K. Spectrum recorded using a Bruker E580 with a Bruker MD5 dielectric resonator mounted inside an Oxford Instruments CF935 continuous flow liquid helium cryostat.

5.6 Conclusion

A suite of one type IIa and six type IIb diamonds have been electron irradiated at 100 K. The difference between low-temperature and room temperature electron irradiation has been discussed. For samples which received the same electron dose, the number of neutral vacancies present post-irradiation was found to depend approximately linearly on the initial boron concentration. In all cases, the neutral vacancy and interstitial concentrations were lower than those measured in a type IIa sample which was irradiated simultaneously.

Excluding absorption due to $(V)^0$ and $(B_s)^0$, an infrared transition at 0.553 eV was the most significant absorption feature observed in a low-temperature electron-irradiated CVD sample, being approximately approximately a factor of 25 stronger than other absorption lines. The transition was present post-irradiation and decreased in intensity upon annealing before a transient increase at 900 °C, and finally annealing out at 1200 °C.

A number of transitions observed by luminescence have been tracked in intensity as a function of annealing temperature. Characteristic spectral features of several of the lines have been highlighted, and the production of different features discussed where possible. In particular, the transition with energy 1.521 eV seems strongly related to the presence of boron: further experiments are required to determine whether this is due to a charge effect, or that the production of the centre requires boron directly.

It has been shown that charge effects alone cannot account for the lower concentration of neutrally-charged intrinsic defects in type IIb material following irradiation. It has therefore been suggested that some of the loss must be structural in nature.

Finally, all the available data on irradiation and annealing of type IIb material have been used to form a basic but self-consistent explanation of the recorded observations of type IIb diamond following electron irradiation. In contrast to nitrogen-related defects in diamond, which tend to interact primarily with vacancies, the proposed model of boron-related irradiation-produced defects depends on interaction with interstitials.

Further studies are required to gain a more complete understanding. In particular, a suite of highly homogeneous, single sector CVD-grown samples would be advantageous. An experiment whereby samples of different boron concentrations are cut up, with different pieces irradiated to different doses, would directly allow correlations of optical / EPR features with both boron concentration and electron dose and would therefore significantly increase understanding of both intrinsic defects in type IIb material, and boron-related features. It would also provide a second set of data to those provided by Collins on successive irradiations of the same sample [2], and those presented here on simultaneous irradiation of samples containing different boron concentrations.

References

1. C. D. Clark, R. W. Ditchburn, H. B. Dyer, *Proceedings of the Royal Society of London A* **234**, 363 (1956).
2. A. T. Collins, presented at the Radiation Effects in Semiconductors 1976, ed. by N. B. Urli, J. W. Corbett, p. 346.
3. Y. V. Pleskov, *Russian Journal of Electrochemistry* **38**, 1275 (2002).
4. L. Hutton *et al.*, *Analytical Chemistry* **81**, 1023 (2009).
5. Y. Gurbuz *et al.*, *Solid-State Electronics* **49**, 1055 (2005).
6. J. Achard *et al.*, *Diamond and Related Materials* **20**, 145 (2011).
7. R. Edgington *et al.*, *Biosensors & Bioelectronics* **33**, 152 (2012).
8. R. S. Balmer *et al.*, *Journal of Physics: Condensed Matter* **21**, 364221 (2009).
9. J. F. Prins, *Semiconductor Science and Technology* **18**, S27 (2003).
10. H. Amekura, N. Kishimoto, *Journal of Applied Physics* **104**, 063509 (2008).
11. D. Hunt *et al.*, *Physical Review B* **61**, 3863 (2000).
12. D. Twitchen *et al.*, *Physical Review B* **54**, 6988 (1996).
13. D. Hunt *et al.*, *Physical Review B* **62**, 6587 (2000).
14. J. P. Goss *et al.*, *Physical Review B* **63**, 195208 (2001).
15. G. Davies *et al.*, *Physica Status Solidi (A)* **186**, 187 (2001).
16. M. Newton *et al.*, *Diamond and Related Materials* **11**, 618 (2002).
17. D. Hunt, PhD thesis, St. Peter's College, Oxford, 1999.
18. C. Coulson, M. Kearsley, *Proceedings of the Royal Society of London A* **241**, 433 (1957).
19. A. Mainwood, A. M. Stoneham, *Journal of Physics: Condensed Matter* **9**, 2453 (1997).
20. J. Friedel, M. Lannoo, G. Leman, *Physical Review* **164**, 1056 (1967).
21. F. Larkins, *Journal of Physics and Chemistry of Solids* **32**, 2123 (1971).
22. J. Isoya, H. Kanda, Y. Morita, presented at the Advances in New Diamond Science and Technology, ed. by S. Saito *et al.*, p. 351.
23. M. H. Saani *et al.*, *The European Physical Journal B* **65**, 219 (2008).
24. S. Dannefaer, *Physica Status Solidi (C)* **4**, 3605 (2007).

25. B. Campbell, PhD thesis, King's College London (University of London), 2004.
26. J. W. Steeds *et al.*, *Acta Materialia* **47**, 4025 (1999).
27. S. J. Charles *et al.*, *Diamond and Related Materials* **11**, 681 (2002).
28. S. J. Charles *et al.*, *Journal of Applied Physics* **94**, 3091 (2003).
29. J. P. Goss *et al.*, *Physical Review B* **69**, 165215 (2004).
30. G. Davies *et al.*, *Physical Review B* **46**, 13157 (1992).
31. J. Goss, P. Briddon, *Physical Review B* **73**, 85204 (2006).
32. J. P. Goss, R. J. Eyre, P. R. Briddon, *Physica Status Solidi (B)* **245**, 1679 (2008).
33. C. Weigel *et al.*, *Physica Status Solidi (B)* **63**, 131 (1974).
34. X. Hu *et al.*, *Physica B: Condensed Matter* **327**, 39 (2003).
35. Y. Pogorelov, V. Loktev, *Physical Review B* **72**, 075213 (2005).
36. A. Gruber *et al.*, *Science* **276**, 2012 (1997).
37. Y. Dumeige *et al.*, *New Journal of Physics* **13**, 025015 (2011).
38. Y. Nishi, R. Doering, Eds., *Handbook of Semiconductor Manufacturing Technology* (CRC Press, ed. 2, 2007).
39. G. Davies, *Physics Reports* **176**, 83 (1989).
40. A. T. Collins, *Diamond and Related Materials* **1**, 457 (1992).
41. G. Davies, M. Crossfield, *Journal of Physics C: Solid State Physics* **6**, L104 (1973).
42. T. Evans, S. T. Davey, S. H. Robertson, *Journal of Materials Science* **19**, 2405 (1984).
43. D. Twitchen *et al.*, *Diamond and Related Materials* **8**, 1572 (1999).
44. A. T. Collins, presented at the 61st Diamond Conference, P5.
45. I. Kiflawi *et al.*, *Journal of Physics: Condensed Matter* **19**, 046216 (2007).
46. L. Allers, A. T. Collins, J. Hiscock, *Diamond and Related Materials* **7**, 228 (1998).
47. S. Dannefaer, K. Iakoubovskii, *Journal of Physics: Condensed Matter* **20**, 235225 (2008).
48. M. A. Lea-Wilson, J. N. Lomer, J. A. Van Wyk, *Philosophical Magazine Part B* **72**, 81 (1995).

49. C. D. Clark, R. W. Ditchburn, H. B. Dyer, *Proceedings of the Royal Society of London A* **237**, 75 (1956).
50. S. Dannefaer *et al.*, *Physica B: Condensed Matter* **308-310**, 569 (2001).
51. I. Kiflawi *et al.*, *Diamond and Related Materials* **6**, 146 (1997).
52. G. Davies, C. Foy, K. O'Donnell, *Journal of Physics C: Solid State Physics* **14**, 4153 (1981).
53. D. Twitchen, PhD thesis, University of Oxford, 1997.
54. J. Walker, *Journal of Physics C: Solid State Physics* **10**, 3031 (1977).
55. D. Wight *et al.*, *Journal of Luminescence* **4**, 169 (1971).
56. A. M. Zaitsev, *Optical Properties of Diamond* (Springer, 2001).
57. B. Dischler, *Handbook of Spectral Lines in Diamond* (Springer-Verlag, Berlin, 2012).
58. A. M. Zaitsev, *Physical Review B* **61**, 12909 (2000).
59. R. Brout, W. Visscher, *Physical Review Letters* **9**, 54 (1962).
60. T. Feng, B. D. Schwartz, *Journal of Applied Physics* **73**, 1415 (1993).
61. C. D. Clark *et al.*, *Physical Review B* **51**, 16681 (1995).
62. J. P. Goss *et al.*, *Physical Review Letters* **77**, 3041 (1996).
63. A. T. Collins, *Journal of Physics C: Solid State Physics* **11**, 2453 (1978).
64. K. P. O'Donnell, *Journal of Physics C: Solid State Physics* **13**, L363 (1980).
65. G. Davies, M. H. Nazaré, M. F. Hamer, *Proceedings of the Royal Society of London A* **351**, 245 (1976).
66. G. Davies, *Journal of Physics C: Solid State Physics* **12**, 2551 (1979).
67. A. T. Collins, *Journal of Physics: Condensed Matter* **14**, 3743 (2002).
68. H. B. Dyer, *British Journal of Applied Physics* **17**, 419 (1966).
69. A. Stoneham, *Materials Science and Engineering: B* **11**, 211 (1992).
70. J. Bourgoin, J. Corbett, *Physics Letters A* **38**, 135 (1972).
71. J. Goss *et al.*, *Physical Review B* **70**, 235208 (2004).
72. M. Gaukroger *et al.*, *Diamond and Related Materials* **17**, 262 (2008).
73. M. R. Brozel, T. Evans, R. F. Stephenson, *Proceedings of the Royal Society of London A* **361**, 109 (1978).
74. J. E. Butler *et al.*, *Semiconductor Science and Technology* **18**, S67 (2003).
75. C. Fernández-Lorenzo *et al.*, *Diamond and Related Materials* **19**, 904 (2010).

76. J. Barjon *et al.*, *Physical Chemistry Chemical Physics* **13**, 11511 (2011).

77. J. Kirui, J. van Wyk, M. Hoch, *Diamond and Related Materials* **8**, 1569 (1999).

78. B. Coomer *et al.*, *Physica B: Condensed Matter* **273-274**, 520 (1999).

79. J. van Wyk *et al.*, *Physical Review B* **52**, 12657 (1995).

80. G. Davies, *Nature* **269**, 498 (1977).

Chapter 6

The 1.913 eV centre in photoluminescence

6.1 Background

Upon both low and room-temperature electron irradiation of type IIb diamond, one of the least-studied luminescence lines visible immediately post-irradiation emits at 1.913 eV (648.2 nm). Previous reports on the transition come from a single group; the luminescence was reported following electron irradiation of type IIb synthetic samples grown by both HPHT and CVD methods [1]. The samples contained 0.5–50 ppm [$(B_s)^0$] and were irradiated with 5×10^{18}–5×10^{20} $e^- cm^{-2}$ at an energy of 200 keV: the 1.913 eV transition was visible post-irradiation [1].

From the limited data available, the intensity of the emission appears to increase linearly with electron dose in high-boron regions [2]. The authors note that under excitations of 2.71–2.41 eV the emission intensity increased as the temperature was lowered from 80 to approximately 7 K, indicating that the excited state of the 1.913 eV emission does not require thermal population. A strong dependence of the emission intensity on the incident laser power was observed suggesting that, for these excitation energies, the pumping mechanism is not straightforward.

A representative spectrum of the 1.913 eV emission is given in figure 6-1. High-frequency phonon coupling and an associated local mode are visible at 1.73–1.78 meV: these features are discussed further in §6.4.5.

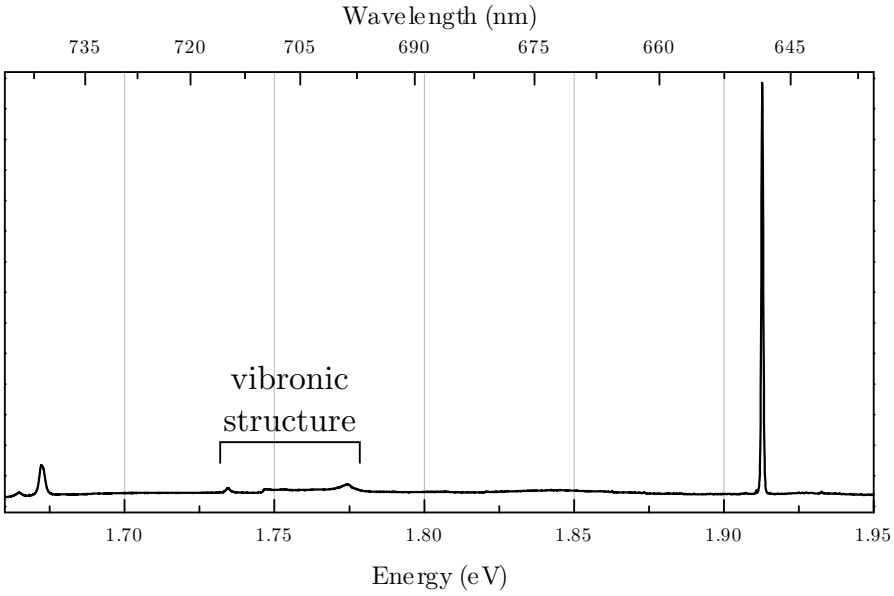

Figure 6-1 Representative photoluminescence spectrum of 1.913 eV emission from sample i. Measurement performed with sample held at 80 K and photoexcitation at 2.808 eV (441.6 nm). GR1 emission is visible at approximately 1.67 eV (741.1 nm); all other features belong to the emission at 1.913 eV.

6.2 Samples

The 1.913 eV emission has been investigated in natural samples, and HPHT and CVD-grown synthetic samples. Two natural samples exhibiting a strong 1.913 eV luminescence were chosen: both samples were heavily plastically deformed with strong slip bands along the ⟨1 1 1⟩ direction, as shown in figure 6-2.

Sample	Growth	$[(B_s)^0]$ (ppm)	Orientation
h	Natural	0.01	⟨0 0 1⟩, ⟨1 1 0⟩, ⟨1 $\bar{1}$ 0⟩
i	Natural	0.03	⟨1 1 1⟩, ⟨1 1 $\bar{2}$⟩, ⟨1 $\bar{1}$ 0⟩
e	HPHT	2.7	⟨0 0 1⟩, ⟨1 1 0⟩, ⟨1 $\bar{1}$ 0⟩
f	CVD	0.8	Grown on ⟨1 0 0⟩ substrate

Table 6-1 Details of the samples employed during the investigation of the 1.913 eV emission. Error in $[(B_s)^0]$ is approximately ±0.1 ppm, and was measured by IR absorption using the constants given in §5.3.1.

Measurements were also performed on two synthetic samples, to understand the annealing behaviour of the 1.913 eV emission and to aid in understanding of the physics at the defect centre (see §6.4.3.1). One sample was HPHT-grown (sample

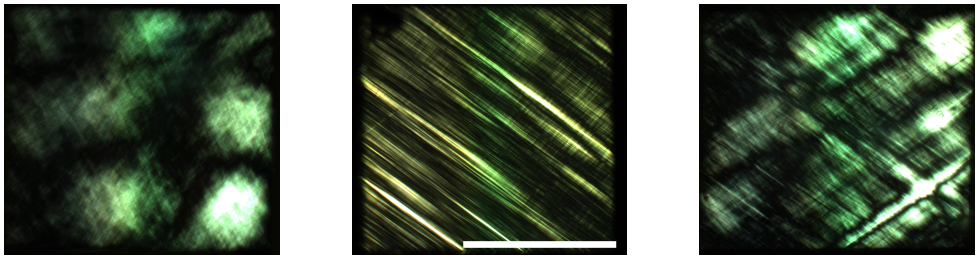

[0 0 1] [1 1 0] [1 $\bar{1}$ 0]

(a) Sample h, used for [0 0 1] stress measurements

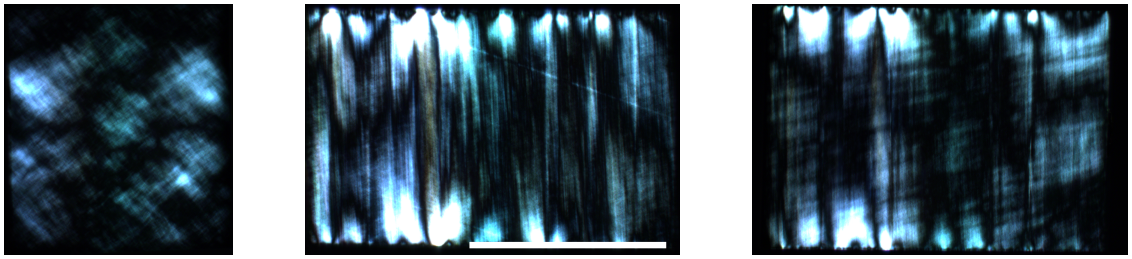

[1 1 1] [1 $\bar{1}$ 0] [1 1 $\bar{2}$]

(b) Sample i, used for [1 1 1], [1 $\bar{1}$ 0] stress measurements

Figure 6-2 The natural samples used in this investigation as viewed through crossed polarisers when illuminated with white light. In each case, the bar in the central image gives a scale for 1 mm.

e), and one CVD-grown (sample f). See table 6-1 for a summary of each sample.

6.3 Experiment

Samples e and f were irradiated at 100 K with 5×10^{17} e^- cm^{-2} at an electron energy of 2 MeV (see chapter 5). During the annealing study of last chapter, the 1.913 eV emission intensity was monitored in sample f to determine the annealing behaviour of the transition (see next section). Samples h and i had not been artificially irradiated but in common with virtually all natural diamonds, they had been exposed to small amounts of naturally-occurring radiation.

Uniaxial stress measurements were performed on samples h, i and e using a Renishaw inVia Reflex Raman spectrometer with photoexcitation at 2.808 eV (441.6 nm) and 1.959 eV (632.8 nm) combined with diffraction gratings of density 2400 l mm^{-1} and 1800 l mm^{-1} respectively. All uniaxial stress measurements were

performed between 4 and 100 K using the modified Oxford Instruments Optistat described in §4.3.

6.4 Results

6.4.1 Annealing

Sample f was annealed as per the procedure outlined in §5.2 in order to find the processing temperature which maximised the 1.913 eV emission. Each 14 h anneal was carried out under a non-oxidising atmosphere, with anneals taking place every 100 °C between 100–1000 °C (figure 6-3).

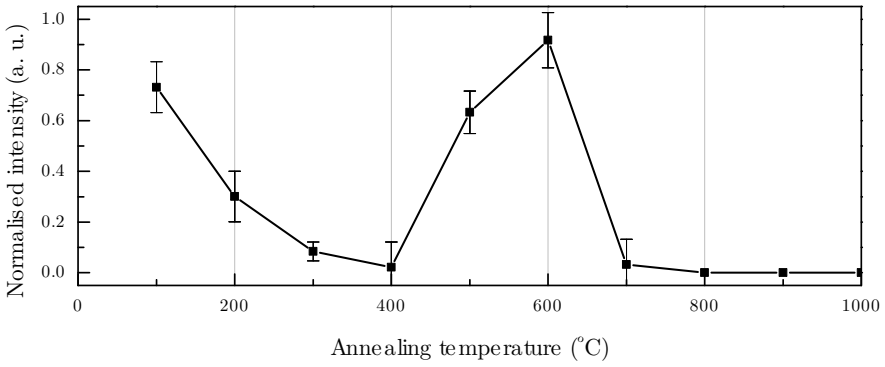

Figure 6-3 Normalised integrated intensity of the 1.913 eV emission at different annealing temperatures for sample f. Each 14 h was performed under a non-oxidising atmosphere. After each anneal, several photoluminescence measurements were performed. The integrated intensity of each scan was normalised by the first-order Raman line before being averaged together at each annealing temperature. All measurements were taken at the same incident laser power.

Luminescence at 1.913 eV was observed post-irradiation, becoming significantly weaker (relative to the first-order Raman scattering line) by 400 °C before reaching a maximum intensity at 600 °C. The line was undetectable at 800 °C. In this sample, the neutral vacancy annealed out at 700 °C. The observed annealing behaviour is not straightforward, and is discussed further at the end of the chapter (§6.6).

Sample e was annealed to 600 °C for 14 h to maximise 1.913 eV emission before uniaxial stress measurements were performed.

6.4.2 Uniaxial stress

Uniaxial stress measurements were performed with stress applied along ⟨0 0 1⟩ (sample h), ⟨1 1 1⟩ and ⟨1 1 0⟩ (sample i). The unusual decision to perform the ⟨1 1 0⟩ measurement on the sample with a ⟨1 1 1⟩ face (rather than the sample containing an ⟨0 0 1⟩ face) was taken due to the significantly higher intensity of 1.913 eV luminescence in this sample.

High-stress spectra for each applied stress direction are given in figure 6-4. For each stress direction, the shift rates of each of the stress-split components were found to be linear in terms of applied stress. The shift rates of all of the components in all applied stress directions were fitted simultaneously to each of the possible point group and transition symmetries using a least-squares procedure. The best fit was achieved for a transition at a monoclinic I centre (figure 6-5): the components are marked using the nomenclature of Davies [3] for uniaxial stress effects at a monoclinic I centre, and the parameters producing the best fit are given in table 6-2.

Parameter	Value (meV GPa^{-1})
A_1	−1.18
A_2	1.54
A_3	−1.23
A_4	±0.17

Table 6-2 Parameter values obtained by a least-squares fit of the stress-split components to the parameterised shifts expected at a centre of monoclinic I symmetry. Uncertainties in each case are approximately ±0.1 meV GPa^{-1}.

6.4.3 Dipole orientation & transition symmetry

Once the geometric symmetry of a defect has been determined, the next step in the physical investigation of a defect is to determine the orbital symmetry of the two states between which the transition occurs. In the case of monoclinic I, only two orbital symmetries are possible: $\mathbf{A}'$ & $\mathbf{A}''$.

For a point group symmetry which supports only non-degenerate orbital states,

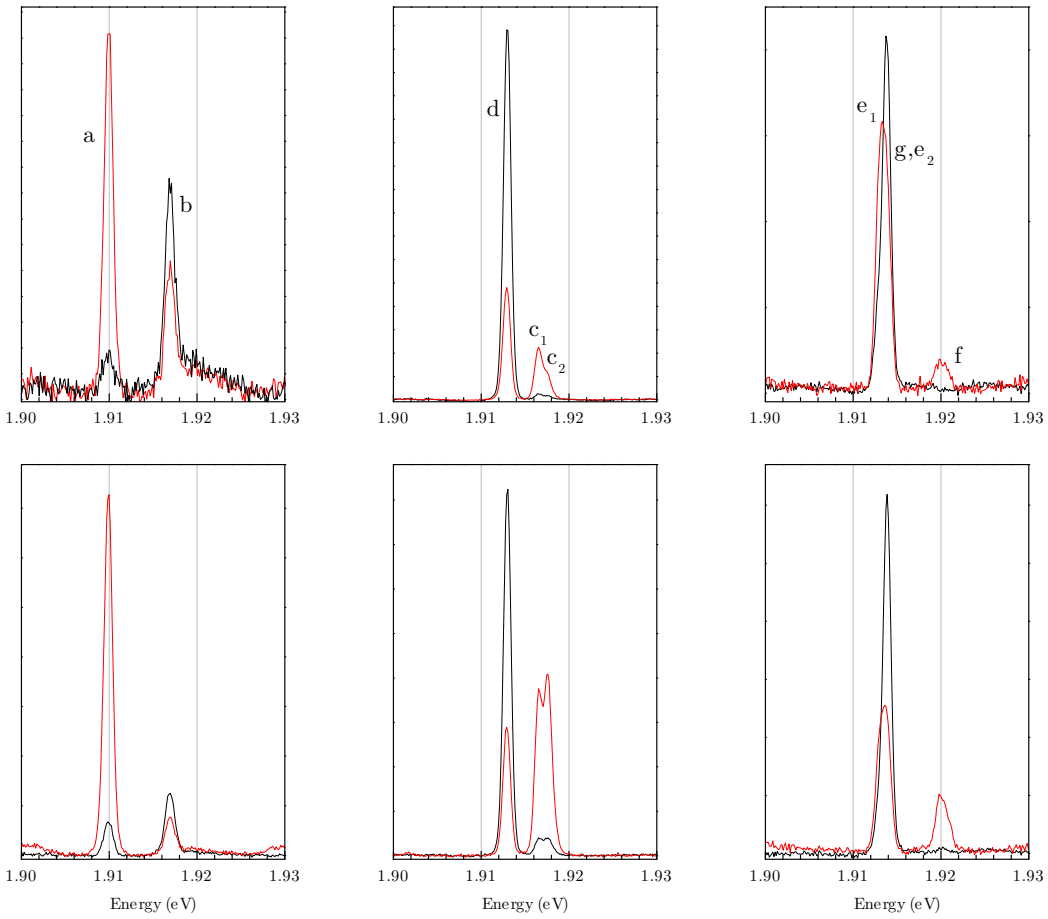

(d) [0 0 1], $\sigma \approx 2.5\,\mathrm{GPa}$ **(e)** [1 1 1], $\sigma \approx 2.7\,\mathrm{GPa}$ **(f)** [1 $\bar{1}$ 0], $\sigma \approx 3.0\,\mathrm{GPa}$

Figure 6-4 High-stress spectra of the 1.913 eV luminescence. All spectra were obtained using a HeNe laser operated at 1.959 eV (632.8 nm) at $T = 80\,\mathrm{K}$. The top row contains spectra taken with $\boldsymbol{i}_{\parallel}$, and the bottom row, $\boldsymbol{i}_{\perp}$. The spectra are black and red for detection parallel and perpendicular to the stress axis, respectively. The letters identify each stress-split component as described in table 6-3. No correction has been made for losses due to the introduction of waveplates into the incident and detection beams.

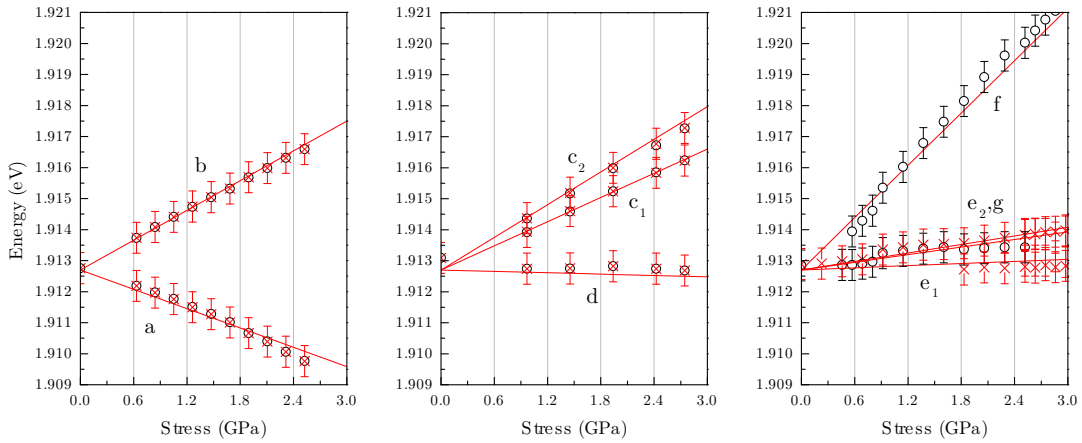

(a) [0 0 1] **(b)** [1 1 1] **(c)** [1 $\bar{1}$ 0]

Figure 6-5 Results of uniaxial stress measurements performed on the 1.913 eV feature in photoluminescence. The data measured with $\boldsymbol{i}_{\parallel}$ are given by ◯; data measured with $\boldsymbol{i}_{\perp}$ are denoted by ×. The lines give the best fit of monoclinic I theory using the parameters given in table 6-2.

state symmetry determination is performed by comparing measured relative intensities to predicted relative intensities. For transitions between states of like symmetry, the associated electronic dipole is oriented along the Z-axis of the defect; for transitions between unlike states the dipole may be oriented anywhere in the XY (1 1 0) plane. In the former case, relative intensities are determined uniquely (assuming equal populations for all sites) and given in table 3-10. However, in the latter case, the emission intensities of different stress-split transitions will change smoothly as a function of dipole orientation.

It is evident from the measured intensities given in table 6-3 that the observed values do not correspond to the Z case. A small computer program was written in order to investigate the theoretical emission intensities arising from a dipole oriented anywhere in the (1 1 0) plane of symmetry for each site: no dipole orientation satisfactorily reproduced the intensities observed in the two natural samples.

There are a number of physical reasons why these simple models may not predict the observed emission intensities [4]:

Phonon interactions in the excited state If a phonon of a given symmetry interacts with the excited electronic state, the dipole by which the centre

absorbs the incident energy may not be the same dipole through which the centre emits. This may result in e.g. absorption at a Z dipole, with emission at an XY dipole (and vice versa); or absorption at an XY dipole, with emission by a differently-orientated XY dipole.

Non-equilibrium site populations The emission and absorption by each site will simply be scaled by the relative site population.

Absorption and emission occur at different defects If the centre is excited by emission from another colour centre, rather than directly by the incident laser light, then the input E-field orientation is unknown (and almost certainly is not a single linearly polarised field due to different centre orientations, relative positions etc.).

Excited state population via conduction band If the photoexcitation is significantly higher in energy than the emission energy of the centre, then the excited state may be populated via ionisation of an unrelated defect into the conduction band, with the electron relaxing back by emission at a different centre.

Centre reorientation After excitation, the centre reorientates to an equivalent orientation before emission.

Stress-induced reorientation If the barrier to centre reorientation is low, then the centre may reorientate itself away from the axis of applied stress: this will manifest as a change in relative intensity of at least two transitions as a function of stress.

Short-range resonance Excitation of the centre occurs through a short-range resonance mechanism with a nearby defect which directly absorbs the incident light.

Birefringence Rotation of the electric field polarisation vector as it propagates through the material.

If the experimentally observed intensities are compared against those given in table 3-10, it is evident that the simple theoretical cases are unsatisfactory fits to

the experimental data, even when preferential orientation is taken into account. Of the other processes which may be taken into account during the simulation, several lead to problems which are impracticable e.g. including multiple incident dipoles of arbitrary orientation essentially gives an infinite problem space, and many of the solutions will bear no relation to the processes occurring inside the material. Short-range resonance effects may be neglected due to low absolute density of observed defects in these samples. The interaction of phonons in excited electronic state, however, is a process intrinsic to the centre that potentially leads to real physical insight and occurs within a finite problem space. Therefore, a consistent solution would be one which involves an identical excited state phonon interaction across samples, but which potentially incorporates different site populations due to the nature of the plastic deformation in each of the samples.

6.4.3.1 Uniaxial stress measurements of the HPHT-grown sample

The heavy plastic deformation present in the natural samples (see figure 6-2) can significantly complicate the analysis of uniaxial stress data, as discussed above. In order to first understand the processes intrinsic to the centre, without also trying to take into account the added complexity of strain, uniaxial stress measurements were performed on the HPHT-grown sample (sample e). The stress was applied along the $\langle 0\,0\,1 \rangle$ direction: a comparison of the transition splitting rates in the natural and synthetic sample is given in figure 6-6.

The relative intensities of the $\langle 1\,0\,0 \rangle$ results from the HPHT-grown sample (sample e) were fitted assuming that all sites were populated equally, and allowing the absorption and emission dipoles to rotate independently. A map of the residual sum of squares is given in figure 6-7, and shows minima at $\pm 52^\circ$ and $\pm 70^\circ$ for the absorption and emission dipoles, respectively. The corresponding relative intensities are given in the top row of table 6-3, and are a perfect fit to within the combined errors imposed by experimental setup and fitting procedures. The 1.913 eV emission is therefore a transition between states of $\mathbf{A}'$ and $\mathbf{A}''$ orbital symmetry.

Using the dipole orientation results from the synthetic sample, interpretation of

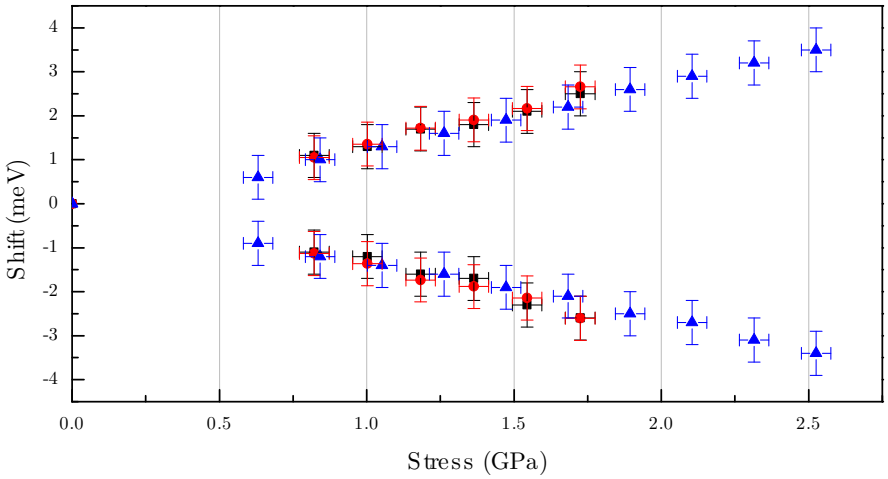

Figure 6-6 Shift rates of the 1.913 eV emission line in a natural sample (sample h, ▲) and an HPHT-grown sample (sample e, ●). The shift rate of the associated 178.2 meV local mode (see §6.4.5) as measured in sample e is indicated by ■. Best fit lines have been omitted for ease of comparison.

the measurements on the natural samples was reattempted. The problem was formulated as an input for the genetic algorithm optimiser `ga` built into the software environment MATLAB[1]. The absorption and emission dipoles were fixed to the values gained from the synthetic sample, and the population for each of the twelve sites was varied between the bounds of 0 & 1 independently for each sample. At each test point, the sum of squares was computed between the normalised experimental values and the output from the search algorithm. The best fits for the ⟨0 0 1⟩ & ⟨1 1 1⟩ directions are given in table 6-3. It should be noted that if the absorption and emission dipoles were allowed also to vary, the best fit was achieved within 10° of each dipole obtained from the synthetic sample results.

Even in the case that the absorption and emission occur from dipoles with different orientations in each sample, the fit to the experiment is still unsatisfactory. There are, therefore, one or more processes which have not been taken into account and which have a significant effect on the observed intensities.

[1]MATLAB version 8.0, `www.mathworks.com`

$\boldsymbol{\sigma}$	Component	Measured ($\mathrm{meV\,GPa^{-1}}$)	Theoretical shift rate	Best fit ($\mathrm{meV\,GPa^{-1}}$)	Measured intensities $\boldsymbol{i}_{\parallel}$ $d_{\parallel} : d_{\perp}$	Measured intensities $\boldsymbol{i}_{\perp}$ $d_{\parallel} : d_{\perp}$		Theoretical intensities $\boldsymbol{i}_{\parallel}$ $d_{\parallel} : d_{\perp}$	Theoretical intensities $\boldsymbol{i}_{\perp}$ $d_{\parallel} : d_{\perp}$
Sample e (synthetic)									
$\langle 0\,0\,1\rangle$	a	−1.40	A_1	−1.18	2.3 : 9.2	1.5 : 6.2		2.1 : 8.9	1.4 : 6.1
	b	+1.51	A_2	+1.54	13.1 : 8.6	12.1 : 7.7		13.1 : 9.2	12.1 : 7.7
Sample h (natural)									
$\langle 0\,0\,1\rangle$	a	−1.21	A_1	−1.18	0.7 : 4.6	2.3 :22.5	[a]	0.8 : 4.6	4.2 : 22.5
	b	+1.50	A_2	+1.54	2.7 : 1.7	4.2 : 2.5		2.7 : 2.4	2.8 : 1.9
Sample i (natural)									
$\langle 1\,1\,1\rangle$	d	−0.15	$\frac{1}{3}(A_1 + 2A_2 + 2A_3)$	−0.19	45.0 :13.1	22.5 : 7.9		45.0 :13.1	22.5 : 12.9
	c_1	+1.30	$\frac{1}{3}(A_1 + 2A_2 - 2A_3 - 4A_4)$	+1.23	0.7 : 5.2	0.9 : 8.1	[b]	0.0 : 0.0	0.0 : 0.0
	c_2	+1.64	$\frac{1}{3}(A_1 + 2A_2 - 2A_3 + 4A_4)$	+1.68	0.5 : 3.8	1.3 :12.9		0.1 : 0.0	0.2 : 0.0
$\langle 1\,1\,0\rangle$	g	+0.30	$A_2 + A_3$	+0.31	15 :15	15 : 8			
	e_1	+0.02	$\frac{1}{2}(A_1 + A_2 - 2A_4)$	+0.01	2 :17	0 :15	[c]	Not computed due to unsatisfactory fit in $\langle 1\,1\,1\rangle$ direction.	
	e_2	+0.35	$\frac{1}{2}(A_1 + A_2 + 2A_4)$	+0.35	39 :24	61 :22			
	f	+3.00	$A_2 - A_3$	+2.78	0 : 7	0 :17			

Table 6-3 Measured transition shift rates and intensities compared to the theoretical values (using parameters given in table 6-2). Components are those given in figure 6-5, but the order used in §3.9 has been followed for ease of comparison. Theoretical best fit values were calculated with absorption and emission dipoles along approximately $\langle 1\,1\,1\rangle$ and $\langle 5\,5\,3\rangle$, with site populations in each case given below.

[a] Site populations: [0.27, 0.99, 0.44, 1.00, 0.02, 0.90, 0.70, 0.00, 0.84, 0.04, 0.18, 0.68].
[b] Site populations: [0.01, 0.00, 0.00, 0.00, 1.00, 0.00, 1.00, 0.04, 0.00, 1.00, 0.01, 1.00].
[c] Only two significant figures have been given here, due to the difficulty of attempting to fit three overlapping components (see figure 6-5).

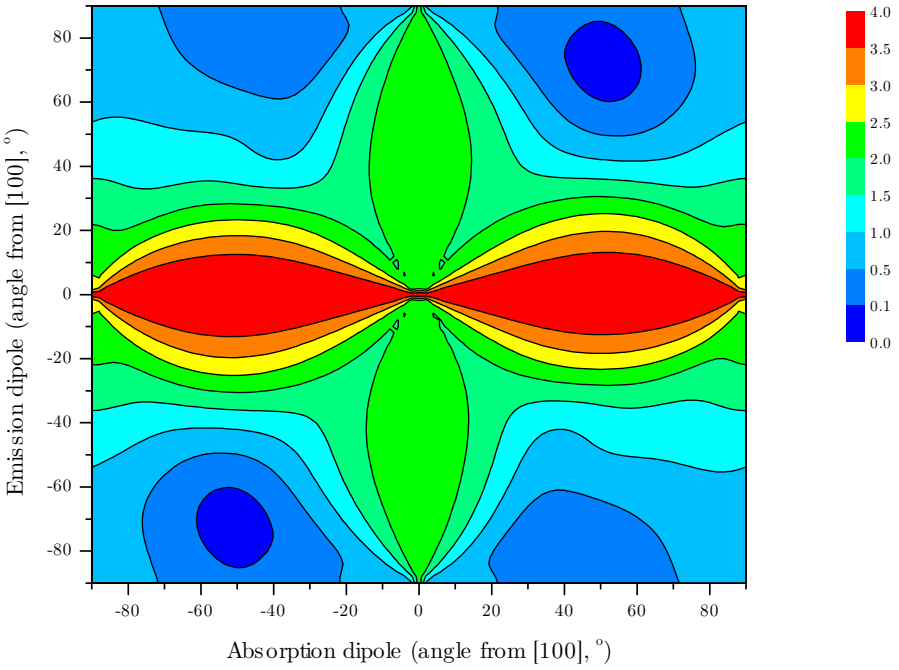

Figure 6-7 Contour plot of the sum of squares between the experimentally observed relative intensities of sample e under stress, and their theoretical values at various dipole angles. The best fit is found at absorption and emission dipoles of ±52(5)° and ±70(5)° from [0 0 1] in a [1 1 0] plane, respectively.

6.4.4 Linewidth

A difference in the 1.913 eV luminescence linewidth was noted between the two natural samples and the two synthetic samples: the luminescence from the synthetic samples was approximately a factor of 2.5 times smaller in linewidth. In turn, fine structure was resolved in the synthetic samples which was obscured by the broad linewidth in the natural samples — a small shoulder is visible to the high-energy side of the emission from the two synthetic samples (figure 6-8). Assuming identical linewidths, the ratio of the integrated intensity of these two lines is 4.5(5). Additionally, the splitting and relative heights of these two lines is identical across two synthetic samples produced by different synthesis methods (CVD and HPHT), and across all annealing temperatures encountered: this suggests that this split is a property of the defect centre itself, rather than being due to random strain or another defect centre with similar emission energy. Furthermore, the fact that the transition occurs between orbitally non-degenerate states precludes the presence of Jahn-Teller effects in the ground state, and close-lying

states may be excluded due to the linear response as a function of stress and lack of observed thermalisation.

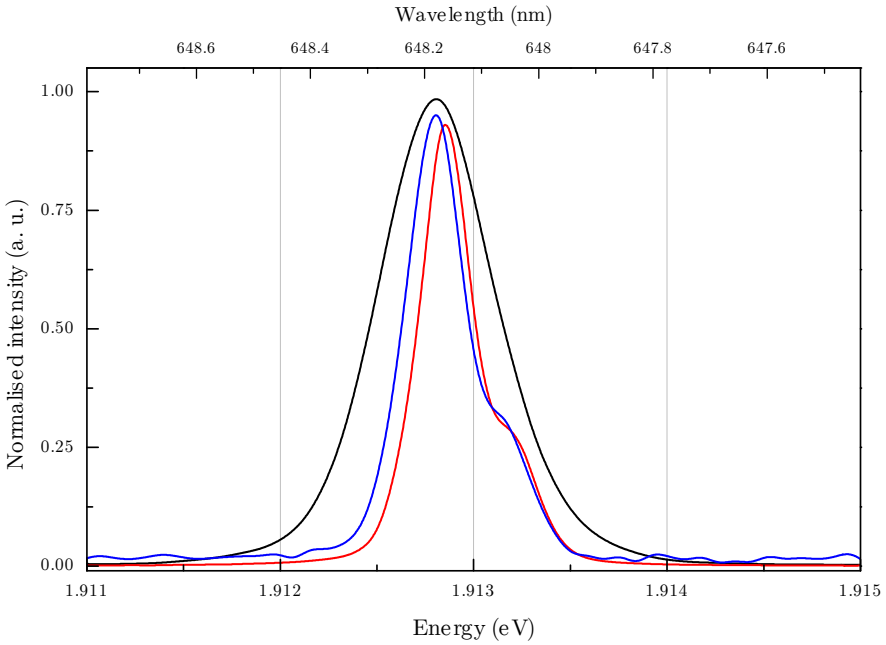

Figure 6-8 The 1.913 eV emission in natural sample i (black, largest linewidth) and synthetic samples e and f.

As mentioned in §6.1, 1.913 eV is only encountered in type IIb material. The relative natural abundances of ^{10}B:^{11}B are 1:4 respectively [5] — it is not unreasonable, therefore, to suggest that the optical fine structure is due to emission at centres with identical atomic configurations but containing different boron isotopes. If this is the case, the simple relationship between the isotopic content and optical properties would be a reflection of the fact that the transition occurs between orbitally non-degenerate states.

Isotopic effects on impurity-related defect states have been demonstrated in diamond previously [6] for isotopes of silicon [7], nickel [8] and nitrogen [9]. The observed splitting of $-0.4(1)$ meV, if an isotope effect, is noteworthy as it would be a negative shift for a lighter isotope — the simple anharmonic theory usually employed (see §4.1.1.3) can account only for a positive shift. (It is convention to describe a shift as positive if the transition energy increases with the substitution of a heavier isotope.) Negative shifts are uncommon but not unprecedented [10, 11]: a detailed account of the calculation of a negative shift is given in [12], but requires detailed knowledge of the ZPL transition energy as a function of

temperature.

In order to determine definitively whether the observed optical fine structure is an isotopic effect, synthetic samples with modified isotopic boron ratios are required: 1:1 or 1:0 ^{10}B:^{11}B, for instance. Unfortunately, such samples are expensive and time-consuming to produce, and none were made available during the course of these experiments.

6.4.5 Local vibrational mode

The electron-phonon coupling at the 1.913 eV emission is weak (small Huang-Rhys factor) as evident in the representative spectrum of figure 6-1. However, the coupling that is present is to high-frequency modes (figure 6-9), including a local mode at 178.2 meV (1437 cm^{-1}).

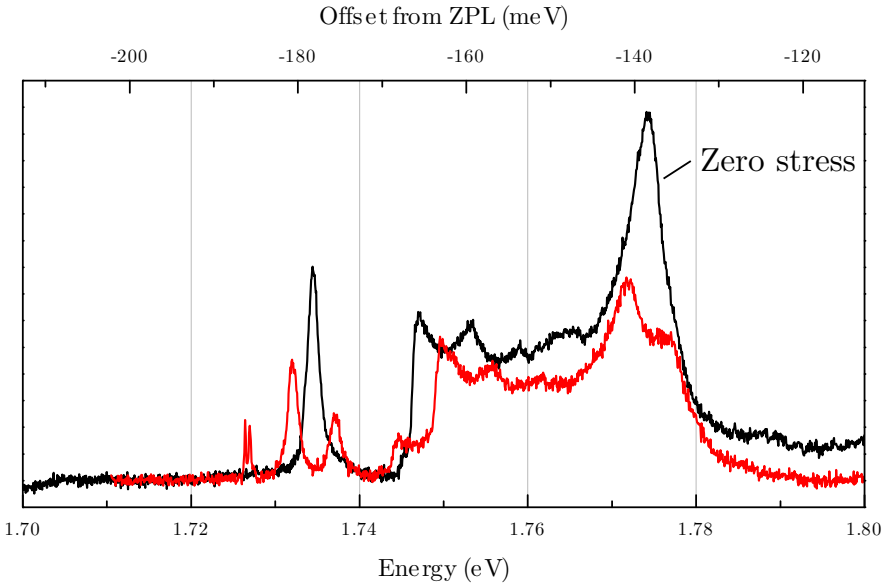

Figure 6-9 High-frequency vibronic modes and local mode associated with the 1.913 eV emission, measured in sample e with applied stresses of 0 and 1.73(5) GPa. The low-energy doublet at high stress is unrelated to 1.913 eV.

During the uniaxial stress measurements on the HPHT-grown sample, sample e, the energy shifts of the LVM were recorded in addition to the shifts of the ZPL (see figure 6-6). The energy shifts as a function of applied stress were identical to the shifts measured for the ZPL, as expected for an LVM at a low-symmetry centre

[13]. Additionally, the relative intensities under different incident and detection polarisations matched those for the ZPL: the mode therefore has symmetry $\mathbf{A}'$ and is a totally symmetric vibration.

If the local mode involved the motion of a boron atom, then one would expect to see two modes, whose relative frequencies are roughly the square root of the ratio of the boron isotopes ($(10/11)^{1/2}$) [14] (see §4.1.2). The higher frequency mode (observed, at 1437 cm^{-1} (178.2 eV)) would belong to ^{10}B, placing the ^{11}B mode at approximately 1370 cm^{-1} (170 meV): this mode is not observed.

6.5 Stress measurements on natural samples

As discussed previously, the use of natural samples for uniaxial stress measurements can significantly complicate analysis. When the end goal is gem history discrimination, it is these very difficulties which are useful and may aid in future identification: however, when investigating a new system it is advantageous to simplify the problem as far as possible.

In addition to the problems associated with loss of polarisation information in highly strained samples, the strain may also be of the order of the applied stress (in an unknown or random direction) and hence quantitative analysis may be impossible. This effect is compounded by the practicalities of the experiment: as higher stresses are applied to the samples, the silvered steel anvils deform and the sample moves relative to the microscope objective collecting the luminescence. In the case that the strain is inhomogeneous, dramatically different spectra can be recorded for only modest changes in applied stress.

An illustration of the effect of internal strain in natural samples is shown in figure 6-10. The luminescence line being mapped is at 2.526 eV (490.8 nm), a luminescence line which is strongly related to slip bands and plastic deformation in natural type IaB and type IIa samples [15–17].

Example spectra from different points on the same sample (at zero applied stress) are given in figure 6-11. For this emission, the observed splittings of approximately

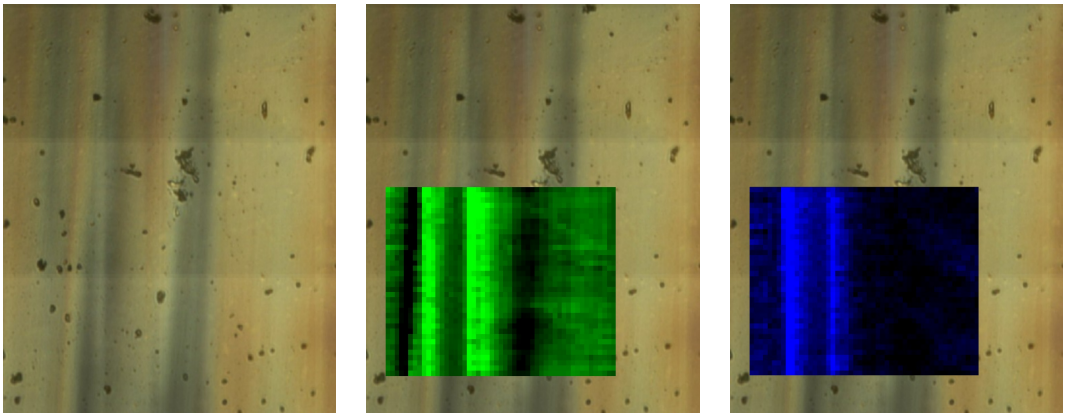

(a) White light

(b) Centroid. Dark to light: 2.527–2.524 eV (490.7–491.2 nm)

(c) Linewidth. Dark to light: 2.6–6.7 meV (0.5–1.3 nm)

Figure 6-10 Photoluminescence map of the 2.526 eV (490.8 nm) emission line with no applied stress. Left to right: under crossed polarisers and illuminated with white light; a map of the central emission energy (wavelength); and a map of the emission linewidth. The mapped area is approximately 200 × 145 µm. All scans taken with the sample held at 153 K (−120 °C); the flecks are small ice crystals.

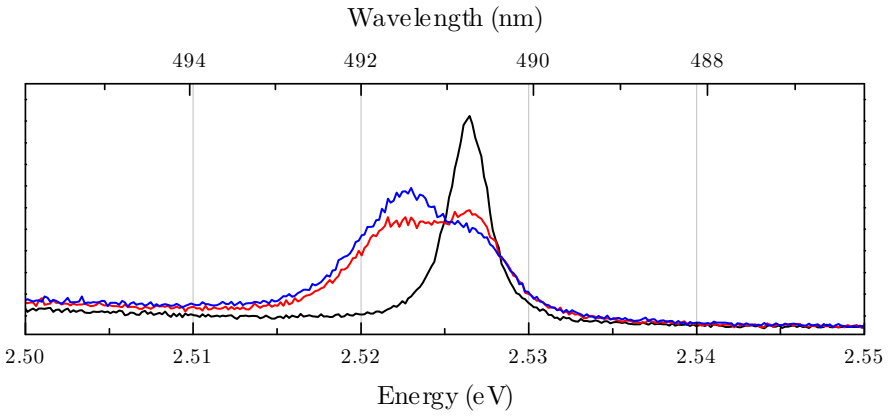

Figure 6-11 Comparison of 2.526 eV (490.8 nm) spectra taken at different points in the same sample (figure 6-10). The sample was held at 153 K (−120 °C) and with no applied stress.

0.5 meV would correspond to applied stresses of the order of 1.3 GPa according to the data in [16] and independently verified by the author. The strain at the defect appears to be anisotropic: randomly oriented strain would manifest simply as a broadening of the line, rather than splitting.

During a uniaxial stress measurement on such a sample, the sample would move underneath the microscope objective as stress were applied, and the measurements

would be sampling different configurations of local strain, significantly complicating any quantitative analysis. As shown by the study on the 1.913 eV emission, the production of a line of interest in a synthetic, high crystalline quality sample can be instrumental in trying to understand the physics of a defect centre.

6.6 Discussion

The 1.913 eV emission is observed only in samples which contain boron, and can be produced upon electron irradiation at both room temperature and liquid nitrogen temperature. Using arguments similar to those given in the previous chapter (§5.5), the latter observation is suggestive of a complex which is formed by the migration of high-mobility interstitials. The post-irradiation annealing behaviour of the 1.913 eV transition, shown in figure 6-3, consists of three distinct regions: a gradual decrease between 0–400 °C; a dramatic increase to maximum intensity at 500–600 °C; and then loss of the transition at 700 °C.

The slow decrease in intensity between the processing temperatures of 100–400 is well fitted by a single exponential decay, as might be expected for a thermally activated process such as charge transfer between traps. Simple chemical kinetic processes, such as those encountered in the previous chapter for e.g. vacancies, figure 5-19, usually result in abrupt changes of intensity when anneals as long as 14 h are employed. However, if the kinetic process involved were second-order or higher (see §4.6), and the reactants were of low concentration, then slow changes in intensity as a function of annealing temperature would be expected.

The intensity increase of 1.913 eV at 500 °C is above the migration temperature of the self-interstitial $I_{\langle 0\,0\,1\rangle}$, which is expected to migrate significantly during 14 h anneals at 300 and 400 °C (using a migration energy of 1.6 eV [18, 19]). 500 °C is also below the vacancy migration temperature in that sample, measured at approximately 700 °C in the previous chapter (figure 5-6). Several interstitial-related defects in the previous chapter, namely 2.519 and 1.693 eV (492.2 and 732.3 nm, respectively), achieved maximum intensity after annealing at 400 °C before destruction after a 500 °C anneal (see 5-10). If the increase in 1.913 eV

intensity at 500 °C is a structural change (rather than a charge state change) it is therefore consistent with an interstitial-related process, and with the initial suggestion that the production of 1.913 eV during irradiation was by interstitial migration.

Finally, the destruction of the 1.913 eV transition at an annealing temperature of 700 °C coincides with the migration of vacancies: its destruction is therefore assumed to proceed by vacancy capture. At no annealing stage was the 1.913 eV transition visible in optical absorption, and nor has it been reported in the literature. It is possible that the excited state of 1.913 eV is populated by (non)radiative decay of another defect / transition, but the visibility of 1.913 eV under photoexcitation at 1.959 eV (632.8 nm) narrows the possible absorption transition to a window of approximately 50 meV. However, the simple explanation is that the defect responsible for the 1.913 eV emission is present in too low concentrations to be visible by absorption measurements.

The production of the 1.913 eV transition appears to be dependent on the presence of boron in the sample. The requirement for boron may be indirect e.g. a charge state effect, or the defect may directly incorporate boron as part of its atomic structure. The high-energy shoulder observed in the two synthetic samples may be taken as weak evidence for the involvement of boron as a component in the defect producing the emission, but further experiments are required before any such conclusion is reached.

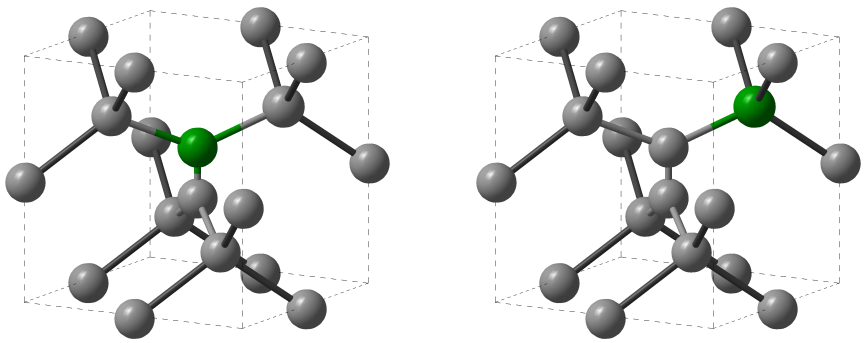

(a) $\mathscr{C}_{2v}$ **(b)** $\mathscr{C}_{1h}$

Figure 6-12 Two possible configurations for a B-interstitial complex. In each case, the symmetry of the structure is given.

According to DFT calculations [20], an interstitial complex which contains one interstitial and one boron atom is stable in one of the two structures given in figure 6-12. In particular, the configuration in figure 6-12b has the same symmetry as the defect producing the 1.913 eV emission. Furthermore, the absorption dipole for this centre should be oriented approximately along $\langle 1\,1\,1 \rangle$, as observed in the synthetic sample. Finally, theoretical calculations of this model predict a local mode within $10\,\mathrm{cm}^{-1}$ of the $1437\,\mathrm{cm}^{-1}$ mode observed at this centre [21]: further predicted (very high frequency) modes would be buried under other photoemission from unrelated defects in these samples.

No EPR centre is associated with the 1.913 eV emission, and no optical absorption has ever been reported. The most powerful technique for gaining further information on the centre producing the luminescence is isotopic enrichment. Boron isotopic enrichment would prove or disprove the existence of an isotope-dependent emission energy, and 1:1 ^{12}C:^{13}C enrichment would indicate the number of carbon atoms participating in the local mode.

6.7 Conclusion

The 1.913 eV (648.2 nm) luminescence transition has been investigated in several type IIb samples. Its annealing behaviour in a CVD-grown electron-irradiated sample was measured, and its intensity was found to be maximised by a 14 h anneal at 600 °C.

Uniaxial stress measurements on two heavily plastically deformed natural type IIb samples determined the symmetry of the centre producing the 1.913 eV emission as monoclinic I, $\mathscr{C}_{1\mathrm{h}}$. A numerical investigation into the dipole orientation of the transition was unable to satisfactorily fit the experimental data. Possible physical reasons for the lack of agreement have been discussed.

Uniaxial stress measurements on an electron-irradiated and annealed synthetic sample were consistent with the $\mathscr{C}_{1\mathrm{h}}$ symmetry assignment. The lack of internal strain in this sample allowed the orientation of the absorption and emission dipoles to be ascertained. The absorption and emission dipoles were measured as $\pm 52(5)^\circ$

(approximately $\langle 1\,1\,1 \rangle$) and $\pm 70(5)^\circ$ (approximately $\langle 5\,5\,3 \rangle$) from $[0\,0\,1]$ in a $[1\,1\,0]$ plane, respectively. In turn, this identifies 1.913 eV as a transition between states of orbital symmetry $\mathbf{A}'$ & $\mathbf{A}''$.

The local mode at 178.2 meV (1437 cm^{-1}) associated with the 1.913 eV was studied by uniaxial stress measurements on the HPHT-grown sample. The mode was found to have $\mathbf{A}'$ symmetry.

The linewidth of 1.913 eV in the CVD and HPHT-grown samples was found to be approximately a factor of 2.5 smaller than in the natural samples. Consequently, fine structure in the ZPL was resolved, with two components visible at a ratio of 4.5(5):1. It is suggested that this may be an isotopic effect due to boron, which is present in the ratio ^{11}B:^{10}B of 4:1.

Finally, the potential problems of performing uniaxial stress on highly strained samples have been discussed. An illustrative example of a transition at 2.526 eV (490.8 nm) was given, and internal strains of the order of 1.3(5) GPa identified.

Future studies on the 1.913 eV transition would ideally involve samples with modified boron and carbon isotopic ratios to determine the atoms contributing to the local vibrational mode, and to check whether the ZPL fine structure is an isotope effect.

References

1. J. W. Steeds *et al.*, *Acta Materialia* **47**, 4025 (1999).
2. S. J. Charles *et al.*, *Journal of Applied Physics* **94**, 3091 (2003).
3. G. Davies *et al.*, *Physical Review B* **35**, 2755 (1987).
4. C. D. Clark, G. W. Maycraft, E. W. J. Mitchell, *Journal of Applied Physics* **33**, 378 (1962).
5. M. E. Wieser, M. Berglund, *Pure and Applied Chemistry* **81**, 2131 (2009).
6. G. Davies, *Physica Scripta* **T66**, 113 (1996).
7. C. D. Clark *et al.*, *Physical Review B* **51**, 16681 (1995).
8. M. Nazaré, A. Neves, G. Davies, *Physical Review B* **43**, 14196 (1991).
9. G. Davies *et al.*, *Journal of Physics: Condensed Matter* **9**, 3871 (1997).
10. P. Dahan *et al.*, *Physical Review B* **57**, 9690 (1998).
11. B. Campbell, PhD thesis, King's College London (University of London), 2004.
12. A. T. Collins *et al.*, *Journal of Physics C: Solid State Physics* **21**, 1363 (1988).
13. S. C. Lawson *et al.*, *Journal of Physics: Condensed Matter* **4**, 3439 (1992).
14. A. T. Collins, G. S. Woods, *Journal of Physics C: Solid State Physics* **20**, L797 (1987).
15. A. T. Collins, G. S. Woods, *Philosophical Magazine Part B* **45**, 385 (1982).
16. M. Nazaré, G. Woods, *Materials Science and Engineering* **1**, 341 (1992).
17. A. Collins, H. Kanda, H. Kitawaki, *Diamond and Related Materials* **9**, 113 (2000).
18. L. Allers, A. T. Collins, J. Hiscock, *Diamond and Related Materials* **7**, 228 (1998).
19. M. Newton *et al.*, *Diamond and Related Materials* **11**, 618 (2002).
20. J. Goss, P. Briddon, *Physical Review B* **73**, 85204 (2006).
21. J. Goss, private communication.

Chapter 7

Nitrogen aggregates in ^{15}N-doped synthetic diamond

Nitrogen isotopic substitution can be a powerful technique: it has been employed to study isotope shifts of ZPLs and LVMs in order to identify spectral features which are directly related to nitrogen [1–4]. In EPR, it has the potential to be instrumental in the understanding of a defect — isotopic substitution of ^{15}N for ^{14}N removes the quadrupole interaction (see §4.4) and hence can substantially simplify the resulting spectrum [5–7].

General isotopic enrichment is a well-established technique in the study of defects in diamond: nitrogen enrichment has been employed for over 30 years [2, 8]; carbon enrichment for a similar period [1, 9, 10]. Carbon isotopic enrichment is now relatively routine in CVD-grown material for quantum computing applications, where the reduction in nuclear spin density by growing a host lattice of 100 % ^{12}C can significantly increase spin-spin relaxation times [11, 12]. In contrast, nitrogen isotopic enrichment in CVD material is less common [13], and high nitrogen concentrations present significant challenges.

The addition of small amounts of nitrogen (up to approximately 100 ppm) into the source gasses during the growth phase of CVD diamond is well-known to increase the diamond growth rate by up to approximately a factor of three [14, 15], in addition to having a positive effect on growth morphology [16]. However, high nitrogen

concentrations in the gas phase are known to promote non-diamond growth, with sample morphology becoming a major concern [17, 18]. The incorporation efficiency of nitrogen (probability of being incorporated onto the surface relative to a carbon) is between 10^{-5}–10^{-4} [13, 14], so that doping in the region of hundreds of ppm requires very high nitrogen concentration in the gas phase.

All of the samples used in this chapter were grown using the HPHT temperature-gradient method [19, 20]. The isotopic enrichment was performed by the method given in a 2006 patent [21], and the relevant parts will be summarised here with reference to figure 7-1.

7.1 Synthesis of diamond in a highly-controlled atmosphere

Initially, the carbon source (1) and solvent/catalyst (2) are heated to 1100 °C in a high-vacuum furnace (4×10^{-6} mbar) for 6–48 h in order to outgas the growth materials. Careful consideration must be given to the carbon source, as the outgassing process will remove only materials which are adsorbed onto the surface, and not those which are locked into the matrix of the material: for instance, any nitrogen contained in diamond grit which is then used as a carbon source will be incorporated into the new material.

The source materials, once cooled, are transferred to an adjoining argon-filled glove box. The carbon source and solvent/catalyst are pressed into cylinders and placed into a pyrophyllite (aluminium silicate hydroxide) tube (4), and then each end plugged with pyrophyllite discs (3,7). One of the discs (3) is drilled in order to seat several seed crystals at the bottom of the capsule. The pyrophyllite assembly is then inserted into a tantalum cup (5) and lid (6). Finally, vacuum braze wire is placed along the seam between cup and lid (8) and a small circle is placed on the top of the lid (9).

The entire assembly is transferred in an argon-filled sealed box to a brazing furnace, where it is heated to above the melting point of the braze wire under high

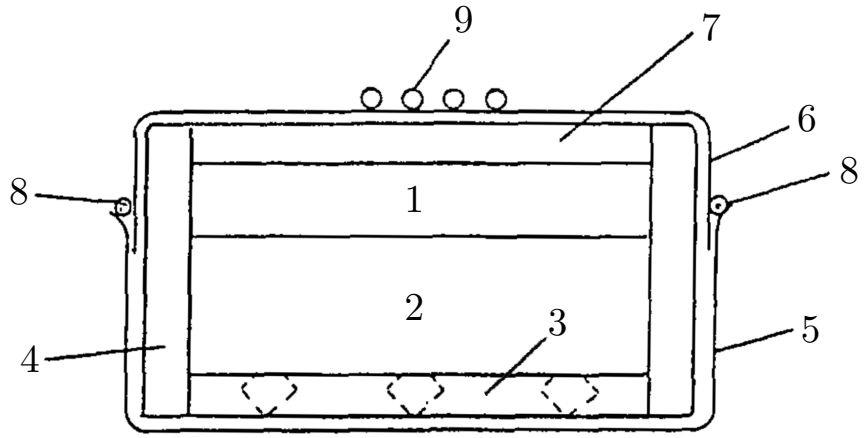

Figure 7-1 The sealed growth capsule used for synthesis of diamond with a high degree of control over elemental impurities. See text for a description of the capsule. Adapted from the original patent [21].

vacuum (7×10^{-6} mbar). Upon cooling, the cup and lid are hermetically sealed together, and a circle of braze persists on the top of the lid. At this point, the capsule is free from undesirable gasses and is sealed against further atmospheric ingress; the desired process gasses must now be introduced into the capsule without contamination.

A small ring of low-temperature solder is placed on the top of the brazed section of the lid (9), and the sealed assembly is transferred into a specially-designed chamber held at 50 °C, with valves for vacuum pumps and gas filling. A backing gas (methane) is used to purge the chamber of atmosphere, before the desired process gas (in this case $^{15}N_2$) is introduced to a pressure of 1 bar. The brazed section of the lid of the capsule is pierced with a sharpened steel rod, and the uptake of the gas into the capsule is monitored by means of a high-precision manometer and allowed to equilibriate for 1 h. Finally, a resistive heating element is used to melt the solder and seal the top of the capsule, which is now full of the desired process gasses and free from atmospheric contaminants.

The growth capsule may be employed in a conventional press used for temperature-gradient HPHT growth. The method described above is remarkably successful: the samples measured in this chapter contain approximately 95:5 ^{15}N:^{14}N, within a few percent of the purity of the original $^{15}N_2$ source gas (current highest isotopic

purity gas available is 98 % ^{15}N[1]).

7.2 Aggregation of nitrogen in diamond

Nitrogen was first identified as the dominant impurity in most (type I, > 95 %) natural diamonds in 1959 [22], during an investigation in which a number of diamonds were graphitised at 2000 °C (burnt) and the gaseous products measured. As a consequence, much of the literature on diamond properties has focused on type I material, with particular emphasis on the aggregation of nitrogen induced by heat treatments.

Dispersed substitutional nitrogen is very rare in natural samples, with the vast majority of natural type I material containing nitrogen in various forms of aggregate. The energy required for concerted exchange of a nitrogen and neighbouring carbon atom has been calculated to be 6.3 eV [23]: at the temperatures usually reached inside HPHT presses, this process is expected to be negligible. The aggregation of nitrogen is therefore understood to proceed by a vacancy-assisted mechanism, active at temperatures as low as 1500 °C [24]:

$$\begin{aligned} \mathrm{N} + \mathrm{V} &\rightarrow \mathrm{NV} \\ \mathrm{NV} &\rightarrow \mathrm{VN...} \\ \mathrm{NV} + \mathrm{N} &\rightarrow \mathrm{NVN} \rightarrow \mathrm{NNV} \rightarrow \mathrm{NN} + \mathrm{V}\ . \end{aligned}$$

At any point during this aggregation, intermediate products may be frozen in — NV and NVN (also known as H3 if in the neutral charge state; H2 suspected to be the negative charge state) have both been observed. It should be noted that, despite NV and NVN supposedly being intermediate steps on the way to NN (A-centre) formation, it is possible to devise treatments to target a particular final product. For instance, irradiating type Ib (dispersed nitrogen) material and annealing it will first produce NV centres and then NN, with significantly lower NVN concentration at all points. Irradiation of type IaA material (nitrogen primarily in NN form) and then annealing will produce small amounts of NV but significant

[1] Cambridge Isotope Laboratories

amounts of NVN: the NN aggregate appears to be an efficient vacancy trap at intermediate temperatures (800–1500 °C).

Further (high-temperature) annealing leads to the formation of higher-order aggregates: N_3V (P2 in EPR, N3 in optical measurements); N_4V (B-centre aggregate, measured by infrared absorption); and N_4V_2 (H4 in optical measurements). It is thought that these aggregates are formed by the breakup of A-centres, and the subsequent vacancy-assisted migration of the constituents to other aggregated nitrogen centres; the exact details, however, are unclear [25]. For instance, NVN may be produced by NN + V or by NV + N (or both).

7.3 $(NVN)^-$ in synthetic diamond

The H2 defect in diamond was first reported in 1956 as a broad absorption band after irradiation and annealing [26]. At 80 K, it is observed in both luminescence and absorption with a zero phonon line (ZPL) at 1.257 eV (986.4 nm) and accompanying vibronic band. A local mode is observed in absorption 167.1 meV (1348 cm^{-1}) higher in energy than the ZPL; it is absent in photoluminescence [27]. Photochromism studies on the H2 defect suggested that the defect was the negative charge state of the H3 defect [28], which was ascribed the atomic model $(NVN)^0$ following uniaxial stress measurements and analysis of annealing results on nitrogen-containing natural diamond [29, 30]. Uniaxial stress measurements on the H2 ZPL gave a symmetry of $\mathscr{C}_{2v}$, consistent with the model $(NVN)^-$ (figure 7-2) [27].

The H2 and H3 transitions present an interesting window into the state of the understanding of VN_n centres in diamond. The one-electron model is accurately described by considering only orbital states arising at sites which are nearest-neighbour to the vacancy, as in the original vacancy model produced by Coulson and Kearsley [31]. (The one-electron states can be simply calculated using a 4-dimensional basis of sp^3 orbitals at each nearest-neighbour pointing into the vacancy.) Lowther observed that the effect of replacing one or more nearest-neighbour carbon atoms with nitrogen was very largely described by simply chang-

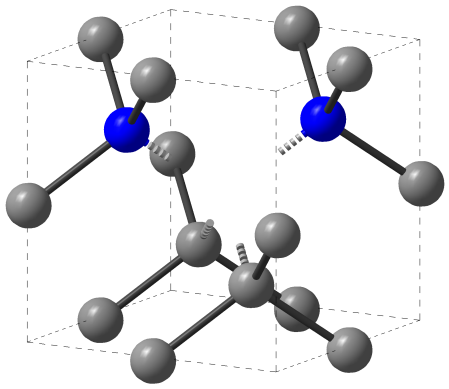

Figure 7-2 The structure of the (NVN) defect in diamond. Blue (dark) atoms are nitrogen. The defect has $\mathscr{C}_{2v}$ symmetry.

ing the charge state and symmetry of the vacancy in accordance with the extra electrons (and lower symmetry) provided by the nitrogen [32]: elemental considerations beyond the change in valency were not required to describe the gross results. This concept is illustrated in figure 7-3 — Lowther considered H3 as a low-symmetry $(\mathrm{V})^{2-}$.

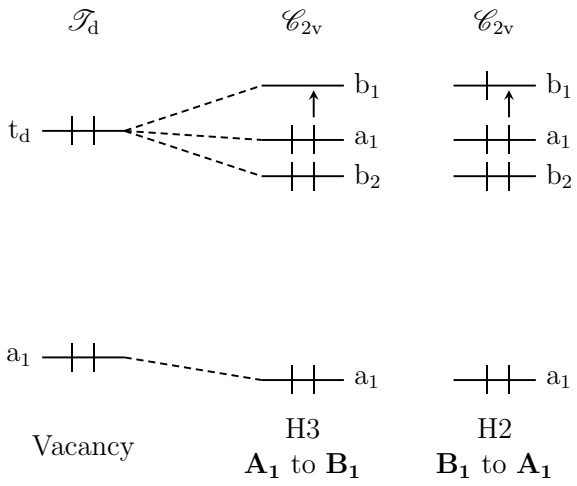

Figure 7-3 Effective one-electron picture produced by starting with the structure of the vacancy, lowering the symmetry and adding two (three) electrons for H3 (H2) using the procedure described in [32]. Electronic occupancy of orbitals indicated by vertical bars, with arrows indicating electronic transitions. Adapted from [27].

The assignment of H2 and H3 to different charge states of the same defect presents a problem: at least one should be EPR-active, but neither has been observed [27, 33]. One report of the observation of H2 by EPR does exist, but the results were very incomplete: no g-anisotropy was measured, the nitrogen quadrupole

was neglected, and the parameters are a poor fit to the experimental data [34].

7.3.1 Experiment

7.3.1.1 Sample

The sample used in this investigation was grown by the method described in §7.1, with $\gtrapprox 95\,\%$ of atmospheric nitrogen replaced with ^{15}N. Using the infrared absorption calibration factor $H_{1121} = 1.5(1) \times 10^{-16}$ $[(^{15}\mathrm{N_s})^0]\,\mathrm{cm}^{-2}$ [4], the sample contained $[(^{15}\mathrm{N_s})^0] = 105(5)\,\mathrm{ppm}$ and $[(^{14}\mathrm{N_s})^0] = 5(2)\,\mathrm{ppm}$ immediately post-synthesis. The sample showed good octahedral growth, with large $\langle 1\,1\,1 \rangle$ faces and small $\langle 1\,0\,0 \rangle$, $\langle 1\,1\,0 \rangle$ faces.

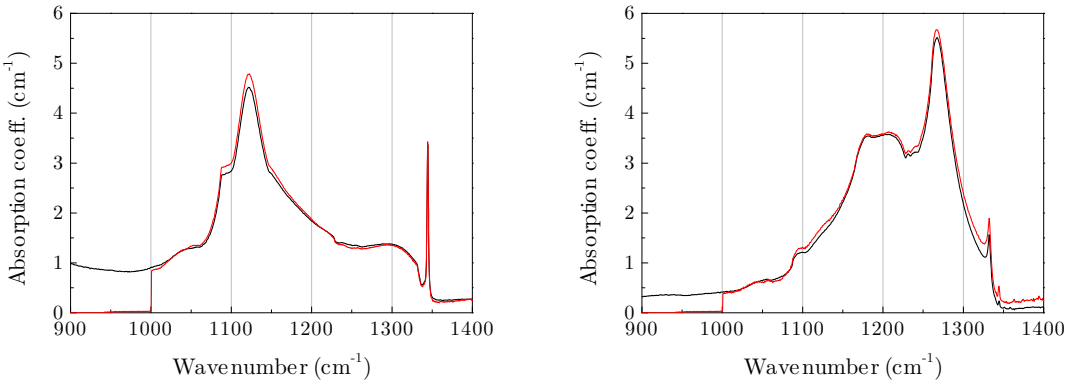

(a) As-grown

(b) Post-HPHT and irradiation

Figure 7-4 One-phonon region IR spectra of the sample before and after processing. In each case, the black (non-zero at low wavenumber) line is the experiment and the red is the fit, with the fit being produced using the components described in the text.

In order to aggregate a significant portion of the nitrogen, the sample was HPHT processed at Suncrest Diamonds with the result that $> 85\,\%$ of nitrogen aggregated to A-centre form (nitrogen pairs nearest-neighbour). The sample was then irradiated[2] for 6 h with 4.5 MeV electrons; unfortunately, the beam waist and beam current were not measured, but EPR and optical measurements of samples irradiated simultaneously allow the total vacancy concentration to be estimated as $5(1)\,\mathrm{ppm}$. The following concentrations were calculated from post-irradiation

[2]Courtesy of B. L. Cann, DTC Maidenhead

infrared absorption measurements: $[(^{15}N_s)^0] = 10(1)$ ppm; $[(^{15}N_s)^+] = 6(2)$ ppm; and $[^{(15)}A] = 90(5)$ ppm, where $^{(15)}A$ is an A aggregate composed of two ^{15}N atoms. The oscillator strengths for $^{(15)}A$ and $(^{15}N_s)^+$ have been assumed to be the same as those for $^{(14)}A$ and $(^{14}N_s)^+$, respectively — this situation was quantitatively found to be the case for $(^{15}N_s)^0$ and $(^{14}N_s)^0$ [4]. The $6(2)$ ppm of $(^{15}N_s)^+$ is in good agreement with the estimated $5(1)$ ppm of vacancies.

Finally, the sample was annealed at 800 °C for 14 h, to allow the vacancies to become mobile in order to create $(NVN)^-$ and $(NV)^-$. These defects were both observed primarily in the negative charge state as their combined concentrations $[(NVN)^-] + [(NV)^-] \approx 5$ ppm were less than the total nitrogen concentration. Additionally, these defects are expected to be produced in nitrogen-rich sectors.

7.3.1.2 EPR measurements

Room-temperature X-band EPR measurements were performed using a Bruker EMX-E spectrometer equipped with a Bruker E41-GX microwave bridge and 90 dB attenuator. The sample was mounted in a dual axis goniometer inside a Bruker ER4122SHQ spherical resonator. Room temperature Q-band measurements were performed on a Bruker EMX spectrometer equipped with a Bruker E41-KQ microwave bridge and a Bruker cylindrical TE_{011} resonator.

Illuminated and low-temperature measurements were performed with the E41-GX bridge attached to the EMX spectrometer. A Bruker ER4105DR dual cavity resonator was mounted into an Oxford Instruments ESR-900 continuous flow helium/nitrogen cryostat. The sample was polished in order to remove the seed crystal and to provide a flat face (within 1° of $(1\,0\,0)$) for sample mounting. The sample was glued to an annealed quartz lightguide and mounted into a single axis goniometer, allowing $\langle 1\,0\,0\rangle$ and $\langle 1\,1\,0\rangle$ directions to be measured.

In-situ illumination was provided by an Oriel 66926 Xe arc lamp operating at 1 kW input power. The output of the lamp was focused through a distilled water heat filter and onto a Newport 77566 liquid lightguide. The other end of the lightguide was affixed to the flared end of the quartz sample mount and the light transmitted

to the sample.

7.3.2 Results

7.3.2.1 Room temperature EPR

A typical room-temperature centre-field scan of the sample post-irradiation and anneal is given in figure 7-5. Components that have been previously identified are labelled [7]. The structure in the centre is currently unidentified in the literature and will be shown during the course of this section to belong to $(NVN)^-$.

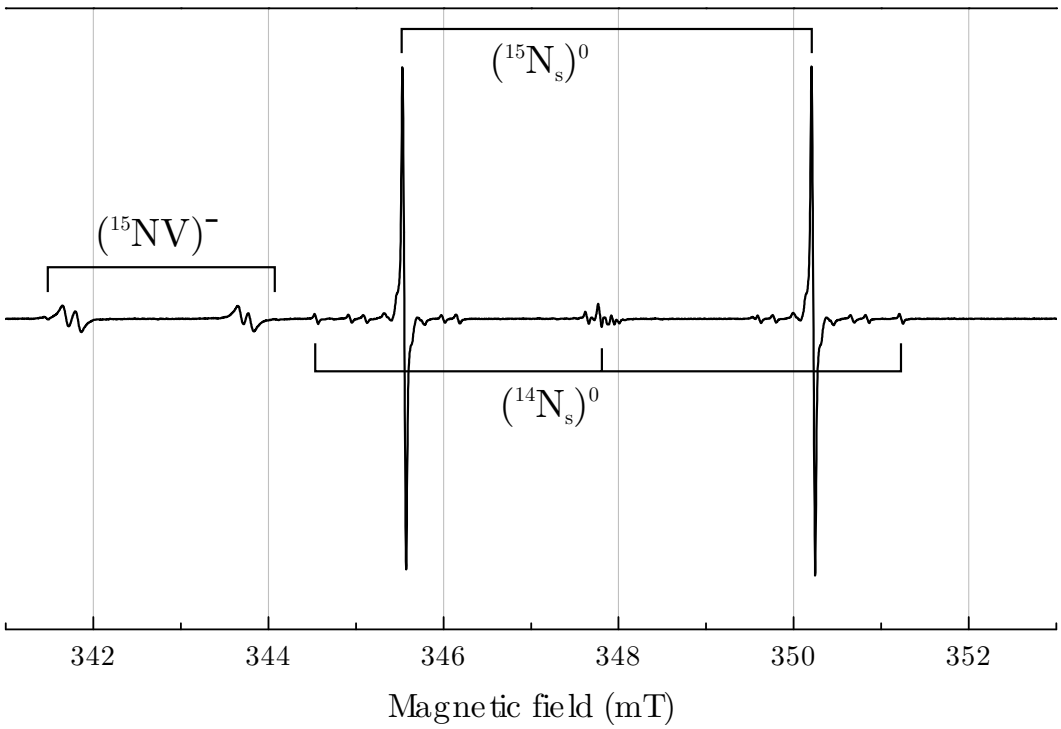

Figure 7-5 Room-temperature X-band EPR measurement of the sample post-irradiation and anneal, and with the magnetic field along ⟨1 0 0⟩. The components that have been identified in the literature are labelled. The structure in the centre has a small contribution from $(^{14}N_s)^0$ but is primarily due to $(NVN)^-$.

A room-temperature roadmap was taken from ⟨0 0 1⟩ to ⟨1 1 0⟩ in a (1 1 0) plane (figure 7-6); the symmetry of the g-tensor was determined to be rhombic I ($\mathscr{C}_{2v}$). Close analysis of the ⟨1 0 0⟩ spectrum (figure 7-7) suggested that the spectrum could be decomposed into two different g-values with the intensity ratio 2:1. The resonance at each g-value was then further split by two identical $I = \frac{1}{2}$ nuclei,

giving a 1:2:1 intensity structure. (Note that in figure 7-7 the line at ≈ 348.82 mT belongs to $(N_s)^0$.)

The only point group symmetry in which all sites are equivalent along a ⟨1 0 0⟩ direction is trigonal (tetrahedral may be ignored due to the anisotropy evident in the roadmap): this suggested that the hyperfine interaction for each of the $I = \frac{1}{2}$ nuclei was aligned along a ⟨1 1 1⟩ direction. With the magnetic field along the ⟨1 1 1⟩ direction, a rhombic I centre possesses (generally) 2 different g-values, with site populations 3:3. For ⟨1 1 1⟩ hyperfine interactions, one set of sites has equivalent hyperfines yielding a 1:2:1 structure; the hyperfines for the other trio of sites are inequivalent and lead to the pattern 1:1:1:1.

With the relatively simple spectra thus sufficiently well-understood, the transitions belonging to each site could be identified. The precise experimental resonance fields and microwave frequencies for all three principal directions at both X- and Q-band were entered into the simulation program EPR-NMR [35], and a least-squares fit was performed. EPR-NMR allows sets of parameters to be locked together: here, the principal directions (within each site axis system) and magnitudes of the two hyperfine interactions were tied together, and the g-tensor was confined to (1 1 0) symmetry. Releasing these constraints did not improve quality of the fit. The results of the fitting procedure are given in table 7-1.

Parameter	Value	Direction
g_1	2.003 45(5)	[1 1 0]
g_2	2.002 74(5)	[0 0 1]
g_3	2.002 71(5)	[1 $\bar{1}$ 0]

Parameter	Value (MHz)	Direction
A_1	±3.47(2)	3.5(5)° from [1 1 $\bar{2}$] toward [0 0 1]
A_2	±4.51(2)	3.5(5)° from [1 1 1] toward [0 0 1]
A_3	±4.09(2)	[1 $\bar{1}$ 0]

Table 7-1 The measured spin Hamiltonian parameters for the $(NVN)^-$ defect in ^{15}N-doped diamond. The g-tensor values are given assuming that $(N_s)^0$ has an isotropic g-value of 2.0024.

The defect is associated with $(NVN)^-$ by its hyperfine structure and g-tensor symmetry. It has been shown that the hyperfine structure is well-described by two

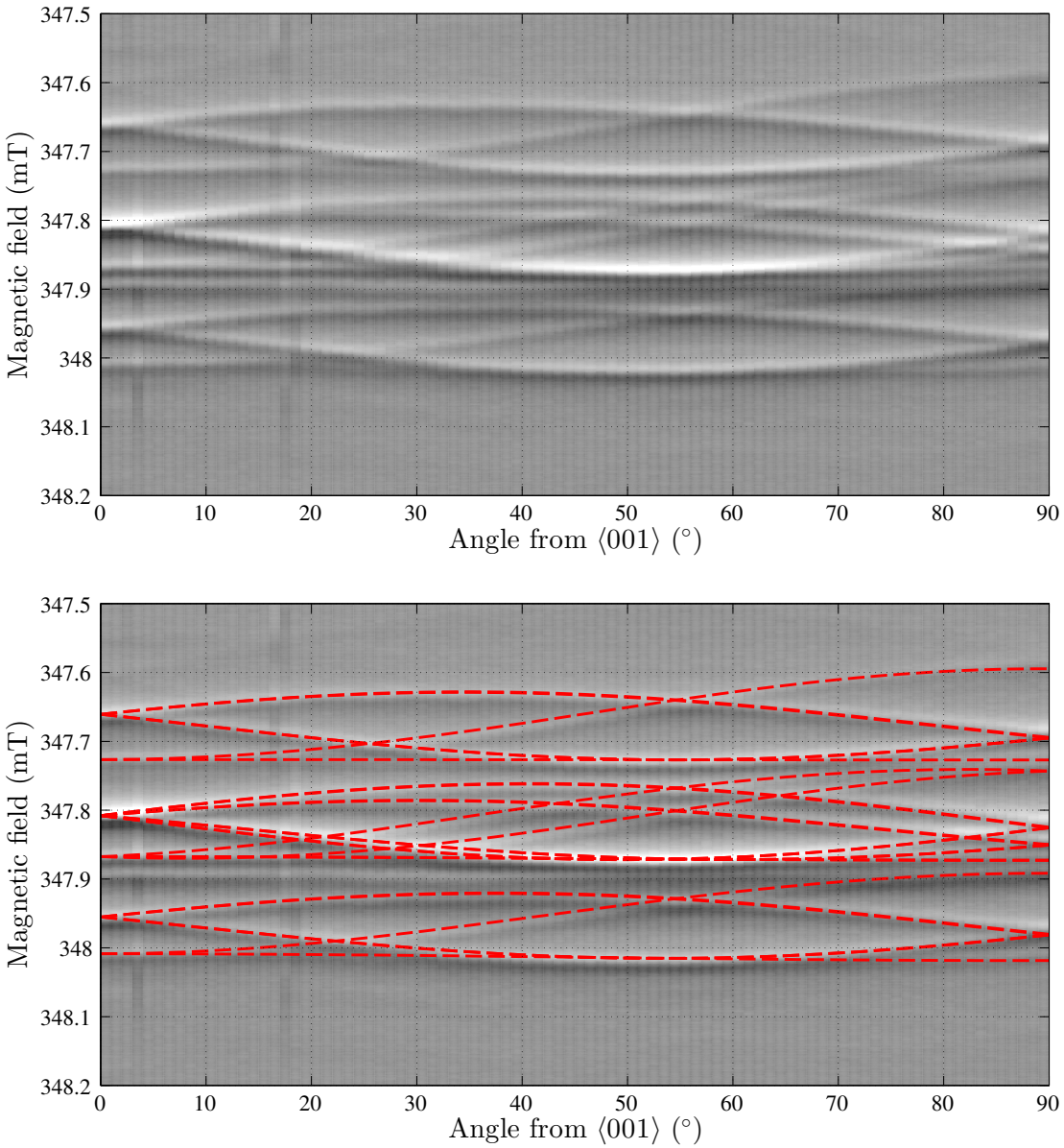

Figure 7-6 Room-temperature roadmap of $(\mathrm{NVN})^-$. Taken with the sample rotating in a $(1\,1\,0)$ plane from $\langle 0\,0\,1\rangle$ and at a microwave frequency of 9.753 GHz. The smooth grayscale image is a projection of experimental data, with white being high positive intensity and black being high negative intensity (top). Grey corresponds to zero. The red lines superimposed on the lower image are a simulation produced using the parameters given in table 7-1. $(^{14}\mathrm{N_s})^0$ is visible as the isotropic line at approximately 347.9 mT, and lines from $(^{15}\mathrm{NV})^-$ are visible at approximately 4 and 18°.

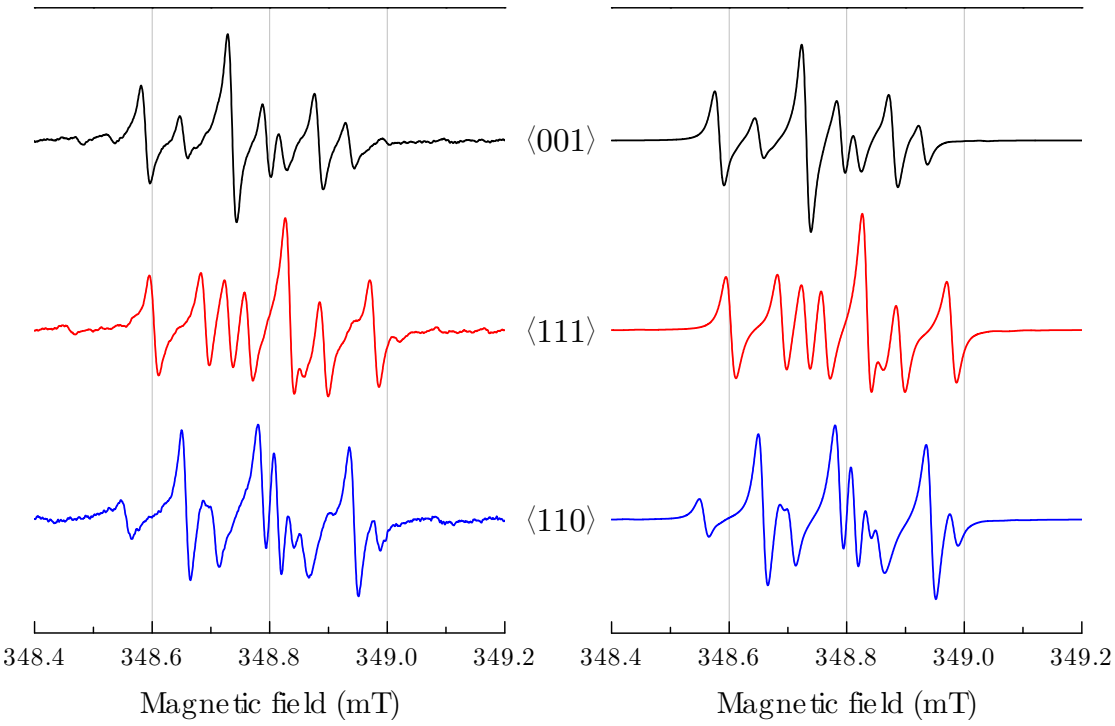

Figure 7-7 A comparison of experimental (left) and simulated spectra at a microwave frequency of approximately 9.755 GHz. The orientation of the magnetic field for each spectrum is given in the centre. The simulations include $(\mathrm{NVN})^-$ and $(^{14}\mathrm{N_s})^0$ (visible at 348.82 mT), and have been field-corrected assuming that $(\mathrm{N_s})^0$ has an isotropic g-value of 2.0024.

$I = \frac{1}{2}$ nuclei. In this material, the most abundant $I = \frac{1}{2}$ nuclei are ^{13}C and ^{15}N. If the nuclei in question were ^{13}C then additional (much more intense) spectra arising at atomically similar defects but containing only one ^{13}C would be expected: as no such spectra are observed then the hyperfine interactions are assigned to ^{15}N nuclei. The following analysis will reinforce the assignment of $(\mathrm{NVN})^-$.

7.3.3 Discussion

7.3.3.1 The nitrogen hyperfine interaction

The hyperfine parameters as given in table 7-1 are non-axial; that is to say $A_1 \neq A_2 \neq A_3$. This may be due to a number of reasons, including core spin-polarisation and extended interactions with higher-order orbitals [36], or the symmetry of the defect in question.

A simple treatment suggests that each nitrogen atom possesses a lone pair pointing into the vacancy, and that by Pauli exclusion further electrons must reside in higher energy states: therefore 50% of the unpaired electron probability density is assumed to be localised at a point along each ⟨1 1 1⟩ "bond" between each of the carbon atoms and the vacancy. In the simple case (ignoring spin-orbit effects), the hyperfine interaction can be described as the sum of an isotropic component a arising from non-zero spin density at the nucleus, and an anisotropic dipolar component b. The isotropic component of the hyperfine interaction at each point is then $a = (A_1 + A_2 + A_3)/6 = 2.01\,\text{MHz}$. In its principal axis frame, the matrix describing a dipolar interaction is diagonal with values $-b, -b, +2b$. In considering the dipolar component, a dipolar matrix is constructed at each of the assumed spin density locations, and then transformed into the crystal axes. The matrices may be summed to give a macroscopic dipolar interaction matrix, and compared against the experimentally measured values.

Using the approach described above, a calculation for the $(\text{NVN})^-$ defect was performed. The interaction was constrained to the {1 1 0} planes containing one each of the nitrogen and carbon atoms, and the vacancy. The only free parameters were θ, the in-plane angle between the interaction vector and the ⟨1 1 1⟩ direction connecting the nitrogen and vacancy, and b, the strength of the interaction in MHz. θ and b were varied to minimise the difference between the observed values and the calculated values. The values which give the best fit to experiment are given in table 7-2.

The best fit is achieved at an angle of $\theta = 35.26°$, and an interaction strength of $b = -0.46\,\text{MHz}$. This corresponds to 50 % of the electron spin density being localised at each of the carbon atoms, with the hyperfine interaction for each location being along the ⟨1 1 0⟩ direction between the carbon and nitrogen atoms — consistent with the initial assumptions of the electron localisation of the carbon atoms. The resulting macroscopic interaction is a good fit to experiment; a comparison of eigenvalues and eigenvectors is given in table 7-2b.

For high-symmetry hyperfine interactions, the relative signs of the principal hyperfine values are ambiguous; the construction of the macroscopic interaction in

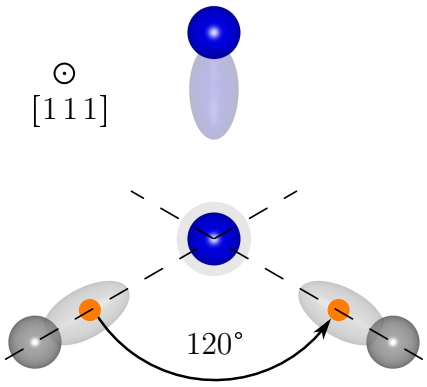

(a) The localisation of the unpaired electron probability density along the "bonds" between each carbon and the vacancy. The planes which in which θ is defined (see text and below figure) are shown as dotted lines.

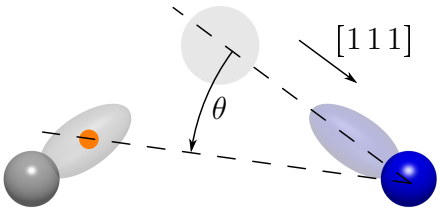

(b) The angle θ is defined as the angle between the $\langle 1\,1\,1\rangle$ direction connecting the vacancy and nitrogen sites, and the localised unpaired electron probability density. The angle is confined to the $(1\,1\,0)$ plane which contains all three lattice sites.

Figure 7-8 The geometry used for the dipolar calculation described in the text. The unpaired electron probability density is localised at a point along the $\langle 1\,1\,1\rangle$ "bond" between each of the carbon atoms and the vacancy (orange dot): at each of these two points a dipolar interaction matrix is constructed and transformed into the crystal axes. The results are summed to give a macroscopic interaction.

this way allows the same sign to be attributed to all three principal values. The local spin-DFT calculations performed by Goss [37] (using the methods described in [38]) also give a similar polarity to all values, the absolute sign of which could be confirmed experimentally by ENDOR measurements.

In order to check the calculated values are reasonable, the expected interaction magnitude may be calculated. For a simple dipolar interaction, the interaction strength is given by

$$b = \frac{\mu_0}{4\pi} \frac{g_e\,\mu_B\,g_n\,\mu_n}{h} \left\langle \frac{1}{r^3} \right\rangle ,$$

where r is the distance between the unpaired electron and the nucleus, assumed to be a point dipole. For a ^{15}N nucleus at a distance $r = 2.52$ Å (next nearest neighbour separation), the interaction strength is -0.50 MHz (c.f. -0.46 MHz obtained

b (MHz)	Eigenvalues (MHz)	Eigenvectors
−0.46	−0.58, +0.12, +0.46	$[1\,1\,\bar{2}]$, $[1\,\bar{1}\,0]$, $[1\,1\,1]$

(a) Orientation and interaction strength of the macroscopic dipolar matrix for each nitrogen atom. Constructed using an interaction strength of b at each carbon atom and summed in the crystal axes.

	Eigenvalues (MHz)	Eigenvectors
Experiment	3.47(2), 4.51(2), 4.09(2)	3.5° from $[1\,1\,\bar{2}]$, 3.5° from $[1\,1\,1]$, $[1\,\bar{1}\,0]$
Simulation	3.44, 4.48, 4.14	$[1\,1\,\bar{2}]$, $[1\,1\,1]$, $[1\,\bar{1}\,0]$
DFT[37]	2.6, 3.7, 3.2	3.8° from $[1\,1\,\bar{2}]$, 3.8° from $[1\,1\,1]$, $[1\,\bar{1}\,0]$

(b) Comparison of the experimental and calculated hyperfine values. Calculated values are as those given above with the isotropic component 2×2.01 MHz added.

Table 7-2 Results of calculations designed to minimise the difference between the calculated and observed hyperfine values for $(NVN)^-$. See text for details.

by least squares fit). Given the crudeness of the model employed, the agreement with experiment is remarkably good. No geometric relaxation was included in this model, and the electron spin density was taken to be localised at two points only. For a more precise calculation, information about shape and amplitude of the electron wavefunction is required in addition to knowledge about the minimum energy geometrical configuration.

7.3.3.2 The unpaired electron wavefunction

With knowledge of the origin of the hyperfine interaction, the electronic wavefunction localisation may be investigated. In general, the unpaired electron wavefunction may be written as a linear combination of atomic orbitals

$$\Psi = \sum_{n}^{N} \eta_n \psi_n$$

with summation over all atoms where the unpaired electron probability density is non-zero [39]. In diamond, the wavefunctions for carbon and nitrogen atoms are constructed from linear sums of $2s$ and $2p$ orbitals

$$\psi_n = \alpha_n (\phi_{2s})_n + \beta_n (\phi_{2p})_n \, .$$

Ignoring overlap, normalisation requires that $\alpha_n^2 + \beta_n^2 = 1$, and $\sum \eta_n^2 = 1$ [40]. As a consequence of the contributions being s and p-type in character, the interaction is axial with values

$$A_{\parallel} = a_n + 2b_n \qquad A_{\perp} = a_n - b_n \ .$$

Whilst a_n and b_n are known from experiment, knowledge of the equivalent values for 100 % occupancy (a^* and b^*) are required in order to calculate unpaired electronic probability density localisation. (As a note on nomenclature, it is common to refer to a and b as A_s and A_p respectively when not explicitly performing hyperfine analysis.) The values a^* and b^* are given by [41]

$$a^* = \frac{2\mu_0}{3} g_e \, \mu_B \, g_n \, \mu_n \, \Psi^2(0)$$
$$b^* = \frac{\mu_0}{10\pi} g_e \, \mu_B \, g_n \, \mu_n \left\langle \frac{1}{r^3} \right\rangle \ ,$$

where $\Psi^2(0)$ is the electron probability density at the nucleus, and r is the radial coordinate [40]. The electron wavefunction must first be computed (Hartree-Fock methods or similar) in order to obtain $\Psi^2(0)$ and $\langle r^{-3} \rangle$: the results for a^* and b^* are tabulated (for free atoms) in standard references e.g. [42]. The localisation of the unpaired electronic probability density may then be calculated from

$$a_n = a^* \alpha_n^2 \eta_n^2 \qquad b_n = b^* \beta_n^2 \eta_n^2 \ .$$

For ^{15}N, $a^* = -2540$ MHz and $b^* = -77.9$ MHz [42]. Using the experimentally-obtained values $a_{\mathrm{N}} = 2.01$ MHz and $b_{\mathrm{N}} = 0.46$, the s and p-type characters are $\alpha_{\mathrm{N}}^2 = 6.7$ % and $\beta_{\mathrm{N}}^2 = 93.3$ %; a total unpaired electron localisation on each nitrogen of $\eta_{\mathrm{N}}^2 \approx 1$ % is calculated. This result is consistent with the small magnitude of the observed nitrogen hyperfine interaction and the earlier assumption of the unpaired electron probability density localisation being between the two carbon atoms.

It should be noted that the method used here makes several approximations and omissions (listed in [43]), but these effects are expected to be small for a simple system such as $(\mathrm{NVN})^-$ and the approach is nevertheless useful for generating a picture of the physics involved.

7.3.3.3 The carbon hyperfine interaction

Acquiring a roadmap of the ^{13}C hyperfine structure, which could be up to a factor of 180 weaker than the central lines, was impracticable due to the low concentration of $(NVN)^-$ in this sample. Additionally, it was determined that there was a high probability of the $(NVN)^-$ hyperfine structure being buried under the hyperfine structure from $(N_s)^0$. In an attempt to estimate the strength of the interaction, the ^{13}C hyperfine interactions at the $^4A_2$ state of $(V)^-$ and the $^5A_2$ state of $(V)^0$ were considered (table 7-3). In each case, all hyperfine interactions are along $\langle 1\,1\,1\rangle$ with the ratio of A_s to A_p between approximately 3 and 4, suggesting the general ratio might also apply for other vacancy cage-type defects. The $^5A_2$ state at $(V)^0$ is an excited state, and the smaller spin density on nearest neighbours is not unexpected: the values for $(V)^-$ will therefore be used.

	A_s (MHz)	A_p (MHz)	η^2
$^4A_2 : (V)^-$	81.8	19.9	0.827
$^5A_2 : (V)^0$	53.73(5)	18.70(3)	0.753

Table 7-3 ^{13}C nearest-neighbour hyperfine interactions at $(V)^-$ [44] and $(V)^0$ [45]. Table adapted from [45].

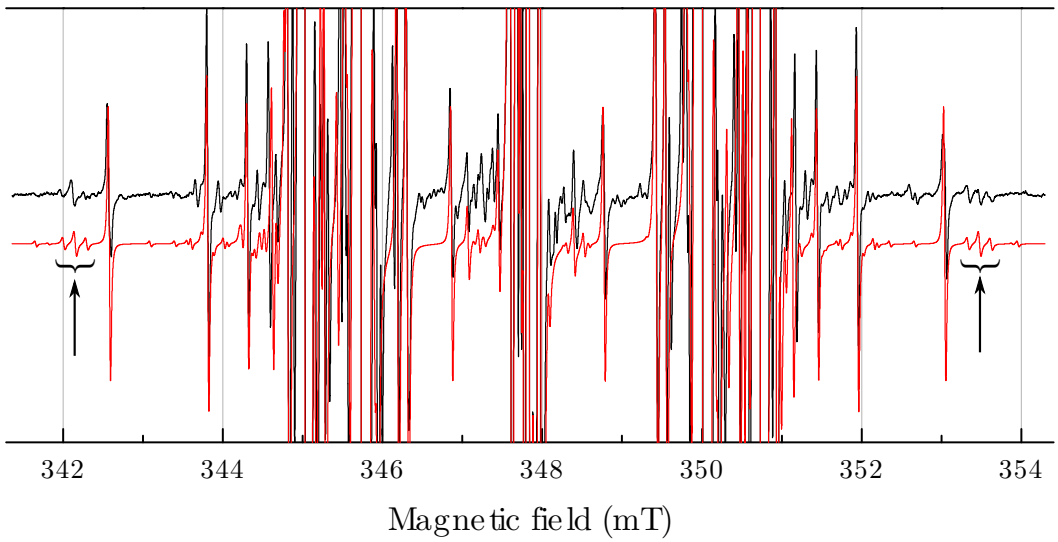

Figure 7-9 Comparison of experiment (top) and simulation of a two-week accumulation with the magnetic field along $\langle 1\,1\,1\rangle$. The ^{13}C hyperfine satellites for three of the $(NVN)^-$ sites are indicated. The simulation includes contributions from $(^{15}N_s)^0$, $(^{14}N_s)^0$ and $(NVN)^-$.

The estimated hyperfine values for $(\mathrm{NVN})^-$ were constructed by taking those from $(\mathrm{V})^-$ and multiplying them by two, to account for the spin density being distributed between two nearest neighbours rather than four. Subsequent simulations of $(\mathrm{NVN})^-$ and $(\mathrm{N_s})^0$ suggested that the hyperfines would be most visible (i.e. least likely to be buried under intensity from $(\mathrm{N_s})^0$) with the magnetic field along a $\langle 1\,1\,1 \rangle$ direction.

A spectrometer was left running for approximately fourteen days at high resolution to attempt to observe the hyperfine structure: the resulting scan and corresponding simulation are given in figure 7-9. The visible ^{13}C satellites are for those sites with equivalent nitrogen hyperfine interactions and so the 1:2:1 structure is replicated in each satellite. Due to the lengthy experimental time, only one direction has been obtained and hence no anisotropy information is available: the simulation has been constructed assuming the ratio of A_s to A_p discussed above and then scaling both values by the same factor, giving $A_s = 214\,\mathrm{MHz}$ and $A_p = 52\,\mathrm{MHz}$ for each ^{13}C interaction.

Analysis of the unpaired electron probability density (using the process in §7.3.3.2) indicates $\eta^2 \approx 50\,\%$ for each carbon atom. This value will be sensitive to relative contribution of A_s and A_p and should cause no alarm. The analyses of the nitrogen and carbon hyperfine interactions are therefore consistent: the electron is localised essentially 100 % on the two nearest-neighbour carbon atoms, with virtually zero spin density on the two nearest-neighbour nitrogen atoms.

7.3.3.4 The ^{14}N quadrupole interaction

Following previous discussion on the magnitude of ^{14}N quadrupolar interaction strengths [39], the $(\mathrm{NVN})^-$ spectrum in ^{14}N-doped synthetic diamond may be estimated. Using an electron localisation in the ^{14}N $2p$ orbital of 0%, as observed in experiment, a value of $P_\parallel \approx -5.2\,\mathrm{MHz}$ may be estimated [39]. Assuming the interaction is along the $\langle 1\,1\,1 \rangle$ direction and scaling the hyperfine parameters by the ratio of the isotopic γ values produces the simulations shown in figure 7-10a.

Using the speculative ^{14}N $(\mathrm{NVN})^-$ parameters, a simulation can be produced for a

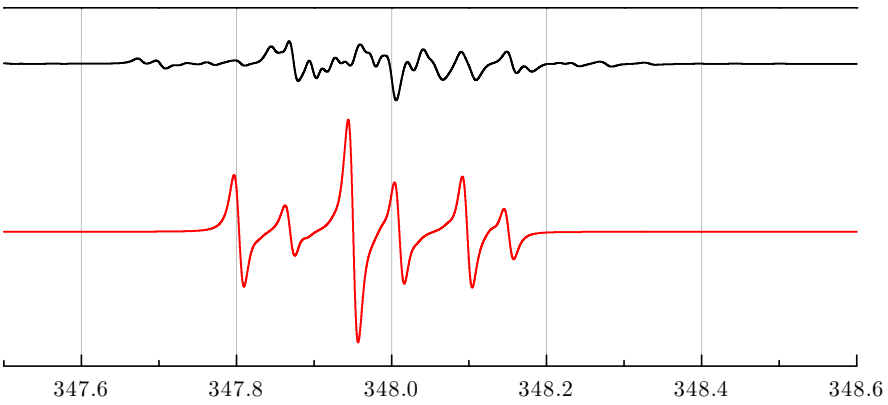

(a) Simulated spectra of $(NVN)^-$ in ^{14}N- (top) and ^{15}N-doped diamond. The total integrated intensity is the same in each simulation.

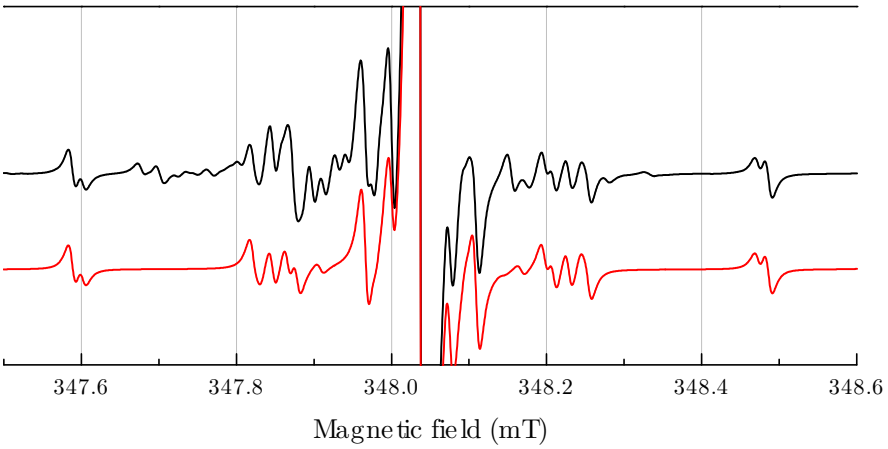

(b) Simulated spectra of a ^{14}N-doped diamond containing the same relative concentrations of $(NVN)^-$ and $(N_s)^0$ as the sample used in the experiments presented (top, c.f. 7-5). A simulation containing just $(N_s)^0$ is given below for comparison.

Figure 7-10 Simulations to illustrate the additional complexity of the $(NVN)^-$ spectrum in ^{14}N-containing material relative to the ^{15}N equivalent. Each spectrum is simulated with the magnetic field oriented along $\langle 1\,0\,0 \rangle$ at 9.755 GHz and with a pseudo-modulation amplitude of 0.1 G for all components.

^{14}N-doped diamond with equivalent relative concentrations of $(N_s)^0$ and $(NVN)^-$ as the ^{15}N-doped diamond used in these experiments (figure 7-10b). As the assumed quadrupolar interaction is similar in magnitude to the measured hyperfine interaction strength, many of the degeneracies present in the ^{15}N spectrum are lifted, having the effect of "smearing out" the spectrum. The exact profile of the spectrum will be sensitive to the magnitude and direction of the quadrupolar interaction but will inevitably be significantly more difficult to interpret relative to

the ^{15}N case.

To attempt to identify ^{14}N-doped $(NVN)^-$ in an experimental spectrum, a heavily nitrogen-doped (natural isotopic abundance, $[(N_s)^0] = 300\,\text{ppm}$) HPHT-grown type Ib diamond was measured by EPR. The sample had been irradiated with 1×10^{18} neutrons cm^{-2}, producing approximately 90 ppm of vacancies [46], and was subsequently annealed for 12 h at 1450 °C. The primary features visible in UV-Vis and IR measurements were $(NV)^-$ and H2. The EPR spectrum and corresponding simulations are given in figure 7-11, and demonstrate the need to take $(NVN)^-$ into account even in ^{14}N-containing material, where the spectrum may not be well-resolved. No attempt has been made to fine-tune the quadrupolar interaction due to the linewidth, but the residual suggests that the estimated $P_\parallel \approx -5.2\,\text{MHz}$ is approximately correct.

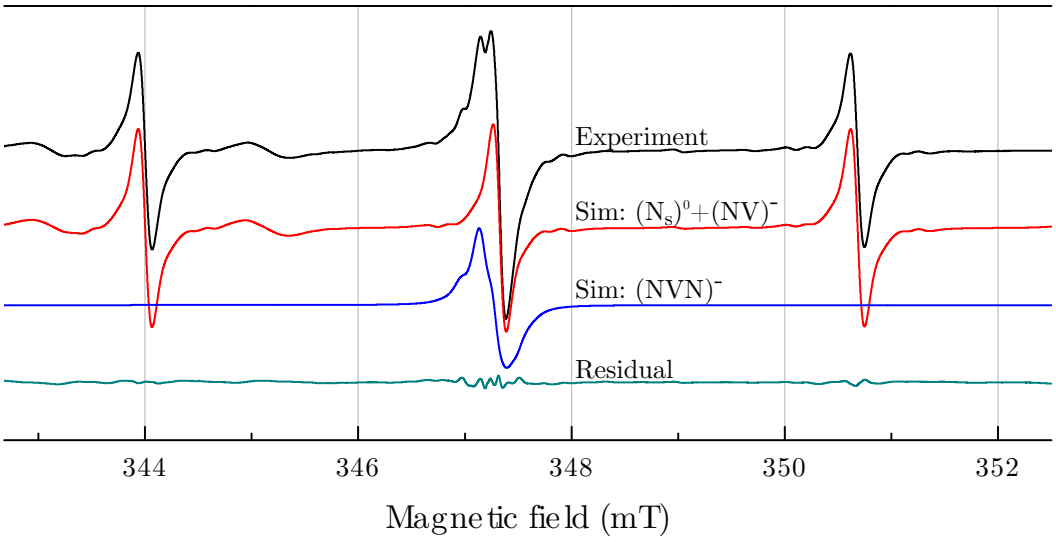

Figure 7-11 Room-temperature experimental spectrum of a ^{14}N-doped sample which initially contained $[(N_s)^0] = 300\,\text{ppm}$, was subsequently irradiated with 10^{18} neutrons cm^{-2}, and was finally annealed at 1450 °C for 12 h. Top to bottom: experimental spectrum; simulation of $(N_s)^0$ and $(NV)^-$; simulation of $(NVN)^-$ using the ^{14}N parameters discussed above; residual between experiment and all three simulations. Experimental spectrum collected by Matthew Dale at a microwave frequency of 9.735 GHz.

7.4 Conclusion

HPHT-grown ^{15}N-doped diamond has been studied by EPR. Following HPHT annealing, electron irradiation and further annealing, a rhombic $S = \frac{1}{2}$ defect has been identified. Analysis of the hyperfine interaction identified two equivalent $I = \frac{1}{2}$ nuclei in next-nearest-neighbour positions, with the dipolar interactions approximately along $\langle 1\,1\,1 \rangle$. The two most abundant $I = \frac{1}{2}$ nuclei in this material were ^{13}C and ^{15}N: the nuclei involved in the defect were unambiguously identified as nitrogen by the lack of corresponding spectrum containing only one $I = \frac{1}{2}$ nucleus, as would be the case for carbon.

The hyperfine interaction with one of the nearest-neighbour carbon atoms was identified by analysis of a very high signal-to-noise spectrum. The unpaired electron spin density was identified as being effectively 100 % localised on the two carbon nearest-neighbours, with zero localisation on the two nitrogen atoms: this is what would be expected from a simple one-electron picture. A self-consistent description of a centre with two carbon and two nitrogen nearest neighbours has been put forward, identifying for the first time the $(\mathrm{NVN})^-$ defect in diamond.

Finally, an argument has been presented which explains why this centre, which is assumed to be present in high concentration in many natural and synthetic samples, has not previously been identified in ^{14}N-containing diamond. An experimental spectrum of a ^{14}N-doped sample has been shown to contain strong spectral features consistent with the new $(\mathrm{NVN})^-$ parameters.

Future work should aim to identify the $(\mathrm{NVN})^-$ EPR defect with its optical analogue, assumed to be H2. Photochromism studies in infrared absorption, where H2 and $(\mathrm{N_s})^0/(\mathrm{N_s})^+$ can be monitored simultaneously, are expected to confirm that H2 photochromism is due to interaction with $(\mathrm{N_s})^0$. A similar experiment in EPR would monitor the EPR-active $(\mathrm{NVN})^-$ and $(\mathrm{N_s})^0$ simultaneously, and a direct correlation between the EPR and IR results should confirm the assignment. Although no data have been presented as part of this thesis, the sample studied here did show a decrease in $(\mathrm{NVN})^-$, and an increase in $(\mathrm{N_s})^0$ in EPR when illuminated with a mercury arc lamp.

References

1. A. T. Collins, G. S. Woods, *Journal of Physics C: Solid State Physics* **20**, L797 (1987).
2. A. T. Collins, M. Stanley, G. S. Woods, *Journal of Physics D: Applied Physics* **20**, 969 (1987).
3. G. Davies *et al.*, *Journal of Physics: Condensed Matter* **9**, 3871 (1997).
4. S. Liggins, PhD thesis, University of Warwick, 2010.
5. A. Cox, M. E. Newton, J. M. Baker, *Journal of Physics: Condensed Matter* **6**, 551 (1994).
6. S. Felton *et al.*, *Journal of Physics: Condensed Matter* **21**, 364212 (2009).
7. S. Felton *et al.*, *Physical Review B* **79**, 075203 (2009).
8. A. T. Collins, G. S. Woods, *Philosophical Magazine Part B* **46**, 77 (1982).
9. T. R. Anthony *et al.*, *Physical Review B* **42**, 1104 (1990).
10. D. G. Onn *et al.*, *Physical Review Letters* **68**, 2806 (1992).
11. G. Balasubramanian *et al.*, *Nature Materials* **8**, 383 (2009).
12. P. C. Maurer *et al.*, *Science* **336**, 1283 (2012).
13. R. Samlenski *et al.*, *Applied Physics Letters* **67**, 2798 (1995).
14. A. Tallaire *et al.*, *Diamond and Related Materials* **15**, 1700 (2006).
15. J. Achard *et al.*, *Journal of Physics D: Applied Physics* **40**, 6175 (2007).
16. S. Jin, T. D. Moustakas, *Applied Physics Letters* **65**, 403 (1994).
17. J. Achard *et al.*, *Diamond and Related Materials* **16**, 685 (2007).
18. W. Ahmed *et al.*, *Vacuum* **56**, 153 (2000).
19. F. P. Bundy *et al.*, *Nature* **176**, 51 (1955).
20. R. Burns, G. Davies, in *The Properties of Natural and Synthetic Diamond*, ed. by J. E. Field (Academic Press, London, 1992), p. 395.
21. C. Strömann *et al.*, WO 2006/061672 (2006).
22. W. Kaiser, W. L. Bond, *Physical Review* **115**, 857 (1959).
23. A. Mainwood, *Physical Review B* **49**, 7934 (1994).
24. A. T. Collins, *Journal of Physics C: Solid State Physics* **13**, 2641 (1980).
25. R. Jones, J. P. Goss, in *Properties, Growth and Applications of Diamond*, ed. by M. Nazaré, A. J. Neves (IEE - Inspec, London, 2001), A5.1.

26. C. D. Clark, R. W. Ditchburn, H. B. Dyer, *Proceedings of the Royal Society of London A* **237**, 75 (1956).
27. S. C. Lawson *et al.*, *Journal of Physics: Condensed Matter* **4**, 3439 (1992).
28. Y. Mita *et al.*, *Journal of Physics: Condensed Matter* **2**, 8567 (1990).
29. G. Davies, M. H. Nazaré, M. F. Hamer, *Proceedings of the Royal Society of London A* **351**, 245 (1976).
30. G. Davies, *Journal of Physics C: Solid State Physics* **9**, L537 (1976).
31. C. Coulson, M. Kearsley, *Proceedings of the Royal Society of London A* **241**, 433 (1957).
32. J. Lowther, *Journal of Physics and Chemistry of Solids* **45**, 127 (1984).
33. A. T. Collins, *Diamond and Related Materials* **8**, 1455 (1999).
34. Y. Nisida *et al.*, presented at the International Conference on Defects in Semiconducting Materials.
35. M. J. Mombourquette, J. A. Weil, D. G. McGavin, *EPR-NMR*, 1997, `www.chem.queensu.ca/eprnmr`.
36. B. R. McGarvey, *The Journal of Physical Chemistry* **71**, 51 (1967).
37. J. Goss, private communication.
38. M. K. Atumi *et al.*, *Journal of Physics: Condensed Matter* **25**, 065802 (2013).
39. O. Tucker, M. Newton, J. Baker, *Physical Review B* **50**, 15586 (1994).
40. G. Watkins, J. Corbett, *Physical Review* **121**, 1001 (1961).
41. C. Van de Walle, P. Blöchl, *Physical Review B* **47**, 4244 (1993).
42. J. R. Morton, K. F. Preston, *Journal of Magnetic Resonance (1969)* **30**, 577 (1978).
43. J. M. Baker, M. E. Newton, *Applied Magnetic Resonance* **7**, 209 (1994).
44. J. Isoya *et al.*, *Physical Review B* **45**, 1436 (1992).
45. J. van Wyk *et al.*, *Physical Review B* **52**, 12657 (1995).
46. A. Mainwood, *Diamond and Related Materials* **7**, 504 (1998).

Chapter 8

$^{15}N_3V$ EPR centre in synthetic diamond

8.1 Background and previous research

The P2 EPR centre was first observed in yellow diamonds in 1959 [1]. Due to the complexity of the observed spectrum (figure 8-1) and previous reports of aluminium in diamond [2], P2 was interpreted as belonging to a substitutional aluminium acceptor. Numerical simulations showed that the aluminium assignment provided a poor fit to the experimental data, with ENDOR experiments on the hyperfine structure giving excellent agreement with a model based on three equivalent nitrogen atoms [3]. Subsequent EPR measurements supported the structure N_3V (figure 8-3) (albeit with poor spectral fit) and attributed the observed unpaired spin to the dangling orbital of the unique carbon pointing into the vacancy (see §8.1.1) [4]. The hyperfine interaction at the unique carbon was observed in 1982 [5], but improved spectral fit was achieved only after further ENDOR work was analysed with more powerful computing facilities [6].

The optical transition N3 was one of the first optical features observed in diamond, having been first reported in 1891 [7]. It was named N3 (natural line 3) during the irradiation and annealing study of Clark, Ditchburn and Dyer [8]. The N3 optical spectrum consists of a strong ZPL at 2.985 eV (415.2 nm), a strong vibronic structure, and several associated weak, broad transitions — N2 at 2.596 eV (477.6 nm) [7, 8] and N4 at 3.603 eV (344.2 nm).

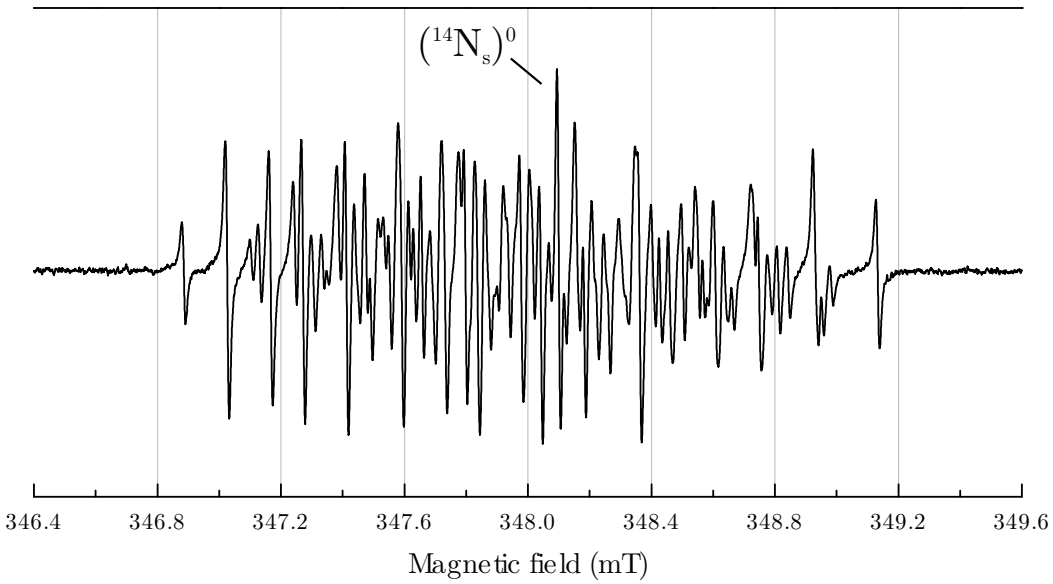

Figure 8-1 Representative spectrum of the P2 EPR centre in a natural type Ia diamond. Spectrum collected at room temperature and with the magnetic field orientated along a ⟨1 0 0⟩ crystal axis and at a microwave frequency of 9.756 GHz. The central hyperfine of $(^{14}N_s)^0$ is indicated.

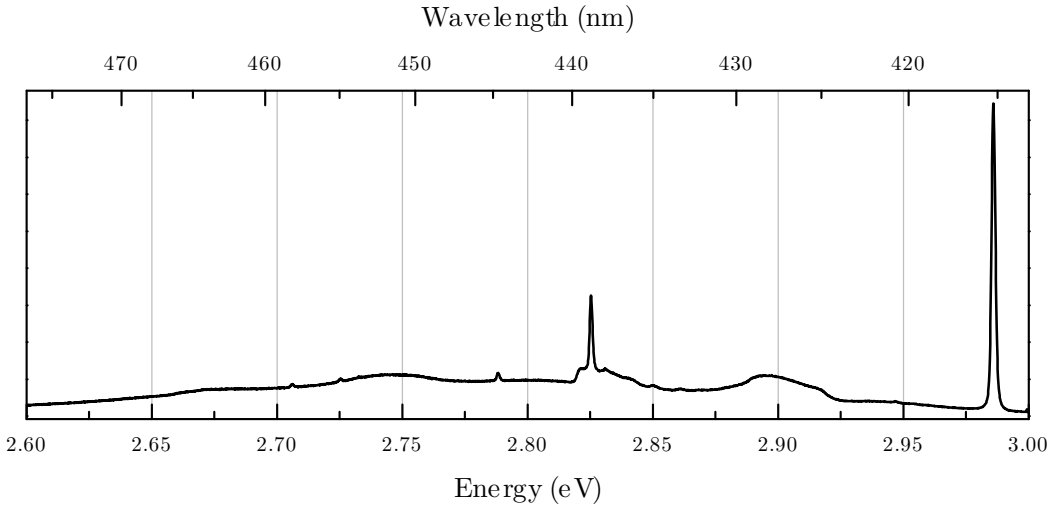

Figure 8-2 The N3 spectrum in a ^{15}N-doped HPHT diamond and measured by photoluminescence at 80 K. Spectrum collected using laser excitation at 3.815 eV (325.0 nm). Broad structures are vibronic features of N3 (ZPL at 2.985 eV), but other sharp peaks are unrelated.

A correlation between the P2 EPR spectrum and the N3 optical spectrum was first noted in 1965 [9], and was later corroborated over an order of magnitude in concentration [7]. Furthermore, both EPR and optical spectra were shown to react similarly to photoexcitation [7], providing further evidence that the two signals

originate at the same point defect.

8.1.1 Electronic structure of N_3V

The Coulson and Kearsley model for N_3V is very similar to that for NV, but with the valances of the constituents swapped according to the interchange of carbon and nitrogen atoms. The centre possesses point group symmetry $\mathscr{C}_{3v}$, and the dangling orbitals pointing into the vacancy from each nearest neighbour are chosen as the one-electron basis (see figure 8-3). The basis spans $2\mathbf{A_1} \oplus \mathbf{E}$ with the following molecular orbitals (see figure 8-3):

$$\begin{aligned} \mathrm{a_{1C}} &\left\{ \quad \phi_d \right. \\ \mathrm{e} &\left\{ \begin{array}{l} 2\phi_a - \phi_b - \phi_c \\ \phi_b - \phi_c \end{array} \right. \\ \mathrm{a_{1N}} &\left\{ \quad \phi_a + \phi_b + \phi_c \, , \right. \end{aligned}$$

where the subscripts C, N indicate that the orbital is predominantly on the carbon atom or nitrogen atoms, respectively.

The N3 transition is understood to originate at the neutral charge state of N_3V and thus possesses 7 electrons, giving rise to the following many-electron states:

$$\begin{aligned} \mathrm{a_{1N}^2\, e^4\, a_{1C}^1} &\rightarrow {}^2\mathrm{A_1} \\ \mathrm{a_{1N}^2\, e^3\, a_{1C}^2} &\rightarrow {}^2\mathrm{E} \\ \mathrm{a_{1N}^1\, e^4\, a_{1C}^2} &\rightarrow {}^2\mathrm{A_1} \, . \end{aligned}$$

Uniaxial stress studies assign the N3 ZPL to a transition between $^2A_1$ and ^2E states, with the $^2A_1$ state being the electronic ground state [10, 11].

This description of $(N_3V)^0$ presents a problem for the vacancy-cage model, in that it is not possible to understand the N2 and N4 transitions within the model. The transitions between each of the different many electron states are all symmetry- and spin-allowed (the dipole operator symmetry in $\mathscr{C}_{3v}$ is $\mathbf{A_1} \oplus \mathbf{E}$) and cannot account for the weak intensities observed for both transitions.

Luminescence lifetime measurements on N3 show a dramatic increase in radiative decay rate for temperatures above approximately 400 K [12], suggesting that

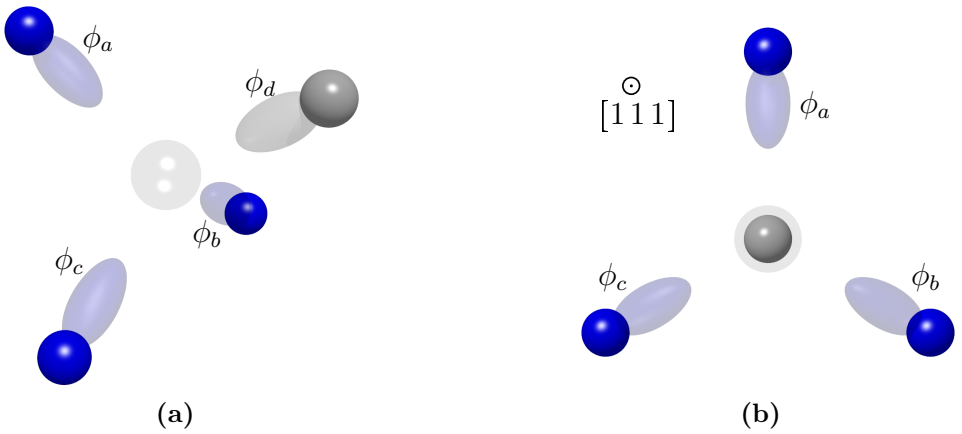

Figure 8-3 The Coulson and Kearsley vacancy-cage model for N_3V. Generic sp^3-like electronic wavefunctions are chosen as the one-electron basis.

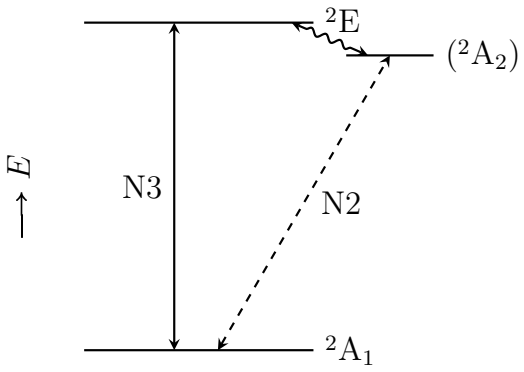

Figure 8-4 Energy level structure of the in-gap states for N_3V according to the model proposed by Thomaz and Davies [12]. Solid line is a spin- and symmetry-allowed transition, dashed line is forbidden by symmetry, and wavy line indicates a vibrational transition.

radiative decay pathways became thermally accessible at high temperature. The authors of that study also noted that the linewidth of the N2 transition was significantly larger than those usually observed in diamond (e.g. 3.5 and 26.7 meV for the N3 and N2 transitions, respectively [7]). These two pieces of information were combined to suggest that the N2 transition was in fact vibronic, with no ZPL present [12]. The lack of a ZPL was explained by assigning $^2A_2$ symmetry to the excited state of N2 (figure 8-4): optical transitions between the ground $^2A_1$ state and N2 excited state would therefore be symmetry-forbidden ($\mathbf{A_1} \notin \{\mathbf{A_2} \times (\mathbf{A_1} + \mathbf{E})\}$, §3.6.1).

Population transfer between the ^2E and $^2A_2$ states would occur via **E** phonons, and required a weak pseudo-Jahn-Teller distortion of the ^2E state [12]. The lifetime observations could then be explained: phonon-assisted decay from the excited ^2E state into the $^2A_2$ state, from where no luminescence was possible, would cause long lifetimes at low temperature; at higher temperatures, thermal excitation from the $^2A_2$ state back into the ^2E state (from where it would rapidly luminesce) accounts for the decrease in lifetime.

This model then explains the weak intensity of the N2 line and the observed lifetime behaviour, but fails to account for the N4 transition and requires states of unknown origin: a trigonal centre can generate an $\mathbf{A_2}$ state only by possessing two electrons in an e state — not possible here due to the available one-electron configurations (above).

The electronic structure of N3 was later addressed with spin-polarised DFT calculations. The calculations demonstrated that even for the lowest-energy excited states, calculations must take into account orbital levels outside the vacancy-cage and therefore not accounted for in the Coulson and Kearsley model [13]. A similar model has been suggested for the GR2–8 transitions at $(V)^0$: these states can be visualised as an electron orbiting a $(V)^+$ nucleus [14].

In this case, the authors report an orbital state whose wavefunction is localised outside the vacancy-cage with symmetry $\mathbf{A_1}$; the authors named this higher-energy level a_1^* (figure 8-5). No details on the spatial extent of the "external" wavefunction are given.

Within this orbital model the low intensity of the N2 and N4 transitions is due to small wavefunction overlap between the in-cage ground state and the external excited state wavefunctions: the matrix elements are correspondingly small and hence observation of the ZPL is not expected. The authors suggest that the distortions associated with phonon activity modify the wavefunction overlap, such that the vibronic structure becomes weakly visible [13]. Finally, the luminescence lifetime change observed at high temperature is ascribed to thermal excitation from the $^2A_1^*$ state to the ^2E state.

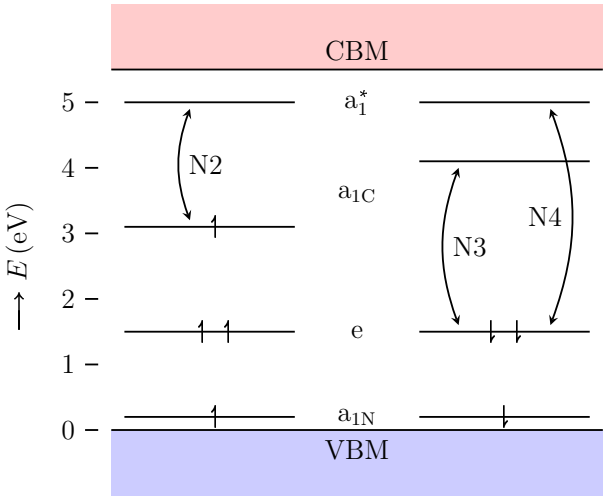

(a) One-electron picture for spin-up (left) and spin-down levels. The a_{1C} state is split by the exchange interaction [13].

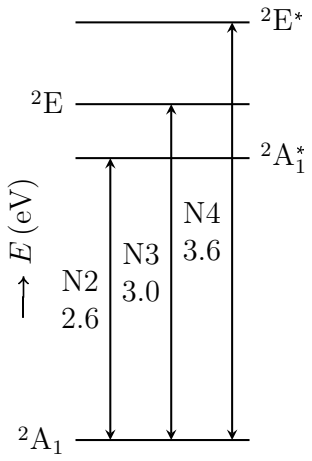

(b) Many-electron picture. States not accounted for by the vacancy-cage model are marked $*$.

Figure 8-5 Energy level structure for N_3V according to the model proposed by Jones et al. and adapted from the paper [13]. The one- and many-electron configurations associated with each transition are shown, and the transition energies are given to the right.

8.1.2 Production of $^{15}N_3V$ in synthetic diamond

The sample used in this study was grown by the highly-controlled process described in §7.1. Post-growth the sample contained approximately $[(^{15}N_s)^0] = 80(2)$ ppm and $[(^{14}N_s)^0] = 4(3)$ ppm. The sample was cut along crystal axes in anticipation of uniaxial stress measurements. In order to maximise the final sample mass, the sample was from multiple sectors and as a result the nitrogen distribution was highly heterogeneous (figure 8-6).

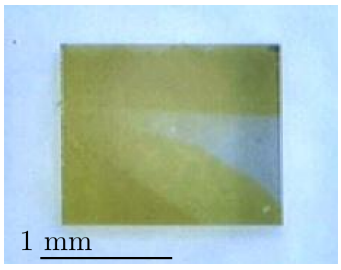

Figure 8-6 Optical micrograph of the sample used for this study (taken before irradiation). The contrast is due to differential nitrogen uptake in each of the sectors during growth.

The sample was irradiated to a total dose of 5×10^{17} neutrons cm^{-2} under atmo-

spheric conditions, at an estimated sample temperature of approximately 200 °C [15]. The sample was then annealed for 15 h at 1500 °C in a non-oxidising atmosphere, before being annealed further under HPHT conditions for 1 h at a nominal temperature of 1900 °C. After processing, the sample was measured (by IR absorption) to contain $[(^{15}N_s)^0] \approx 20$ ppm; $[(^{15}N_s)^+] \approx 5$ ppm; and $[^{(15)}A] \approx 40$ ppm. The fits for the post-processing spectrum are relatively poor (figure 8-7b) and hence the concentrations given must be taken as very approximate. In figure 8-7b, the red plot is a sum of the components given above; the blue plot is produced with the addition of 15 ppm of $^{(14)}B$ (atomic constituents $^{14}N_4V$) due to the lack of a suitable $^{(15)}B$-centre reference. The resulting spectral profile is qualitatively similar to the experimental data, and displays a shift of approximately 4 cm^{-1} in the 1178 cm^{-1} peak: this value is very close to the 5 cm^{-1} shift observed in the 1130 cm^{-1} peak of $(N_s)^0$ when moving from ^{14}N to ^{15}N [16].

The total concentration of $(^{15}N_3V)^0$ generated by this processing regime was approximately 1.0(2) ppm, as measured by EPR. Photoluminescence measurements of the sample post-processing were dominated by N3 ($(N_3V)^0$), H3 ($(NVN)^0$), H2 ($(NVN)^-$), $(NV)^-$ and $(NV)^0$.

In terms of nitrogen concentration post-growth, the sample used here (80 ppm) and the sample used in the previous chapter (100 ppm) were very similar. Both samples were HPHT annealed, with the higher-nitrogen sample held at a higher temperature during processing. However, the lower-nitrogen sample used here contains significant concentrations of $(N_3V)^0$ and negligible (< 0.1 ppm) $(NVN)^-$, whereas the higher-concentration sample contained nitrogen predominantly in the $(N_s)^0$ and $(NVN)^-$ forms ($[(N_3V)^0] < 0.1$ ppm), despite the higher processing temperature. The difference in aggregation levels is ascribed to the high neutron dose this sample received before processing, which accelerated aggregation due to the high concentration of vacancies present [17].

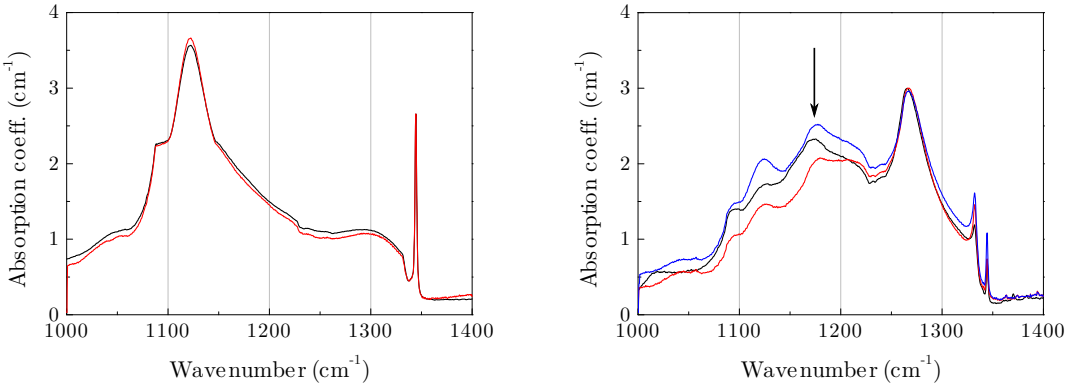

(a) As-grown

(b) Post-irradiation, annealing and HPHT processing

Figure 8-7 One-phonon region IR spectra of the sample before and after processing. In each case, the black (non-zero at low wavenumber) line is the experiment and the red and blue lines are are fits using the components described in the text. The energy shift in the 1178 cm^{-1} between the $^{(14)}$B reference and $^{(15)}$B sample measurement has been highlighted.

8.2 EPR of $^{15}N_3V$

After the HPHT processing and characterisation by infrared spectroscopy, the sample was measured by EPR. Spectra were collected at both X- and Q-band using the experimental setup described in §7.3.1.2. A typical EPR spectrum with the magnetic field applied along ⟨0 0 1⟩ is given in figure 8-8. $^{15}N_3V$ was identified by modifying the published Hamiltonian parameters for $^{14}N_3V$: the hyperfine interaction strengths were scaled by the ratio of the isotopic nuclear g-values (g_{14} = 0.403 761 and g_{15} = −0.566 378 [18]) and the quadrupolar interaction was removed.

For a $\mathscr{C}_{3v}$ centre observed along ⟨0 0 1⟩, all sites are equivalent and hence only one g-value is observed. Furthermore, the hyperfine interactions for each nitrogen are also equivalent, and for three equivalent $I = \frac{1}{2}$ nuclei at an $S = \frac{1}{2}$ centre, a 1:3:3:1 intensity pattern is expected. In fact, the approximate pattern is 1:1:2:2:1:1 (figure 8-8), with the highest-intensity lines split by second-order hyperfine effects.

The difference in complexity between the $(^{14}N_3V)^0$ (figure 8-1) and $(^{15}N_3V)^0$ spectra is striking. Consider $(^{14}N_3V)^0$: ^{14}N is an $I = 1$ nucleus and the number of energy levels per m_S manifold is 3 per nucleus, $3^3 = 27$ in total per site. The

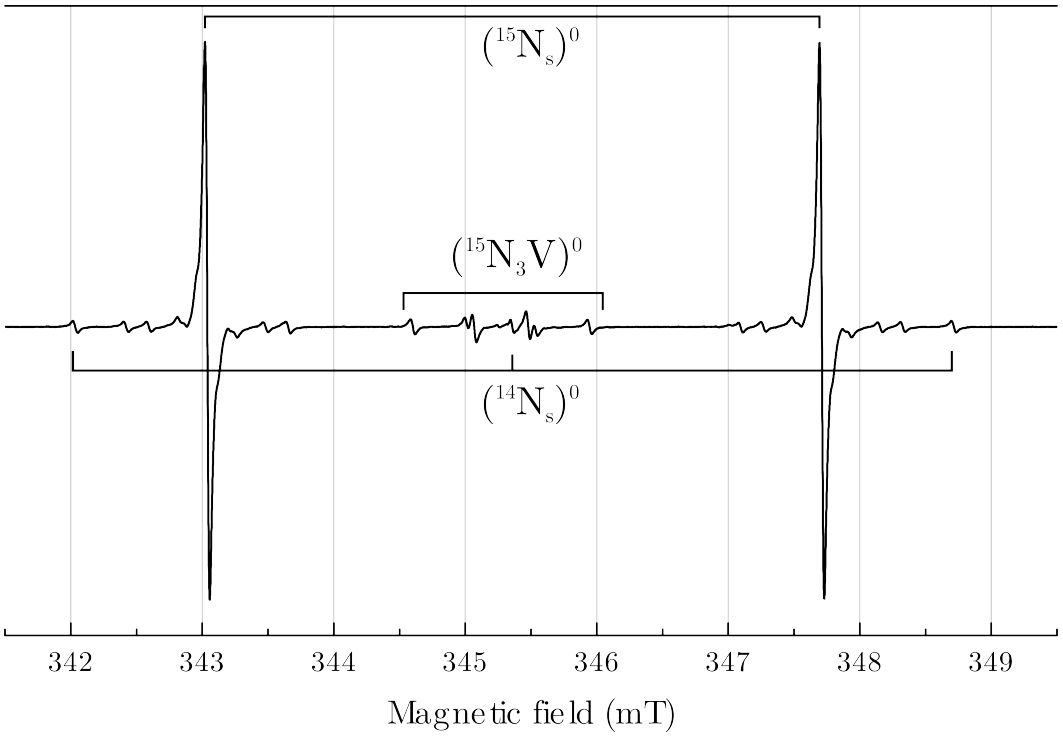

Figure 8-8 X-band measurement of the sample post-irradiation, annealing and HPHT processing. Spectrum collected with the sample at room temperature and with the magnetic field along ⟨1 0 0⟩. Components are labelled for clarity.

quadrupole interaction mixes allowed ($\Delta m_S = 1$; $\Delta m_I = 0$) and forbidden ($\Delta m_S = 1; \Delta m_I \neq 0$) transitions with the effect that forbidden transitions acquire significant intensity: as a result, the spectrum consists of up to $27^2 = 729$ transitions per site. Conversely, ^{15}N has $I = \frac{1}{2}$ and is not therefore not quadrupolar, so the total number of transitions per site is $2^3 = 8$.

Historically, the difficulties in trying to deconvolve the ^{14}N spectrum has meant that Hamiltonian parameter values were difficult to extract and subject to large uncertainties (§8.1). The most successful approach thus far has been to perform ENDOR measurements [3, 6], which have the advantage over EPR of much narrower linewidths and reduced spectral complexity [19]. Nevertheless, the most recently-published parameters are still a poor fit to experiment for any applied magnetic field direction other than ⟨1 0 0⟩ (see figure 8-10) and hence quantification of $(N_3V)^0$ has remained a challenge.

The observation of $(^{15}N_3V)^0$ in this sample allows the g-values and hyperfine parameters to be accurately measured without the additional complexity of the

quadrupole interaction. As in the previous chapter, the X- and Q-band data were analysed to extract resonance fields (magnetic field strength for a particular transition at a given microwave frequency) for each of the different sites and field directions, and the Hamiltonian parameters were varied to minimise the sum of the squares using EPR-NMR [20]. The g-values are given assuming that $(^{14}N_s)^0$ possesses an isotropic g-value of 2.0024. The best-fit Hamiltonian parameters are given in table 8-1, and a comparison of the experimental spectra and simulated spectra is given in figure 8-9. Allowing the g-tensor to deviate from ⟨1 1 1⟩ did not improve the fit.

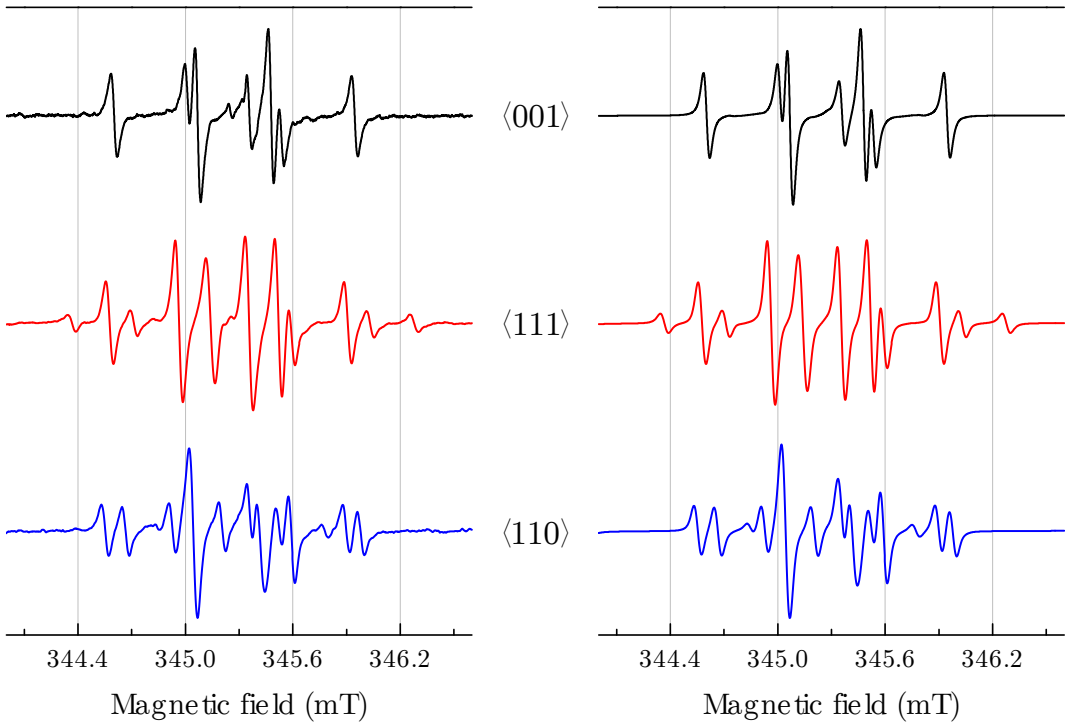

Figure 8-9 A comparison of experimental (left) and simulated spectra at a microwave frequency of approximately 9.680 GHz. The orientation of the magnetic field for each spectrum is given in the centre. The simulations include $(^{15}N_3V)^0$, $(^{14}N_s)^0$ (visible at 345.4 mT) and $(^{15}N_s)^0$ (outermost lines in the ⟨1 1 0⟩ direction are forbidden transitions of $(^{15}N_s)^0$), and have been field-corrected assuming that $(^{14}N_s)^0$ has an isotropic g-value of 2.0024.

Having obtained high-precision hyperfine and g-tensor values for $(^{15}N_3V)^0$, the only unknown parameters in the $(^{14}N_3V)^0$ Hamiltonian were the quadrupole interaction strength, direction and rhombicity. A natural sample containing a high concentration of $(^{14}N_3V)^0$ was measured at room temperature using the high-sensitivity, low-power 90 dB X-band bridge in order to obtain reference ^{14}N spec-

		Published [6] $(^{14}N_3V)^0$	This work $(^{14}N_3V)^0$	$(^{15}N_3V)^0$
g-tensor	$g_\parallel$	2.0023(2)	2.002 52(5)	[a]
	$g_\perp$	2.0032(2)	2.003 36(5)	
	$\theta(^\circ)$[b]	35.26	35.26	
A-tensor (MHz)	A_1	7.4(1)	7.51(4)	10.54(5)
	A_2	7.4(1)	7.57(4)	10.62(5)
	A_3	11.2(1)	11.24(4)	15.77(5)
	$\theta(^\circ)$	158(1)	157.8(2)	
P-tensor (MHz)	$P_\parallel$	−4.8(1)	−4.68(5)	N/A
	η[c]	0	0	
	$\theta(^\circ)$	145(2)	144.7(5)	

[a] Blanks indicate values are as $(^{14}N_3V)^0$
[b] θ measured from [1 1 0] toward [0 0 1]
[c] Rhombicity: $\eta = (P_x - P_y)/P_z$

Table 8-1 The measured spin Hamiltonian parameters for the N_3V defect. Parameters have been given for ^{14}N-doped diamond by scaling the measured ^{15}N hyperfine values by the ratio of the nuclear g-values $g_{14} : g_{15}$ ($g_{14} = 0.403\,761$ and $g_{15} = -0.566\,378$ [18]). The g-tensor values are given assuming that $(^{14}N_s)^0$ has an isotropic g-value of 2.0024.

tra. Due to the multitude of lines in the centre of each spectrum, it was only possible to obtain accurate resonance field values for approximately 10 transitions on the high- and low-field sides of each spectrum. The measured $(^{15}N_3V)^0$ hyperfine values were scaled using the nitrogen isotopic g-values and a least-squares fit to the data was performed, with the only free parameters relating to the quadrupole.

All Hamiltonian parameters obtained during this study are within the uncertainties given for the published values (see table 8-1): nevertheless, these small changes have a dramatic effect on the quality of spectral fit. The differences are greatest for spectra taken with the magnetic field along the ⟨1 1 1⟩ direction (where the previous Hamiltonian parameters fail to reproduce the spectrum in any way (figure 8-10)), are significantly smaller for the ⟨1 1 0⟩ direction and are essentially nil for the ⟨1 0 0⟩ direction.

Simulations show that taking the published parameters and replacing the g-values with those determined here greatly improves the fit: the primary difference be-

tween the sets of parameters is therefore the g-values. The effect of changing the g-values on the different directions may be explained thus: with the field along $\langle 1\,0\,0\rangle$, all sites for a $\mathscr{C}_{3v}$ centre are identical and hence all have the same effective g-value — by changing the g-values, the only change is a small field-shift of the whole spectrum. For $\langle 1\,1\,0\rangle$, there are two effective g-values and the spectral profile will be sensitive to the difference between them. With the field aligned along an arbitrary direction, the effective g-values are given by

$$g_{\text{eff}}^2 = g_\perp^2\left(\cos^2(\theta_{B,X}) + \cos^2(\theta_{B,Y})\right) + \left(g_\parallel \cos(\theta_{B,Z})\right)^2 ,$$

where $\theta_{B,N}$ is the angle between the applied magnetic field and the Nth primary axis of the g-tensor [21]. Computing the effective g-values for both sets of g-tensors along $\langle 1\,1\,0\rangle$ gives a relative field shift of the two g-values of only 0.006 mT at a microwave frequency of 9.75 GHz (calculated using $\hbar\omega = g_{\text{eff}}\mu_B B$): as the linewidth in this sample is approximately 0.01 mT, the effect is almost imperceptible. Finally, with the field along $\langle 1\,1\,1\rangle$, the calculated relative field shift due to the two effective g-values is still small at approximately 0.01 mT. However, the spectrum contains a large number of accidental degeneracies (accidental in the sense that they occur due to the numerical g-values involved, rather than any restrictions by symmetry etc.), and hence small relative g-value shifts have the effect of introducing many further lines (as is the case in the central spectrum of figure 8-10).

8.2.1 Spin-polarisation

In 1997, a report was published demonstrating photochromic behaviour of the N3 optical absorption: the strength of the absorption was shown to increase in a neutron-irradiated and annealed type Ib diamond when photoexcited by the 2.410 eV (514.5 nm) line of an Ar^+ laser [22]. Based on the history of the sample, the authors assigned this to a charge transfer effect between $(N_s)^0$ and $(N_3V)^0$:

$$(N_3V)^- + (N_s)^+ \rightarrow (N_3V)^0 + (N_s)^0 ,$$

although no measurements of $(N_s)^0$ changes were performed.

EPR is an ideal technique to study this phenomenon, as both $(N_3V)^0$ and $(N_s)^0$ are EPR-active and therefore any changes in concentration of either could be recorded

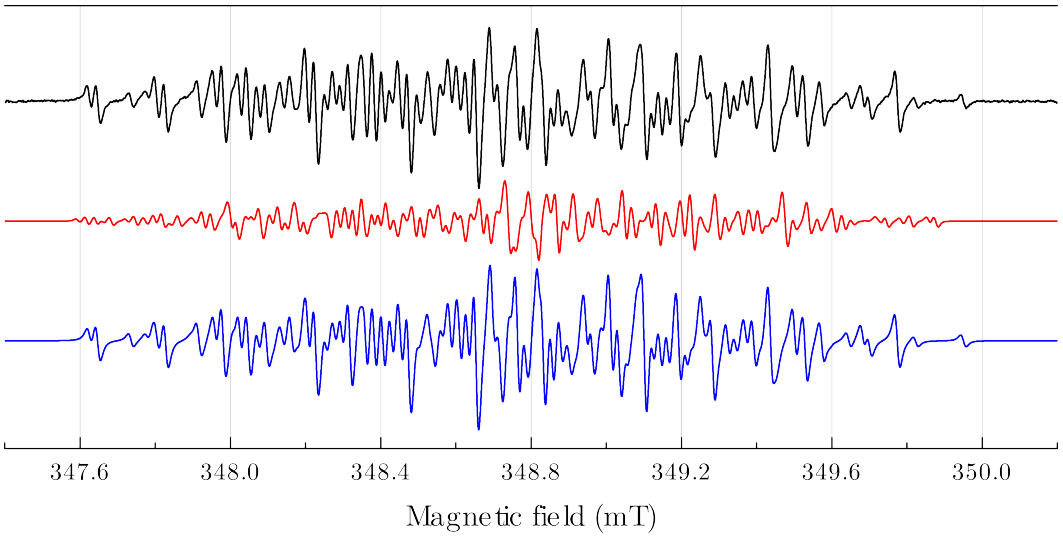

Figure 8-10 A comparison of experimental and simulated $(^{14}N_3V)^0$ spectra with the applied magnetic field along ⟨1 1 1⟩. Top to bottom: experiment; simulation using the parameters given in the most recent literature [6]; simulation using parameters determined in this study. Simulations include $(^{14}N_s)^0$.

simultaneously. Additionally, the improved fitting allowed by the Hamiltonian parameter study in the previous section will permit changes to be quantified with much smaller uncertainties than was previously possible, and with negligible fitting errors in the case of the ^{15}N-doped sample.

To investigate any possible photochromic behaviour at room and low temperature, the ^{15}N-doped sample was glued onto the end of a quartz lightguide (§7.3.1.2) and placed inside a continuous flow nitrogen cryostat mounted into a cylindrical cavity resonator. As with the previous chapter, a 1 kW Xe arc lamp was employed as a light source, and glass absorption filters were used to select the energies of light passed to the sample.

Initial measurements at room temperature showed no change in either $(N_s)^0$ or $(N_3V)^0$, within fitting errors. Liquid helium was then used to perform low-temperature measurements under photoexcitation. At very low temperatures, spin-lattice (longitudinal) relaxation times tend to become very long in diamond, with the effect that it is difficult not to saturate transitions even with a low-power microwave source: this will account for the asymmetry of some of the observed peaks at low temperature. Nevertheless, it was immediately apparent upon the

first illuminated measurement that saturation could not account for the collected spectrum (figure 8-11). The areas highlighted in the figure show evidence of non-(thermal) equilibrium spin populations.

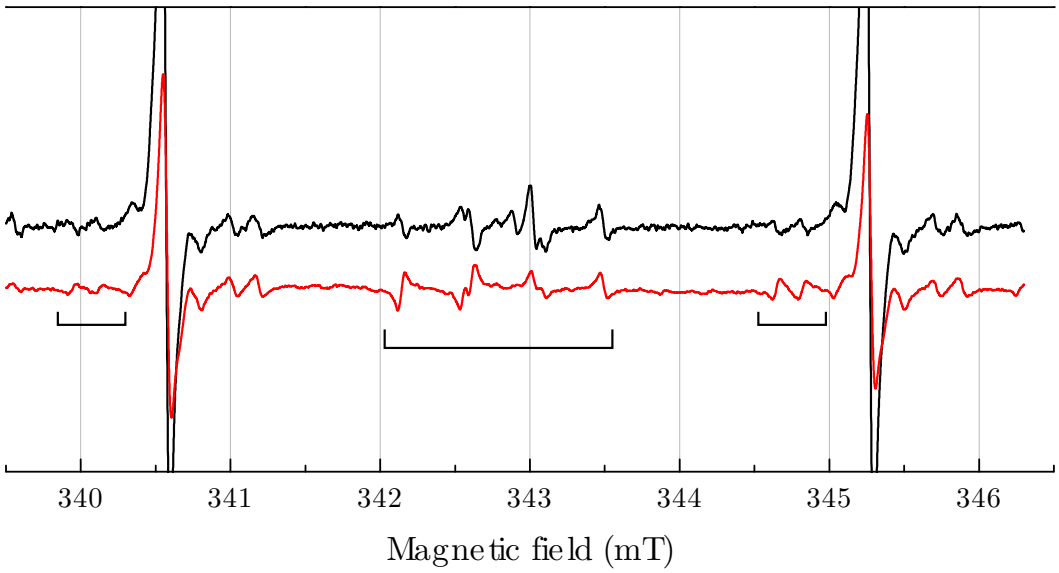

Figure 8-11 Experimental spectra collected with (bottom) and without (top) photoexcitation from a Xe arc lamp. The spectra were collected with the field along ⟨1 0 0⟩ at a temperature of 40 K. Areas highlighted indicate non-equilibrium spin population. Outer pair of lines belong to $(^{15}N_s)^0$; inner lines belong to $(^{15}N_3V)^0$. The spectra have each been normalised by the number of accumulated scans.

In a steady-state situation (all parts of the sample in thermal equilibrium), the relative populations of two states separated by energy ΔE is given by the Maxwell-Boltzmann distribution [21]

$$\frac{n_u}{n_l} = \exp\left(\frac{\Delta E}{k_B T}\right) ,$$

where n_u and n_l are the populations of the upper- and lower-energy states, respectively. At resonance, this condition is equivalent to

$$\frac{n_u}{n_l} = \exp\left(\frac{\hbar\omega}{k_B T}\right) .$$

When on resonance, the rates of stimulated absorption and emission are identical, so the observed signal intensity is proportional to the population difference of the two levels between which the resonance occurs [19]. The effect of level populations on transition intensities is illustrated in figure 8-12.

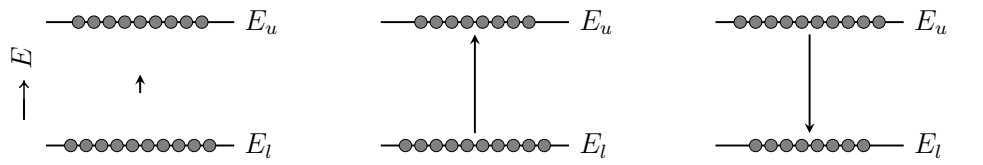

(a) 300 K **(b)** 40 K **(c)** Non-equilibrium population

Figure 8-12 Illustration of level populations and their effect on transition intensity. In the first two cases, the level populations are in thermal equilibrium, and the length of the arrow is proportional to the relative signal strengths observed in experiment (and also to the population difference between the two levels). In the third case, a process has caused population inversion and hence the transition would be observed as an emission line, not absorption.

The two defects involved, $(^{15}N_s)^0$ and $(^{15}N_3V)^0$, are both $S = \frac{1}{2}$, $I = \frac{1}{2}$, and so the energy levels are dependent on both electronic and nuclear interactions. Two different types of spin-polarisation must therefore be defined:

Electronic spin-polarisation A non-equilibrium population in one or more of the $|m_S\rangle$ states. For a simple $S = \frac{1}{2}$ defect, this will correspond to the entire spectrum changing intensity whilst maintaining the same relative transition intensities. Increased population in the lower state will cause enhanced absorption, and increasing populations in the higher-energy state will, in turn, lead to diminished absorption, no signal ($n_u = n_l$), and then emission ($n_u > n_l$).

Nuclear spin-polarisation A non-equilibrium population in one or more of the $|m_I\rangle$ states. This will correspond to a change in relative intensity of the hyperfine-split transitions.

The macroscopic interpretation of the lower spectrum in figure 8-11 must therefore include both effects: the optical pumping leads to enhanced population of some nuclear sublevels of the higher-energy electronic state (see figure 8-13).

The polarisation mechanism becomes much more efficient with the magnetic field along $\langle 1\,1\,1\rangle$ (figure 8-14). Here, nuclear and spin polarisation of both $(^{15}N_s)^0$ and $(^{15}N_3V)^0$ has occurred, with some hyperfine satellites no longer visible in the case of $(^{15}N_3V)^0$ (high field pair, approximately 342.4 mT).

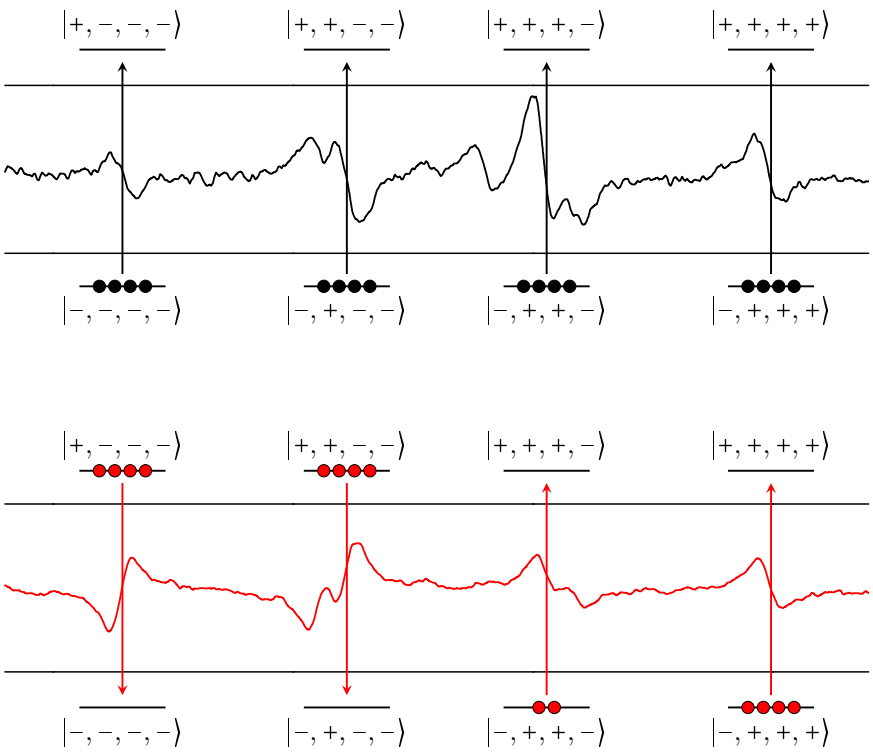

Figure 8-13 Illustration of the $(N_3V)^0$ spin-polarisation behaviour observed with the magnetic field along $\langle 1\,0\,0 \rangle$. The black spectrum (top) was measured with no illumination, and the red spectrum with the full range of the Xe arc-lamp as transmittable by the liquid light-guide. The basis for the states given is $|m_S, m_I, m_I, m_I\rangle$ with $|m_S| = |m_I| = \frac{1}{2}$ (state-mixing and second-order hyperfine effects have been neglected). Allowed transitions ($\Delta m_S = 1$) have been marked in absorption (transition upward) or emission (transition downward), and excess populations are indicated by dots. For purely electronic spin-polarisation, the populations in all four red states would be equal. Vertical scales are the same in each case.

The strength and nature of the spin-polarisation effect were not observed to change up to the highest temperature measured (140 K), although no effect upon illumination was observed at room temperature. As would be expected for a non-equilibrium state, the signal intensity did not follow a Curie law dependence (i.e. $I \not\propto \frac{1}{T}$). Long-pass (low-energy pass) optical absorption filters were used to investigate the energy-dependence of the spin polarisation at a temperature of 40 K. The integrated intensity of $(^{15}N_s)^0$ peaks 1–4 (highlighted in figure 8-14) were tracked as a function of the cutoff energy of the filters: the results are given in figure 8-15.

Small changes are noted in one of the $(^{15}N_s)^0$ hyperfine satellites at relatively low

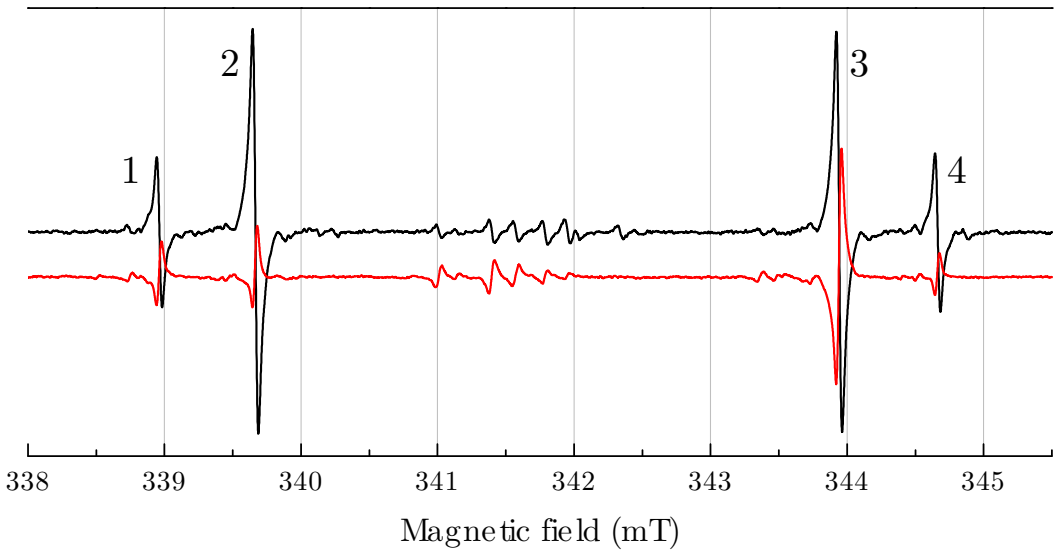

Figure 8-14 Experimental spectra collected with (bottom) and without (top) photoexcitation from a Xe arc lamp. The spectra were collected with the field along ⟨1 1 1⟩ at a temperature of 40 K. The outer pair of lines on either side belong to $(^{15}N_s)^0$, with $(^{15}N_3V)^0$ in the centre. The spectra have each been normalised by the number of accumulated scans. Peaks are numbered as described in the text.

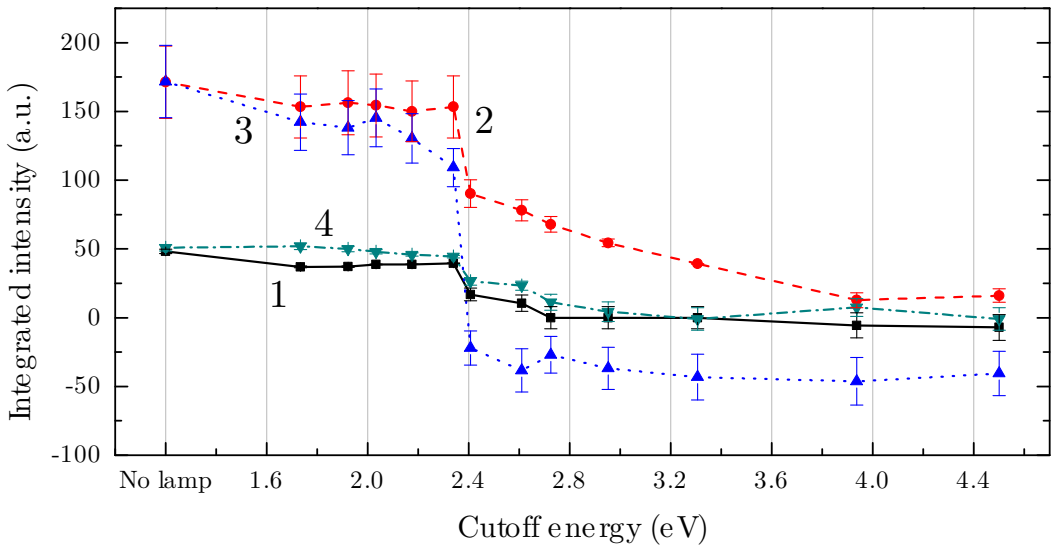

Figure 8-15 Integrated intensity of $(^{15}N_s)^0$ peaks 1–4 (figure 8-14) as a function of illumination energy. Values collected without illumination are given on the left; 4.5 eV corresponds approximately to the upper edge of the liquid lightguide passband.

energy, but the major changes are between 2.2–2.6 eV. The $(^{15}N_3V)^0$ spectrum followed a similar pattern, with small changes to the lowest-field line at low energy, but with the majority of the spectrum inverting between the energies of 2.2(1) eV and 2.4(1) eV. It is unclear whether further changes are due to higher energy

incident light, or simply higher intensity.

8.2.1.1 Mechanism

The author is unaware of any reports of spin-polarisation effects for either $(N_s)^0$ or $(N_3V)^0$. ^{15}N-doped diamond has been studied in EPR under photoexcitation previously (even to investigate spin polarisation effects in $(^{15}NV)^-$) but spin polarisation of $(^{15}N_s)^0$ was not observed [23–25]. Therefore, the spin-polarisation of $(^{15}N_s)^0$ is due to interaction with external effects, rather than being intrinsic to $(^{15}N_s)^0$ itself.

From the data collected, it cannot be unambiguously determined whether the spin-polarisation of $(^{15}N_3V)^0$ is due to internal transitions or interaction with other defects. The similar optical energy dependence of $(^{15}N_s)^0$ and $(^{15}N_3V)^0$ suggests that either the defects are coupled directly or they both couple to the same source of external polarisation.

At the most abstract level, the observation of spin-polarisation requires a transition which is spin-sensitive i.e. does not behave identically for unlike spin-states. Here, two mechanisms will be discussed, both of which rely on a phenomenon known as intersystem crossing.

Direct optical transitions are spin-conserving i.e. $\Delta m_S = \Delta m_I = 0$. For example, an electronic dipole transition between a singlet state ^{1}X and a triplet state ^{3}Y is forbidden in the absence of other interactions, even in the case that it is allowed by orbital symmetry. However, in the presence of spin-orbit coupling, an intersystem crossing may occur whereby an excited state with a given spin-multiplicity may undergo decay into a lower-energy state with a different spin-multiplicity [26]. Spin-orbit effects have been previously identified in the $(N_3V)^0$ system, observed as a splitting of the ^{2}E excited state of the N3 transition [7, 27].

The intersystem crossing process is shown schematically in figure 8-16 for $(NV)^-$, a defect which is structurally similar to $(N_3V)^0$ and which possesses a spin-polarisation mechanism based on spin-spin and spin-orbit interactions [28]. In $(NV)^-$, the $|m_S\rangle = \pm 1$ and $|m_S\rangle = 0$ spin sublevels of the $^3A_2$ ground state are split

by approximately 2.88 GHz at zero field [29] (figure 8-16): the intersystem crossing mechanism preferentially populates the $|m_S\rangle = 0$ sublevel, and can be very efficient — polarisations of greater than 90 % have been observed [30].

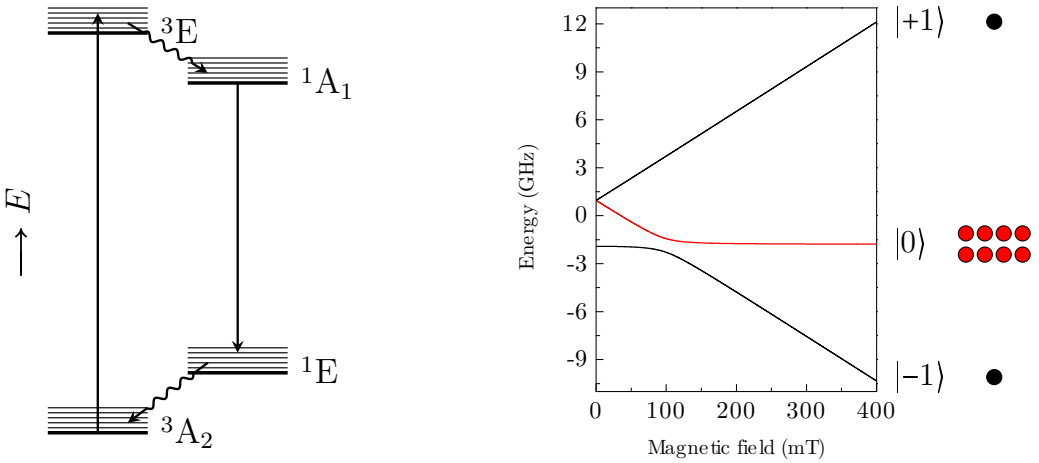

(a) Electronic energy levels of $(NV)^-$

(b) Spin sublevels of the $^3A_2$ ground-state.

Figure 8-16 A simplified version of the spin-polarisation mechanism of $(NV)^-$, as put forward by Delaney et al. [28]. Left: nonradiative intersystem crossings (primarily due to spin-orbit coupling) are shown as wavy lines, and direct optical transitions as solid arrows. Thick bars indicate purely electronic states, and thin bars are higher-energy vibronic levels of the same orbital state. Relative energies of states are not to scale. Right: the spin sublevels of the spin-triplet ground state as a function of applied magnetic field (in a $\langle 1\,1\,1\rangle$ direction). The basis given is $|m_S\rangle$: state-mixing has been ignored. As with previous figures, the dots indicate the relative level populations, in this case under illumination from a 2.33 eV (532 nm) laser [31].

Intersystem crossings have also been observed in $(NV)^0$: upon optical excitation, significant population crosses from the $^2A_1$ excited state into a lower-energy $^4A_2$ state. The state is long-lived and highly-populated enough to perform CWEPR [32]. Intersystem crossings therefore appear to be a feature common to both N_1V and N_3V.

An intersystem crossing process requires states of two different spin-multiplicities. Starting from the one-electron model of $(N_3V)^0$ by Jones [13] (summarised in §8.1.1), the resultant many-electron states may be computed from the one-electron states (§3.5). The one-electron states in this model may contain a total of ten electrons (two each for the a_1 states, four for the e), and $(N_3V)^0$ contains a total of

seven: therefore there are several different configurations, many of which will lead to many-electron states of the same symmetry and spin. In order to simplify the calculation, it is noted that $\mathbf{A_1} \otimes \mathbf{A_1} = \mathbf{A_1}$ and therefore the three a_1 one-electron states may be combined into a state x, which transforms as $\mathbf{A_1}$ and contains up to six electrons. Furthermore, as holes and electrons transform identically and an e state may contain four electrons (holes), it follows that $e^1 = e^3$ [33]. The one-electron configurations and resultant many-electron states are therefore

$$\begin{aligned} e^4x^3 &\rightarrow {}^4A_1, {}^2A_1 \\ e^3x^4 &\rightarrow {}^4E, {}^2E \\ e^2x^5 &\rightarrow {}^2A_1, {}^4A_2, {}^2E \ , \end{aligned}$$

where multiple states of the same symmetry and spin have been omitted. Any of the several spin-quartet levels computed above might lead to a similar intersystem crossing phenomenon to $(NV)^-$, but without knowledge of the energetic ordering of the different many-electron states, any attempts at trying to identify the levels involved are of limited utility.

The energy-dependence of the spin-polarisation (figure 8-15) makes it unlikely that the spin polarisation is due to the N3 transition itself (at 2.985 eV), but does not rule out lower-energy transitions. The N2 transition, at 2.596 eV, is in closer proximity to the observed polarisation effects around 2.3 eV.

The second spin-polarisation mechanism discussed here, proposed by Watkins [34], relies on the creation of $(N_3V)^0$ by ionisation of a different charge state of N_3V. Watkins noted that the capture of charge from either the valence or conduction bands would lead to equilibrium populations and hence cannot explain the polarisation behaviour. However, if ionisation of either $(N_3V)^-$ or $(N_3V)^+$ produces $(N_3V)^0$ in an excited state from which intersystem crossing may occur, then spin-polarisation is possible. In this material, with an abundance of single nitrogen (donors), it is likely that if N_3V does exist in a charge state other than neutral, it will be negatively charged.

Spin-polarisation by ionisation is interesting in light of the $(N_3V)^0$ photochromism reported by Mita and summarised at the beginning of section 8.2.1 [22]. In that

report, the strength of the photochromic effect (measured as change of absorption coefficient at 2.985 eV) was recorded as a function of excitation energy by using a Xe arc-lamp in conjunction with 10 nm bandpass filters. The photochromic effect began with illumination of approximately 1.6 eV, rising sharply in magnitude by 2.0 eV, and was essentially constant for higher energies before dropping off at approximately 4.0 eV. This behaviour does not match the spin-polarisation energy dependence given in figure 8-15, and hence the two effects are unlikely to be simply related.

Whichever mechanism is responsible for the observed spin-polarisation, it is relatively fast: neither the build-up or decay of non-equilibrium populations was visible, appearing instantaneous on the timescale of the experiment (approximately one second). Although electronic spin-polarisation tends to be fast (microseconds or less, as in the case of $(NV)^-$), nuclear polarisation is often a slow process, with many examples taking minutes to achieve maximal polarisation due to very slow cross-relaxation rates [35]. The speed of the process here suggests that the nuclear and electronic spin-polarisation effects have the same origin.

Finally, this effect has not previously been observed in $(^{14}N_3V)^0$: this is ascribed to the strong quadrupolar interaction causing significant state-mixing and therefore preventing significant population build-up in any one state. Using the improved Hamiltonian parameters determined in the previous section, careful measurements of $(^{14}N_3V)^0$ should allow any effect of illumination to be investigated.

8.2.1.2 Coupling to external defects

In general, defects in diamond possess very localised wavefunctions, as evidenced by the difficulties in finding shallow acceptor and donor states [36]. Measurements of $(NV)^-$ show that the wavefunction is localised essentially over atoms involved in the defect itself, and its external magnetic field sensitivity is due to dipolar coupling with external magnetic fields [37, 38]. The coupling observed here between the $(^{15}N_3V)^0$ and $(^{15}N_s)^0$ defects here is proposed to be due to direct wavefunction overlap of the two defects causing polarisation transfer: it is suggested that the delocalised wavefunction in question is the orbit external to the vacancy predicted

by DFT calculations (§8.1.1) [13].

The spatial extent of a delocalised electronic wavefunction in a semiconductor may be very roughly estimated using the hydrogenic model of an impurity [39]. Within the model, the donor electron is modelled as a negative charge orbiting the positive nucleus (the structural defect / impurity). For the lowest-energy orbit, the radius in this model is given by

$$r = \frac{\epsilon_r \hbar^2}{e^2 m^*} ,$$

where ϵ_r is the relative permittivity, e is the elemental charge, and m^* is the effective mass of conduction electrons in the material. For diamond, $\epsilon_r \sim 10$ [40], and DFT calculations give a mean effective mass of $m^* \approx 0.45 m_e$ [41]. The spatial extent of the orbit is therefore of the order of $r \sim 10\,\text{Å}$, or approximately 3 unit cells: this is the same order of magnitude as previous calculations of hydrogenic orbits in diamond [42].

The mean spacing between N_3V and $(N_s)^0$ can be estimated purely on statistical grounds. Simulations show that if a substitutional defect X is distributed randomly throughout a crystal which contains $[(N_s)^0] = 10\,\text{ppm}$, then approximately 5 % of the population of X will be within ten lattice spacings ($\approx 15\,\text{Å}$) of a nitrogen atom [43]. Furthermore, aggregates such as N_3V will be produced in higher-nitrogen sectors and hence the mean separation will be less than in the randomly distributed case.

The simple arguments presented here suggest that direct polarisation transfer between defects in diamond is possible, and that this mechanism is consistent with the experimental data available.

8.3 Conclusions and further work

Following EPR measurements on both ^{15}N- and ^{14}N-doped diamond, the spin-Hamiltonian parameters for $(N_3V)^0$ have been improved for both isotopes. It was found that the primary differences between the parameters determined here and the published values were small changes in g-values. These changes lead to a

much-improved spectral fit, and for the first time an unambiguous assignment to three equivalent nitrogen atoms.

Electronic and nuclear spin-polarisation has been observed in both $(^{15}N_3V)^0$ and $(^{15}N_s)^0$. It has been argued that the polarisation of $(^{15}N_s)^0$ is not due to an internal transition at that defect, and is instead suggested to arise from coupling to a delocalised excited state of $(^{15}N_3V)^0$. Two mechanisms for the electronic spin-polarisation of $(^{15}N_3V)^0$ have been discussed, both of which rely on intersystem crossing from the spin doublet to spin quartet states.

Given the current emphasis on defects in diamond for potential quantum computing applications, the external coupling is very interesting. For instance, $(^{15}N_3V)^0$ could be employed as an optically-controlled gate to mediate interaction between multiple $(NV)^-$ centres, allowing the construction of multiple-qubit systems [44]. Furthermore, the spin polarisation mechanism is viable up to at least 140 K and possibly higher, placing it within the reach of cheap cryogens and purely electronic cooling systems.

Future work should include pulsed EPR experiments such as ELDOR / DEER to directly prove coupling between $(^{15}N_s)^0$ and $(^{15}N_3V)^0$, and to quantify the coupling strength. Pulsed measurements will also determine the rate of polarisation and depolarisation when the illumination is switched on and off. Any further experiments on the spin-polarisation behaviour will be intimately concerned with state populations, and so a density-matrix description is particularly appropriate [45]. Finally, theoretical investigations into the electronic level structure of $(^{15}N_3V)^0$ might identify the states involved in any intersystem crossing processes, in a similar manner to the theoretical work on $(NV)^-$ [28, 29, 46].

References

1. W. Smith, I. Gelles, P. Sorokin, *Physical Review Letters* **2**, 39 (1959).
2. F. A. Raal, *American Mineralogist* **42**, 354 (1957).
3. J. H. N. Loubser, A. C. J. Wright, *Diamond Research*, 16 (1973).
4. M. Y. Shcherbakova, V. A. Nadolinnyi, E. V. Sobolev, *Journal of Structural Chemistry* **19**, 261 (1978).
5. J. A. van Wyk, *Journal of Physics C: Solid State Physics* **15**, L981 (1982).
6. J. A. van Wyk, J. H. N. Loubser, *Journal of Physics: Condensed Matter* **5**, 3019 (1993).
7. G. Davies, C. Welbourn, J. H. N. Loubser, *Diamond Research*, 23 (1978).
8. C. D. Clark, R. W. Ditchburn, H. B. Dyer, *Proceedings of the Royal Society of London A* **237**, 75 (1956).
9. L. du Preez, PhD thesis, University of the Witwatersrand, 1965.
10. W. A. Runciman, *Proceedings of the Physical Society* **86**, 629 (1965).
11. P. Crowther, P. Dean, *Journal of Physics and Chemistry of Solids* **28**, 1115 (1967).
12. M. F. Thomaz, G. Davies, *Proceedings of the Royal Society of London A* **362**, 405 (1978).
13. R. Jones *et al.*, *Physical Review B* **56**, R1654 (1997).
14. A. M. Stoneham, A. Mainwood, presented at the 7th International Conference on Shallow-Level Centers in Semiconductors, ed. by C. A. J. Ammerlaan, B. Pajot, p. 165.
15. S. Liggins, PhD thesis, University of Warwick, 2010.
16. A. T. Collins, M. Stanley, G. S. Woods, *Journal of Physics D: Applied Physics* **20**, 969 (1987).
17. A. T. Collins, *Journal of Physics C: Solid State Physics* **13**, 2641 (1980).
18. N. Stone, *Atomic Data and Nuclear Data Tables* **90**, 75 (2005).
19. A. Abragam, B. Bleaney, *Electron Paramagnetic Resonance of Transition Ions* (Dover Publications, Inc., New York, ed. 2, 1986).
20. M. J. Mombourquette, J. A. Weil, D. G. McGavin, *EPR-NMR*, 1997, `www.chem.queensu.ca/eprnmr`.

21. J. A. Weil, J. R. Bolton, *Electron Paramagnetic Resonance* (John Wiley & Sons, Hoboken, ed. 2, 2007).
22. Y. Mita *et al.*, *Philosophical Magazine Letters* **76**, 93 (1997).
23. S. Felton *et al.*, *Journal of Physics: Condensed Matter* **21**, 364212 (2009).
24. S. Felton *et al.*, *Physical Review B* **79**, 075203 (2009).
25. A. Edmonds, PhD thesis, University of Warwick, 2008.
26. M. de Groot, I. Hesselmann, J. van der Waals, *Molecular Physics* **12**, 259 (1967).
27. J. Walker, *Reports on Progress in Physics* **42**, 1605 (1979).
28. P. Delaney, J. C. Greer, J. A. Larsson, *Nano letters* **10**, 610 (2010).
29. N. B. Manson, J. P. Harrison, M. J. Sellars, *Physical Review B* **74**, 104303 (2006).
30. G. Waldherr *et al.*, *Physical Review Letters* **106**, 157601 (2011).
31. J. Harrison, M. Sellars, N. Manson, *Diamond and Related Materials* **15**, 586 (2006).
32. S. Felton *et al.*, *Physical Review B* **77**, 081201 (2008).
33. C. Coulson, M. Kearsley, *Proceedings of the Royal Society of London A* **241**, 433 (1957).
34. G. Watkins, *Physical Review* **155**, 802 (1967).
35. D. McCamey *et al.*, *Physical Review Letters* **102**, 027601 (2009).
36. J. P. Goss, R. J. Eyre, P. R. Briddon, *Physica Status Solidi (B)* **245**, 1679 (2008).
37. F. Jelezko, J. Wrachtrup, *Physica Status Solidi (A)* **203**, 3207 (2006).
38. P. Maletinsky *et al.*, *Nature Nanotechnology* **7**, 320 (2012).
39. C. Kittel, *Introduction to Solid State Physics* (John Wiley & Sons, New York, ed. 3, 1968).
40. P. T. Narasimhan, *Proceedings of the Physical Society. Section B* **68**, 315 (1955).
41. H. Löfås *et al.*, *AIP Advances* **1**, 032139 (2011).
42. A. M. Stoneham, A. H. Harker, G. W. Morley, *Journal of Physics: Condensed Matter* **21**, 364222 (2009).
43. A. T. Collins, *Journal of Physics: Condensed Matter* **14**, 3743 (2002).

44. A. Bermudez *et al.*, *Physical Review Letters* **107**, 150503 (2011).

45. A. Schweiger, G. Jeschke, *Principles of pulse electron paramagnetic resonance spectroscopy* (Oxford University Press, Oxford, 2001).

46. J. P. Goss *et al.*, *Physical Review Letters* **77**, 3041 (1996).

Chapter 9

Conclusions

The majority of the research presented in this thesis has focused on samples doped with either boron or nitrogen, the two most abundant impurities in diamond. A multi-technique approach has been used to try to understand fundamental irradiation damage in different classes of diamond, and to study the physics of several specific point defects. Advances in growth combined with isotopic substitution have been instrumental in the identification and analysis of several defects in nitrogen-containing diamond.

9.1 Irradiation damage in boron-doped diamond

The effects of electron irradiation on several HPHT- and CVD-grown (boron doped) type IIb samples were investigated. Comparisons were made with an HPHT-grown type IIa sample irradiated under the same conditions (at 100 K, to a dose of $5 \times 10^{17}\,\mathrm{e^-\,cm^{-2}}$). The post-irradiation vacancy and interstitial concentrations were found to depend on the initial boron concentration in the type IIb samples: in cases where the pre-irradiation boron concentration was greater than the vacancy / interstitial concentrations that would be expected for a type IIa sample receiving the same dose ($[(\mathrm{B_s})^0]_i \gg [(\mathrm{V})^0]_f$), the boron concentration was reduced by irradiation and no vacancies or interstitials were observed; for $[(\mathrm{B_s})^0]_i \lesssim [(\mathrm{V})^0]_f$, the neutral boron was removed by the irradiation, no interstitials were observed, and the vacancy concentration was lower than for the cor-

responding type IIa sample; and for $[(B_s)^0]_i \ll [(V)^0]_f$, no neutral boron was observed post-irradiation, with both vacancy and interstitial concentrations lower than the type IIa sample. It was argued that this difference cannot arise solely due to charge effects — in all cases, the combined difference in vacancy and interstitial concentrations in the type IIb samples relative to the type IIa sample was larger than the starting boron concentration.

The post-irradiation CVD type IIb sample was annealed at 100 °C intervals between 100–1400 °C. The majority of spectral features in measurements recorded by all applied techniques had been previously reported in type IIa irradiation studies. This suggests that when moderately boron-doped samples are electron-irradiated at low temperature and $[(B_s)^0]_i \lesssim [(V)^0]_f$, the primary damage centres are identical to those in type IIa material. No evidence was found for either I^+ or $(V)^+$, and no neutral interstitials ($I^0_{\langle 0\,0\,1\rangle}$) were observed post-irradiation, giving an upper limit of $[I^0_{\langle 0\,0\,1\rangle}] \lesssim 0.1 \times [(V)^0]$ (c.f. $[I^0_{\langle 0\,0\,1\rangle}] = [(V)^0]$ in the type IIa sample). These data are consistent with the previous remark that charge compensation alone cannot account for the post-irradiation observations: rather than substitutional boron acting as an isolated acceptor, so that different charge states of familiar defects are observed, the boron appears to be complexing to form aggregated defects (e.g. substitutional boron and carbon interstitials aggregation to form boron-interstitial complexes) during irradiation.

The strongest feature which has only been observed in type IIb material was an absorption line in the mid-infrared, at 0.553 eV (4460 cm^{-1}). The absorption line was produced immediately upon irradiation, and increased in intensity by approximately a factor of 3 at annealing temperatures of 900–1000 °C, before annealing out by 1200 °C. Previous reports show that the 0.553 meV feature is approximately linearly related to the irradiation dose in highly-doped samples, and quickly saturates with dose in moderately-doped samples, suggesting that it is directly related to the boron concentration [1].

A qualitative description of irradiation damage in boron-doped diamond, consistent with the available data, argued that boron-related irradiation damage features are primarily interstitial-related, rather than vacancy-related as in nitrogen-doped

material. No evidence for a boron-vacancy pair was observed, in any charge state. In stark contrast to the established nitrogen annealing behaviour in diamond, at least 60 % of the neutral boron acceptor concentration is recovered at moderate annealing temperatures.

Future work on irradiation of type IIb diamond should include the study of highly homogeneous type IIb samples of varying boron concentration and irradiation dose, to definitively identify those defects which incorporate boron. Existing investigations have focused on optical characterisation of samples post-irradiation: a thorough EPR annealing study could potentially correlate EPR-active defects with optical transitions, in addition to identifying defects with no optical features. The results presented here suggest that the study of $(\mathrm{V})^+$ will require samples irradiated such that $[(\mathrm{B_s})^0]_i \gg [(\mathrm{V})^0]_f$; in turn this may make EPR measurements difficult due to the conductivity of the samples.

9.1.1 The 1.913 eV luminescence transition

One of the luminescence transitions observed in the type IIb irradiation and annealing study, 1.913 eV (648.2 nm), was investigated further. Its integrated intensity was found to be maximised by a 14 h anneal at 600 °C. The centre was found to be present after both room temperature [2] and low temperature electron irradiation of boron-doped diamond.

Uniaxial stress measurements were performed on both natural and synthetic samples and identified the 1.913 eV luminescence with an $\mathbf{A}' \leftrightarrow \mathbf{A}''$ transition at a centre with $\mathscr{C}_{1\mathrm{h}}$ symmetry. Absorption and emission dipoles of the centre were shown to be oriented approximately along $\langle 1\,1\,1 \rangle$ and $\langle 5\,5\,3 \rangle$, respectively. An associated local mode at 178 meV (1437 cm^{-1}) was found to have $\mathbf{A}'$ symmetry.

Numerous differences between the same centre in natural and synthetic samples were highlighted. Problems with trying to ascertain the dipole orientations in the natural samples were attributed to non-equilibrium populations of different orientations of the centre. Furthermore, internal strains (of the order of 1.3(5) GPa) in plastically-deformed natural diamonds were shown to significantly complicate

the analysis of optical transitions. The linewidth of the transition was noticeably smaller in the studied synthetic samples (one CVD-grown, one HPHT-grown): a 4:1 intensity structure resolved in narrow-linewidth samples could indicate the incorporation of boron at the centre. A sample grown with modified boron isotopic ratios would determine whether the observed fine structure is boron-related.

The 1.913 eV transition was tentatively assigned to a defect containing a boron atom nearest-neighbour to a carbon interstitial: this model is the favoured boron-interstitial complex structure, although several other configurations are similar in energy [3]. The transition has not been observed in optical absorption measurements, suggesting that total concentration of the defect producing the transition is low: if the defect is a boron-interstitial complex then it may be in an unfavourable charge state or geometrical configuration, with the majority of the boron-interstitial complexes in the form producing the 0.553 eV absorption. A more advanced understanding of irradiation in type IIb material would also provide insight when trying to interpret the complicated annealing behaviour of the 1.913 eV transition.

9.2 Nitrogen aggregates in synthetic diamond

9.2.1 $(NVN)^-$

$(NVN)^-$ has been identified in HPHT-grown ^{15}N-doped diamond following electron irradiation and annealing. The symmetry, electronic structure, charge state and elemental constituents have all been identified. Analysis of the nitrogen and carbon hyperfine interactions were consistent with the assignment, and found that the unpaired electron spin density was almost 100 % localised on the two nearest-neighbour carbon atoms: this simple dipole-dipole approach is consistent with spin-polarised DFT calculations [4]. All available evidence supports the assignment of $(NVN)^-$ to the H2 optical transition.

It is commonly accepted that nitrogen aggregation in diamond is vacancy-assisted. NVN is therefore important in that any aggregate containing more than one ni-

trogen atom is assumed to have NVN as a precursor: NN, N_3V and N_4V are all understood to pass through NVN. The observation of $(NVN)^-$ in both ^{15}N- and ^{14}N-doped samples will allow the calibration of optical oscillator strengths and hence concentration measurements directly by optical measurements.

Future work should aim to positively identify the EPR-active $(NVN)^-$ defect with an optical analogue, assumed to be H2: optically detected magnetic resonance measurements would provide direct confirmation. Photochromism studies in infrared absorption, where H2 and $(N_s)^0/(N_s)^+$ can be monitored simultaneously, are expected to confirm that H2 photochromism is due to interaction with $(N_s)^0$. The sample investigated during the $(NVN)^-$ study was highly inhomogeneous, making optical oscillator strength measurements unreliable: either studying a single sector of this sample or producing $(NVN)^-$ in a more homogeneous sample will allow accurate oscillator strengths to be measured. H2 emits into the infrared (1.257 eV, 986.4 nm), and due to its photochromic behaviour has the potential for use in communication technologies.

9.2.2 $(N_3V)^0$

Following its production by irradiation and annealing, the P2 spectrum has been analysed in ^{15}N- and ^{14}N-doped diamond. ^{15}N enrichment significantly reduced the complexity of the EPR spectrum, and for the first time has enabled accurate analysis of the EPR arising from the ground state of this system. The P2 spectrum has been unambiguously assigned to the $(N_3V)^0$ model for the first time, and in ^{14}N-doped diamond the spin Hamiltonian parameters are now accurate enough to allow quantitative analysis along arbitrary crystallographic directions.

It is worthy of note that $(N_3V)^0$ was produced in the studied type Ib sample at an annealing temperature of 1900(100) °C — this is significantly lower than the published value of approximately 2300 °C for electron-irradiated type Ib samples [5]. This is ascribed to the initial neutron irradiation that the sample received (to a dose of 5×10^{17} neutrons cm^{-2}), so that the initially high vacancy concentration resulted in nitrogen aggregation at rates well above those usually observed in

electron-irradiated diamond [6].

Optical electron and nuclear spin polarisation of $(^{15}N_3V)^0$ was observed, and the energy and temperature dependence of the polarisation was studied. The activation energy for polarisation was found to be 2.4(2) eV, and the polarisation behaviour was unchanged up to the highest measured temperature of 140 K. Additionally, spin polarisation of $(^{15}N_s)^0$ was investigated: no spin polarisation of $(N_s)^0$ in either ^{15}N- or ^{14}N-doped diamond has been previously reported, even in samples which also contain $(NV)^-$. The $(^{15}N_s)^0$ spin polarisation was suggested to arise from coupling to $(^{15}N_3V)^0$. The coupling of these defects was taken as evidence for the failure of the localised dangling bond model, where only orbits inside the vacancy "cage" are required to describe the electronic structure — this is in contrast to $(NV)^-$, whose orbits are highly localised and whose external field sensitivity is due to dipolar interactions. A long-distance (up to ≈ 10 Å) wavefunction overlap was favoured as the cross-polarisation route from $(^{15}N_3V)^0$ to $(^{15}N_s)^0$. The observation of long-range electronic interaction between defects in diamond has technological potential: with the current focus on defects in diamond for quantum computing applications, defects such as $(^{15}N_3V)^0$ can be exploited as optically-activated gates to mediate interactions between neighbouring defects.

Any future work should investigate the coupling between $(^{15}N_3V)^0$ and $(^{15}N_s)^0$. When combined with a high time resolution laser, pulsed EPR measurements should be able to monitor the build-up and decay of polarisation on each defect and hence state lifetimes. Theoretical investigation into the electronic states involved might help to replicate these results in other samples, and to guide the direction of future experiments.

References

1. S. Dannefaer, K. Iakoubovskii, *Journal of Physics: Condensed Matter* **20**, 235225 (2008).
2. J. W. Steeds *et al.*, *Acta Materialia* **47**, 4025 (1999).
3. J. Goss, P. Briddon, *Physical Review B* **73**, 85204 (2006).
4. J. Goss, private communication.
5. A. T. Collins *et al.*, *Journal of Applied Physics* **97**, 83510 (2005).
6. A. T. Collins, *Journal of Physics C: Solid State Physics* **13**, 2641 (1980).

Appendix A

Site orientation reference

Given below are the site references for different point group symmetries, to be used in conjunction with §3.9.

	$\mathscr{D}_{2d}$		
	X	Y	Z
1	[1 0 0]	[0 1 0]	[0 0 1]
2	[0 1 0]	[0 0 1]	[1 0 0]
3	[0 0 1]	[1 0 0]	[0 1 0]

	$\mathscr{C}_{3v}$		
	X	Y	Z
1	[1 $\bar{1}$ 0]	[1 1 $\bar{2}$]	[1 1 1]
2	[$\bar{1}$ 1 0]	[$\bar{1}$ $\bar{1}$ $\bar{2}$]	[$\bar{1}$ $\bar{1}$ 1]
3	[1 1 0]	[1 $\bar{1}$ 2]	[1 $\bar{1}$ $\bar{1}$]
4	[$\bar{1}$ $\bar{1}$ 0]	[$\bar{1}$ 1 2]	[$\bar{1}$ 1 $\bar{1}$]

	$\mathscr{C}_{2v}$		
	X	Y	Z
1	[1 1 0]	[$\bar{1}$ 1 0]	[0 0 1]
2	[$\bar{1}$ 1 0]	[1 1 0]	[0 0 $\bar{1}$]
3	[0 1 1]	[0 $\bar{1}$ 1]	[1 0 0]
4	[0 1 $\bar{1}$]	[0 $\bar{1}$ $\bar{1}$]	[$\bar{1}$ 0 0]
5	[1 0 1]	[1 0 $\bar{1}$]	[0 1 0]
6	[$\bar{1}$ 0 1]	[$\bar{1}$ 0 $\bar{1}$]	[0 $\bar{1}$ 0]

	$\mathscr{C}_{1h}$		
	X	Y	Z
1	[0 0 1]	[1 $\bar{1}$ 0]	[1 1 0]
2	[0 0 $\bar{1}$]	[1 1 0]	[1 $\bar{1}$ 0]
3	[0 0 1]	[$\bar{1}$ 1 0]	[$\bar{1}$ $\bar{1}$ 0]
4	[0 0 $\bar{1}$]	[$\bar{1}$ $\bar{1}$ 0]	[$\bar{1}$ 1 0]
5	[1 0 0]	[0 1 $\bar{1}$]	[0 1 1]
6	[$\bar{1}$ 0 0]	[0 1 1]	[0 1 $\bar{1}$]
7	[1 0 0]	[0 $\bar{1}$ 1]	[0 $\bar{1}$ $\bar{1}$]
8	[$\bar{1}$ 0 0]	[0 $\bar{1}$ $\bar{1}$]	[0 $\bar{1}$ 1]
9	[0 1 0]	[$\bar{1}$ 0 $\bar{1}$]	[$\bar{1}$ 0 1]
10	[0 $\bar{1}$ 0]	[$\bar{1}$ 0 1]	[$\bar{1}$ 0 $\bar{1}$]
11	[0 1 0]	[1 0 1]	[1 0 $\bar{1}$]
12	[0 $\bar{1}$ 0]	[1 0 $\bar{1}$]	[1 0 1]